UNIVERSITY OF CAMBRIDGE

Extending the astronomical calibration of the geological time scale

by

Heiko Pälike

Clare College

This dissertation is submitted for the degree of

Doctor of Philosophy

University of Cambridge

October 2001

Declaration

"This dissertation is the result of my own work and includes nothing which is the outcome of work done in collaboration. It does not exceed the page limit and is not substantially the same as any work that has been, or is being submitted, to any other University for any degree, diploma, or other qualification."

Heiko Pälike October 2001

Abstract

This thesis arises from the fact that changes in the geometry of the Earth-Sun system, due to the gravitational interaction among the planets, cause quasi-cyclic climatic variations that are imprinted in the geological record.

A speech-recognition method is adapted to provide an automated procedure to calibrate cyclic geological data to astronomical calculations. Synthetic data are used to test the performance of the new method. The new algorithm is then applied to lithological data. Results show that the method is well suited to objectively match geological data to astronomical calculations of the Earth's orbit.

The calibration of the geological time scale is extended into the late Paleogene. This is achieved by generating a lithological proxy record employing an X-ray fluorescence Core Scanner that non-destructively determines elemental concentrations of calcium and iron on split sediment cores. These data exhibit cyclic variations that are shown to be of astronomical origin, and are then used to calibrate the relative duration of magnetochrons C16 through C18. Advanced time series analysis methods are used to extract the astronomical signal. It is shown that the most recent published astronomical solution is not compatible with geological data from the late Paleogene.

This new late Eocene time scale is independently confirmed by measurements of stable isotope ratios of oxygen and carbon, obtained from the same material, providing a high-resolution record of climatic variations over intervals of the late Middle and Late Eocene for the first time.

Astronomically calibrated geological data are analysed to extract parameters that are required for the calculation of detailed astronomical models. Very small changes in the precession constant of the Earth are extracted by developing a new interference method. This leads to the extraction of the long-term evolution of the tidal dissipation and dynamical ellipticity parameters of the Earth.

Geological data spanning the last $\sim$37 million years are used to extract long term amplitude modulation patterns of the climatic signal. A comparison of the long term amplitude modulation derived from published astronomical calculations on the one hand, and those derived from a new calculation on the other hand (J. Laskar, 2001, unpublished) shows that the geological record supports the validity of the new solution. This study forms the basis for a further extension of the astronomical calibration of the geological time scale into earlier parts of the Paleogene.

Acknowledgments

Nick Shackleton has been a constant source of encouragement, enthusiasm, superb ideas, friendship, and excellent food. Without doubt working with him has been the greatest experience during my research. My parents and brother have provided support in every possible way, and I could not be more grateful for their encouragement, interest and help.

Throughout my research I have been encouraged and helped by many superb characters. Jacques Laskar at the Bureau des Longitudes and Paris, and his colleagues Alexandre Correia and Benjamin Levrard, were always interested in the implications of geological research on their invaluable astronomical calculations. They helped me in many ways, and provided excellent hospitality during several trips to Paris. Marie-France Loutre at the Université Catholique de Louvain taught me astronomical theory and spectral analysis during her sabbatical in Cambridge, and was very patient in answering many questions. I also thank her colleagues Michel Crucifix and André Berger.

Jerry Mitrovica and Jon Mound, at the University of Toronto, have been very interested in the implications of this research on mantle convection, and provided excellent feedback and critical comments. Jerry's invitation to Toronto was one of the highlights during my research. Andy Gale and Ewan Laurie at the University of Greenwich introduced me to the delights of Eocene successions on the Isle of Wight, and in addition increased my knowledge of great wines, indigenous sea-food, and were always a good source of humour. Jim Zachos and Lisa Sloan gave immense encouragement, friendship, and support. Bridget Wade allowed me to work with her samples, and was great in every other way.

Didier Paillard (Gif-sur-Yvette), Andreas Prokoph (Ottowa), Athanassios Kassidas (McMaster University) and Benjamin Cramer (Rutgers) provided many software tools that proved invaluable during the course of this research.

I also thank Graham Weedon, Lucas Lourens, Ulla Röhl, Paul Wilson, Tjeerd van Andel, Alan Smith, Nicky White, Dan McKenzie, Paul Pearson, Isabella Raffi, Phil Saxton, Nick McCave and Harry Elderfield for advice. Simon Crowhurst provided inspiration for many things, of which computing was only one aspect. I also thank everyone else in the Department and the Godwin Laboratory, past and present.

Sam Gibbs proved to be a great friend and office partner, providing constant fun and encouragement. Other people that come to mind in no particular order are Fiona, Sam B., Paul F., Paul B., Kitty, Paul W., Steve J., Steve B., Marie, Carrie, Paula, Emily, Emilie, Tim, Hayley, Mark R., Patrizia, Lucia, Luke, Isabel C., Isabel S., John, Jon, Ben W., Chop, Henning, Angus, Martin, Jim, Alex W., Dave L., Ed, Charlie, Dan, Megan, Debs, Mike, Carine, Jemma, and without doubt many others who I inadvertently forgot. Thank you all for great fun!

Financial support was provided by the University of Cambridge, NERC studentship GT4/98/ES/50, the Cambridge Philosophical Society, Clare College, the Cambridge European Trust, a Royal Society-CNRS traveling grant, a Shell postgraduate bursary, and the British Chamber of Commerce in Germany. Writing this dissertation has been greatly facilitated by the use of the LaTeX document preparation system.

Contents

List of Figures

List of Tables

Chapter 1

Introduction, historical overview and astronomical theory

1.1 Introduction

Changes in the geometry of the Earth-Sun system, due to the gravitational interaction between the bodies of the solar system, give rise to quasi-cyclic climatic variations that are recorded in the geological record. The work presented in this dissertation makes use of this phenomenon to extend the astronomical calibration of the geological time scale into the Eocene. As astronomical calculations are inherently limited in the duration over which they can be calculated with confidence, it is necessary to validate astronomical models by extracting orbital parameters from the geological record. The aim of this dissertation is to provide a consistent framework for a further extension of an astronomically calibrated time scale through the generation and analysis of new data, as well as by improving the theoretical understanding of how geological data can be used to validate astronomical models.

1.2 Outline of Dissertation

1.2.1 Chapter one outline

The remainder of chapter one provides a historical overview of the developments that led to the modern understanding of geological time. Chapter one then outlines the historical developments that were specifically concerned with the use of astronomical variations that are recorded in the geological record. A brief summary is given of recent developments in the use of "cyclostratigraphy". An important part of this chapter is a summary of astronomical theory as far as it relates to orbital patterns that can be observed in the geological record. A short summary is given of how long, continuous high-resolution geological records are generated from deep-marine sediments.

1.2.2 Chapter two outline

Chapter two provides a theoretical framework describing how it is possible to quantitatively correlate geological data with templates given by astronomical calculations. A speech-recognition algorithm is adapted to compute age-depth relationships according to certain criteria and constraints. This method is first tested with synthetic data, and then applied to real geological data. The advantages and limitations of an automated approach to stratigraphic and time scale correlation are demonstrated.

1.2.3 Chapter three outline

Chapter three presents new data from the late Middle and Late Eocene that were generated from material recovered during Ocean Drilling Program (ODP) Leg 171B. An X-ray fluorescence core scanner was used to measure elemental concentrations in marine sediments. First it is demonstrated that these data are consistent with an orbital forcing. The quasi-cyclic variations inherent in these data are then used to estimate the relative duration of magnetochrons C16 through C18. These data are also used to extract long term amplitude modulation signals, which are shown to be incompatible with the most recently published astronomical calculation. The new age model is transferred to ODP Site 1090, which allows a validation of the duration of magnetochrons.

1.2.4 Chapter four outline

Chapter four presents additional stable oxygen and carbon isotope data that were generated from the same material as that discussed in chapter three. These data support the conclusions reached in chapter three, and provide an independent check of the plausibility of the age model developed therein. These data provide a high-resolution record of climatic variations over intervals of the late Middle and Late Eocene for the first time.

1.2.5 Chapter five outline

Chapter five deals with the extraction of astronomical parameters from geological data over the last ∼37 million years. It thus presents a complementary approach to work presented in chapters three and four, where astronomical calculations were used to generate a geological time scale. Astronomically calibrated geological data are analysed to extract parameters that are required for the calculation of detailed astronomical models. Very small changes in the Earth's precession constant are extracted by developing a new interference method. This technique leads to the extraction of the long-term evolution of the tidal dissipation and dynamical ellipticity parameters of the Earth for the last 25 million years.

Geological data spanning the last ∼37 million years are used to extract long term amplitude modulation patterns of the climatic signal. A comparison of the long term amplitude modulation derived from published astronomical calculations, and those derived from a new calculation (J. Laskar, 2001, unpublished), shows that the geological record supports the validity of the new solution. This study forms the basis for a further extension of the astronomical calibration of the geological time scale into earlier parts of the Paleogene.

1.2.6 Chapter six outline

Chapter six provides conclusions and suggestions for further work that arise from the work presented in this dissertation. The data of Eocene age from chapters three and four, together with the theoretical approaches presented in chapters two and five, provide a framework that will allow a further extension of the astronomically calibrated geological time scale into earlier parts of the Cenozoic.

1.3 The age of the Earth - A historical overview

Since this dissertation is concerned with the determination of the duration and age of sedimentary layers, it is appropriate to give a short historical overview of the developments that led to the modern understanding of geological age and stratigraphy. Due to its significance for observations of natural processes, and its direct impact on religious and philosophical thinking, the age of the Earth and its sedimentary layers has been the subject of many historical accounts and hypotheses.

The earliest known records that report geological observations, relating to the time and duration of landscape forming processes, date back as far as the sixth century B.C. The Greek philosopher Xenophanes of Colophon observed shells embedded into the cliffs on the island of Malta, and proposed that the land was periodically covered by the sea [1]. He recognised the significance of fossils as a record of former life, and interpreted the layers of sedimentary rocks as the result of sediment accumulating on the bottom of the sea over a long interval of time. Around 450 B.C. the Greek historian Herodotus travelled through the Nile river valley and described and named the Nile delta [2]. His observation of sedimentary layers, and embedded fossils, led him to conclude that the Nile delta must have originated from a large number of floods, representing at least several thousands of years.

During the Renaissance, Leonardo da Vinci (1452-1519) described sea shells from the Apennine Mountains, and postulated that these were the remains of organisms that had been buried by river muds from the Alps, before they were petrified and later uplifted [3]. Following the rise of the power of the western Church, the knowledge accumulated from previous observations was suppressed and ignored during medieval times, when several theologists used a literal interpretation of the book of Genesis to "calculate" the age of the Earth. The most cited example is probably that of Archbishop of Armagh James Ussher, who claimed in 1650 that the year of creation was 4004 B.C. [4][1].

It was not until the pioneering works of the famous Scottish geologist James Hutton (1726-1797) [5; 6] that it was recognised again that the sedimentary deposits on the surface of the Earth resulted from continuing geological processes, rather than being caused by single "catastrophic" events. Hutton observed how weathering, erosion

[1] As a historical curiosity, it was Ussher's contemporary Dr. John Lightfoot (1602-1675), Vice Chancellor of the University of Cambridge, who proposed an exact day and time for the creation of Man, predating the publication of Ussher.

and sedimentation slowly form soft sediments, which are subsequently slowly buried, heated, compressed, and uplifted to complete the sedimentary cycle. He appreciated that the Earth must be immensely old, and famously stated that

> *"The result, therefore, of our present enquiry is that we find no vestige of a beginning, no prospect of an end."*

Together with the subsequent support of Hutton's theories by Charles Lyell (1797-1875) through his influential publication of "Principles of Geology" [7], it was the work of the engineer and surveyor William Smith (1769-1839), through his analysis and map of faunal successions in England and Wales [8], that laid the foundation for modern stratigraphic approaches in the geological sciences. His work, in turn, forms the basis for approaches to the subdivision of geological strata according to relative time. By then it was firmly established within the geological community that sedimentary rocks represent an unfathomably long amount of time. The first calculations of the total age of the Earth were made, accounting for the thickness of sediment observed at the Earth's surface, and assuming that the present rate of erosion and deposition was representative of the past. This uniformitarian approach led to estimates of the age of the Earth of the order of millions to hundreds of millions of years.

In 1862, William Thomson (1824-1907), later Lord Kelvin, made public a calculation of the age of the Earth based on a thermodynamic cooling model [9]. His original age limit was 20 to 400 million years. Considering the physical principles known at the time, and calculating the dissipation of energy from the Sun, he later arrived at an age estimate of the Earth of between 24 and 40 million years. This age was considered much too young by contemporary geologists, including Charles Darwin, but had an enormous impact due to Lord Kelvin's authority in many fields of science.

Lord Kelvin's "strangle-hold" on the age of the Earth was only challenged in 1896 by the discoveries connected with radioactivity by Becquerel [10], Röntgen, and the Curies. Not only did radioactive decay invalidate Lord Kelvin's calculation through the supply of extra heat to the Earth's interior, but also allowed the development of radiometric dating techniques. Boltwood made use of these techniques in 1907 [11] by combining information on the half-life of uranium with the proportion of lead found within uranium deposits, and estimated the age of the Earth as 2.2 billion years. The oldest rocks found on Earth so far, according to radiometric dating methods, have an age exceeding four billion years [12].

The basis for a modern biostratigraphic approach was formalised by William Smith, but it was the discovery of sea-floor spreading (see, e.g., Hess, 1962 [13]), and the magnetic reversal record (Vine and Matthews, 1963 [14]), that provided an important prerequisite for the modern stratigraphic approach in the Earth sciences, where radiometric decay methods allow the dating of bio- and magnetostratigraphic events that can potentially be correlated globally (Cox *et al.* (1963) [15]). The next section outlines the history of the development of a cyclostratigraphic approach, where the relative duration of cyclical patterns in geological records is estimated and correlated by using astronomical theory.

1.4 A history of cyclostratigraphy and "Milankovitch" theory

It is appropriate to give a separate historical overview of the scientific thoughts and discoveries that led to the development of the astronomical theory of palaeoclimates and cyclostratigraphy, i.e. the use of astronomical cycles, recorded in geological successions, as a measure of time. The recognition of changes in climate, reflected in sedimentary rocks, has been the subject of scientific interest for at least the last 170 years, and predates the "modern" approaches of Lord Kelvin, the discovery of radioactivity, and the invention of radiometric dating. Astronomical theory was first invoked by scientists who wanted to explain the occurrence of glaciations in the past, rather than to examine the question of geological time. A thorough historical overview of the quest to solve the mystery of the ice ages was given by Imbrie and Imbrie (1979) [16]. Their book covers the discoveries up to the late 1970s, and here only a brief summary is given for the early history.

Describing the scratches on and the location of boulders found around the Jura mountains, the idea of past glaciations was proposed by Louis Agassiz (1837) [17; 18], who followed the ideas of Jean de Charpentier in the early 1830s. Although at first facing strong opposition from fellow geologists, the ideas of Agassiz were later accepted by most of the geological community, particularly by the influential Charles Lyell in 1841. In 1842, the French mathematician Adhémar was the first to suggest that variations in the orbit of the Earth around the Sun were responsible for glacial periods [19]. The mechanism that Adhémar invoked was the direct gravitational pull of the Sun and Moon on ice-caps. Although this idea was rejected by most contemporaries as absurd, his book, together with the studies of Agassiz, inspired James Croll to begin work on the

causes of ice ages in the 1860s.

Croll was arguably one of the most important figures in the historical development of the relationship between astronomical theory and climate. Building on astronomical calculations by Le Verrier (1856) [20], he published the influential "Climate and time in their geological relations" in 1875 [21]. The contribution of Croll was of great significance because, for the first time, he considered the combined effects of the axial tilt and the precession of the equinoxes of the Earth's orbit, in addition to the orbital eccentricity, on the seasonal variations in insolation during perihelion and aphelion (those points on the orbit of the Earth closest to, and furthest from, the Sun, respectively). Croll developed detailed models of how the volume of ice varies in time, and proposed that the initiation of glacial stages is controlled by cold northern hemisphere winters, and short, hot summers. He was the first to consider the effects of albedo as a positive feedback mechanism. His book contains many ideas about ocean circulation and climatology that are still valid. It would be fair to say that Croll was one of the founders of quantitative palaeoceanography.

Subsequently, however, some of Croll's predictions and ideas dissatisfied geologists and meteorologists alike, and led to the temporary abandonment of his ideas. One of Croll's theories was that the last glacial interval ended 80 thousand years ago, in conflict with new evidence at the time that this time estimate should be much younger. Meteorologists noted that Croll's proposed changes in the heating from the Sun, according to astronomical variations, would cause a change in climate of much smaller amplitude than required, and opposed the implication from Croll's theory that ice ages occurred at alternating times in the southern and northern hemisphere. Interestingly, though, his ideas still led to a revival of the idea that rhythmic sedimentary alternations could be interpreted as a measure of time. This interpretation was proposed by Gilbert in 1895 [22], who attributed cyclic Cretaceous strata to a precessional forcing.

Although several studies challenged Croll's theory that long, cold winters, and short, hot summers favour glaciations, and in fact arrived at the opposite conclusion [23; 24], it was not until the work of Milankovitch during the 1920s through the 1940s that a detailed mathematical approach to the change of insolation became available.

The Serbian mathematician and geophysicist Milutin Milankovitch[2] (1879-1958) advanced the theory of the ice ages by computing the solar irradiance at different lat-

[2] Milanković in the Serbian writing

itudes and different seasons of the year [25; 26]. As a result, he proposed what is now known as the "Milankovitch" theory of glaciations, where the variation in solar radiation at high northern latitudes is responsible for the waxing and waning of ice. In particular, Milankovitch proposed that conditions favouring glaciations are short cold summers, thus preventing the melting of ice accumulated over the winter, aided by enhanced evaporation and precipitation during mild winters. According to Milankovitch, to achieve short and cold summers, the necessary conditions include a northern hemisphere summer during aphelion, a minimum in obliquity leading to a weaker seasonal contrast, and a maximum in eccentricity, leading to an increased distance between the Earth and the Sun at the aphelion during summer.

Milankovitch's theory was not well received at the time, partly for the same reasons that Croll's ideas were criticised. Without consideration of the uneven distribution of land masses between the northern and southern hemispheres, and without considering the complex interplay of ocean circulation patterns and climate, Milankovitch's theory would predict alternating southern and northern hemisphere glaciations. Later research showed that the Quaternary ice age cycles occurred approximately every 100 thousand years (ky)[3], which was at odds with Milankovitch's predictions for the strongest frequency components, which are in fact the obliquity and precession frequency components, rather than the much weaker $\sim$100 ky eccentricity component.

The essence of Milankovitch's astronomical theory, i.e. that variations in insolation drive changes in climate, was finally accepted following the analysis of deep-sea sediment cores in the 1970s, which showed the presence of the obliquity and precession components in addition to the eccentricity component. Following the pioneering statistical evaluation of cyclic patterns in the rock record by Schwarzacher [27; 28], Hays *et al.* (1976) [29] published a seminal paper that demonstrated statistically the presence of obliquity and precession cycles in the geological record. Their analysis was made possible by advances in the analysis of stable isotope ratios by Urey and later by Emiliani (1955, 1966) [30; 31]. The paper by Hays *et al.* spawned a large number of studies investigating the relationship between astronomy, climate and time that have continued until the present, although there are still contrasting views on the exact nature of astronomical forcing and time lags between the forcing and the recording in the geological record (see, e.g., Henderson and Slowey (2000) [32] and Herbert *et al.* (2001) [33]).

[3]Throughout this thesis, durations are denoted by ky for thousands of years, My for millions of years etc., while ages (positive for before present) are denoted by ka, Ma and Ga

Following the work done in the early 1970s, the history of the "ice ages" was more thoroughly investigated and resulted in many ground-breaking publications, including the CLIMAP and SPECMAP projects [34–37]. The discovery of split peaks in the precession frequency band in geological data also tied in neatly with more accurate calculations of the Earth's orbit by Berger (1978) [38], which further enhanced scientific interest in the subject.

1.5 The development of detailed astronomically calibrated time scales

After the presence of orbitally related variations in the climatic record of the Quaternary was confirmed, the search for astronomical frequencies was extended to older parts of the geological record. It can be argued that advances in the use of astronomical cycles as a measure of time were slowed by the initial close linkage between astronomical variations, and records and causes of the ice ages. As shown by Pisias and Moore (1981) [39], and investigated later by Ruddiman *et al.* (1986) [40], the Quaternary shows an unusually strong ∼100 ky long "sea-saw" pattern in marine climate proxies. This regime was preceded (before ∼1.3 Ma) by a more dominant obliquity and climatic precession component with periodicities of ∼41 ky, and 23 ky and 19 ky, which can be more easily reconciled with the relative amplitude of these cycles in the insolation forcing.

This discovery was important, because to some extent it allowed the separation of the detailed investigation of the causes of the ice ages and climatic variations on the one hand, and the use of orbitally controlled cyclicity in the geological record as a tool to estimate time on the other hand. This process was initiated by the landmark paper of Shackleton *et al.* (1990) [41], which proposed for the first time an absolute dating of the Brunhes-Matuyama magnetic reversal that was based on an astronomical calibration, and which implied an age of 780 ka, approximately 5-7% older than previous radiometric estimates. This older age was later confirmed by high-precision $^{40}Ar/^{39}Ar$ dating of lavas close to the Brunhes-Matuyama boundary [42] and demonstrates the use of astronomically calibrated time scales.

Shortly afterwards, several marine successions in the Mediterranean were found to show exceptionally clear astronomically controlled variations in calcium carbonate content at all astronomical frequencies, and allowed a confirmation and extension

of the astronomically calibrated Neogene geological time scale (Hilgen, 1991 [43; 44]). These studies were significant because, for the first time, they allowed the integration of astronomically calibrated ages with the geomagnetic polarity time scale (GPTS) by Cande and Kent (1992,1995) [45; 46] (also reviewed by Kent, 1999 [47]). This is only one example of how the detailed high-resolution study of cyclic variations in the sedimentary record can have an impact on other fields in the Earth sciences.

During the course of the last fifteen years, a very large number of studies have found evidence of orbitally controlled cyclicity in the geological record at intervals throughout the Phanerozoic. Some representative (but non-exhaustive) examples can be given from the Cenozoic era [41; 43; 44; 48–55], the Mesozoic era [56–63], as well as the Paleozoic [64]. There have now also been a large number of attempts to contribute to the understanding of the response of the climate system to orbital forcing through modelling studies (see, e.g., Short *et al.* (1991) [65]). Detailed insights into the behaviour of the climate system in the past have also been obtained from ice cores (see, e.g., Barnola *et al.* (1987) [66] and Petit *et al.* (1999) [67]). Records of past atmospheric composition, obtained from air bubbles trapped inside the ice, provide a very important direct archive of climate change over the last few hundred thousand years, and have recently been used to gain an important understanding of the complex interplay between orbital forcing, ice dynamics, and the climate system (Shackleton, 2000 [68]). It is beyond the scope of this overview to give a detailed account of all publications, but due to the recognition of the significance and prevalence of orbitally controlled cycles in the geological record, there now exist several collections of papers that can be consulted to obtain references to a significant part of the relevant literature [69–74].

1.6 Astronomical theory

The basis for the work presented in this dissertation is the detailed calculation of variations in the Earth's orbit around the Sun. This section aims to provide the necessary framework by summarising celestial mechanics as a far as they are related to Earth's climatic variations. Astronomical theory, and the question of whether or not the solar system is stable over long periods of time, forms an interesting subject in its own right, and detailed discussions of the historical developments in the astronomical theory were given by Laskar (1992, 1994, 1996) [75–77], Loutre (1993) [78] and Berger (1995) [79]. Most of the detailed mathematical theory can be found in Berger *et*

al. (1978,1991,1992,1993) [38; 80–82], Loutre (1993) [78], Laskar (1986,1988,1990,1993) [83–86], and deSurgy and Laskar (1997) [87].

1.6.1 Celestial mechanics

The time-varying motion of the planets and other satellites around the Sun is controlled by their mutual gravitational interaction. It can be described by Newton's laws, corrected by Einstein's principles of general relativity. The behaviour of the solar system is complex, because it is posed as an n-body problem (which can only be solved numerically), and is further complicated by physical parameters such as the tidal dissipation of energy as well as the detailed distribution of mass within each body. As a result of this complexity, the planets do not follow stationary orbits around the Sun, but undergo quasi-periodic as well as chaotic motions that, from a climatic point of view, affect the amount, distribution, and timing of solar radiation received at the top of the Earth's atmosphere.

At any given time, the orbit of a body can be described by six parameters, which are traditionally the six "Keplerian orbital elements". These parameters define the position, shape, and orientation of the orbit, and the location of a body on this orbit, with respect to a frame of reference. The trajectory of the orbiting body follows an ellipse which, in the case of the solar system, has the Sun located at one focal point. Due to the gravitational interaction of the different planets, the orientation and dimension of this ellipse change over time.

Figure 1.1 illustrates the definition of the six Keplerian elements, as applied to the Earth on its orbit. The reference plane, which is fixed with respect to the stars, is typically chosen as the orbital plane of the Earth at a particular time (e.g. 1850, 1950 or 2000 A.D.), and is called the "ecliptic of epoch". Alternatively, for certain calculations, it can be chosen to coincide with the invariable plane of the solar system, which is the "average" plane defined by the total angular momentum of the solar system. This "invariant" plane almost coincides with the orbital plane of Jupiter due to its large mass. The reference plane is defined by two axes. One of these is typically the position of the mean vernal (spring) equinox on the reference plane at a given time, denoted by γ, while the second axis is perpendicular to this axis as well as to the reference plane ("Z"), both originating from the position of the Sun ("S") on the reference plane.

The six Keplerian elements are (a, e, i, λ, $\widetilde{\omega}$, Ω). The parameter a is the semi-major

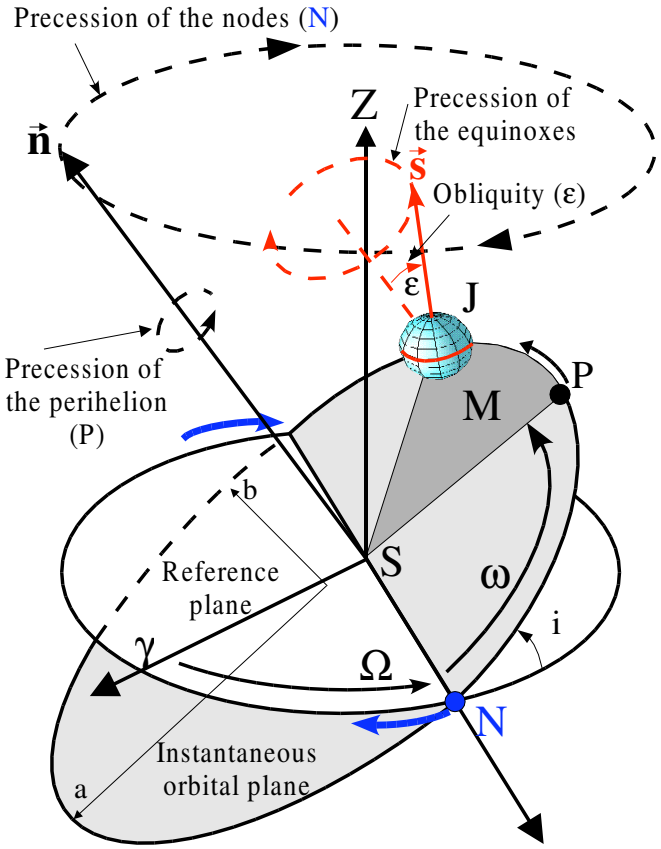

Figure 1.1: Orbital elements of the Earth's movement around the sun.

axis of the orbital ellipse, which corresponds to the average radius. The eccentricity e of the ellipse is defined as $e = \frac{\sqrt{a^2-b^2}}{a}$, where b is the semi-minor axis of the ellipse. The inclination of the orbit with respect to the reference plane is given by the angle i. The position of the ascending node N is specified by the angle Ω ("longitude of the node"), measured from the fixed direction in the reference plane (γ). The parameter $\widetilde{\omega}$ specifies the position of the moving perihelion P (the closest approach to the Sun) and is defined as $\widetilde{\omega} = \Omega + \omega$ ("longitude of the perihelion"). Finally, the sixth Keplerian element λ specifies the position of the orbiting body ("J") on its elliptical orbit, and is defined as $\lambda = \widetilde{\omega} + M$, where M ("mean anomaly") is an angle which is proportional to the area SPJ (Kepler's third law).

1.7 The origin of orbital frequencies

If Earth were the only planet orbiting the Sun, and in the absence of dissipative effects and other physical processes, the position and orientation of its orbit would remain

fixed for all times. In this situation, the only Keplerian element that would change over time would be λ, which describes the position of the body on its orbit. In this case, the position and velocity of the orbiting body would vary according to the Keplerian laws of motion around a fixed ellipse.

However, gravitational interactions between all bodies of the solar system cause changes in the shape and orientation of the elliptical orbit on various time scales, which are typically of the order of $10^4 - 10^6$ years. From a climatic point of view, the relevant variations are those obtained after averaging the planetary orbits over their long-term orbital periods. These are called secular variations, and can be described by a set of fundamental frequencies.

The variation in the orbital elements that characterises the secular variations can be separated into two types, which are related to different types of precession movements. The first group is the variation within the orbital plane, and is described by the variation of the eccentricity e, and the rotation of the location of the perihelion, described by ω. The second group is the variation of the orientation of the orbital plane, and is described by the inclination angle i, and the location of the ascending node N, described by Ω. These oscillations are coupled such that one can investigate the behaviour of these parameters as pairs (e, ω) and (i, Ω).

1.7.1 Fundamental frequencies of the solar system

By computing the orbital elements for the main eight planets (Pluto is excluded), one obtains eight characteristic modal frequencies for each of the paired elements (e, ω) and (i, Ω). Table 1.1 lists these fundamental frequencies, as estimated by Laskar (1990) [85] over the last 20 My. Individual frequencies g_i are related to variations in the pair (e, ω), while frequencies s_i are related to variations in the pair (i, Ω). The individual g_i and s_i frequencies arise as eigenvalues if Poisson equations are used to expand the orbital elements for the eight planets. As eigenvalues of a matrix, they are not strictly associated with a particular planet. However, since the matrix from which they are obtained has a diagonal structure, suppressing a planet removes one set of frequencies while not changing the other frequencies significantly (Laskar, personal communication). Thus, the indices in g_i, s_i can be used to indicate which planet provides the strongest contribution to a particular frequency (g_1, s_1 correspond to Mercury, g_3, s_3 to Earth, and so on). Note that all of the g_i terms are positive, indicating that the perihelia advance

Fundamental orbital frequencies related to (e, ω)			related to (i, Ω)			
term	frequency ($''$/a)	Period (ky)	term	frequency ($''$/a)	Period (ky)	associated Planet
g_1	5.596	231.0	s_1	-5.618	230.0	Mercury
g_2	7.456	174.0	s_2	-7.080	183.0	Venus
g_3	17.365	74.6	s_3	-18.851	68.7	Earth
g_4	17.916	72.3	s_4	-17.748	73.0	Mars
g_5	4.249	305.0	s_5	0.000		Jupiter
g_6	28.221	45.9	s_6	-26.330	49.2	Saturn
g_7	3.089	419.0	s_7	-3.005	431.0	Uranus
g_8	0.667	1940.0	s_8	-0.692	1870.0	Neptune

Table 1.1: Fundamental orbital frequencies of the precession motions in the solar system, computed as mean values over 20 million years by Laskar (1990) [85]. The g_i and s_i are eigenvalues that characterise the evolution of the orbital elements (e, ω) and (i, Ω), respectively, and are loosely associated with the eight planets considered, i.e. g_1, s_1 correspond to Mercury, and g_8, s_8 correspond to Neptune. Periods in years can be calculated from arcseconds per year as $period(a) = \frac{360 \times 60 \times 60}{frequency(''/a)}$.

counter-clockwise if viewed from the "north" of the orbital axis (shown in figure 1.1). In contrast, seven out of the eight s_i terms are negative, indicating that the position of the nodes, which mark the intersection of the orbital plane with the reference plane, regress (rotate clockwise). The frequency s_5 is zero because the invariant plane is close to the orbital plane of Jupiter due to Jupiter's large mass.

1.7.2 General precession of the Earth

In addition to the fundamental orbital frequencies, which apply to the solar system as a whole, there are two additional fundamental frequencies which are necessary to describe the orbital motion of the Earth. The formation of an equatorial bulge is caused by the rotation of the Earth, and other processes redistribute mass on Earth (the formation of ice caps at high latitudes, and mantle convection). These processes result in a torque that is applied to the Earth by the Sun, the Moon, and the other planets. The combined effect from the Sun and the Moon equals approximately two thirds of the total applied torque [88]. Similar to a spinning top, this applied torque results in the nutation and precession of the Earth's spin axis. The nutational component leads to a "nodding" motion of the Earth's spin axis, while the precessional component makes the Earth's spin axis trace out a cone, as illustrated in figure 1.1. From a climatic perspective

only the precession component has a significant effect.

With respect to the fixed stars, the frequency of this precessional cycle is denoted as p, and has a period of approximately 25.8 ky. The precession of the Earth's spin axis has several effects on the Earth's climate system, one of which is that the position of the seasons with respect to the Earth's orbit, defined by the solstices and equinoxes with respect to the perihelion and aphelion of the orbit, changes over time. For this reason the precession of the Earth's spin axis is also called the "precession of the equinoxes". This precession will be discussed in more detail in one of the following sections.

As shown in figure 1.1, the precession of the Earth's spin axis traces out a cone that forms an angle with the Earth's orbital plane. This angle is the obliquity (tilt) of the Earth, and is denoted by ϵ. This angle changes due to the combined effect of the precession of the Earth's spin axis and the changing orientation of the Earth's orbital plane, which will be discussed in more detail in a following section.

As a first order approximation, the fundamental frequencies g_i and s_i can be used together with the precession constant p to explain the origin of almost all periodicities that affect the climate system. They arise from "beats" between the fundamental frequencies. In detail, though, additional resonance terms are present in the solar system, which lead to the presence of chaos (Laskar, 1990 [85]). The presence of chaos in the solar system has important consequences, which will be discussed separately in section 1.7.9. The following sections discuss how the three orbital parameters eccentricity, obliquity, and climatic precession, which are involved in the calculation of the solar radiation, are related to the fundamental frequencies of the solar system

1.7.3 Eccentricity

The Earth's orbital eccentricity e quantifies the deviation of the Earth's orbital path from the shape of a circle. It is the only orbital parameter that controls the total amount of solar radiation received by the Earth when averaged over the course of one year. The present eccentricity of the Earth is $e \approx 0.01671$, as given by the most recent astronomical calculation of Laskar *et al.* (1993) [86]. In the past it has varied between ~0–0.06. The eccentricity value can be used to compute the difference in the distance of the Earth to the Sun between their closest and furthest approach (perihelion and aphelion), and presently amounts to $2e \approx 3.3\%$. Although the exact values of orbital parameters should be computed by numerical integration [85], it is possible to approximate

Five leading terms for Earth's eccentricity			
term	frequency ($''$/a)	Period (ky)	Amplitude
$g_2 - g_5$	3.1996	406.182	0.0109
$g_4 - g_5$	13.6665	94.830	0.0092
$g_4 - g_2$	10.4615	123.882	0.0071
$g_3 - g_5$	13.1430	98.607	0.0059
$g_3 - g_2$	9.9677	130.019	0.0053

Table 1.2: Principal eccentricity frequency components in the astronomical solution La93$_{(1,0)}$, analysed over the last 4 My and reproduced from [89]. The frequency terms g_i refer to those given in table 1.1.

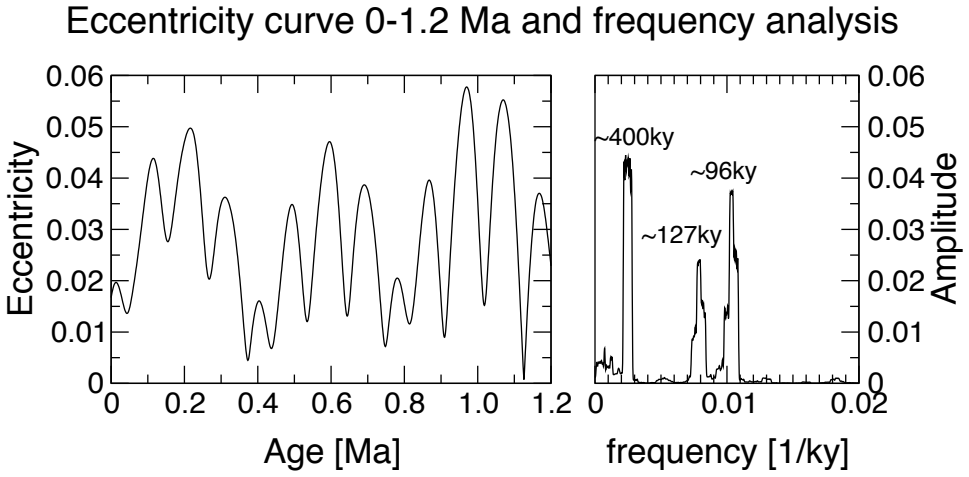

Figure 1.2: Earth's orbital eccentricity from 0-1.2 Ma [85] and Thomson multi-taper frequency analysis [90] from 0-10 Ma.

the calculation as a series of quasi-periodic terms, some of which are listed in table 1.2.

It is important to point out that the eccentricity frequencies are completely independent of the precession constant p. The Earth's eccentricity frequency component with the largest amplitude has a period of approximately 400 ky, and arises mainly from the interactions of the planets Venus and Jupiter, due to their close approach and large mass, respectively. This component is called the "long" eccentricity cycle, and of all of Earth's orbital frequencies it is considered to be the most stable [89]. Additional terms can be found with periods clustered around ∼96 and ∼127 ky. These are called "short" eccentricity cycles.

An important feature of all orbital components is the presence of "beats". These arise from the interaction of different frequency components, and produce a modulation in amplitude. This results, for example, in an amplitude modulation of the short eccentricity cycle, since the difference between the second and third strongest eccen-

Six leading terms for Earth's obliquity

term	frequency ($''$/a)	Period (ky)	Amplitude
$p + s_3$	31.613	40.996	0.0112
$p + s_4$	32.680	39.657	0.0044
$p + s_3 + g_4 - g_3$	32.183	40.270	0.0030
$p + s_6$	24.128	53.714	0.0029
$p + s_3 - g_4 + g_3$	31.098	41.674	0.0026
$p + s1$	44.861	28.889	0.0015

Table 1.3: Principal obliquity frequency components in the astronomical solution La93$_{(1,0)}$, analysed over the last 4 My and reproduced from [89]. The frequency terms g_i and s_i refer to those given in table 1.1.

tricity components is $(g_4 - g_5) - (g_4 - g_2) = (g_2 - g_5)$, which corresponds to the ∼400 ky eccentricity cycle. The same modulation is observed for the fourth and fifth strongest terms. This type of amplitude modulation can be found in all orbital components of the Earth, and will be discussed in detail in a subsequent section.

The nature of eccentricity variations is illustrated in figure 1.2. The superposition of the long and short eccentricity cycles, and their variation in amplitude, are clearly visible. The right hand side of the plot shows the results of a frequency analysis, which was run over a 10 My long interval to better resolve the position of individual peaks. The peaks correspond to the frequencies given in table 1.2.

1.7.4 Obliquity

The obliquity (tilt) ϵ of the Earth's axis with respect to the orbital plane is illustrated in figure 1.1. It is defined by the angle between the Earth's spin vector $\vec{s}$ and that of the orbital plane $\vec{n}$, and can be computed as $\cos\epsilon = \vec{n} \cdot \vec{s}$, using unit vectors. As the inclination and orientation of the orbital plane vary, the obliquity is not constant, but oscillates due to the interference of the precession constant p and the orbital elements s_i. If the variation in obliquity is approximated by quasi-periodic terms, table 1.3 shows that this results in a strong oscillation with a period of approximately 41 ky, with additional periods around ∼54 ky and ∼29 ky. The ∼41 ky period arises from the simultaneous variation in the Earth's orbital inclination, given by s_3, and the precession of the Earth's spin direction, given by p. Table 1.3 also shows that the obliquity signal contains contributions from the g_i as well as the s_i fundamental frequencies due to their combined effect on the change of the orbital plane normal.

The present day obliquity is approximately 23.45 degrees, and has varied between

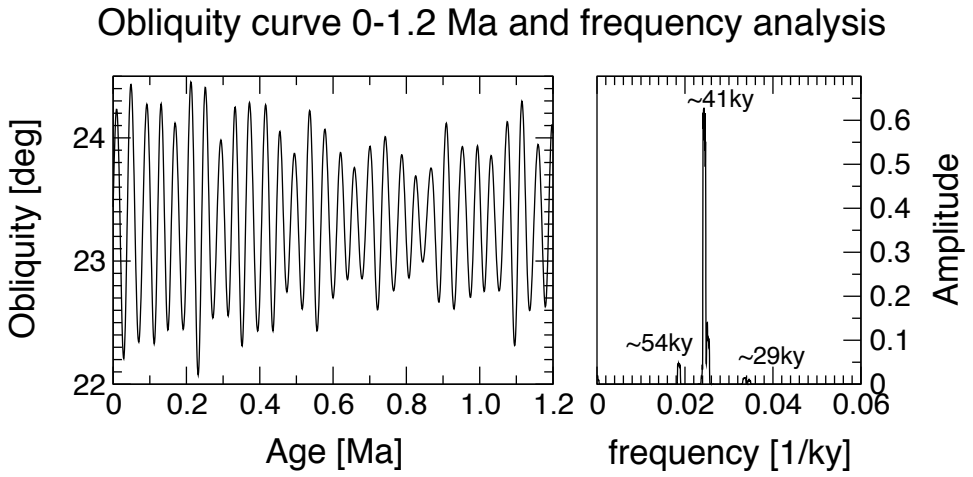

Figure 1.3: Earth's obliquity from 0–1.2 Ma [85] and Thomson multi-taper frequency analysis [90] from 0–10 Ma.

$\sim$22.25 and $\sim$24.5 degrees over the last one million years. The main climatic effect of variations in the Earth's obliquity is its control of the seasonal contrast. The total annual energy received on Earth is not affected, but the obliquity controls the distribution of heat as a function of latitude, and is strongest at high latitudes.

For chapter five of this thesis it will be important to note that the obliquity frequency components all contain the precession constant p. Due to tidal dissipation, the frequency of the precession constant p has been higher in the past. This process also affected the frequencies given in table 1.3, and will be discussed separately. Figure 1.3 illustrates the variation in obliquity from 0–1.2 Ma, according to the calculations of Laskar (1990) [85]. The oscillation is dominated by a $\sim$41 ky period cycle, and a variation in amplitude is also observed. This variation is due to beats arising from the presence of additional $\sim$29 ky and $\sim$54 ky periods, which are just visible in the frequency analysis shown on the right hand side of figure 1.3.

1.7.5 Climatic Precession

The precession of the Earth's spin axis has a profound effect on the Earth's climate, because it controls the timing of the approach of perihelion (the closest approach to the Sun) with respect to the Earth's seasons. At present, perihelion occurs on the 4th January, close to the winter solstice. With respect to the stars the precessional movement of the Earth's spin axis traces out a cone with a period of $\sim$25.8 ky. However, due to the precession of the perihelion within the orbital plane, the period of precession, mea-

Five leading terms for Earth's climatic precession

term	frequency ($''$/a)	Period (ky)	Amplitude
$p+g_5$	54.7064	23.680	0.0188
$p+g_2$	57.8949	22.385	0.0170
$p+g_4$	68.3691	18.956	0.0148
$p+g_3$	67.8626	19.097	0.0101
$p+g_1$	56.0707	23.114	0.0042

Table 1.4: Principal climatic precession frequency components in the astronomical solution La93$_{(1,0)}$, analysed over the last 4 My and reproduced from [89]. The frequency terms g_i refer to those given in table 1.1.

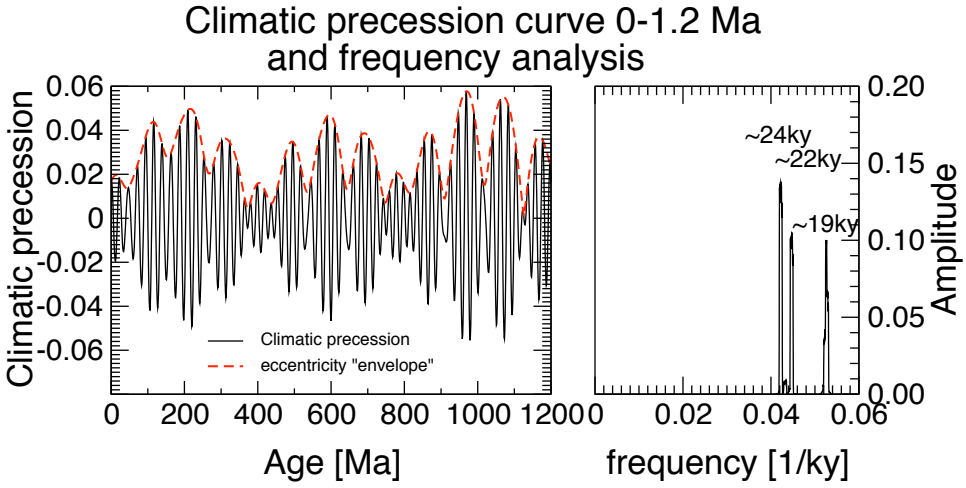

Figure 1.4: Climatic precession index and eccentricity envelope from 0-1.2 Ma [85] and Thomson multi-taper frequency analysis [90] from 0-10 Ma.

sured with respect to the Sun and the seasons, is shorter. The motion of the perihelion is not steady but caused by a superposition of the different g_i frequencies. For this reason the precession of the equinoxes with respect to the orbital plane lurches with a superposition of three periods around ∼19 ky, 22 ky and 24 ky.

The effect of the precession of the equinoxes on the amount of solar radiation received by the Earth also depends on the eccentricity. If the eccentricity is zero, i.e. the orbit of the Earth follows a circle, the effect of the precession of the equinoxes is also zero. From a climatic point of view, the eccentricity and longitude of the perihelion are combined to what is called the climatic precession, defined as $e\sin(\widetilde{\omega})$[4]. This means that the climatic precession index is modulated in amplitude by variations in the Earth's eccentricity.

[4]The exact definition of $\widetilde{\omega}$ depends on whether a heliocentric or geocentric reference frame is used. See Berger *et al.* (1993) [82] for details.

A quasi-periodic approximation of the climatic precession time series reveals the contribution from different frequency components, as shown in table 1.4. Note that the components of climatic precession can be constructed from the precession constant p and the fundamental frequencies g_i. Figure 1.4 illustrates the variation in the climatic precession index, and its modulation in amplitude by eccentricity, from 0-1.2 Ma. The frequency analysis, shown on the right hand side of the plot, reveals three peaks corresponding to frequencies given in table 1.4.

1.7.6 Insolation

Conceptually the actual forcing of the Earth's climate by orbital variations is applied through the radiative flux received at the top of the atmosphere at a particular latitude and time, which is then transferred through oceanic, atmospheric and biological processes into the geological record. The integral of the radiative flux over a specified interval of time is called insolation, and can be computed from the eccentricity e, the obliquity ϵ, and the climatic precession $e\sin(\widetilde{\omega})$. The amount of solar radiation received at a particular location depends on the orientation towards the Sun of that location. Its calculation becomes complex if it is to be calculated over a particular time interval, and details have been given by Berger *et al.* (1993) [82], Laskar *et al.* (1993) [86] and Rubincam (1994) [91].

Averaged over one year and the whole Earth, the only factor that controls the total amount of insolation received, apart from the Solar constant, is the changing distance of the Earth from the Sun, which is determined by the Earth's semi-major axis a and its eccentricity e. However, since the eccentricity only varies by $\sim$6%, and insolation decreases as a function of the squared distance from the Sun, the variation in insolation due to a change of eccentricity is only of the order of a few parts per thousand. This fact is difficult to reconcile with the strong dominance of $\sim$100 ky periodicities in the geological record during the last $\sim$800 ky. Hence, there must be non-linear processes that either amplify or rectify particular frequencies in the forcing [82].

If insolation variations are computed for a particular latitude, and over a particular length of time, the main contribution arises from the climatic precession signal, with additional contributions from the variation in obliquity. The exact nature of the insolation signal is complicated, as demonstrated by Berger *et al.* (1993) [82].

Certain general statements can be made, though. First, the signal arising from the

climatic precession is always present in insolation time series. Second, if the obliquity signal is present, it typically shows a larger amplitude towards high latitudes. Third, the climatic precession signal in the insolation calculation depends on the latitude at which it is calculated, such that the signal in the southern hemisphere shows opposite polarity to that in the northern hemisphere. If the mean monthly insolation is computed for a particular latitude, each month corresponds to a difference in phase (i.e. a difference in time of a particular insolation maximum or minimum) of approximately 2 ky, since twelve months approximately correspond to the (on average) ∼24 ky long climatic precession cycle.

It is unlikely that geological processes which encode the insolation signal are driven by variations at the same latitudes and times of the year throughout geological time. Depending on the latitude and the time interval over which insolation quantities are computed, the calculation can be very complex, and the question of time lags and forcing can only be resolved through the application of climate models [82]. A very revealing study to this effect was reported by Short *et al.* (1991) [65]. At the present level of understanding it is probably appropriate to avoid a strict interpretation of Milankovitch's theory, which would imply that the ice ages are best explained by the summer insolation curve computed at 65°N. Instead, a better understanding of the complex mechanisms of the climate system will have to be achieved through the use of geological data providing boundary conditions for climate models.

1.7.7 Amplitude modulation patterns: the "fingerprint" of orbital cycles

A very important feature of the Earth's eccentricity, obliquity and climatic precession variations is that they display modulations in amplitude and frequency. These modulations provide a "fingerprint" of a particular astronomical calculation at a given time. The modulation terms arise through the interference of individual cycles to produce "beats", with periods ranging from hundreds of thousands to millions of years. The most prominent amplitude modulation cycles are listed in table 1.5. The significance of certain amplitude modulation cycles was first described by Laskar [85; 86; 89], and an extensive review of amplitude and frequency modulation cycles was also given by Hinnov (2000) [92]. An excellent visual representation of amplitude modulation cycles in astronomical calculations can be obtained by computing evolutionary or wavelet spectra, which show the variation in amplitude at different frequencies over time. This

is shown in figure 1.5 for the last ten million years.

The significance of amplitude modulation cycles is twofold. First, if these cycles can be detected in the geological record they allow the placement of geological data into a consistent framework within these amplitude modulation envelopes, even in the absence of individual cycles and the presence of gaps. It was demonstrated by Shackleton *et al.* (1999) [55] how this can be achieved. The extraction of long amplitude modulation cycles typically requires high-fidelity records that are millions of years long. Of particular value for the generation of geological time scales beyond the Neogene is the $\sim$400 ky long eccentricity cycle, because it is considered to be very stable. Laskar (1999) [89] proposed the use of this cycle as a reference frame for geological time scale generation. In addition, if the eccentricity signal could be found in the geological data directly, as well as through its modulation of the climatic precession amplitude, it might be possible to evaluate phase lags between the astronomical forcing and the geological record.

The second significant use of amplitude modulation cycles is that they are related to specific dynamical properties of a given astronomical model, as shown by Laskar [85; 89]. These properties are related to the chaotic nature of the solar system, which will be discussed separately, and potentially allow the use of geological data to provide constraints on the dynamical evolution of the solar system and astronomical models. This approach will be explored in detail in chapter five.

1.7.8 Tidal dissipation and dynamical ellipticity

The mean fundamental orbital frequencies g_i and s_i, as well as the precession constant p, are likely to have changed throughout geological time. While the changes of g_i, s_i are likely to have been small (Laskar, 1990 [85]), the precession constant p is likely to have changed significantly in the past. This change is caused by the effects of tidal dissipation, dynamical ellipticity, and a changing length of day.

In particular, the Earth's tidal response to the gravitational pull from the Sun and the Moon is not instantaneous. This means that a tidal bulge develops on the Earth (and the Moon), which is not aligned with the direction of the Moon's gravitational pull. This pull exerts a torque on the Earth which leads to a gradual decrease in its rotational velocity (see Lambeck (1980) [88] for details). In addition, conservation of angular momentum leads to an increase of the Earth-Moon distance over time, while a change

Short eccentricity amplitude modulation terms

Interfering terms		"Beat" term		Period
$(g_4 - g_5) - (g_4 - g_2)$ $(g_3 - g_5) - (g_3 - g_2)$	=	$(g_2 - g_5)$	$\approx$	400 ky
...		...		...

Short and long eccentricity amplitude modulation terms

Interfering terms		"Beat" term		Period
$(g_4 - g_5) - (g_3 - g_5)$ $(g_4 - g_2) - (g_3 - g_2)$	=	$(g_4 - g_3)$	$\approx$	2.4 My
...		...		...

Climatic precession amplitude modulation terms

Interfering terms	"Beat" term	Period
Identical to eccentricity frequencies and amplitude modulation terms		

Obliquity amplitude modulation terms

Interfering terms		"Beat" term		Period
$(p + s_3) - (p + s_4)$	=	$(s_3 - s_4)$	$\approx$	1.2 My
$(p + s_3 + g_4 - g_3) - (p + s_3 - g_4 + g_3)$	=	$(2g_4 - 2g_3)$	$\approx$	1.2 My
$(p + s_3) - (p + s_3 + g4 - g_3)$ $(p + s_3) - (p + s_3 - g4 + g_3)$	=	$(g_4 - g_3)$	$\approx$	2.4 My
$(p + s_3) - (p + s_6)$	=	$(s_3 - s_6)$	$\approx$	173 ky
...		...		...

Table 1.5: Origin of amplitude modulation terms that affect the Earth's eccentricity, obliquity and climatic precession. Individual g_i and s_i terms refer to those given in table 1.1. The ~100 ky (short) eccentricity cycles are modulated with a period of ~ 400 ky by the long eccentricity cycle. Both short and long eccentricity cycles are modulated with a period of ~ 2.4 My, but with a phase difference of 180°, i.e. an amplitude maximum of the ~100 ky eccentricity coincides with an amplitude minimum of the ~400 ky eccentricity. Since eccentricity directly modulates the climatic precession, all eccentricity amplitude modulation terms are also present in the climatic precession signal. The obliquity signal is weakly amplitude modulated with a period of ~170 ky, and more strongly with a period of 1.2 My. This amplitude modulation cycle is dynamically linked with the 2.4 My cycle present in the eccentricity modulation. All cycles listed here are demonstrated visually in figure 1.5.

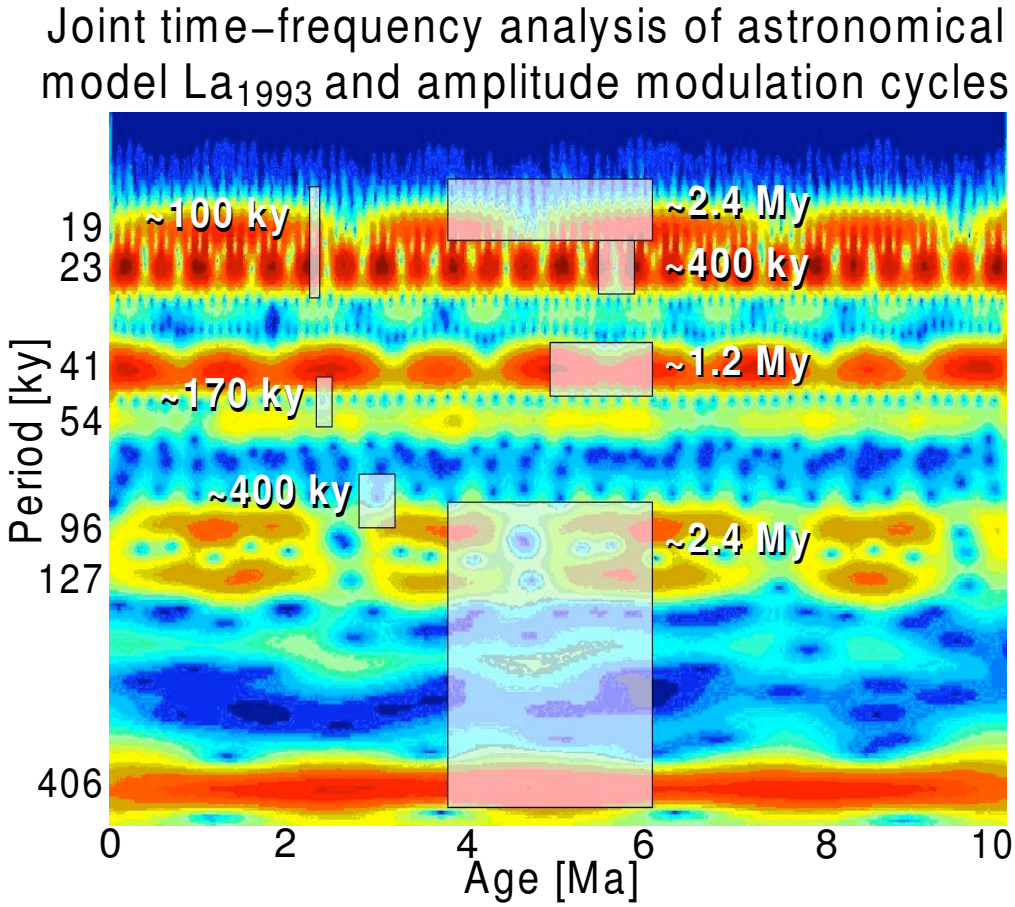

Figure 1.5: Joint time-frequency analysis of astronomical calculation from Laskar (1993) [86] from 0–10 Ma. This plot was generated by using wavelet analysis software developed by Prokoph *et al.* [93; 94]. This software was applied to an arbitrary mixture of the eccentricity, obliquity and climatic precession signal to allow a better visual representation of the main climatically important orbital variations. The amplitude at a particular frequency and time is colour coded, red corresponding to a high relative amplitude. A selection of amplitude modulation terms is highlighted and represents the "fingerprint" of an astronomical model.

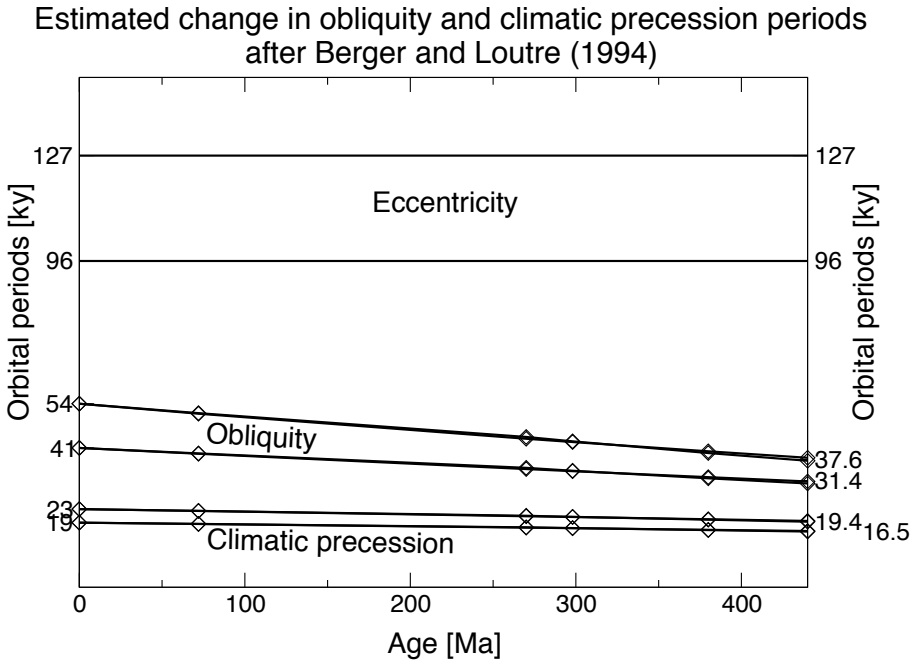

Figure 1.6: Estimated changes in the obliquity and climatic precession periods related to a changing Earth-Moon distance over the last 440 My, according to Berger *et al.* (1989) [95], and Berger and Loutre (1994) [96]. Note that the periods of obliquity and climatic precession change due to a change of the precession constant p, while the eccentricity periods remain unaffected. Note that this figure is for illustrative purposes only, as the exact variation of orbital frequencies over tens of millions of years is not yet known in detail.

in the Earth's rotational velocity leads to a redistribution of mass on Earth ("dynamical ellipticity"), The dynamical ellipticity of the Earth can also be affected my mantle convection and ice loading.

These processes modify the Earth's precession constant p, the frequency of which has decreased over geological time. Since p is contained in the expressions for obliquity and climatic precession (see tables 1.3 and 1.4), the periods of obliquity and climatic precession also change. Berger *et al.* (1989) [95], and Berger and Loutre (1994) [96] estimated possible values for changes of astronomical periods, based on astronomical and geological observations. Their results are illustrated in figure 1.6.

The effect of tidal dissipation was first included in astronomical models by Quinn *et al.* (1991) [97], and later by Laskar *et al.* (1993) [86]. The effects of changing tidal dissipation and dynamical ellipticity values have a large impact on astronomical calculations [89], and have to be obtained from observation. This problem is the focus of work reported in chapter five. Strictly speaking, astronomical calculations cannot be performed independently of the chosen Earth model, and particularly the separate

treatment of the Earth-Moon system. This is the reason why numerical computations, such as those given by Quinn *et al.*, are invaluable.

1.7.9 Chaos in the solar system

Probably the most significant development of astronomical theory in recent times has been the discovery of the chaotic behaviour of the solar system by Laskar (1990) [85]. Laskar established that the dynamics of the orbital elements in the solar system are not fixed for all times, but rather unpredictable over tens of millions of years. This is due to the gravitational interaction of the different bodies in the solar system and makes it theoretically impossible to calculate the exact movements of celestial bodies from their present day masses, velocities and positions over long periods of time. This feature poses limits on the use of astronomical theory for the purposes of creating astronomically calibrated geological time scales, as reviewed in detail by Laskar (1999) [89]. He found that the calculations of orbits diverge exponentially with time for a given set of initial conditions. This implies, for example, that if the position of a planet is known with a relative error of $\sim 10^{-10}$ at present, this error increases to $\sim 10^{-9}$ after 10 My, and reaches the order of 1 after 100 My. Despite these limitations, the determination of astronomical parameters such as the planetary masses, velocities, and positions, is improving due to additional satellite measurements. Together with improved and more detailed astronomical models, the limits of accuracy of astronomical calculations are also likely to extend further back in time.

An important implication of this is that the development of astronomical theory and geological observation have to evolve hand in hand, i.e. geological observation has to be used to constrain astronomical theory, which in turn is then used to extend the astronomical calculation of the geological time scale. Extreme care has to be taken to avoid circularity in this process. Laskar (1999) [89] estimated that the astronomical model of Laskar *et al.* (1994) [86] might be accurate back in time to approximately 20-30 Ma. This prediction will be tested and explored further in chapters three and five.

A clear representation of chaos in the solar system is provided by amplitude modulation terms, as discussed in section 1.7.7. As discovered by Laskar (1990) [85], and reviewed by Laskar (1999) [89], the ∼2.4 My and 1.2 My long amplitude modulation terms that occur in the calculations of eccentricity and obliquity, respectively, are in resonance, and the expression $(s_4 - s_3) - 2(g_4 - g_3) = 0$ can evolve into a new state,

where $(s_4 - s_3) - (g_4 - g_3) = 0$. This implies a change from a $1:2$ resonance to a $1:1$ resonance. Laskar found this behaviour to be the main source and representation of chaos in the solar system. As shown in table 1.5, these terms are present in several astronomical frequencies, and should be possible to detect in the geological record. The astronomical calculation of Laskar from 1993 [86] predicts such a switch in resonance between ~23 and 28 Ma. This switch will be explored in detail in chapter five.

1.8 Construction of continuous geological records

At this stage it is appropriate to discuss how long continuous geological records can be obtained and constructed to provide the data necessary for an astronomical calibration of the the geological time scale. This discussion is instructive, since the construction of a completely continuous geological record is laborious, and it is important to appreciate the range of uncertainty that can be introduced into the data by various processing steps.

So far, the most successful studies that provided an orbital time calibration over millions of years have used material recovered from deep-marine and lake environments. Examples include material of Cenozoic age recovered from Ocean Drilling Program (ODP) Legs 138 [51] and 154 [53; 55], from Lake Baikal [98], marine sediments now exposed around the Mediterranean [43; 44; 54], as well as Triassic records from the Newark rift basin [56].

The reason why ODP material in particular has provided a very good basis for orbital calibration is related to the requirements that are necessary for such work to be accomplished. These can be listed as follows. First, it is crucial to obtain records that are continuous in time, and one has to be able to demonstrate that this is so. Deep-marine sediments can provide a record that is typically less disturbed by sequence boundaries, erosional events, rapid deposition of clastic deposits, or tectonic events than near-shore, clastic deposits. Deep-marine sediments are intimately linked to various (mostly biological) processes, which are likely to reflect variations in ocean circulation and climate.

Second, sedimentation rates, in an ideal situation, are steady over long periods of time, such that one can demonstrate the presence of cyclic signals *a priori*. Accumulation rates of deep-marine sediments have been found to remain relatively steady over long periods of time and distance, with typical rates of the order of several cm/ky. Deep-

marine sediments thus provide the best available material for the long-term recording of climatic variations. They also contain abundant fossiliferous material, as well as recording a palaeomagnetic signature, both of which allow the close correlation of records from different locations.

It is crucial that one is able to demonstrate the continuity of a given record in time. Thus, one has to be able to recognise the presence of hiatuses in the sedimentary record, and it is necessary to compensate for the limitations that result from the technology used to recover deep-marine sediment cores. ODP sediment cores are typically recovered in ∼9.5 m long sections. Depending on the consistency and hardness of the sediment encountered during drilling, different recovery methods are used (e.g. "advanced piston coring" (APC), "extended core barrel" (XCB) coring, or "rotary core barrel" (RCB) coring). There are always recovery gaps present between successive cores. These are at least of the order of tens of centimetres. Depending on the recovery method used, cores can also be affected by core fragmentation, slumping, core stretching and squeezing, and other core deformations.

For this reason, typically more than one hole is drilled at a particular site, which allows an evaluation of the length of core gaps, as well as the construction of a "patched" record. Initially, each ∼9.5 m long core is assigned a depth according to the drill string length. This depth is denoted as "metres below sea-floor" (mbsf). Subsequently, an attempt is made to correlate cores from different holes by using common features such as more or less diagnostic excursions in measurements of physical properties (bulk density, magnetic susceptibility etc.), or biostratigraphic events. Routinely, the depths of cores from different holes are adjusted to a common depth scale by adding a constant offset over the length of each core. This new depth scale is denoted as "metres composite depth" (mcd).

Unfortunately, it has been observed frequently that cores are distorted in length within each ∼9.5 m segment. This distortion is due to the coring methods used, or due to variations in accumulation rates between holes. This problem has been discussed in detail by, for example, Hagelberg *et al.* (1995) [99]. The distortion in depth implies that occasionally geological events that are obviously synchronous in time, such as volcanic ash layers, are not correctly aligned on the mcd depth scale.

This situation is not satisfactory, as far as a detailed correlation and stratigraphic calibration is concerned. Two strategies can be used to alleviate this problem. The eas-

ier one of the two is to construct a "spliced" record from available data by using the mcd depth scale, and by switching between records from different holes. The splicing procedure requires a decision to be made with respect to what constitutes the "best" (or most representative) track, and will depend on the purpose of the particular investigation. For example, one might want to choose, where available, the longest possible track down the core record, assuming that this record results in the highest possible resolution in time. Alternatively, one might want to select a "splice" that corresponds to the average increase in depth, if , for example, the aim is the reconstruction of sediment flux variations. These arguments have been put forward, for example, by the report of the Shipboard Scientific Party during ODP Leg 171B [100].

An alternative to the construction of a "spliced" record is the construction of a stacked record. In this case it is necessary to align individual features between different holes at a high-resolution, allowing differential stretching and squeezing of depths within individual holes. This strategy has been described in detail by Hagelberg *et al.* (1995), and leads to the development of a "revised metres composite depth" (rmcd) scale. As this implies that cores from individual holes are aligned not only at specific depths, but ideally along the entire record, it is possible to "stack" data from different cores covering the same stratigraphic interval. This method can facilitate the generation of an enhanced "signal-to-noise" ratio, i.e. "noise" in the data that is independent on the location of the holes can be reduced by averaging several measurements from the same stratigraphic level. This strategy will be employed in this thesis in chapter three.

It is important to stress that the correlation of geological data is very laborious, and it is likely that errors are introduced into the record if ambiguities exist. It was the strength of the studies of Shackleton *et al.* (1995, 1997, 1999) [51; 53; 55] that the stratigraphic correlation of data from different holes and their calibration to an astronomical model was not only achieved with data from one particular location, but with data from different sites. This approach allowed the elimination of several hiatuses that otherwise would have remained unnoticed. Their work involved many iterations of adjustment and verification of inter-site correlations, as well as calibration to time using orbital cycles present in the data. It is important to realise the complexity of the process that stretches from the initial recovery of individual cores to the final calibration of geological data in order to generate a new time scale based on orbital variations.

Chapter 2

Advanced methods for automated astronomical tuning

2.1 Introduction

This chapter is concerned with orbital "tuning", and its evaluation via spectral estimation methods. In this context, the term "astronomical tuning" refers to the adjustment of stratigraphic events or variations (in the depth domain) to a conceptual "forcing" (in the time domain) that is assumed to be imposed on climatic and geological processes. Such variations, which have been demonstrated to be present in the geological record, can be used in the fashion of a pace-maker or metronome to obtain a record in time from stratigraphic depth or thickness. The output of this is an age model that relates depth to time.

In the most general sense, stratigraphic correlation and the creation of astronomically tuned time scales involves the matching of characteristic features in one record to certain features in a different "reference" record, or to features in theoretically derived curves, such as solar insolation. In either case it is necessary to create a "mapping function" that relates these two records in terms of depth to depth, or depth to time. This step is crucial in the process of creating an astronomically calibrated geological time scale, and relies on different assumptions about how a "forcing" is transferred into the geological record, as well as an appropriate choice of scale in terms of how many correlations or "tie points" are used to create this depth to age mapping.

Several variants of this tuning procedure exist, depending on the choice of the target curve and the type of response. These have been reviewed and statistically evaluated

by Martinson *et al.* (1987) [37]. Due to the nature of geological data, this step often involves a considerable amount of geological judgement, for example in terms of assessing reasonable sedimentation rates and possible sedimentary breaks.

The aim of this chapter is to develop a procedure for adjusting geological data that contain an orbital signal to a reference curve, or template. This new method is then applied to create a refined age model for data from ODP Leg 138 from Shackleton *et al.* (1995) [51]. Preliminary results from this study were presented earlier [101].

2.2 The need for automated and objective tuning methods

Correlating stratigraphic data, which comprises a large part in the process of creating astronomically calibrated time scales, involves geological judgement and interpretation on the part of the investigator. This is due to the fact that geological records are often short, and the data result from the interaction of many geological processes on different spatial and temporal scales that are difficult to separate. Indeed, one could argue that it is the skill of the investigator that can make the difference between a "good" and "bad" correlation, or age model. This is a serious problem, and this subjective element has been used as an argument against the fidelity of astronomical tuning procedures.

Several statistical tests are available that evaluate how well the tuning process has succeeded in matching the geological data and the target curve (e.g., coherency, cross-spectral analysis, evolutive spectral analysis, and correlation coefficients). However, these tests generally compute an average fit for the entire record, and thus give a holistic representation rather than examining each individual feature in the record; nor do they evaluate variations in sedimentation rate that have been imposed in order to generate a given age model.

In later parts of this chapter it will be analysed in detail how it might be possible to quantify the consistency of an age model with astronomical models, and how to use this quantification to create an age model. First, though, it is instructive to compare studies that attempted to create orbital age models with different geological material and with different investigators.

2.2.1 The problem of subjective interpretation of geological data

Kent (1999) compared the ages that were independently obtained by astronomical tuning in the studies of Shackleton *et al.* (1995) [51] and Hilgen *et al.* (1995) [52], in relation to the geomagnetic polarity time scale of Cande and Kent (1995) [46]. This comparison is not entirely justified, as Shackleton *et al.* (1995) did not claim that their age model for the Miocene was astronomically "tuned". The nature of the geological data older than approximately six million years instead required the assumption that the initial geomagnetic polarity time scale of Cande and Kent (1992) [45] was approximately correct.

The difference between the two studies of Shackleton *et al.* and Hilgen *et al.* is illustrated in figure 2.1, and amounts to as much as $\sim$180 ky, with an average difference of $\sim$100 ky. Although slightly different astronomical calculations were used in both studies [51; 52], this difference of approximately one eccentricity cycle can be considered a practical measure of uncertainty that arises from using different data, and more importantly, from different interpretations of the cyclicity present in the data sets. A subset of the data of Shackleton *et al.* (1995) [51] will be used later in this chapter as a case study for a numerical tuning approach.

As investigated by Laskar (1999) [89], and outlined in chapter one, there are practical limits on how far back in time detailed astronomical calculations can be extended with confidence. Beyond approximately 30 My, astronomical tuning in its most simple form relies on the extraction of astronomical parameters from geological material, essentially by counting of individual lithological cycles and an interpretation of their astronomical nature by using astronomical calculations performed for younger ages as an analogue.

This was the approach chosen in the study of Röhl *et al.* (2001) [103], where two authors attempted to give two independent time duration estimates, using identical data. Although the estimated duration of the late Danian magnetochron C27 is similar to within $\sim 2\%$ in both interpretations (for a total duration of $\sim$1.45 My), the authors admit that *"such direct counting procedures are highly subjective"*. One of the authors counted 47 precession and 11 obliquity cycles, while the other counted either 70 precession cycles or 35 obliquity cycles. This example highlights an urgent need for more numerical and less subjective methods to create an astronomical time scale.

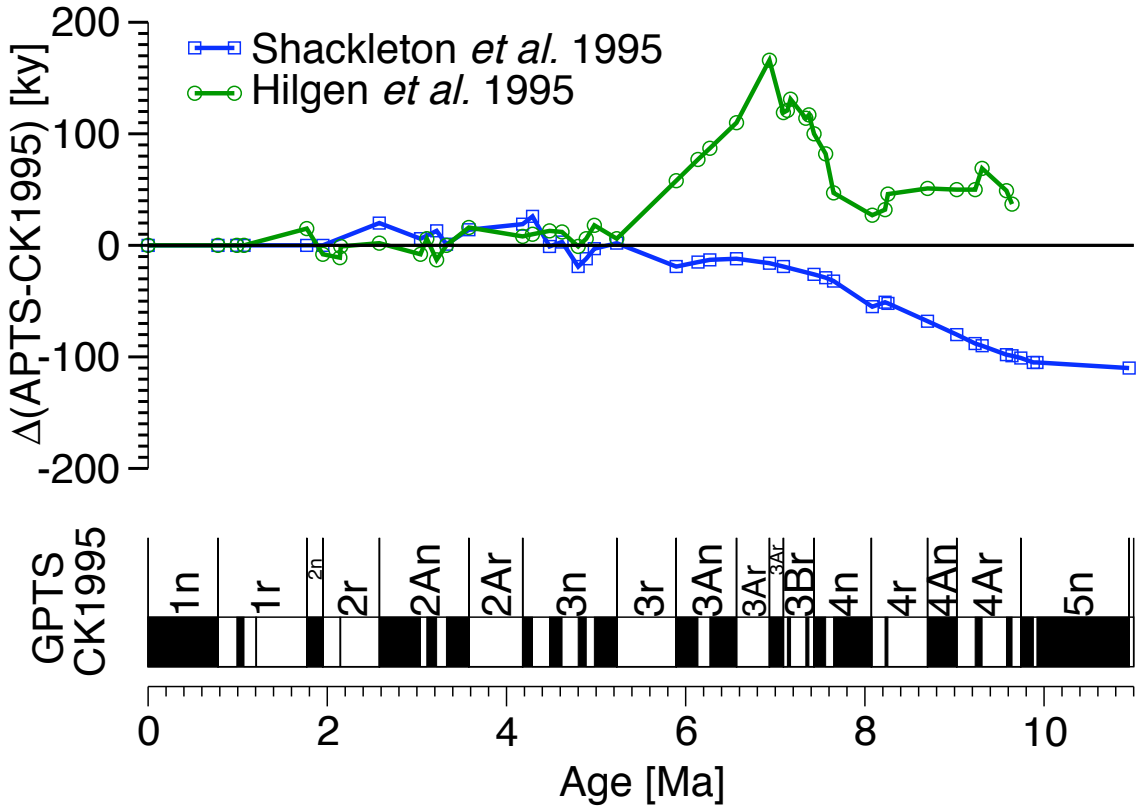

Figure 2.1: Two independent Neogene astronomical polarity time scales (APTS) of Shackleton *et al.* (1995) [51], and Hilgen *et al.* (1995) [52] are compared with the geomagnetic polarity time scale (GPTS) of Cande and Kent (1995) [46]. The geomagnetic polarity time scale already includes the APTS from Shackleton *et al.* (1990) [41] and Hilgen (1991 a,b) [43; 44] from 0–5.23 Ma, which marks the base of magnetochron C3n. Note that the two astronomical calibrations begin to diverge back in time from approximately chron C3r, which coincides with the Messinian interval. This interval is marked by extensive evaporite formations and slumping and has thus proved to be a difficult interval for a detailed astronomical tuning. This situation has recently been resolved by the study of Sierro *et al.* (2001) [102]. This figure is adapted from Kent (1999) [47].

2.2.2 The problem of different orbital calculations and rapid re-calibration

It was explained in chapter one that astronomical solutions can be separated into a planetary and an Earth-Moon system component. The chosen model for the Earth system affects the rate of tidal dissipation and the dynamical ellipticity. This will be explored in detail in chapter five. It has the direct effect that, depending on the chosen model, the astronomical calculations that form the basis for the target or reference curve show small differences that might influence the interpretation of individual cycles. Figure 2.2 demonstrates that the interference between amplitude modulated precession cycles and obliquity cycles can change the relative amplitude of individual cycles in the target curve.

In the light of constantly evolving astronomical models (Le Verrier, 1856; Bretagnon, 1974; Berger, 1978; Laskar, 1990; Berger and Loutre, 1991; Laskar *et al.* 1993) [20; 38; 80; 85; 86; 104], and the need to explore the possible parameter space for the chosen Earth model, it becomes even more important to have a rapid way of re-adjusting an existing astronomical tuning to a different target curve. This is an additional reason for using a more automated approach that can be used to make small modifications to an already existing age model.

Figure 2.2 also shows the type of cycle scale differences that occur between different astronomical solutions. The arrows in figure 2.2 illustrate those points in time where a small phase difference between different astronomical components for different calculations leads to ambiguity in terms of the amplitude of individual insolation cycles. This demonstrates that any tuning strategy based simply on cycle counting is likely to introduce errors in the result. As discussed in chapter one, it is thus necessary to use the precise “fingerprint” contained within astronomical calculations through different amplitude modulation terms that define the overall “envelope” of the calculation. The exact nature of these nodes, which depends critically on the exact phase relationship of orbital components that result from the chosen Earth model, are therefore a good test as to which astronomical solution is better supported by geological data.

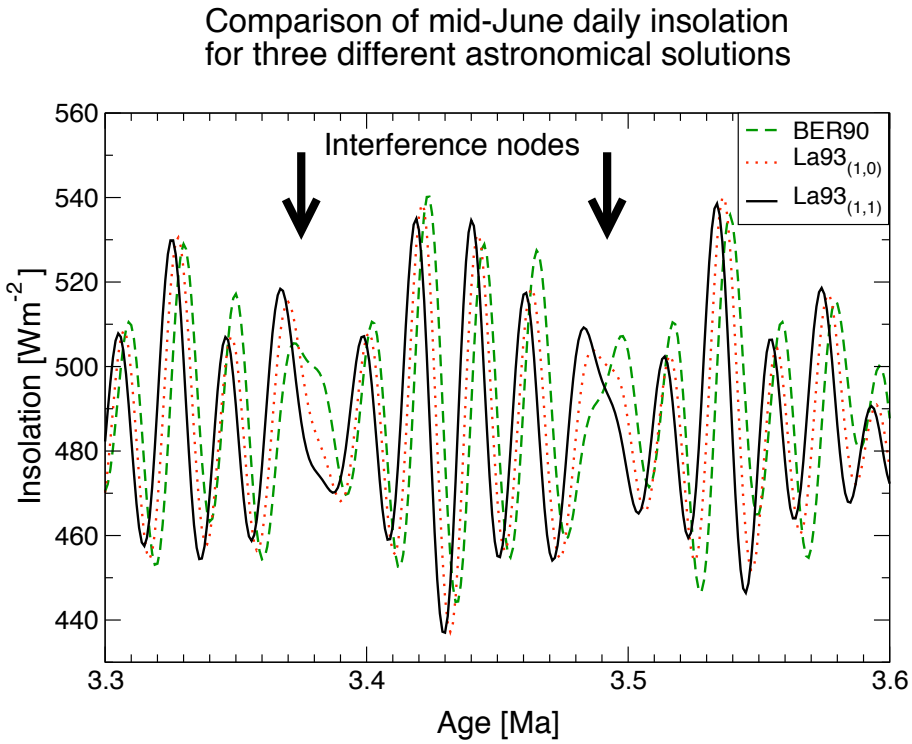

Figure 2.2: This plot shows three different astronomical calculations of mid-monthly June insolation at 65° North. The calculation $La93_{(1,0)}$ is that of Laskar (1990) [85]. The model BER90[80] uses the same eccentricity calculation but is based on a different calculation for obliquity and climatic precession. $La93_{(1,1)}$[86] is similar to $La93_{(1,0)}$, but includes a tidal dissipation term for the Earth-Moon system. Arrows indicate the position of "nodes" that result from interference between the obliquity and climatic precession components. This leads to a relative change in amplitude for the two closest peaks, and can affect the interpretation of individual cycles in the geological record. This problem can be addressed by considering the longer term amplitude modulation patterns.

2.3 Towards an automated correlation and tuning method

2.3.1 The choice of an appropriate target curve

The choice of an appropriate target curve is of great importance, because the choice of the target curve directly controls the exact timing of correlated events. The target curve is controlled by several factors:

- the chosen astronomical calculation
- the chosen Earth model, depending on the parameters chosen for tidal dissipation and dynamical ellipticity, and
- the choice of how the final target curve is constructed from individual astronomical elements (eccentricity, obliquity and climatic precession), given certain assumptions about how the astronomical forcing is interacting with the Earth's climate system to operate as a forcing for geological processes.

The effect of the first two factors was illustrated in figure 2.2 and discussed in chapter one. The parameters that control these effects can be extracted from geological data and will be explored in detail in chapter five. The third factor was reviewed in detail by Martinson *et al.* (1987) [37]. Questions that need to be addressed and quantified include

- do time lags exist between the astronomical forcing and the climate system?
- are the time lags different for individual astronomical components (obliquity, climatic precession, eccentricity) of the forcing?
- can the climate system response be described by the combined effect of the astronomical parameters at the "top of the atmosphere", possibly at a given latitude and a given time of the year, as postulated in the original Milankovitch theory of glaciations?
- is the response of the climate system to the forcing linear or non-linear?

These different factors control the relative amplitude of astronomical components that are recorded by the geological system at a given location, as well as their detailed phase relationship as compared to the direct, astronomical forcing. A selection of several possible target curve types and models is illustrated in figure 2.3.

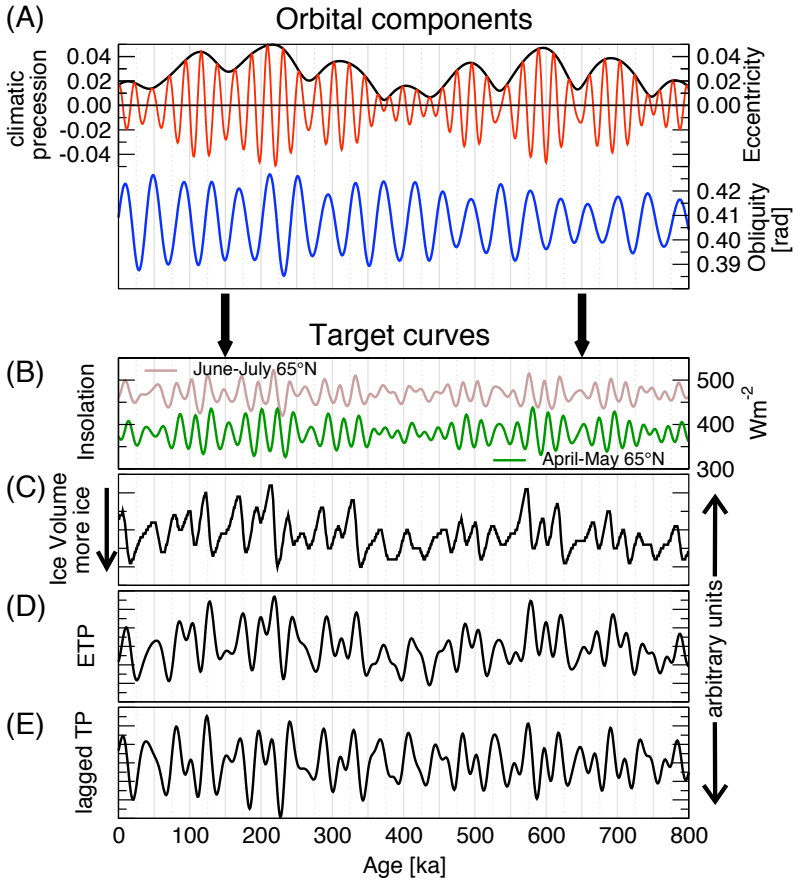

Figure 2.3: Examples of different types of astronomical target curves.

This figure shows four examples of target curves that were constructed from the calculated orbital elements eccentricity, obliquity, and climatic precession, using the solution $La93_{(1,1)}$[86] for the last 800 ky (panel A).

Panel (B) shows two insolation curves, computed as the monthly average for June-July and April-May at 65°N. Note that in addition to a lower average for the April-May curve, there is also a difference in phase, where the June-July curve lags the April-May curve by approximately 4 ky.

Panel (C) shows the calculation of a hypothetical ice volume curve by Imbrie and Imbrie (1980) [35], that is based on a non-linear response to the 65°N June-July insolation curve. In this model, time constants are specified that govern the ablation and build-up of ice. This leads to a a time lag of approximately 6 ky.

Panel (D) shows a target curve that is constructed by adding the normalised (subtracted mean, and divided by standard deviation) orbital components with an amplitude ratio of 1:1:-1 (the sign of climatic precession is reversed when insolation is computed for the northern hemisphere [82]). The construction of an "ETP" curve can help to accentuate the sensitivity towards the longer term variations in eccentricity, and assumes an instant reaction of the response to the forcing.

Panel (E) is similar to D in that orbital components are added to construct an artificial target curve. In this case the contributions of climatic precession and obliquity are added with a pre-determined time lag to the original orbital components. These time lags were determined from geological data (Shackleton, 2000 [68]), with a time lag of 3 ky for climatic precession, and 7 ky for obliquity. Ideally, an automated tuning approach will allow the choice of how the target curve is implemented.

2.3.2 Quantifying the relationship between depth and time

Any correlation, regardless of whether it is obtained in an automated way or not, will produce a certain age-depth relationship, or age model. This age-depth relationship, or "mapping function", is normally subject to certain constraints, such as bio- or magnetostratigraphic datums with associated uncertainty intervals, as well as geologically "reasonable" rates of sediment accumulation. Generally, but not always, it is also appropriate to assume continuity, i.e. geological data are in their true stratigraphic position. This last constraint can be violated by faulting, or by technical core recovery problems, which might lead to a repetition of material from the same stratigraphic position in

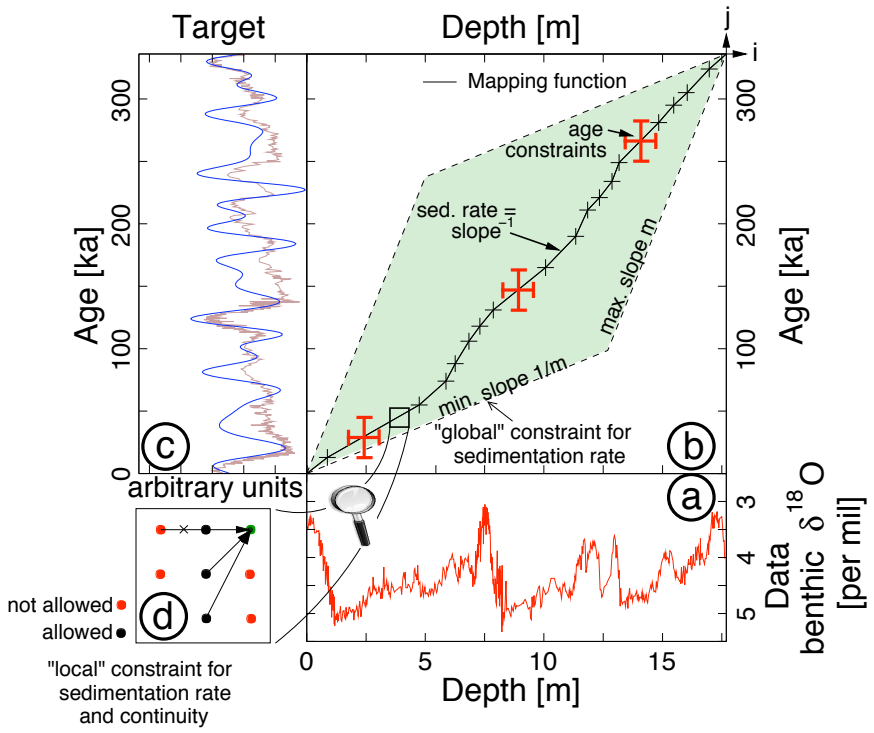

Figure 2.4: Conceptual illustration of depth to time conversion with constraints on sedimentation rate and continuity.

more than one core interval. A typical age-depth relationship that can illustrate the tuning procedure is shown in figure 2.4.

Figure 2.4 demonstrates the transformation of geological data from the stratigraphic depth domain to the target curve time domain. The relationship between depth and time is determined by the mapping function, which in turn is subject to global and local constraints. This approach makes use of features that can be related to orbital variations, as reported by Shackleton (2000) [68].

Panel (a) shows a depth record of δ^{18}O from benthic foraminifera, as used in [68]. On the assumption that light values in δ^{18}O are related to higher values in received solar insolation, this record was then matched to a ”target curve”, as shown in panel (c), by inserting control points that relate depth to time and form the ”mapping function”, as shown in panel (b). The initial depth-to-time conversion is typically achieved by making use of bio- and/or magnetostratigraphic constraints that are shown by red cross bars in panel (b).

The apparent sediment accumulation rate is defined by the slope of the mapping function, which might be subject to certain minimum and maximum constraints

across the entire correlation. One possible version of this type of "global" constraint is indicated by the shaded parallelogram in panel (b).

At each point in the allowable mapping function area one can also introduce a "local" constraint, which limits the possible path of the mapping function from one point to the next. This is shown in panel (d). The indices i and j, marked in the top right corner of figure 2.4, represent the position of individual data points within each data series.

Depending on the type of target curve that is used, there are several ways to evaluate, in a quantitative fashion, how well two records match each other with respect to certain features. The mathematical description of this evaluation is often termed the "figure-of-merit function", or "cost function" in optimisation theory [105]. These methods, as described next, form the basis for automated approaches to tuning and correlation. Each of these has certain advantages and disadvantages that result from the way the match between two records is computed, and what assumptions are necessary for their application.

2.3.3 Using the least squares error as a correlation criterion

The least squares error criterion assumes that the target curve is an exact model for the geological data. Hence, if the target curve is expected to have the same spectral content and phase relationship as the signal contained in the geological data, this method allows a quick and mathematically simple way to match two records. The strategy consists in matching two individual records by minimising the misfit at each point to arrive at a minimum global misfit. This can be described mathematically by the minimisation of the normalised misfit for a set that contains N data points:

$$misfit = \frac{1}{N}\sum_{i=1}^{N}[target_i - data_i]^2 \tag{2.1}$$

where $target_i$ are individual points on the target curve, and $data_i$ are individual points in the geological data set. It is possible to extend this calculation to a situation where there is more than one set of data and target curves. For M sets, of equal length, equation 2.1 then becomes

$$misfit = \frac{1}{M \times N}\sum_{j=1}^{M}\sum_{i=1}^{N}[target_{ji} - data_{ji}]^2 \tag{2.2}$$

Data points in the target curve and the geological data need to be evaluated at the same position, so that it might be necessary to interpolate one of the curves before evaluation. This method can easily be extended to the case of several, different, geological data sets, where each one is fitted to either the same or individual target curves, as appropriate.

Disadvantages of this concept are the strong assumptions that are made about the nature of the signal in the data, as only rarely is it possible to predict *a priori* how the orbital components that form the forcing function are constructed in terms of relative amplitude and phase. In addition, this method is very sensitive to extreme values, as the misfit is computed over the entire data set.

2.3.4 Using the correlation coefficient as an optimisation criterion

A similar approach to the least squares criterion is the computation of the correlation coefficient between two data sets. Instead of assuming that the target curve is an exact representation of all features contained in the data, the correlation coefficient evaluates whether two different records co-vary in a similar fashion, i.e. whether excursions in the data correspond to similar excursions in the target. To some extent, this minimises the problems that are posed by extreme values present in the data. Mathematically the linear correlation coefficient r can be defined as

$$r = \frac{\sum_{i=1}^{N}(target_i - \overline{target})(data_i - \overline{data})}{\sqrt{\sum_{i=1}^{N}(target_i - \overline{target})^2}\sqrt{\sum_{i=1}^{N}(data_i - \overline{data})^2}} \tag{2.3}$$

where $\overline{target}$ and $\overline{data}$ denote the mean of the target and geological data set, and N is again the number of data points considered. Since the correlation has to be computed over a defined interval, rather than at a particular point as in the least squares error method, it is also necessary to define the width, or "window", over which this correlation is computed. To some extent this improves the continuity and diminishes variations in sedimentation rate of established correlations that make use of this method. The correlation coefficient approach has been implemented in the software package "AnalySeries", which allows the creation of age models [106]. Shipboard stratigraphic correlation work for the Ocean Drilling Program (ODP) makes use of the software "Splicer" [107], which uses the correlation coefficient in an interactive way to create a stratigraphic composite from bore-holes drilled at different locations.

One disadvantage of the correlation coefficient method is, however, that it might

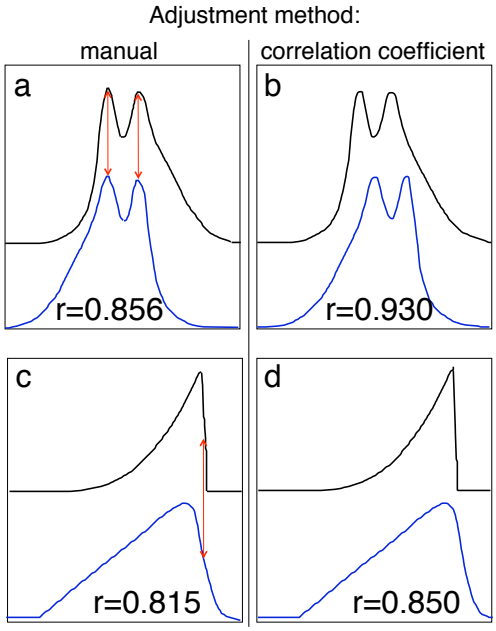

Figure 2.5: Comparing pattern matching based on correlation coefficients and fitting peaks. In all four panels the lower curve is adjusted to the upper curve, using the highest correlation coefficient (r) in panels b and d, and by matching peaks (panel a) and transitions (panel c) manually. It could be argued that the fit in panels a and c is more realistic because it represents the exact timing of two features, even though this results in a lower overall correlation coefficient. This figure is reproduced from Paillard *et al.* (1996) [106].

in fact be sharp transitions in the data that define good time control points, rather than the lower frequency components, which are favoured by the correlation coefficient method. This is the case for the sharp and rapid excursions found in the stable oxygen isotope record, which define deglaciations. This problem has been described in the electronic supplement of Paillard *et al.* (1996) [106], and is illustrated in figure 2.5.

2.3.5 Optimisation over selected frequency bands

A different approach is to evaluate the "cost function" or correlation between two geological data sets, or an astronomical target curve and geological data, over certain frequency bands of interest only. For example, this is useful if one can identify astronomically driven variation at a particular frequency in both records, which can then be used to create an age model based on these variations. This is useful when a stratigraphic correlation is sought between different types of data from different locations, e.g. when comparing stable isotope data with lithological parameters such as magnetic susceptibility. In this case, there might be certain features in both records that are co-varying, while the general appearance of the two curves is very different.

One reason why two geological records might show a different frequency response is the presence of bioturbation. Depending on the sedimentation rate, this process acts to remove high-frequency parts of the signal, and thus performs smoothing and "prefiltering" (see, e.g., Herbert, 1994 [108]).

The concept of optimisation in a selected frequency band is illustrated in figure 2.6. Instead of considering the actual data points in the target curve or the data curve, the best fit is now evaluated for the filtered series only. Again, this approach can be extended to multiple data sets from the same core, or it can be combined with the two approaches described before. This method has not previously been used for an automated tuning, although it was introduced as a "manual" option into the software package "AnalySeries" [106] after a suggestion by the author. An automated implementation of this approach will be developed in a later part of this chapter.

2.3.6 Optimisation in the frequency domain

A different approach towards the creation of an orbital age model consists of working with a representation of the data in the frequency domain. In this case a spectral estimate for the data is compared with a spectral estimate of the chosen target curve, and

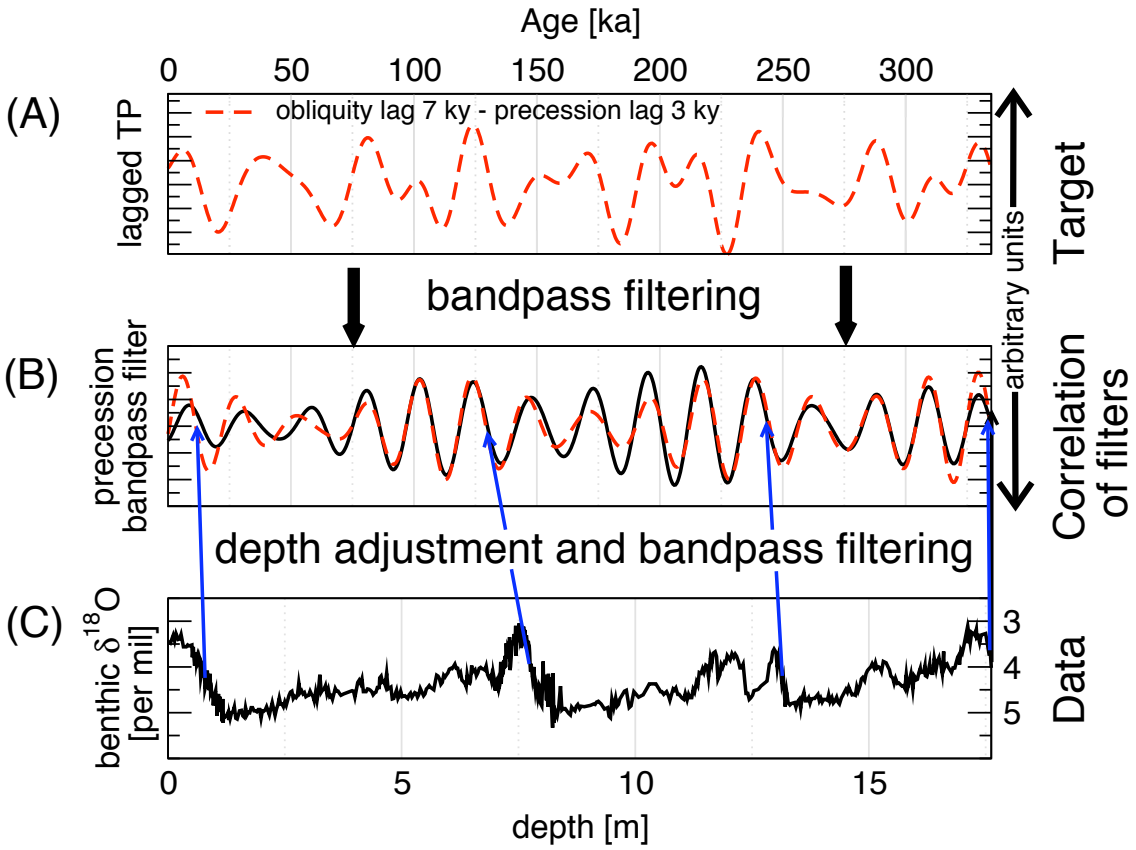

Figure 2.6: This is an example of how one can use filtering of specific frequency components, that are common between the target and the data, to arrive at an age model. (A) shows a target, which is the same as in figure 2.3(E). Instead of an astronomical target one could also select a different geological proxy parameter, if the aim was stratigraphic correlation. (C) shows the data in the depth domain. For illustrative purposes, the data chosen here are the same as in figure 2.4(a). (B) shows the filtered target and filtered data. If this approach is used in an automated fashion, the data are dynamically filtered during correlation after each depth-to-age iteration step. The fit or correlation between these two filters is then used to evaluate the merit of the current age model. Note that for the particular data set shown here, the generation of an age model based on bandpass filtering alone would be very hard, as the precession signal in the data is weak.

the match is optimised by inserting and moving control points that convert from depth to age.

Different versions of this method were employed by several authors [109; 110], but did generally not give results that would allow the use of the obtained time scale for the high resolution determination of stratigraphic events. This is probably caused by the fact that the detailed shape of spectral estimates of noisy geological data is very sensitive to the non-orbitally controlled residual.

In addition, geological data are non-stationary in almost all cases, thus invalidating the assumptions underlying conventional spectral analysis. One approach that could reduce these problems would be to work with evolutionary spectral estimation methods. This, however, would move this approach back into the time domain, for which the other approaches described here are more suitable, and much less computationally intensive.

2.3.7 Optimisation of orbitally controlled sedimentation rates

Some geological processes transfer the orbital forcing of the climate system into variations in apparent sediment accumulation rate. Amongst other processes, this can be the result of varying proportions of sediment source end-members (e.g. terrestrially derived material versus material derived from biogenic sources), or by variations in the rate of sediment production, export, or dissolution.

Shackleton and Crowhurst (1997) [53] demonstrated convincingly that apparent sediment fluxes can be driven at least partially by orbital forcing, and show how it is possible to separate the relative contribution of these processes in deep-marine sediments that contain an input of terrestrial material. Assuming that different geological facies result in different rates of apparent sediment accumulation, Kominz and Bond (1990,1992) [111; 112] tried to exploit this relationship. However, a later study showed that their particular method might not generate a realistic age model [113].

Slightly different versions of this theme were introduced by Herbert (1992, 1994) [58; 108], and employed by Hinnov and Park (1998, 2000) [92; 114], who performed an analysis based on frequency modulation patterns in geological data assuming that they are modulated by longer period orbital cycles.

The “AnalySeries” package contains an implementation of the Martinson *et al.* (1987) [37] algorithm, which tries to model the mapping function, and thus the sedi-

mentation rate, as a combination of sine and cosine terms. This has the distinct advantage that changes in sedimentation rate are usually smooth if the number of harmonic coefficients is low. This method is computationally intensive, though, and is inappropriate for data that contain gaps and thus require sharp changes in sedimentation rates at certain points.

2.4 Developing “Dynamic Time Warping” for automated correlation

2.4.1 Introduction: Similarities between speech recognition and astronomical tuning

A literature research revealed that the fields of speech recognition and cyclostratigraphic correlation share a common set of problems. In both fields one aim is to match a data curve (a speech utterance, or a geological data set) to a known reference curve (a characteristic representation of known utterances, or an astronomical time series).

Both fields face the problem that data series can be distorted in a non-linear fashion, caused, for example, by varying sedimentation rates in the case of geological data, and by variations in length, pitch and inflection of utterances in the field of speech recognition. These distortions require the alignment of time-correlative features of data and “target” series, subject to a number of constraints. In both fields computational speed is an important consideration, in order to complete pattern matching decisions rapidly, or when dealing with a large number of data points.

The following sections present the adaptation of a method that has been successfully used for speech recognition (“Dynamic Time Warping”, DTW) to develop an automated means of matching orbitally driven geological depth series to an astronomical target time series, considering given age constraints, uncertainties in depth and dating, and constraints on allowed changes in sedimentation rate. Dynamic time warping is based on an algorithmic method called “dynamic programming”, which is used to adjust the depths of a data series to the times of target series, such that a minimum misfit, according to a given cost criterion, is obtained [115]. A good general description of this method was given by Sakoe and Chiba (1978) [116]. The inspiration for the work presented here was obtained from Kassidas (1997,1998) [117; 118].

2.4.2 General description of the method used for automated correlation

Before formulating the mathematical details of the method employed in this study, it is useful to explain the general principles that are involved. The overall aim is is to align a geological depth series, denoted as a vector $\mathbf{D}$ with N data points, to a target time series, denoted as a vector $\mathbf{T}$ with M data points, by stretching, squeezing, and possibly shifting of the depth series $\mathbf{D}$. Individual points of the data and target curves will be indicated as D_i and T_j, respectively, where i and j are indices that increase monotonically with depth and time. The general idea of this matching was illustrated in figure 2.4. One can set up an orthogonal co-ordinate system, using depth and time as axes, where the aim is to find an optimal path that maps depth to time (the "mapping function", denoted by an array F, containing depth and associated time index values). Starting from the plane that is defined by the depth and time axes, imposing constraints on possible sedimentation rate changes as well as introducing tie-points with associated uncertainties in depth and time will reduce the area on which the mapping function path can lie, and allows the incorporation of those constraints and conditions outlined in section 2.3.2. The resulting area is called the search region for the pattern matching algorithm.

In principle, one could consider to find the "optimal" mapping function by employing a brute force search of all possible paths, computing a "global" misfit value for each path. However, the number of computations necessary is a factorial function of the number of data points, which renders the brute force approach prohibitive for data series with hundreds or more points. Instead, two simplifications are used here to make the method computationally more tractable. The first simplification consists of representing the target curve data as a set of discrete points along the time axis. The location of these points is not changed by the algorithm. In addition, the time values of the mapping function must coincide with times from the target curve. Also, from each point of the mapping curve to the next, an integer ratio must be maintained between the number of data points allocated to the number of discrete target curve time steps. Although this approach allows a limited number of data curve depths to be allocated between discrete target curve times, in general the pattern matching problem is moved from a continuous representation to a discrete one. A second simplification is achieved by computing the misfit between the data and target curves only for individual points on the mapping path, and finding the complete path in a second stage by assembling the

mapping path that results in the lowest overall misfit. The selection of the optimal path is subject to fulfilling constraints on allowed local sedimentation rate variations that are represented by the slope of the mapping function [119]. The method used for this approach is called "dynamic programming", and explained in the following section.

2.4.3 A "dynamic programming" approach for optimisation

The method of dynamic programming was first introduced by Bellman (1957), and Bellman and Dreyfus (1962) [120; 121]. They formulated the principle of optimality (also known as "Bellman's principle"). This can be described as [122]:

> *An optimal policy has the property that whatever the state the system is in at a particular stage, and whatever the decision taken in that state, then the resulting decisions are optimal for the subsequent state.*
>
> *or*
>
> *An optimal policy is made up of optimal sub-policies.*
>
> *or*
>
> *An optimal policy from any state is independent of how that state was achieved and comprises optimal sub-policies from then on.*

To find an optimal path, this can be translated into two rules [118]:

1. Let F^* be the optimal global path on the depth-time grid (of dimension $N \times M$). If F^* goes through a point (D_i, T_j), then the optimal path to the (D_i, T_j) point from the point (D_1, T_1) is part of F^*.
2. The optimal path to the point (D_i, T_j) depends only on previous grid points.

These rules then define a recursive relationship, where the problem of finding an optimal path is broken down into the sub-problem of finding an optimal local point given a history of decisions about previous path points. This allows the rapid calculation of the optimal global mapping function, since the number of misfit calculations does not increase as a factorial function of the number of data, but approximately as a quadratic function.

The algorithm operates in two steps. The first part starts at point (D_1, T_1) and proceeds to the point (D_N, T_M), covering all points that lie on the search grid (see figure 2.4). At each point, the algorithm computes and stores a local misfit measure (in this study the least squares distance between individual target curve and data points, or the least squares distance between band-pass filtered data and target curve points). The result is then weighted according to sedimentation rate constraints (described in detail in a later section), and added to the lowest stored misfit value of the predecessor points. This new accumulated misfit value for the path up to this point is stored. Also stored is the predecessor point on the mapping grid with the lowest misfit value. When the algorithm arrives at point (D_N, T_M), the second part of the algorithm starts. This simply goes back to the point (D_1, T_1), retrieving the best predecessor point starting from (D_N, T_M). This procedure is described in more detail by Kassidas (1997) [117]. As misfit values are stored for all points of the mapping path that lie within the search region, it is possible in principle to plot maps of the misfit values on the search grid and to evaluate the robustness of the obtained mapping path. This was not attempted in this study, but would be useful to assess the influence of local minima. The following two sections provide the formal definitions for sedimentation rate constraints.

2.4.4 Specification of global and local constraints

A number of conditions need to be enforced for the optimisation problem to be well posed and mathematically well defined. These conditions involve constraints on the end points of correlation, global constraints on the allowable search region (see figure 2.4), local constraints that define the path of the mapping function from one point to the next, as well as conditions that ensure continuity and monotonicity in time and/or depth:

- End points can initially be specified by the mapping:

$$D_1 \longrightarrow T_1 \qquad D_N \longrightarrow T_M \tag{2.4}$$

  This constraint will be relaxed later to allow the introduction of uncertainty intervals for bio- and magnetostratigraphic datum points, which will form start and end points.

- Monotonicity is imposed by the following condition for points of the mapping function on the search grid:

$$\text{if} \quad D_i \longrightarrow T_j, \quad \text{then} \quad D_{i+1} \longrightarrow T_{j'} \quad \text{where} \quad j' \geq j$$

  This assumes there is no stratigraphic repetition in the geological data. This assumption can be violated by, e.g., coring problems. For mathematical simplicity this condition will be retained here, assuming that any such intervals could be identified on visual and geological grounds prior to the analysis.

- Continuity, i.e. a limitation on the possible change of implied sedimentation rate, is imposed by constraints on how the next point along the mapping path can be reached from previous points. Several possible examples are illustrated in figure 2.7. These conditions implicitly impose monotonicity. The condition used in this study is that shown in figure 2.7(A).

The local constraints can implicitly specify the global search path. For example, the local constraint shown in figure 2.7(A) leads to a global search area as shown in figure 2.4, where the possible path of the mapping function on the search grid has the shape of a parallelogram. The sides of this region are bounded by lines that have the minimum and maximum slopes of the local constraint, which in this case are $1/2$ and 2 with respect to the data and target curve indices.

There are at least two possible ways to adjust the possible range of sedimentation rate changes. Sakoe and Chiba (1978) [116] introduced a general approach, where one can specify two parameters a, b, such that the increment of the mapping function along the data index i cannot be greater than a steps until b steps have been taken in the direction of the target axis j index, and vice versa. This would result in an allowed slope range of $[a/b, b/a]$ with respect to the data and target curve indices. Alternatively, in this study the same result was achieved by adjusting the sample rate between consecutive points.

2.4.5 Normalisation of the cost function and the optimisation problem

When comparing data and target patterns with different lengths it is necessary to apply a weighting and normalisation in order to make the total misfit of different possible mapping functions comparable. The weighting of each local misfit measure depends

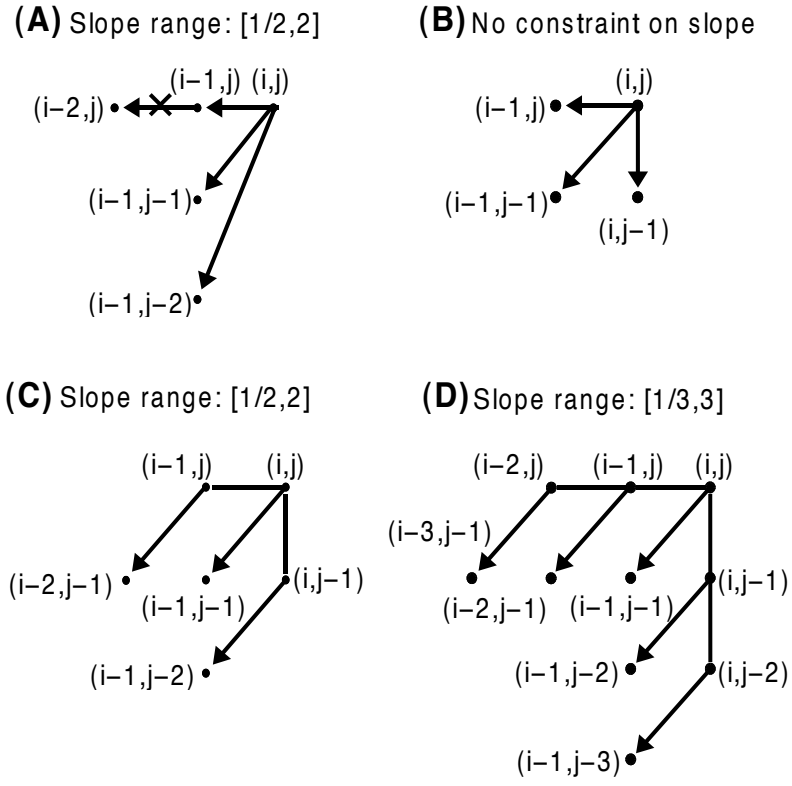

Figure 2.7: Typical slope constraints on the warping function used in dynamic time warping. Arrows indicate from which previous mapping points the next point can be chosen, as indicated by the data curve index i, and the target curve index j. (A) shows a constraint described in [119] ("Itakura" local constraint), which results in a minimum slope of 0.5 and a maximum slope of 2 (with respect to the data and target curve indices). The cross indicates that only one consecutive horizontal transition is allowed. This was the local constraint that was employed in this study. (B) to (D) show various constraints as described in [116] ("Sakoe-Chiba" local constraints). Figure modified from Kassidas (1997) [117].

on the chosen local sedimentation rate constraint, while the normalisation depends on the number of data points, the length of the mapping function between end points, as well as the sedimentation rate constraint. Kassidas *et al.* (1998) [118] specified different weighting functions for each of the local constraints shown in figure 2.7. Here, only the local constraint shown in figure 2.7(A) is used, for which the normalisation is the number of depth index values N which are mapped to the time indices, and the weighting function is unity for all allowed transitions. For each allowed mapping from D_i to T_j a local least squares misfit measure is calculated as

$$z_{(i,j)} = (D_i - T_j)^2$$

to which the lowest accumulated misfit value out of all three allowed predecessor points is added. The predecessor with the lowest misfit is stored as the optimal predecessor for the index pair (i, j).

For the local constraint that was used here, shown in figure 2.7(A), the transition from one mapping function point to the next that involves a larger than one increment of the data (depth) index per increase of the target (time) index is omitted from the list of allowed predecessor points, thus preventing sedimentation rates smaller than $1/2$ and greater than 2, with respect to the depth and time indices, and resulting in N total mapping pairs. All three remaining transitions are weighted equally, and the total accumulated misfit at the last mapping point only contains contributions from points on the mapping path that follow allowed transitions. The normalised total misfit of the final mapping path for the local constraint of figure 2.7(A) is then given by

$$Z = \frac{\sum_{i=1}^{N} z_i}{N}$$

where each data point with index i has one associated local misfit z_i with respect to the target curve point it was mapped to, with N total mapping pairs.

The next section describes how this procedure is modified to allow the incorporation of uncertainties of the exact position of the starting and end points of the mapping function, corresponding to uncertainties in the dating and/or stratigraphic depth of magneto- and biostratigraphic tie-points.

2.4.6 Extending the dynamic time warping approach

As described so far, the implementation of the dynamic time warping method has not allowed the specification of uncertainty intervals, nor has it allowed the use of a band-

pass filter approach for the cost function calculation. This section describes the full implementation of the dynamic time warping method that was used in this study to perform an automated astronomical tuning. This implementation was written as an ANSI C language programme and is available on the enclosed CD-ROM, and can be downloaded [123]. The software makes use of the signal processing library from McGill University [124].

To work properly, the dynamic programming approach requires a normalisation to the number of points that are present in the mapping function, although it is possible to relax the conditions imposed on the first and last point, as well as on the search region. Figure 2.8 shows the generalised search area specification as used in the newly developed computer software. This study used the "Itakura" local constraints shown in figure 2.7(A). Extensions to the DTW method are as follows:

- Multiple bio- or magnetostratigraphic constraints are allowed. These are separately processed as individual segments by using the DTW method. If uncertainty intervals are allowed, as described next, the newly determined last path point on the mapping function for each segment then forms the first one for the next.

- One can allow the first and last point to move in the area that is specified by the parameter γ in figure 2.8. The movement in the direction of the target axis index j according to γ does not require any change in the algorithm, as the normalisation only depends on the number of data points in the data curve **D**, which is not affected by γ. Strictly, allowing the mapping function end points to move along the data index i according to δ invalidates the dynamic programming approach, since now the number of path points is not known during the calculation of individual local distances. However, Kassidas (1997) [117] showed that a heuristic normalisation, first mentioned by Rabiner *et al.* (1978) [125], can be used for those accumulated distances that move along δ:

$$Z_{norm} = Z_{accum}(i, M_s)\frac{N_s}{i}$$
$$\text{with} \qquad N_s - \delta_s \leq i \leq N_s$$

  where Z_{norm} denotes the heuristically normalised accumulated distance Z_{accum} up to a given point (specified by indices inside parentheses), and the subscript s denotes individual segments between tie points.

- Multiple data and target curves are allowed. The total distance or misfit measure is then computed as the sum for each data target pair. The relative contribution of each can be adjusted by using different weights.

- The bandpass local distance measure can be introduced. This requires the convolution of a filter series in the time domain up to the path point being considered. This computation requires a minimum path length, and can thus not be employed over the entire length of the record. Instead, a local distance measure, such as the least squares distance, is used up to the first path point where the length of the path is long enough to allow filtering. Combined with the previous modification, it is possible to use different (bandpass) filters for the same record, e.g. a combination of filters for "short" eccentricity, obliquity and precession.

2.4.7 The full DTW algorithm

In algorithmic form, the entire age model generation via DTW can be summarised by algorithm 1, as given on one of the following pages. This is a modified version of that given by Kassidas (1997)[117].

2.5 Testing the DTW algorithm with synthetic data

The DTW algorithm has not been applied in the field of geological correlation and astronomical tuning before, and in this study a completely new programme was used. For this reason it was necessary and instructive to run a series of tests to evaluate the performance of the algorithm, and to discover its limitations. This study found, that the algorithm performs exceptionally well, particularly when computing age models that rely on a quasi-periodical signal for correlation, which is the fundamental basis for astronomical "tuning". The following sections report the results from some of these experiments. The general methodology consists of designing "synthetic" target and data

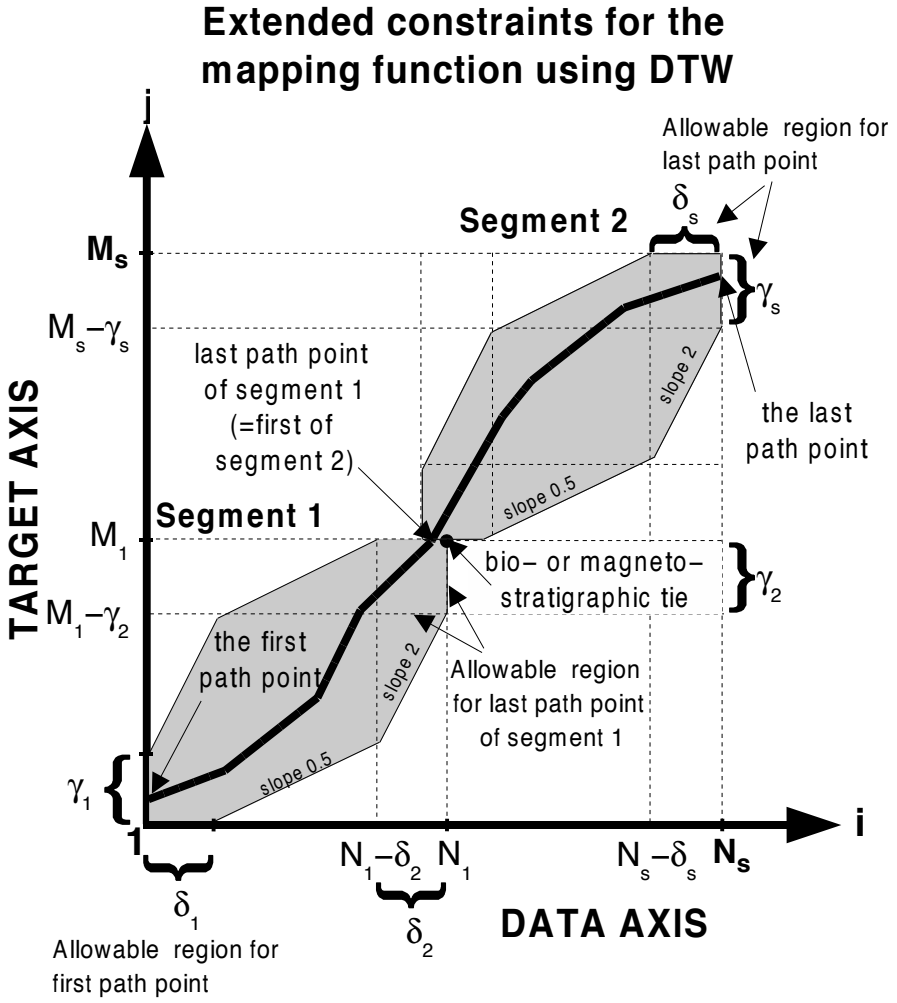

Figure 2.8: Generalised and extended constraints for DTW orbital tuning. The allowed region for the search path is shaded in grey. Each segment, which is defined by bio- or magnetostratigraphic constraints at its end points and denoted by the subscript s, is computed separately by the algorithm. The local constraint is that of Itakura (see figure 2.7(A)), resulting in a parallelogram with slopes 0.5 and 2 for each segment. Uncertainty intervals for the tie points can be specified by using appropriate values for γ_s and δ_s. The last path point of segment 1 then forms the first path point for segment 2, and so on.

Algorithm 1 Finding a mapping function using DTW

Split data and target curves into s segments, according to tie points.
for all segments **do**
  For each segment, assign the first point as index 1, and the last one M or N for the target and data curve, respectively.
  given values for δ and γ at the start and end of each segment,
  compute the allowable search path:
  compute lower target index boundary $l(i)$ for each data index i and
  compute upper target index boundary $u(i)$ for each data index i
  Set accumulated misfits $Z_{accum}(1,j) = z(1,j)$ for $1 \leq j \leq \gamma$
  for $i = 2, \cdots, N$ **do**
    for $j = l(i), \cdots, u(i)$ **do**
      if $(1 \leq i \leq \delta + 1)$ or $(N - \delta + 1 \leq i \leq N)$ **then**

$$Z_{accum}(i,j) = \min \left\{ \begin{array}{ll} Z_{accum}(i-1,j) & +z(i,j) \\ Z_{accum}(i-1,j-1) & +z(i,j) \\ Z_{accum}(i-1,j-2) & +z(i,j) \end{array} \right\}$$

      else if predecessor of point $(i-1,j)$ is point $(i-2,j)$ **then**

$$Z_{accum}(i,j) = \min \left\{ \begin{array}{ll} Z_{accum}(i-1,j-1) & +z(i,j) \\ Z_{accum}(i-1,j-2) & +z(i,j) \end{array} \right\}$$

      else

$$Z_{accum}(i,j) = \min \left\{ \begin{array}{ll} Z_{accum}(i-1,j) & +z(i,j) \\ Z_{accum}(i-1,j-1) & +z(i,j) \\ Z_{accum}(i-1,j-2) & +z(i,j) \end{array} \right\}$$

      end if
      Store the optimal predecessor for the (i,j) mapping point
    end for
  end for
  Compute the minimum normalised distance at the last point:

$$Z = \frac{1}{N} \min \left\{ \begin{array}{ll} Z_{accum}(i,M)\frac{N}{i} & ,N-\delta+1 \leq i \leq N \\ Z_{accum}(N,j) & ,M-\gamma+1 \leq j \leq M \end{array} \right\}$$

  Reconstruct the optimal path F^* for this segment, starting from the last path point. Then travel backward as each stored optimal predecessor indicates, and locate first path point.
  Use last path point of this segment as first path point for the next segment.
end for

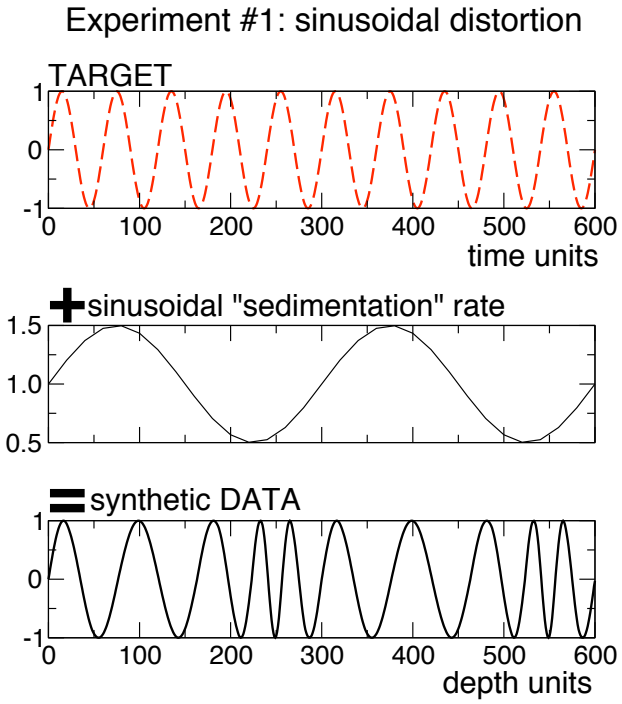

Figure 2.9: Synthetic input data for testing DTW algorithm. Experiment #1: matching a sine wave with a sinusoidally distorted sine wave to an undistorted sine wave.

curves that test a particular feature of the algorithm. The numerical experiments here generally increase in complexity.

2.5.1 Experiment #1: Testing variable sedimentation rates

The input data for the first experiment are shown in figure 2.9. The target curve consists of a sine function with ten oscillations, sampled by 601 points. This first test was designed to validate the operation of the software in general, and its ability to detect and compensate for variations in sedimentation rate. The synthetic data curve was thus created by applying differential compression and expansion to the initial target curve, using a relative sedimentation rate as shown in the centre of figure 2.9. The term "relative" sedimentation rate refers to the sedimentation rate between individual data points. Thus, if one "depth" unit corresponds to one "time" unit, and both series are sampled at equal distances, the relative sedimentation rate corresponds to the target sedimentation rate.

In all numerical experiments reported in this section the local and global "Itakura" constraints were used, as illustrated in figures 2.7 (A) and 2.8. These constraints specify that the local relative sedimentation rate as computed by the DTW algorithm can lie

only between $1/2$ and 2. The sedimentation rate for this experiment was designed to test the algorithm to the limit of this constraint, while at the same time ensuring that the last point of the data curve remains in its initial position, i.e. the overall compression over the length of the curve amounts to zero.

For this test, the parameters δ and γ were set to zero, which implies that the first and last points of the data and target curve are not allowed to move with respect to each other. This condition will be relaxed in later experiments.

Figure 2.10 shows how the DTW algorithm adjusted the synthetic "depth" curve to the target curve, using the least squares method as a correlation criterion. The algorithm managed to recover the imposed variation in sedimentation rate, which confirms the general working of the algorithm in this simple situation. The actual sedimentation rate, as used by the algorithm on a point to point basis, is shown in the lower part of the figure. This serves to remind us that, while the input sedimentation rate was a continuous function, the algorithm uses integer values only. That is to say, that a smoothly varying sedimentation rate is approximated by a combination of discrete steps on the grid, and inside the algorithm, these can only take values of 0.5, 1 or 2.

This produces essentially the same result for the input and output age model, but suggests that one should not use the recovered mapping function directly, but instead a running mean. Note that on figure 2.10 computed sedimentation rates appear with a value of $\sim 2/3$, which is caused by interpolation for one depth value that was allocated to two consecutive time values. This is an artifact of how the computed sedimentation rate was represented on this plot.

2.5.2 Experiments #2 and #3: Testing relaxed end point conditions

The next numerical experiments were designed to test the effect of relaxing the end point conditions as suggested in section 2.4.6 and illustrated in figure 2.8. This simulates a situation where bio- or magnetostratigraphic constraints have an associated uncertainty in either their stratigraphic position, or their exact timing.

Figure 2.11 shows the input curves that were used for experiment #2. Here, the data curve has one extra cycle compared to the target curve. In this experiment one of the end point constraints was relaxed by setting the parameter $\delta = 70$, while keeping $\gamma = 0$. This implies that the algorithm is allowed to discard up to 70 "depth" units at the beginning and end of the data curve in total, and is equivalent to an uncertainty in the depth

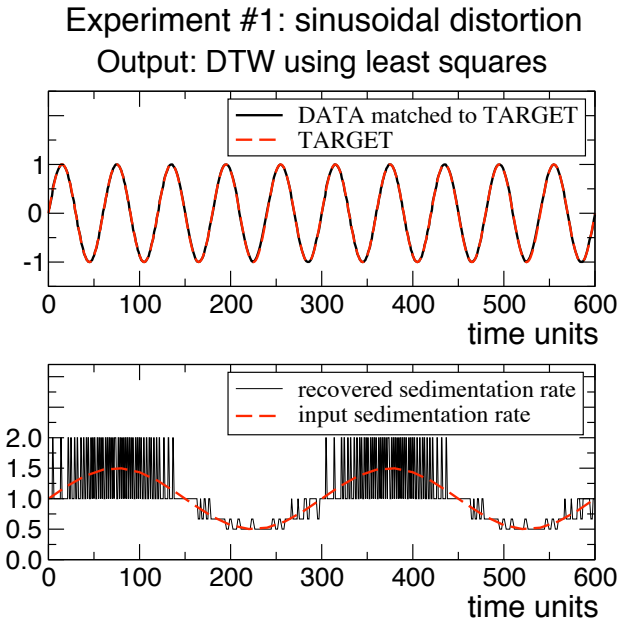

Figure 2.10: DTW algorithm output for experiment #1. The top panel shows the data curve as adjusted by the DTW algorithm, superimposed on the target curve. The bottom panel shows the relative "sedimentation rate" that was used as input to create the data curve, and that computed by the algorithm.

domain for a given tie point.

After running the DTW algorithm, the output with these constraints is shown in figure 2.12. The algorithm discarded 9 points at the beginning, and 45 points at the end of the depth series, which corresponds exactly to one extra cycle present in this curve (where the number of points is calculated as $600/11$).

In experiment #3 the situation was reversed, such that the target curve contains one extra cycle. This is not exactly equivalent to the situation given in experiment #2, since this time the algorithm does not have to make use of a heuristic approximation to allow the dropping of points on the target curve. This is achieved by setting the value of the parameter $\gamma > 0$, as outlined in section 2.4.6. The input configuration for experiment #3 is shown in figure 2.13.

The output for experiment #3, shown in figure 2.14, shows that the algorithm again succeeded in matching the data cycles to the target cycles. In this experiment the parameters δ and γ were both set to 70 points. The algorithm correctly only used the relaxed constraints for γ by dropping points of the target series. 21 points were dropped at the beginning of the target curve, and 39 at the end. Again, this correctly amounts to one full cycle in the target curve.

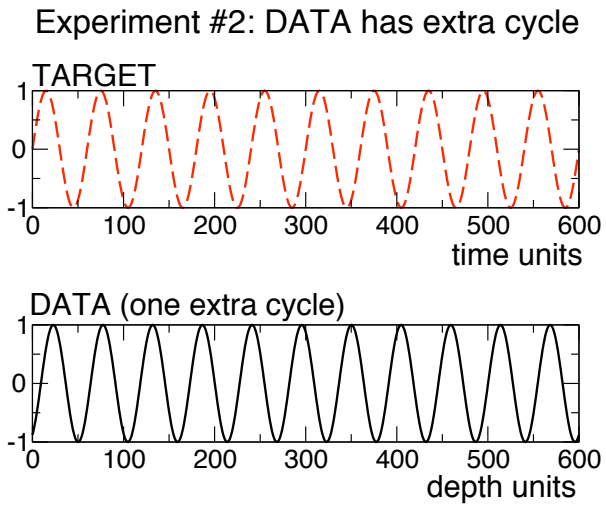

Figure 2.11: Synthetic input data for testing DTW algorithm. Experiment #2: matching a data curve with one extra cycle to a target.

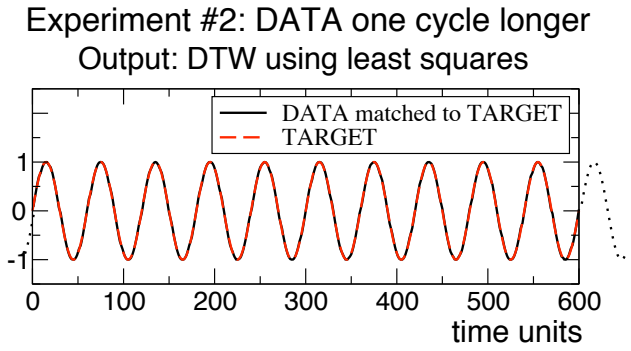

Figure 2.12: DTW algorithm output for experiment #2.

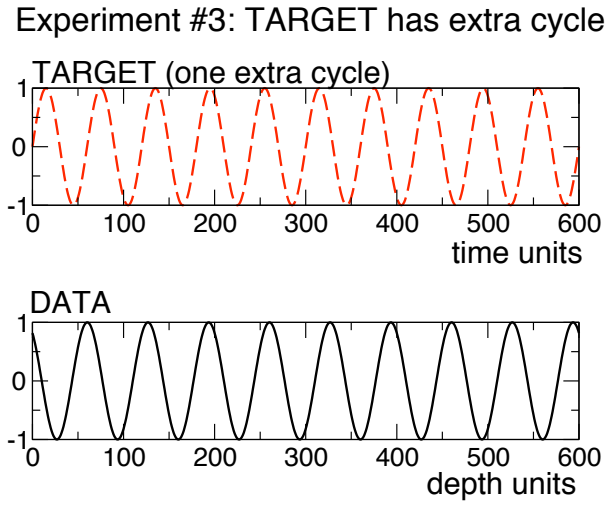

Figure 2.13: Synthetic input data for testing DTW algorithm. Experiment #3: matching a data curve to a target with one extra cycle.

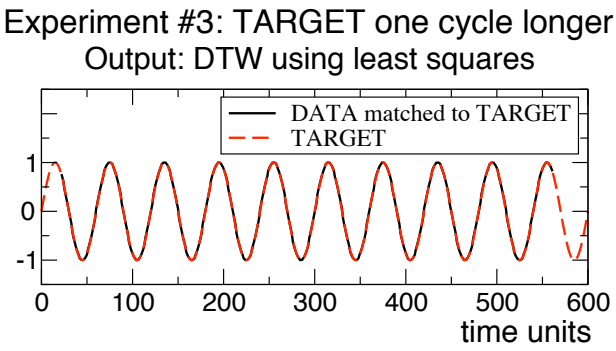

Figure 2.14: DTW algorithm output for experiment #3.

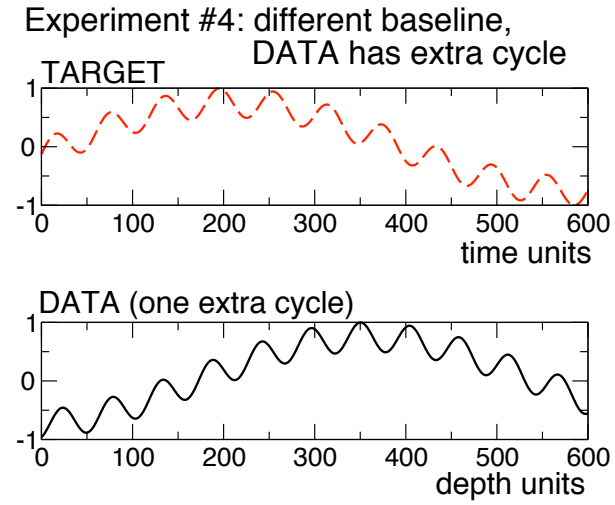

Figure 2.15: Synthetic input data for testing DTW algorithm. Experiment #4: data and target curves have a different low frequency baseline, and the data curve has one more higher frequency cycle.

2.5.3 Experiment #4: Testing bandpass filtering as correlation tool

Experiment #4 was conducted to compare two different ways to compute the "local" misfit between data and target curve. Most other correlation software packages and approaches make use of either the correlation coefficient or the least squares method, and the latter was used in the experiments described in this study so far. In the experiments up to now, the target and data curves were essentially very similar in that both consisted of oscillations at a single frequency around a zero mean. In experiment #4, data and target curves are constructed such that they have a different underlying "baseline" low frequency component. Superimposed on this baseline, both contain a higher frequency component, where the data curve contains one extra higher frequency cycle. This set of input data is shown in figure 2.15.

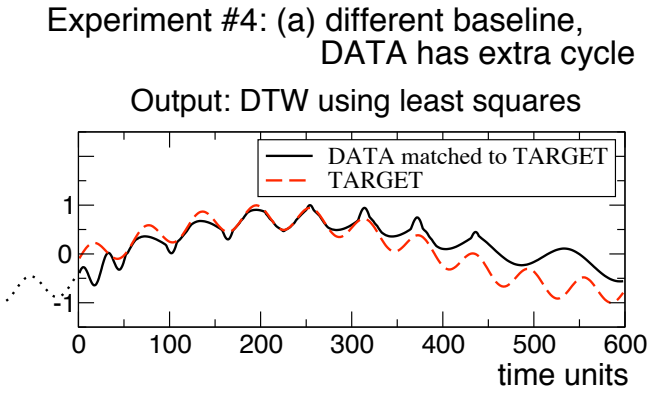

Figure 2.16: DTW algorithm output for experiment #4 (a).

First, the DTW algorithm was run as before, by using the least squares misfit criterion, and setting the parameter δ to 70, to allow the algorithm to discard points from the beginning and the end of the data curve. The output for this is shown in figure 2.16.

As expected, the resulting match is almost entirely controlled by the underlying low frequency base line component. This is matched rather well, while the higher frequency component is only considered as a secondary feature. However, in the process of astronomical tuning, one might be primarily concerned with matching oscillations of a particular set of frequencies only, regardless of the general trend of the data. One example for this would be large excursions of stable isotope data as described near the Oligocene/Miocene boundary (Zachos *et al.*, 2001) [126], or near the Eocene/Oligocene boundary (Zachos *et al.*, 1996) [127].

For this reason, the experiment was conducted again using a different criterion for evaluating the local mismatch between data and target curve at each point. A bandpass filter was designed to pass the higher frequency components and block the low frequency base line. This filter was designed with the software "METEOR" (Steiglitz *et al.*, 1992 [128]), and has a length of 71 points. The output that results from this form of pattern matching is shown in figure 2.17.

Note how in this figure the individual peaks of the higher frequency cycles are very well matched between the target curve and the data curve, regardless of the underlying trend. The individual cycles of the data curve are slightly distorted. This is the result of the bandpass filter used. A trade-off has to be achieved between the sharpness of this filter, and its length. Generally, one would like to have a filter as short as possible.

This is because the filter can only be used for correlation after enough points are

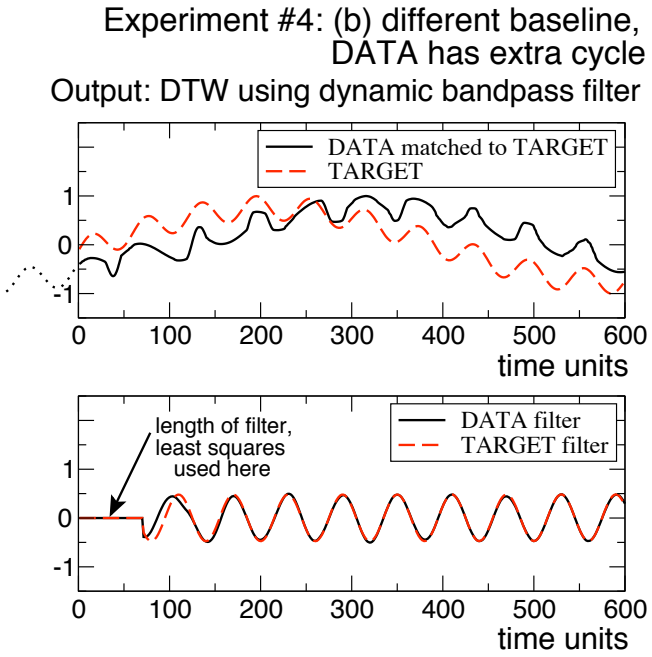

Figure 2.17: DTW algorithm output for experiment #4 (b).

available to compute the filtered values. Before this condition is satisfied, the algorithm reverts back to the least squares method. This is indicated by the arrow in the lower part of figure 2.17. Since the filter chosen was quite short, the pass band of the filter is quite wide, thus leading to a small distortion of the data curve.

The lower panel of figure 2.17 shows the filter output that was actually used by the algorithm to achieve the correlation, which shows a good match between data and target, despite the visible distortion. Note that there is a short transition period where the least squares matching switches to the bandpass filter matching, which is unfortunately not avoidable. This is the first time that an algorithm designed for the correlation of geological data or astronomical tuning allows the use of bandpass filtering, and this experiment demonstrated that its application is feasible in principle, but that care must be taken when designing a particular filter.

2.5.4 Experiment #5: bandpass filtering of multiple frequencies

The last numerical experiment reported from this study is described here, and employs astronomically computed time series as synthetic input data, rather than combinations of pure sinusoidal waves. Experiment #5 investigates how the DTW algorithm (with bandpass filtering) copes in a situation where both data and target curves have a rich frequency spectrum, and where the data curve is distorted in the depth domain.

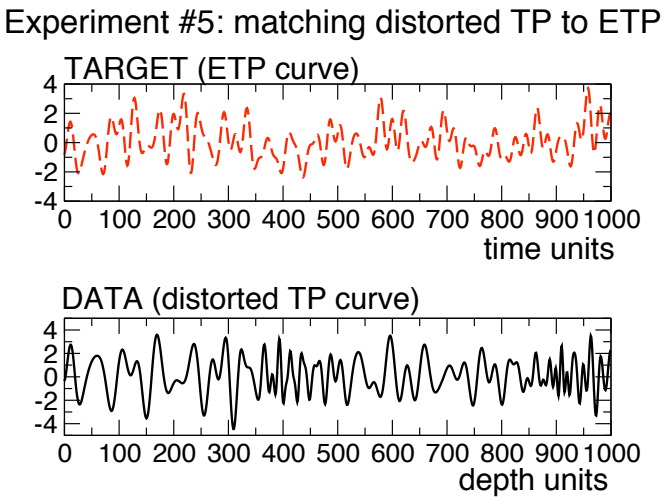

Figure 2.18: Synthetic input data for testing DTW algorithm. Experiment #5: the data curve consists of an astronomical time series constructed by adding the normalised obliquity and flipped climatic precession components of the La1993$_{(1,1)}$ solution ("TP" curve), which was distorted as in experiment #1. The target curve also contains an eccentricity component ("ETP" curve), and has not been distorted.

The input data for this experiment are shown in figure 2.18. The target curve was constructed by first normalising the eccentricity, obliquity, and climatic precession components of the La1993$_{(1,1)}$ calculation (Laskar, 1993) [86] for the last 1000 ky to zero mean and a standard deviation of one, adding these components with a ratio of 1:1:-1, and finally normalising again. This construction of an "ETP" curve is described by Shackleton (2000) [68]. This target curve is shown in the upper panel of figure 2.18, and clearly shows a low frequency eccentricity base line with periods of $\sim$100 ky, and $\sim$400 ky, on which the obliquity components and climatic precession "bundles" are superimposed.

For the generation of the data curve, the same procedure was employed, but without using the eccentricity component, thus constructing a "TP" curve. Additionally, this curve was distorted by using a sinusoidally varying sedimentation rate similar to that used in experiment #1, i.e. two cycles over the length of the data series. The resulting curve is shown in the lower part of figure 2.18.

In the first part of this experiment, a bandpass filter was used for correlation. This filter was designed to only pass the obliquity components of the signal, and the resulting output is shown in figure 2.19.

In this case, the DTW algorithm did not recover the original age model, as shown by

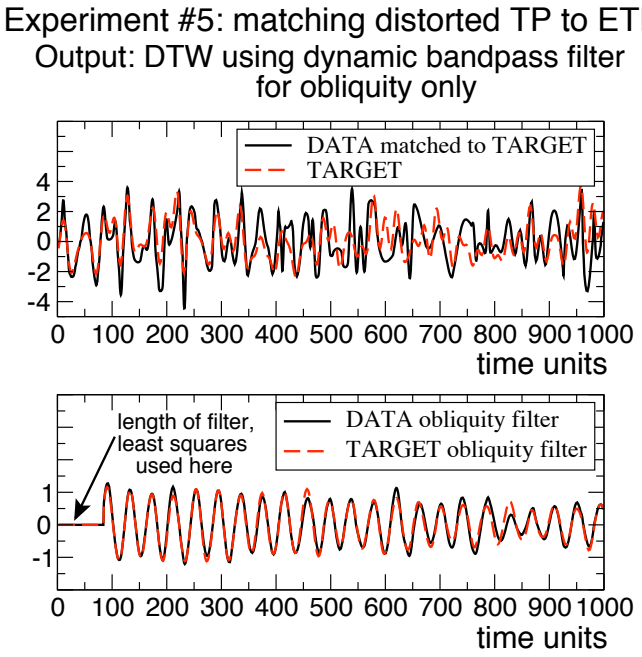

Figure 2.19: DTW algorithm output for experiment #5, using only a dynamic obliquity band pass filter for correlation.

the mismatch of data and target curves between ~450 and 850 ky, even though the filters for the two series do match well. On closer investigation, the algorithm decided to map two precession cycles into one obliquity cycle, thus creating a "wrong" age model. When repeating the experiment with a climatic precession bandpass filter only (not shown here), the correct age model was recovered.

This suggests that bandpass filter correlation approaches should make use of the highest frequency component present, if possible, to avoid mismatching of cycles, although this might be hampered by a "noisy" data set. In this context, noise can be defined as any variability in the geological data that is not related to the orbital signal. This noise can influence the correlation if it occurs at orbital frequencies. In addition, if the sedimentation rate varies by a factor of two or more, it will always be difficult and problematic to distinguish between obliquity and climatic precession cycles, as their frequencies occur with a ratio of approximately two.

Alternatively, the DTW algorithm developed for this study can consider two or more bandpass filters simultaneously. If one makes use of this facility by using a precession and obliquity bandpass filter at the same time, one can retrieve an improved age model, as shown in figure 2.20.

To compare the different parts of this experiment, the input as well as the three out-

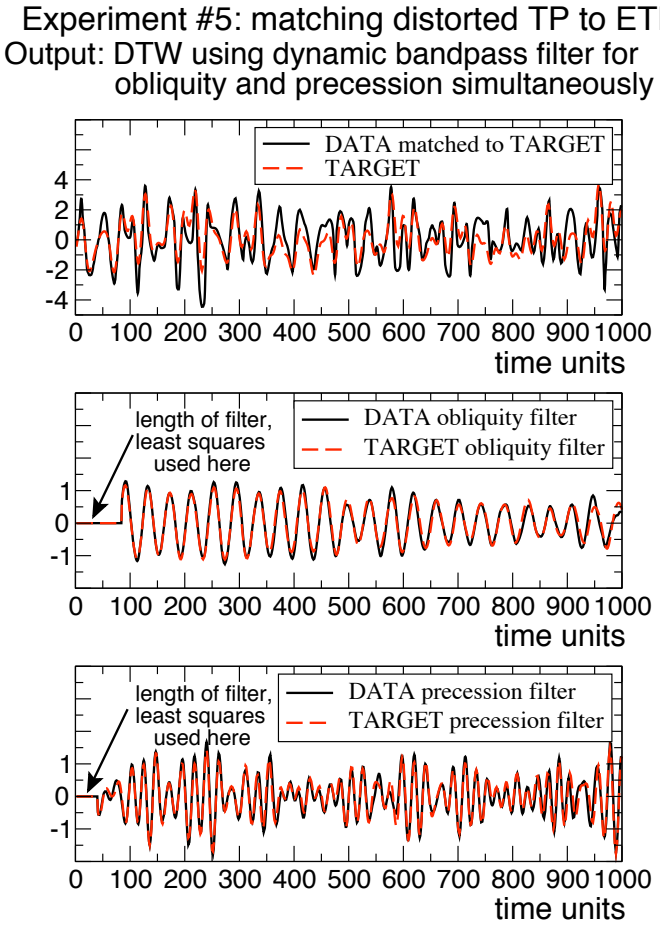

Figure 2.20: DTW algorithm output for experiment #5, using a dynamic bandpass filter for obliquity and precession for correlation simultaneously.

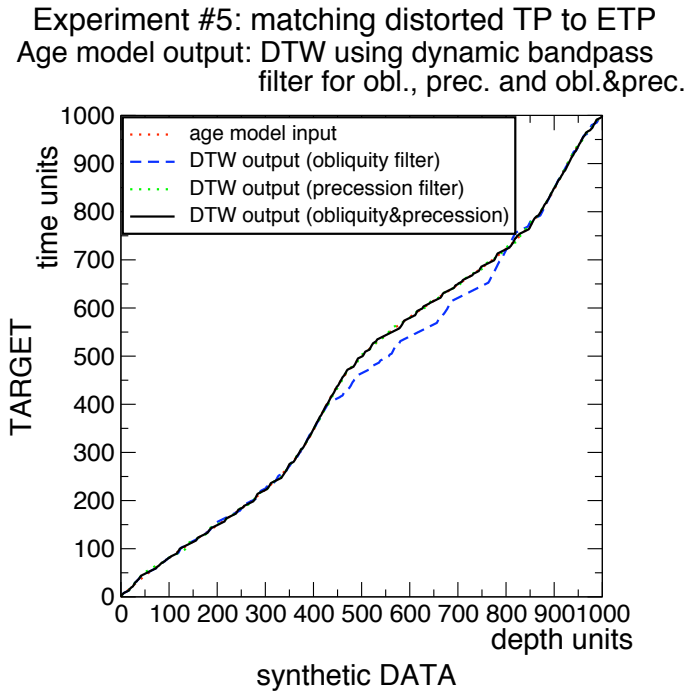

Figure 2.21: Input and DTW output age models for experiment #5.

put age models are shown in figure 2.21. In this particular experiment, only the obliquity bandpass filter failed to recover the original age model. Given that real geological data will most likely contain noise, including at frequencies higher than the highest astronomical frequency, the combination approach of using multiple bandpass filters is considered to be the most stable and useful. The relative weight attached to each component can be adjusted in the light of the predominant astronomical frequency expressed in the data.

2.6 Using the DTW algorithm with geological data: a case study

This section summarises the results that were obtained from testing the performance of the DTW algorithm when applied to the matching of geological data to astronomical target curves. The original impetus for the development of an automated and more objective astronomical tuning procedure was given by the need to re-tune the astronomical calibration of Neogene data from Ocean Drilling Program (ODP) Leg 138 as reported by Shackleton *et al.* (1995) [51].

The original age model needed adjustment for two reasons. First, in the original study the astronomical calculation used as a target curve was that of Berger and Loutre (1991) [80], henceforth denoted as BER91. In order to make different astronomical cal-

ibration studies comparable, the ODP 138 data set needed to be adjusted to the more recent astronomical calibration of Laskar *et al.* (1993) [86], henceforth denoted as LA93 for the solution with present day values for tidal dissipation and dynamical ellipticity (denoted as "La1990$_{(1,1)}$" in the paper of Laskar *et al.*). This more recent calculation shows very small differences compared to that of Berger and Loutre, as illustrated in figure 2.2. Second, the study of Hilgen *et al.* (1995) [52] resulted in slightly different ages around the Pliocene/Miocene boundary. A re-tuning of the material from ODP Leg 138 should be able to test whether the Leg 138 data can also be compatible with the interpretation of Hilgen *et al.*

The focus of the study presented here is to test the performance of the DTW algorithm by creating "objective" age models based on cyclic variations in the data only, rather than creating a new age model that is completely consistent with magneto- and biostratigraphic constraints or existing chronologies from other studies. The age models that are presented in the remainder of this chapter are thus those that would be generated in the absence of additional constraints or geological interpretations and judgement. Thus the presented age models will not necessarily be the "correct" ones, but, in comparison with published age models that do take into account these constraints, serve to illustrate the strengths and limitations of the DTW automated tuning approach.

Of all the data available from ODP Leg 138, this study only makes use of data from Site 846. This is because a high-resolution stable isotope record is available from this Site ([129]) from approximately 2 to 6 Ma, which facilitates a comparison with other astronomically calibrated data sets. To generate their age model, Shackleton *et al.* (1995) [51] made use of the GRAPE density records. Initially, they worked with "spliced" composite GRAPE records, which were later substituted by a stacked GRAPE density record following Hagelberg *et al.* (1995) [99]. Shackleton *et al.* gave two different versions of their age model for the most recent one million years: one that was based on GRAPE data alone, while the second one took into consideration established oxygen isotope stratigraphies. In this study, only the stacked GRAPE density record from Site 846 was used to avoid bias in the generated age models. This study focused on the time interval from 0 to $\sim$6.2 Ma.

2.6.1 Methods and parameters used for DTW age model generation

This section describes the tuning experiments that were performed, and the parameters that were chosen for the DTW algorithm, to generate different age models. In the remaining discussion, as well as in the remaining figures, these experiments will be referred to by the letters A to H. The initial age model, as given in [51] table 3, is labelled as A. In all cases, this age model was used as a starting point. For all automatically generated age models, the aim of the experiments was to use as few constraints as possible. Thus, only the start and end points, close to 0.1 Ma and ∼6.2 Ma, respectively, were specified. The time 0.1 Ma was chosen instead of 0 ka to allow the use of bandpass filtering, which requires a certain length of record to be available before a filter can be computed.

In addition, the "Itakura" local constraint was used, as shown in figure 2.7 (A). This constraint allows the relative sedimentation rate to vary between a factor of 0.5 and 2, compared to the original age model. For all DTW runs, two bandpass filters were used simultaneously to extract the obliquity and climatic precession components of data and target curves. The filters used are identical to those used in the synthetic experiment #5 (section 2.5.4). The age model experiments B to H are specified as follows:

- Experiment B

  Experiment B was designed to test whether the original age model A would be recovered by the DTW algorithm, while only considering the GRAPE density data. The chosen target curve was identical to that one used for the generation of the initial age model A in [51], i.e. BER91. The start and end points were fixed such that the times 0.1 Ma and 6.2 Ma are forced to coincide exactly between the initial age model A and the computed age model. Thus, the DTW parameters δ and γ were set to zero, implying that the tie points are fixed rather than relaxed on both axes of the mapping function.

- Experiment C

  Experiment C was designed to investigate how the DTW algorithm would modify the initial tie points if the end point constraints are slightly relaxed. To achieve this, the parameter δ was set to 300 ky. In addition, an age of 6.1 Ma in the computed age model was set to coincide with an age of 6.3 Ma in the initial age model A. This modification was introduced such that the computation could not be bi-

ased towards the original age model A at the oldest tie point. The new age range is allowed to vary more towards older ages because the study of Hilgen *et al.* (1995) [52] suggested ages for this interval that are older by ∼100-150 ky compared to age model A. As a test for the sensitivity of the chosen approach to changes in the tie point constraints, the youngest tie point was also allowed to move by 300 ky.

- Experiment D

  Experiment D is similar to experiment C, but in addition the parameter γ was set to 200 ky. This serves as a sensitivity test for how the response of the algorithm changes as the constraints at the tie points are relaxed. With reference to figure 2.8, the parameter δ determines how many points may be dropped at the ends of the data curve, while γ determines how many points may be dropped at the older end of the target curve. To allow the movement of the tie point along the target curve axis, according to the parameter γ, requires the use of a heuristic normalisation of the total computed distance measure, as outlined in section 2.4.6. Thus, this configuration has the potential to be numerically less stable compared to the previous experiment, which only use the parameter δ.

- Experiments E, F, and G

  Experiments E, F, and G correspond exactly to experiments B, C and D, but use the insolation calculation of the model LA93 as the target curve.

- Experiment H

  The age model H was not derived by using the DTW algorithm. Instead, the initial age model A was adjusted manually such that the available benthic δ^{18}O data from Site 846 [129] match the benthic δ^{18}O data available from ODP Leg 154 that were generated by Pfuhl (2000) [130]. The age model for the data from Leg 154 Site 925 was obtained by making use of the LA93 astronomical solution and could thus provide an indirect way to arrive at new ages for the data from Leg 138.

2.6.2 Comparison of initial and generated age models

In this section the newly computed age models are compared with the initial age model. Figure 2.22 illustrates the age differences of the experiments B to H to the initial age model A. The absolute time axis is that of the initial age model A. Also shown is the magnetostratigraphy from Leg 138 as discussed in [51]. Note that the magnetic po-

larity signal of Site 846 was very weak. The record shown here is that recovered from other Leg 138 Sites (mostly Site 851), that was transferred to Site 846. Some uncertainty arises with respect to the exact position of magnetic polarity reversals in Site 846, although biostratigraphic constraints show that these are likely to be small. The upper panel shows the results obtained from experiments B and E, for which the oldest tie point was not allowed to move. The lower panel shows the age differences for the other experiments with relaxed end point conditions. Both panels show the age differences between the initial age model for Leg 138, and the ages of magnetic reversals obtained by the study of Hilgen *et al.* (1995) [52] for comparison. In both panels positive age differences imply that that particular age model is older with respect to the initial age model A.

Several interesting observations can be obtained from this age comparison. First, it is quite surprising how small the differences to the initial age model are, given that only two points spanning approximately 6 My were constrained. For all new age models, the maximum absolute difference in age does not exceed $\sim$240 ky, even though the DTW algorithm theoretically could have changed the ages at the centre between the two tie points (at $\sim$3 Ma) by up to $\sim$1.5 My in either direction.

Second, the set of new age models fall into distinct bands, with two general paths leading from the youngest to the oldest tie point, both of which are separated by either $\sim$100 ky or $\sim$200 ky. This suggests that the different solutions were slotted into different $\sim$100 ky short eccentricity cycles.

Third, for those experiments with relaxed end point conditions (shown in the lower half of the figure) there is a considerable age difference between 0–1 Ma. This is probably caused by a less clear astronomical signal in the GRAPE data over this time interval, as noted in the initial age model derivation of Shackleton *et al.* (1995) [51]. A similar deviation can be observed between 4–6 Ma. Experiment B, which was designed to use the same data and assumptions as the initial age model, shows a deviation from the initial age model at approximately 5 Ma, which coincides with an interval of the GRAPE data that is characterised by more erratic variations in density [51], and episodes of deposition of laminated sediments [131].

Interestingly, all experiments for which the older tie point position was allowed to move show a distinct increase in ages relative to the initial age model, and these ages are more consistent with the age estimates of Hilgen *et al.*

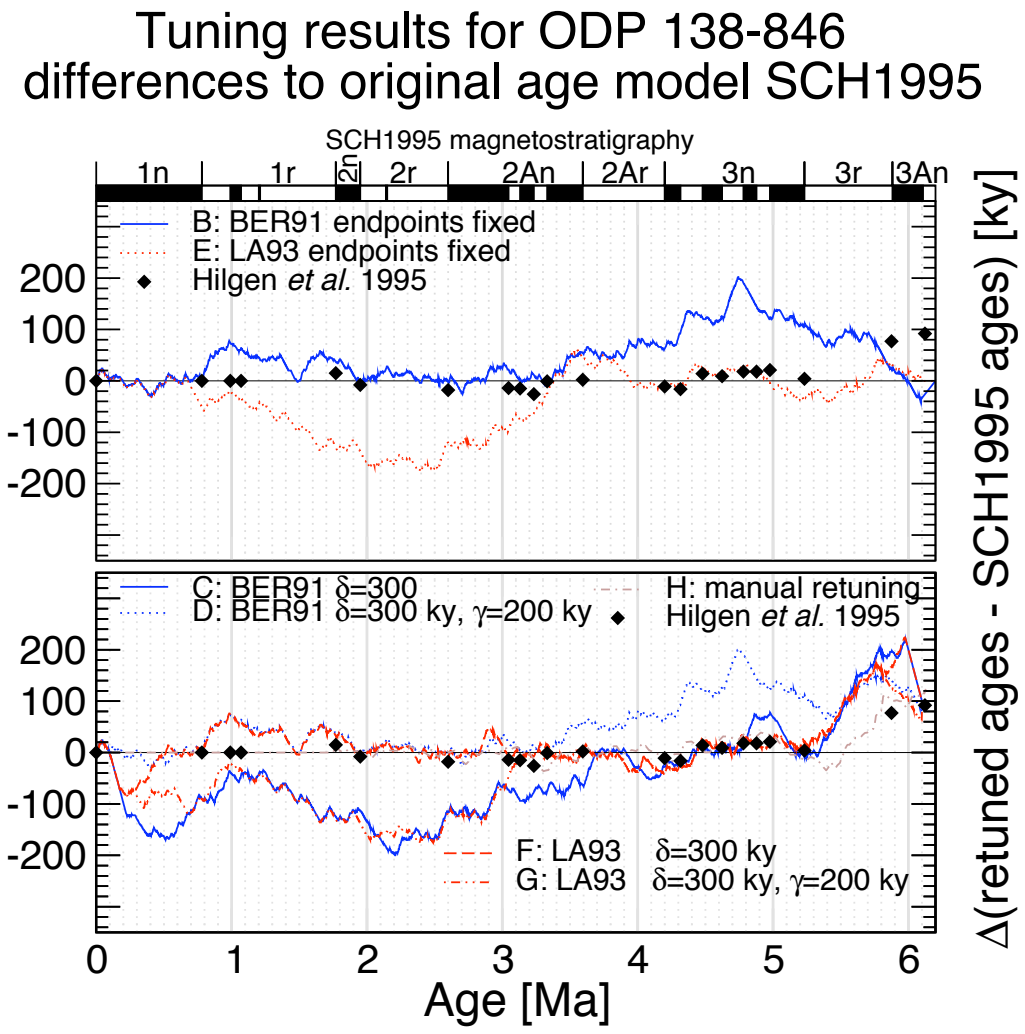

Figure 2.22: Tuning results for ODP 138-846 GRAPE density: age differences with original tuning.

To compare the generated age models in more detail it is worthwhile to study the GRAPE data plotted against the ages of the different age models. Figures 2.23 and 2.24 show the GRAPE data and the two target curves used.

The two vertical shaded bars are intended to illustrate that the DTW algorithm has moved high amplitude variations in the GRAPE data into separate ∼100 ky eccentricity controlled climatic precession envelopes. Generally, the automatically generated age models show a clearer expression of individual precession cycles. This can be attributed to the adjustment of every data point by the algorithm, compared to 208 tie points in the initial age model. The increase in age for the oldest part of the interval studied can be explained as an expansion of the data to cover five rather than four eccentricity cycles in the lower part of magnetochron C3r. This might be the main reason for the discrepancy between the initial age model of Shackleton *et al.* and Hilgen *et al.*

It is interesting to compare the different GRAPE time series after applying bandpass filters to extract the obliquity and precession components, since this is how the data were "seen" by the DTW algorithm. Figure 2.25 shows the data after applying a Gaussian bandpass filter with a central frequency of 0.025 ky^{-1} and a bandwidth of 0.006 ky^{-1}.

The obliquity filters obtained from the data for the initial age model and those computed are not very different in total amplitude range, although the computed age models F and G improved the obliquity amplitude modulation fit with the astronomical calculations between ∼3.5–5.5 Ma.

Figure 2.26 shows the data after applying a bandpass filter with a central frequency of 0.05 ky^{-1} and a bandwidth of 0.012 ky^{-1}, which extracts variations in the climatic precession frequency band.

It is clear from this figure that all automatically generated age models show a drastically increased power in the precession frequency band, while also showing the eccentricity amplitude modulation cycles. The data show less of this characteristic pattern between ∼4.6–5.4 Ma, which might explain the greater differences between computed age models at this age.

In order to investigate whether the automated tuning procedure introduced unreasonable variations in implied sedimentation rate, the sedimentation rate was computed for all age models against the composite depth values. To enhance visual comparison, the sedimentation rate was averaged over 50 ky intervals, as shown in figure 2.27.

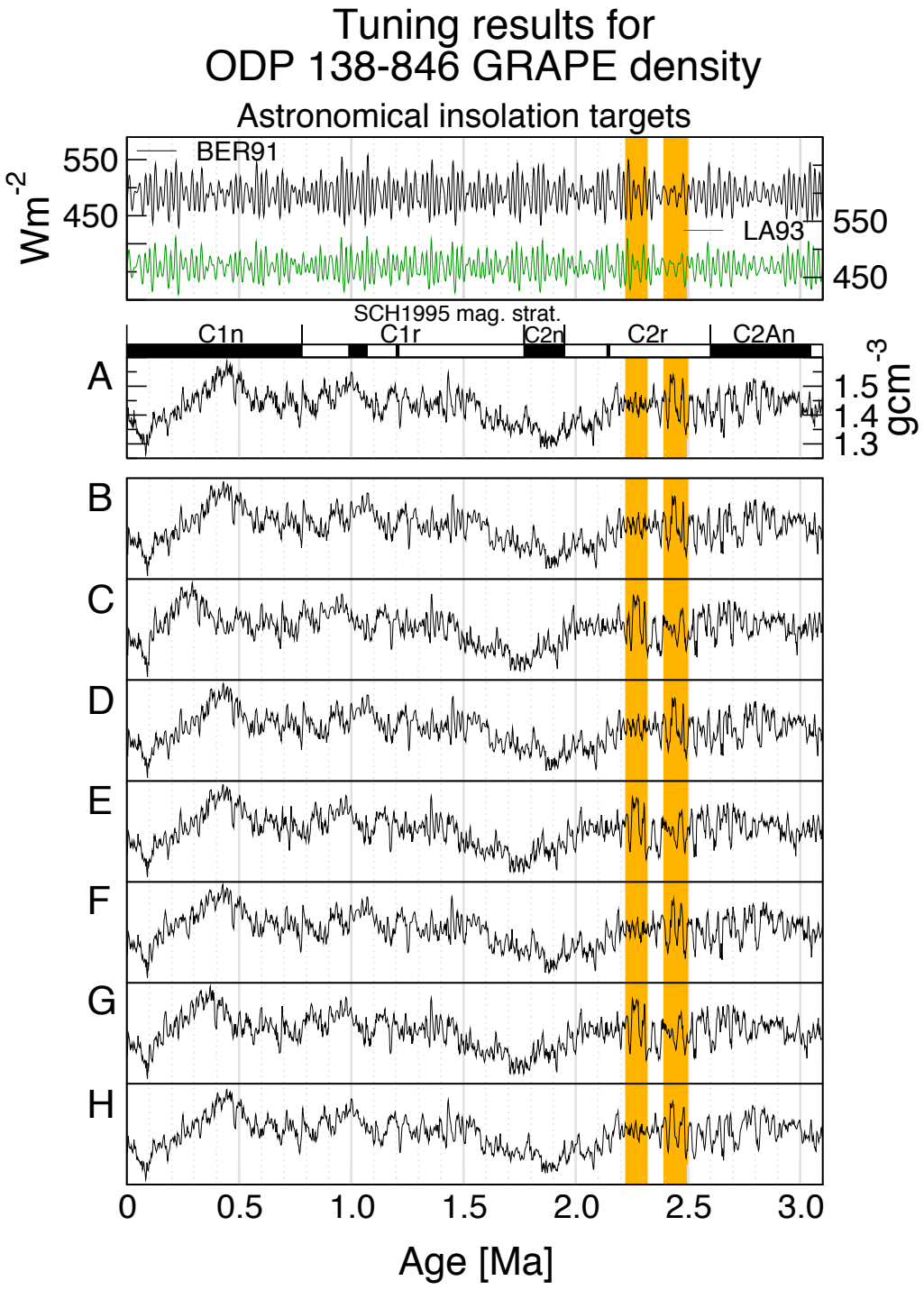

Figure 2.23: Tuning results for ODP 138-846 GRAPE density 0–3.1 Ma.

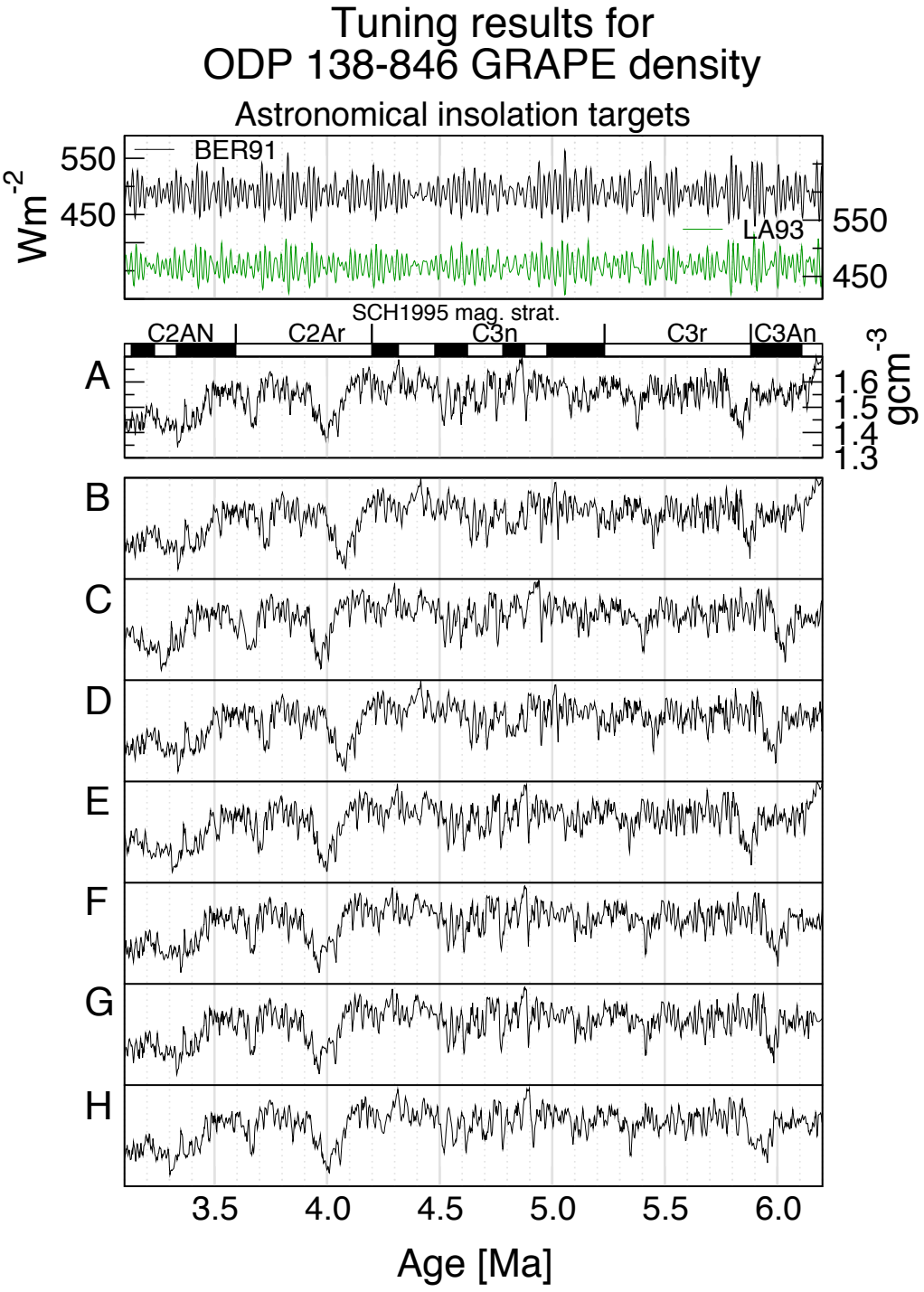

Figure 2.24: Tuning results for ODP 138-846 GRAPE density 3.1–6.2 Ma.

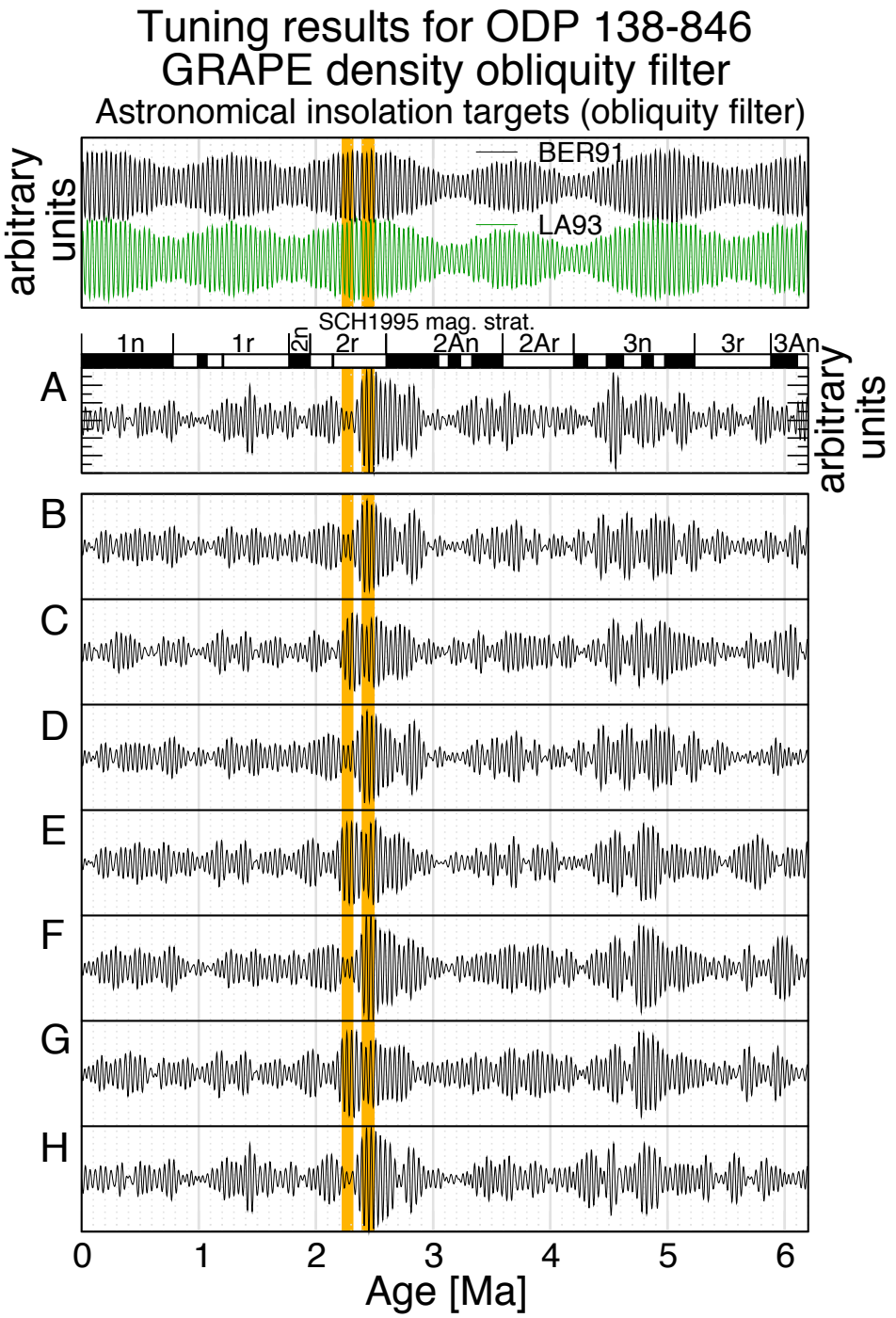

Figure 2.25: Tuning results for ODP 138-846 GRAPE density: obliquity filters.

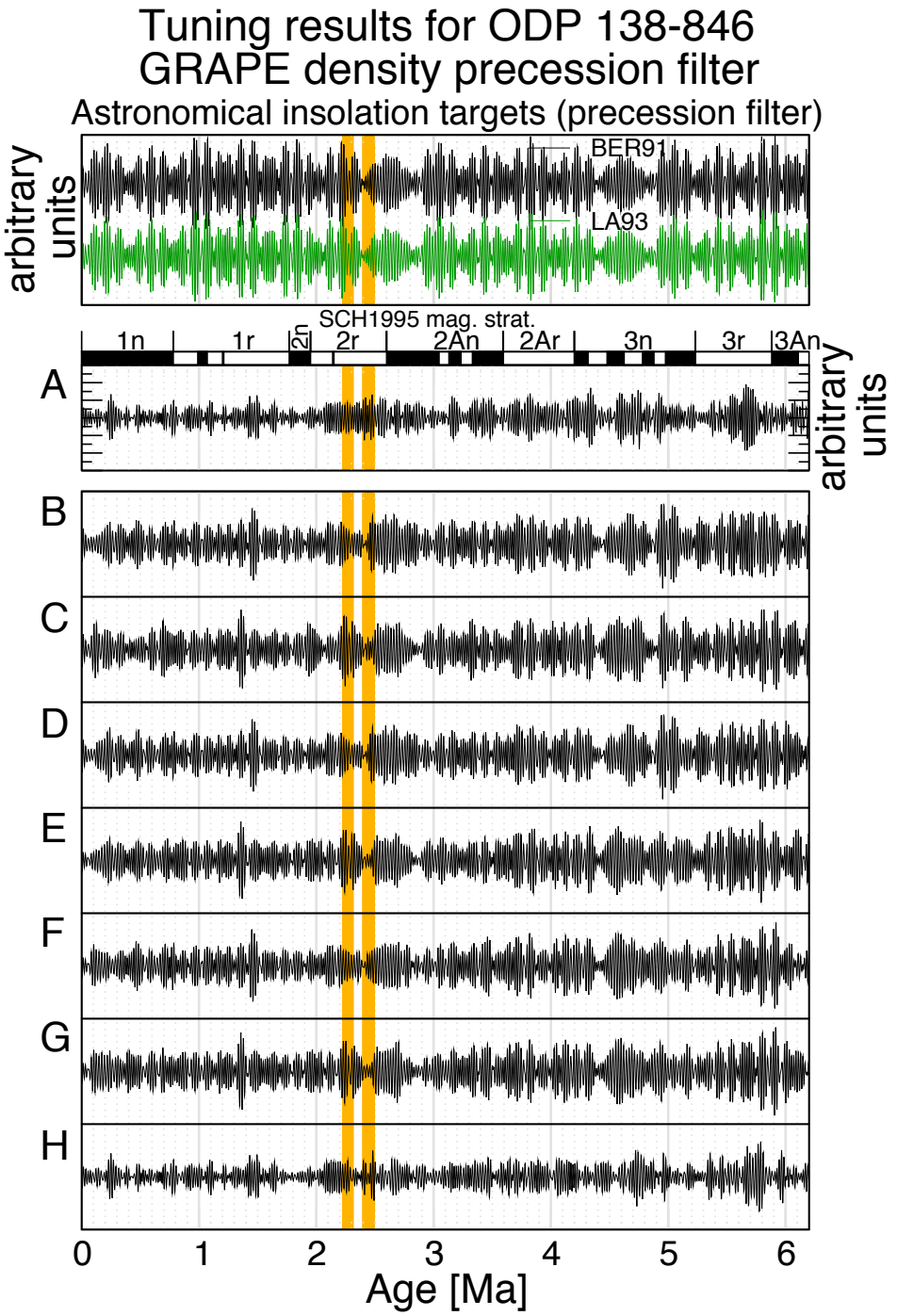

Figure 2.26: Tuning results for ODP 138-846 GRAPE density: precession filters.

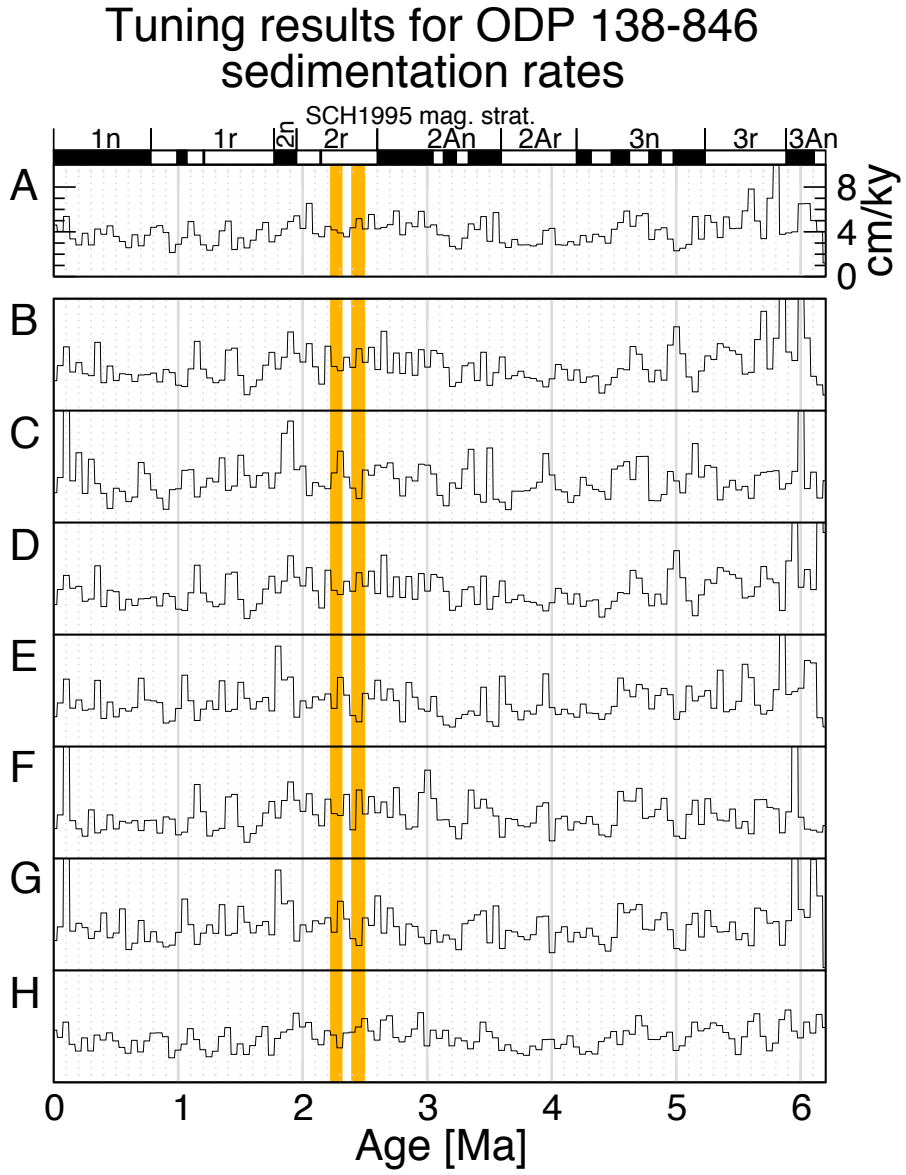

Figure 2.27: Tuning results for ODP 138-846 GRAPE density: sedimentation rates.

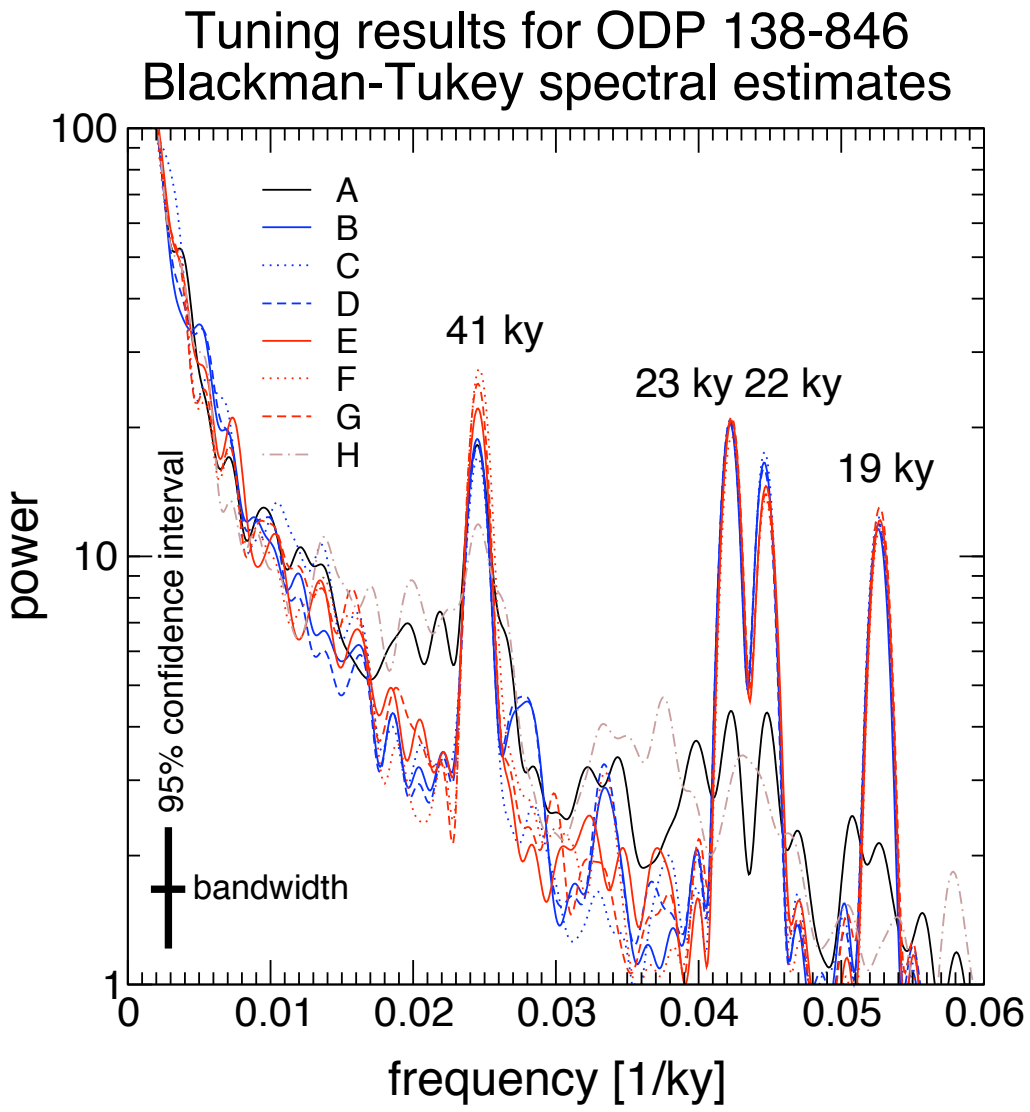

Figure 2.28: Tuning results for ODP 138-846 GRAPE density: Blackman-Tukey spectral estimates.

On shorter time scales the variation is of similar amplitude. Apart from the youngest and oldest parts of the studied time interval, all models give sedimentation rate variations that are comparable to those of the initial age model, although a slightly higher rate of fluctuation can be observed. This is again due to the larger number of adjustments made in the computed age models. Despite this, sedimentation rate changes appear geologically feasible. The larger spikes for most of the computed age models at around 6 Ma are possibly related to the previously mentioned presence of laminated sediments, caused by diatom mats.

Figure 2.28 shows a comparison of the spectral characteristics of the GRAPE data for all age models. This frequency analysis was computed using the Blackman-Tukey

method as implemented in the AnalySeries computer package [106]. All age models result in a statistically significant peak at the 41 ky obliquity frequency, but the age models generated by the DTW algorithm additionally show a strongly enhanced signal at the three climatic precession peaks with a 19, 22 and 23 ky period. There is no statistically significant evidence of an eccentricity component in the data, neither in the original age model, nor in the age models that were computed by using the DTW algorithm.

To investigate the evolution of the astronomical signal in the data over time, an evolutive spectral analysis was performed using the multi-taper method of Thompson [90; 132]. The results of this analysis are shown in figure 2.29.

The evolutive spectra were computed over a 600 ky long window, and with a step size of 100 ky. Warmer colours indicate high relative power on these plots, with amplitude being plotted as colour variations on a log scale. It is clear that the initial age model A and the manually re-tuned age model H generally only show a weak astronomical signal at the obliquity period, and only very little power at the climatic precession periods. In contrast, the automatically tuned age models show a clear concentration of power at the obliquity and precession frequencies. The amplitude modulation patterns in both obliquity and precession are also visible. Age models B to D show a deviation from this clear pattern at the obliquity frequency between around 3 to 5 Ma, while the age models F and G, in particular, show a "cleaner" signal that continues across the entire record.

Finally, figure 2.30 shows benthic oxygen isotope data from ODP Leg 138, Site 846 [129] using the age model H of this study, compared to the isotope data from ODP Leg 154, Site 925, after Pfuhl (2000) [130]. Generally, the match of excursions is very reasonable, although the records do not match perfectly. This figure would suggest that age model H is consistent with the astronomical tuning that was performed for the data from Leg 154 (see e.g. Shackleton and Crowhurst, 1997 [53]).

The age models for Site 846 presented in this section are not necessarily the correct ones for several reasons, though. This is so because for each time interval, a different one among the Leg 138 sites is optimal [51], while the study reported here only made use of one type of data from one particular site. The work reported here is thus primarily an exercise to investigate the performance of the DTW algorithm, rather than providing the best possible age model. As material from Leg 154 and the Mediterranean

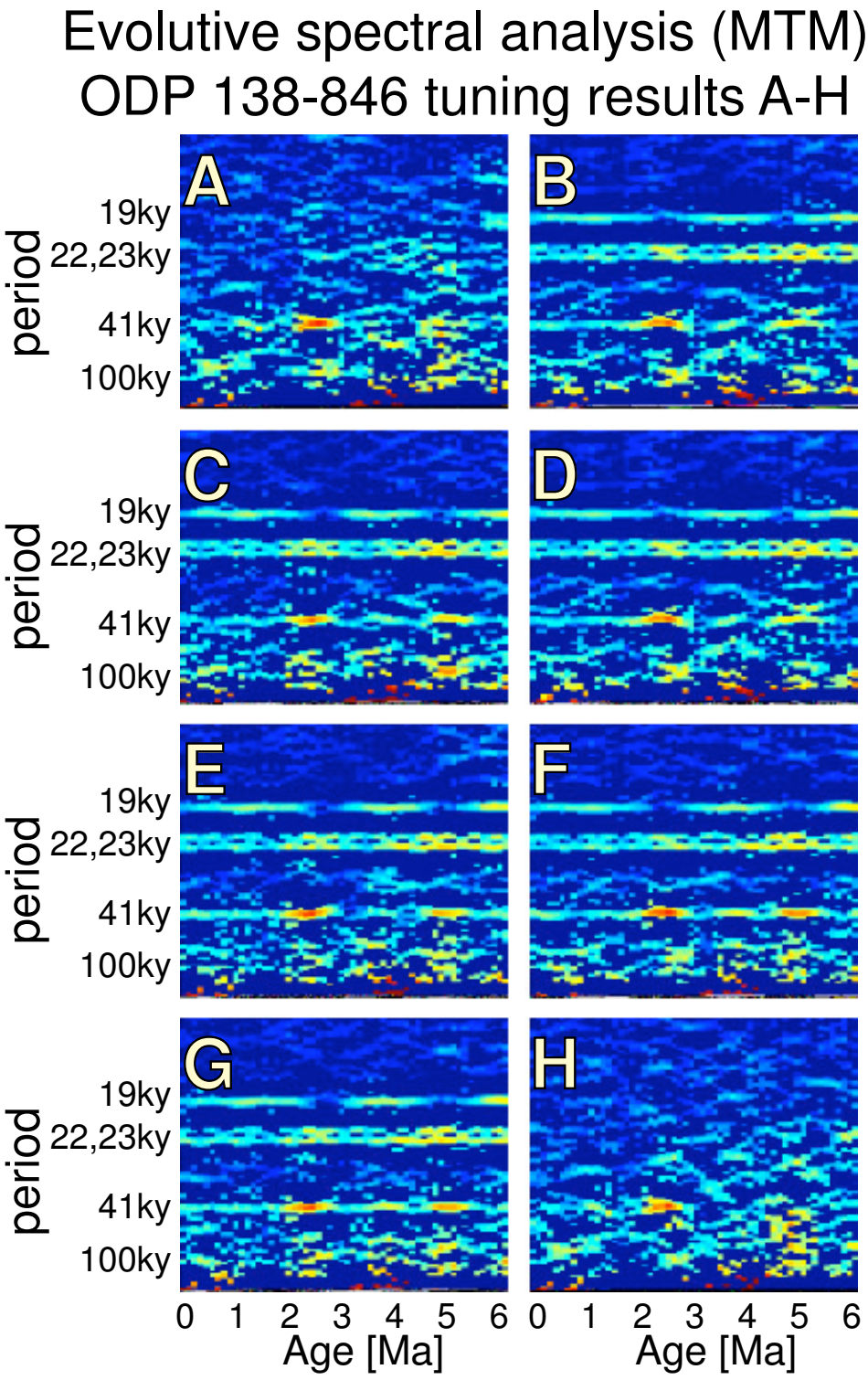

Figure 2.29: Tuning results for ODP 138-846 GRAPE density: evolutive spectra using multi-taper method (MTM) (Thompson 1982,1990 [90; 132]).

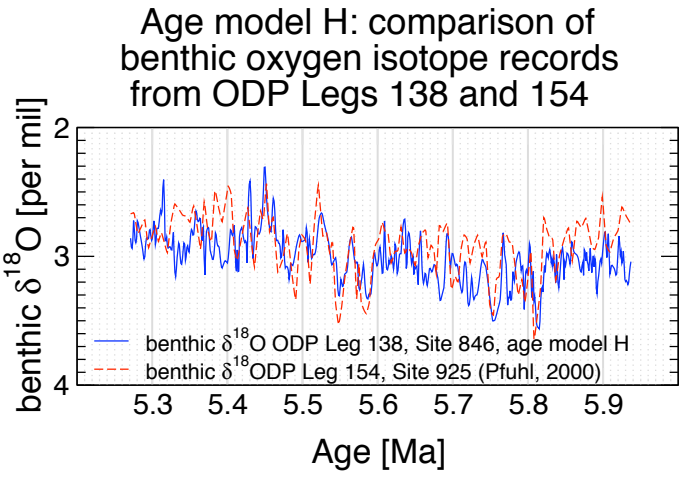

Figure 2.30: Comparison of benthic oxygen isotope data from ODP Leg 138 (Site 846, age model H) and ODP Leg 154, Site 925 after Pfuhl (2000) [130].

is easier to calibrate astronomically, the "correct" tuning of material from ODP Leg 138 must be one that does not conflict with the data from Hilgen *et al.* [52] or Leg 154 [53].

In order to arrive at the best possible time scale for the interval from 0 to 6 Ma, a strategy will have to be devised that takes into account all available data in a more comprehensive fashion. One possibility would be to generate a self-consistent common depth scale using data from Legs 138 and 154, as well as data from the Mediterranean, in order to create a stacked record. Ideally this would be done using data that can be correlated with confidence, such as stable isotope data. Experiments by the author have shown that a method called multi-channel singular spectrum analysis (MSSA) [133; 134] is able to extract features that are common between different types of data from different sites. A stacked data set could then be used to generate a new and self-consistent astronomical calibration.

2.7 An automated tuning approach: Conclusions

This chapter outlined the development of an automated and objective calibration and tuning approach. The newly developed software can make use of dynamically computed filters that were shown to deal effectively with the extraction of a frequency limited signal in the presence of a low frequency background trend. The performance of the algorithm was first tested using synthetic data. This showed that the algorithm fulfils its design goals by giving the best fitting objective age model subject to constraints on local and global sedimentation rates, continuity, and uncertainty ranges

for start and end points. The method is computationally efficient and allows the fast re-adjustment of existing age models to different target curves.

Applying the algorithm to geological data demonstrated that using a given data set with different constraints and assumptions can lead to a range of possible age models. Using data from ODP Leg 138, the variation in the generated age models in terms of assigned ages was of the order of a few hundred thousand years, using tie points that span an age range of approximately six million years. This could be interpreted as an "objective" uncertainty estimate for astronomically calibrated age models if other magneto- and biostratigraphic constraints are not considered. Given that the newly developed method can rapidly generate new age models, it is suggested that other astronomically driven geological data should be subjected to this method to perform sensitivity tests.

The DTW method relies on the presence of a target curve. Thus it can only be usefully applied for age model generation if an astronomical calculation exists, and if the calculation can be demonstrated to accurately reflect the actual evolution of the solar system. Thus, it would be difficult to apply this method to geological material beyond the limits of current astronomical calculations [89], which is around the late Eocene for current astronomical models. It also became clear that non-orbitally controlled variations in geological data can have a severe effect on the age models generated. Hence, the automated approach cannot replace sound geological judgement and interpretation.

Evaluating and comparing the newly generated age models for ODP Leg 138 material suggests that age model F is probably closest to the true age depth relationship, because this age model agrees well with constraints on the established ages of bio- and magnetostratigraphic events in the interval from ∼2–3 Ma, as well as with those ages established by Hilgen *et al.* (1995) [52]. In the time interval younger than 1 Ma, the GRAPE data do not reflect the predicted astronomical forcing. Age model F results in the "cleanest" evolutive spectrum, and does not show geologically unfeasible sedimentation rates.

Improvements and extensions to the DTW tuning algorithm are possible in many ways. As part of this study experiments were also made to include a dynamic complex demodulation algorithm for the computation of misfit measures. This approach can make use of amplitude modulation patterns in the data that are a characteristic "fingerprint" of astronomically driven variations in geological data. First tests show

that this method does give reasonable results, but the testing has not progressed sufficiently to allow the inclusion of these extensions in the present study. Further studies could make use of different types of geological proxy data, that are considered simultaneously, when computing new age models. Combined with further sensitivity studies, this would permit for the first time the development of "objective" estimates for the robustness of astronomically calibrated ages, rather than relying on spectral estimates and amplitude modulation features alone.

Chapter 3

Extending the astronomical calibration into the Eocene

3.1 Introduction

Cyclicity attributed to orbital (Milankovitch) forcing has been suggested for the Mesozoic [57; 59; 61–63] and Paleozoic [64], and has been used to calibrate the ages and durations of large parts of the Cenozoic geological time scale [41; 51; 53–55; 103]. In particular, the astronomical forcing recorded in marine sediments facilitated the extension of an astronomically calibrated geological time scale to the base of the Oligocene by Shackleton *et al.* (1999) [55]. The study of Shackleton *et al.* currently provides a non-floating astronomical calibration that extends furthest back in time, although the lower most part of the Oligocene was only tuned tentatively.

This chapter is concerned with the extension of an astronomically calibrated geological time scale into pre-Oligocene time. As astronomical calculations are less reliable further back in time [89], a good strategy for extending the astronomically calibrated geological time scale would be to work with material of Oligocene and older ages, ideally linking with the work done by Shackleton *et al.* to allow the anchoring of calibrated geological sections in time.

The Eocene/Oligocene transition was marked by a number of key changes in ocean circulation, climatic, and glacial boundary conditions, which will be outlined as part of this introduction. Unfortunately, these dramatic changes in ocean chemistry resulted in the unusually poor preservation of deep-marine carbonate sediments, and many hiatuses across the Eocene/Oligocene boundary world wide. During the course of this

research, the only available material suitable for an extension of the astronomically calibrated time scale back in time appeared to be that recovered during Ocean Drilling Program (ODP) Leg 171B in the western Atlantic. The youngest material suitable for the work in this study was found to be of Late Eocene age [100].

This chapter is subdivided into two main parts. The first part reports the results from an astronomical calibration of the Middle and Late Eocene, making use of X-ray fluorescence elemental measurements that were obtained from ODP Leg 171B, Site 1052. For the first time, these data allowed a detailed stratigraphic correlation of bore-holes from this site, which in turn made it possible to generate a "stacked" record from different bore-holes to bridge core gaps and disturbances. This ultimately facilitated the calibration of orbital cycles, as recorded by lithological parameters, to an astronomical calculation. Parts of this section have been accepted for publication [135].

The second part of this chapter reports the findings of an attempt to verify the new age calibration of magnetic reversal events obtained for the Middle and Late Eocene by analysing data from ODP Leg 177, which became available at a later stage of this research. The next chapter documents the use of this new bore-hole inter-correlation and age model to investigate a high-resolution foraminiferal stable isotope record obtained from ODP Site 1052.

The time interval from the Middle Eocene to the Early Oligocene features some of the most dramatic geological and climatic transitions during the Cenozoic. It marks the transition from a globally warm and most likely non-glaciated Late Cretaceous towards a cooler and glaciated Neogene. This change extends over approximately ten million years and witnesses the occurrence of major turnovers in the marine and terrestrial biota, as well as significant changes in geological proxies that are thought to be controlled by parameters of the climate and ocean circulation system. A very thorough review of a wide range of geological data available from this critical interval of geological time, and different interpretations as to their significance, was published as a collection of papers edited by Berggren and Prothero (1992) [136].

A refined chronology for the Middle and Late Eocene, as presented in this chapter, is of special geological and astronomical significance for a number of reasons. The Late Eocene marks the transition from a minimally glaciated "doubt-house world" [137] to an "ice-house world" in the earliest Oligocene that is well documented by stable isotope measurements from different sites [127; 138]. In addition, the Middle to Late Eocene

has been a time of enhanced cosmic bombardment that might have influenced the global climate [139–142]. The Middle to Late Eocene also showed increased explosive volcanic activity in Central America [143].

3.2 A new time scale for the Middle and Late Eocene

3.2.1 Background and introduction to ODP Site 1052

Sites from Ocean Drilling Program (ODP) Leg 171B form a transect along "Blake Nose", an elevated feature that protrudes from the Blake Plateau on the Atlantic margin of northern Florida into the Atlantic Ocean, as shown in figure 3.1. A detailed overview of the geological background for sites from ODP Leg 171B is given in the Initial Reports volume of the Ocean Drilling Program [144].

An X-ray fluorescence (XRF) Core Scanner was used to obtain records of elemental concentrations in sediment cores from ODP Leg 171B, Site 1052 [100]. This record spans the Middle to Late Eocene, as indicated by bio- and magnetostratigraphy, and displays cyclicity that can be attributed to the orbital forcing of a combination of climate, ocean circulation, or biological productivity. XRF counts of iron and calcium are used as a proxy for the relative contribution from calcium carbonate and terrestrial material to construct a new composite depth record. This new composite depth record provides the basis to extend the astronomically calibrated geological time scale into the Middle Eocene, and results in revised estimates for the age and duration of magnetochrons C16 through C18.

The sedimentary sequence from Site 1052 contains several volcanic ash layers which might be correlatable with other sedimentary records from the Caribbean. An astronomically tuned time scale over this period will thus be useful to constrain the exact timing of these events, which had a potential impact on global climate. It might allow also to test predictions of climate models that were computed for this time interval [145; 146], and comparisons with existing stable isotope records (see [138; 147–152] and references therein).

The commonly used magnetic reversal time scale of Cande and Kent [46] contains three calibration points during the Eocene: at 55 Ma (chron C24r.34, the base of the Eocene), at 46.8 Ma (C21n.67, lower Middle Eocene), and at 33.7 Ma (C13r.14, base of Oligocene). A South Atlantic ridge profile implies an increase in half-spreading rates

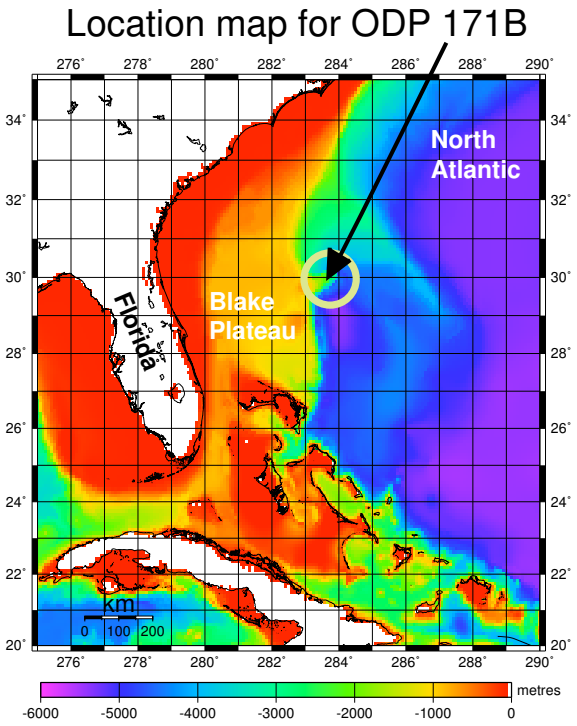

Figure 3.1: A bathymetric map showing the location of the ODP 171B drilling sites.

from ~15 km/My to ~25 km/My from the Early to the Late Eocene. Due to the widely spaced calibration points, and the errors that are involved in creating the geomagnetic polarity time scale (GPTS), improvements to the GPTS have been proposed [153]. Therefore, an astronomical tuning of individual magnetochrons during the Eocene can make a direct contribution towards refining the GPTS, which serves as the prime tool for global stratigraphic correlation.

Laskar *et al.* (1993) [86] showed that the orbital solutions that are used as a template in the process of astronomical tuning are chaotic, and that the computation of the exact nature of obliquity and climatic precession cycles is probably only valid over the last ~10–20 Ma. This implies that a new tuning strategy needs to be employed for earlier times. Laskar (1999) [89] proposed to make use of the ~400 ky amplitude modulation cycle of the climatic precession signal, since this seems to be the most stable feature of astronomical calculations. The presence of this amplitude modulation cycle has been demonstrated convincingly in marine sediments recovered during ODP Leg 154 for the Miocene and Oligocene [55; 126]. Therefore, a sensible strategy for astronomical calibration of Eocene sediments would be to use this modulation cycle pattern as the prime tuning target, and to use the resulting chronology to test and refine current astronomical models. This might allow the determination of Earth's orbital pa-

rameters, as studied for younger intervals [154–156]. Laskar (1999) [89] also suggested a changing resonance between the amplitude modulation of climatic precession, and the amplitude modulation of obliquity (∼2.4 My and ∼1.2 My periods, respectively). The determination of the presence or absence of this switch could allow further testing and refinement of astronomical models.

3.2.2 Magnetostratigraphy

During ODP Leg 171B, the shipboard scientific party [100] put forward an interpretation for the magnetostratigraphy of Site 1052, based on results obtained from the shipboard pass-through cryogenic magnetometer. These data show quite variable inclination values that often fluctuate around a low level. The initial interpretation was refined and supported by the laboratory analysis of mini-cores obtained from Hole A at Site 1052 [100; 157]. The identified magnetic reversals compare well with data from at and near the type location for the Eocene-Oligocene boundary [158]. Data from Leg 171B were re-evaluated in order to estimate the stratigraphic uncertainties for each magnetochron, based on the nature of reversals in each hole, as well as their match on the inter-hole calibration based on XRF data reported in this chapter.

All chrons from C15.r down to C18n.2n are present in the combined record from all holes, while the top of Hole D might contain the very bottom of C15.n. Figure 3.5 shows estimates for the uncertainties associated with all chrons that were identified with confidence. Table 3.1 shows the depth estimates for uncertainty intervals, together with age estimates from Cande and Kent (1995) [46] and Wei (1995) [153]. Also shown are new age estimates obtained from astronomical tuning as described in the following sections.

3.3 XRF scanning

This study makes use of a relatively recent analytical method to generate a record of lithological parameters. X-ray fluorescence (XRF) scanning allows the fast, close-spaced and non-destructive analysis of elemental concentrations on split sediment cores. The sediment surface is irradiated by X-rays of known energies. Inner shell electrons of atoms are discharged, and then filled by electrons cascading in from outer shells, resulting in the dissipation (“fluorescence”) of the energy difference in the form

Chron (top)	rmcd [m]	min. [m]	max. [m]	CK95 [Ma]	Wei95 [Ma]	this study [Ma]	min. [Ma]	max. [Ma]
C16.1n	12.00	10.30	13.70	35.343	35.586	35.185	35.137	35.241
C16.1r	23.60	22.60	24.60	35.526	35.760	35.524	35.502	35.557
C16.2n	26.10	25.00	27.20	35.685	35.909	35.605	35.572	35.635
C16.2r	41.50	39.40	43.60	36.341	36.518	36.051	35.994	36.130
C17.1n	50.40	49.20	51.60	36.618	36.771	36.404	36.362	36.446
C17.1r	78.10	76.70	79.50	37.473	37.543	37.300	37.262	37.334
C17.2n	81.70	81.00	82.40	37.604	37.660	37.399	37.378	37.419
C17.2r	88.35	87.50	89.20	37.848	37.877	37.618	37.585	37.648
C17.3n	90.60	90.00	91.20	37.950	37.941	37.692	37.674	37.710
C17.3r	97.30	96.00	98.60	38.113	38.112	37.897	37.862	37.939
C18.1n	107.70	106.40	109.00	38.426	38.389	38.186	38.155	38.225
C18.1r	128.15	127.70	128.60	39.552	39.382	39.441	39.424	39.457
C18.2n	129.60	129.00	130.20	39.631	39.451	39.486	39.467	39.505
C18.2r	139.50	138.00	141.00	40.130	39.892	39.828	39.773	39.886

Table 3.1: Identified magnetic reversals and their depth uncertainty on the rmcd (revised metres composite depth) scale. Columns five and six give the corresponding ages according to Cande and Kent (1995) [46] and Wei (1995) [153], followed by the ages derived in this study, and their uncertainties that arise from the uncertainty in depth.

of X-rays, the energy level and distribution of which are indicative for a given element. The measurement output is counts per second (cps),which can be converted to an elemental concentration by measuring standards of known composition.

3.3.1 Methods and Parameters

This study employed the computer-controlled XRF Core Scanner of Bremen University [159], which allows the measurement of the entire suite of elements from potassium (K, atomic number 19) to strontium (Sr, atomic number 38)[160]. Röhl *et al.* (2000) [159; 161] gave details of technical parameters used. A photograph of the instrument installed in Bremen is shown in figure 3.2. It is mounted inside a standard self-contained shipping container, and is mobile and sea-worthy in principle.

Using the standard parameters of the apparatus in Bremen, counts were determined for the elements K, Ca, Ti, Mn, Fe, Cu and Sr. Based on the bio- and magnetostratigraphy [100], the aim was to sample cores at 8 cm intervals (equivalent to $\sim$3-4 ky). Where necessary, the sampling plan was adjusted to avoid core gaps and disturbances. In total, 3904 measurements were taken from Holes 1052 A (cores 2X-12H), B (cores 2H-13H), C (core 2H) and F (cores 1H-6H, 8H).

Figure 3.2: A photograph of the XRF Core Scanner of Bremen University that was used to obtain measurements for this study. On the right hand side a sediment core is visible. During operation the lid is closed, and the instrument visible along the centre of the right hand wall takes measurements. The computer equipment controls the operation of the instrument and is used for analysis.

3.3.2 Results from XRF scanning

Of all seven element concentrations determined[1], calcium is the most abundant with an average response of 9060 counts per second (cps), followed by iron (441 cps) and potassium (193 cps). The other elements that were calculated from the spectrum (strontium, 66 cps; copper, 57 cps; manganese, 34 cps; and titanium, 6 cps) were close to or below the nominal sensitivity of the instrument. These element measurements were excluded from further analysis, although certain features, such as volcanic ash layers, are visible despite the low counts, and some still show variation that co-varies with iron and calcium counts. No attempt was made to convert cps values to elemental concentrations because it is the variation in elemental concentrations that is of interest, rather than absolute values. Absolute concentrations can, however, be obtained in principle by calibration with discrete samples of an international set of standards [160].

Iron shows the clearest signal, with peaks spaced at around 0.6-0.8 m and 1.2-1.4 m intervals, corresponding to variations in the precession and obliquity frequency bands, as estimated by bio- and magnetostratigraphy. Principal component analysis reveals that iron and calcium are strongly anti-correlated. As calcium is a much lighter element than iron, an element which is at the lower end of the energy range used, and as the penetration depth of the XRF analysis depends on the wavelength of the fluorescence radiation, the Ca counts are more sensitive to core quality. It can be expected that at small undetected gaps and disturbances both Ca and Fe counts decrease. It was thus decided to use the Ca/Fe ratio for subsequent cross-hole correlation work since this increases the signal-to-noise ratio. This decision was supported by linear regression analysis that was performed between chemically measured $CaCO_3$ concentrations (weight %) [100] and XRF measurements (counts per second) for Ca and Fe. The results of this are shown in figure 3.3, which demonstrates that by computing the XRF Ca/Fe ratio the correlation with chemical measurements can be improved.

The scatter in the cross-plots is partly due to the fact that chemical measurements and XRF measurements were not taken at exactly corresponding depth intervals, although measurements are generally from core depths not separated by more than $\sim$3 cm.

[1]The complete data set is available in electronic form on the enclosed CD-ROM, as well as in downloadable form [123]. The nature of the data is illustrated in Appendix A

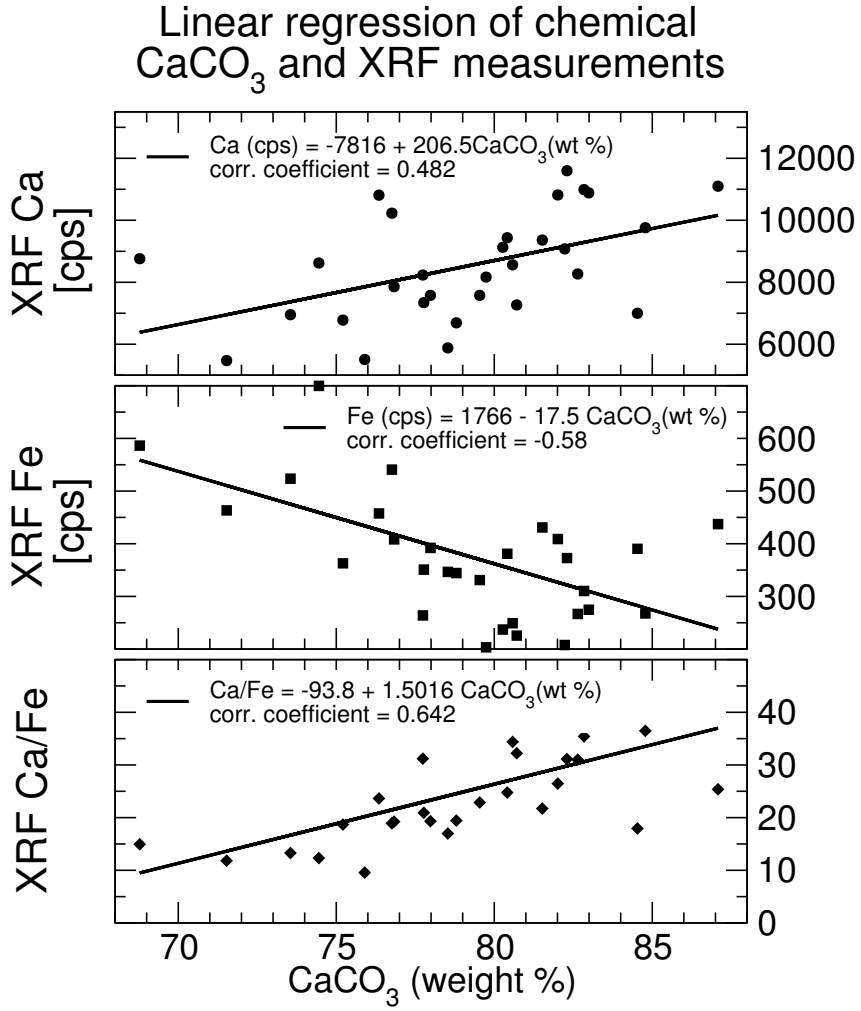

Figure 3.3: Comparison of chemical $CaCO_3$ measurements and XRF measurements of Ca, Fe (counts per second, cps) and Ca/Fe. Linear regression lines were computed for all three panels and are given together with resulting correlation coefficients. The computed XRF Ca/Fe ratio shows the highest correlation coefficient. Note that individual measurements were not taken at exactly the same interval but are within $\sim$3 cm.

3.4 A new rmcd scale

The initial shipboard construction of a composite depth scale (mcd) [100] for individual holes showed that it was not entirely possible to align prominent features across all holes by simply applying a constant depth offset to the top of each core. In addition, the measurements that were used to construct the mcd scale showed a rather low signal-to-noise ratio. This is particularly true for the variations in magnetic susceptibility data, which were often only just above the background level. The presence of large amplitude spikes in the susceptibility data, that were found to be due to volcanic ash layers and hard calcareous chalk layers that are not present or not recovered across all holes, further complicated the exact alignment of holes.

In order to obtain a signal with a larger signal-to-noise ratio, and to verify what parts of the signal are present across all holes, it is necessary to stack available data from all holes. This requires the cm-scale alignment of cores by applying differential stretching and squeezing within each core. A detailed discussion of such a "revised metres composite depth" (rmcd) scale was given by Hagelberg *et al.* (1995) [99]. The strategy to arrive at a new rmcd scale is based on comparing the available magnetic susceptibility, colour reflectance, density (GRAPE) and XRF data, as well as making use of the various ash layers that were found in the interval studied. In most cases the Ca/Fe ratio from the XRF measurements proved to allow the least ambiguous cross-hole correlation[2]. A combination of the other proxy data was used where XRF data were not available.

3.4.1 Differences in relative stratigraphic thickness between holes

For each part of the new rmcd scale an attempt was made to leave the relative thickness from at least one hole unchanged, so that it is possible to compare the actual variation in the apparent sedimentation rate. The two criteria that were used to decide whether a particular section should be used as a reference was either that it was the only one that spanned a core gap, or that it seemed to show a clearer signal than data from the other holes. Conceptually, the holes used to make up the reference rmcd scale can be compared to those that are used to make a splice [100].

Next a computation was made to evaluate the relative amount of squeezing or stretching that was required to align data from the other holes on the new rmcd scale

[2]The resulting mbsf-rmcd mapping pairs are given in Appendix B, and are available in electronic form on the enclosed CD-ROM, as well as in downloadable form [123]

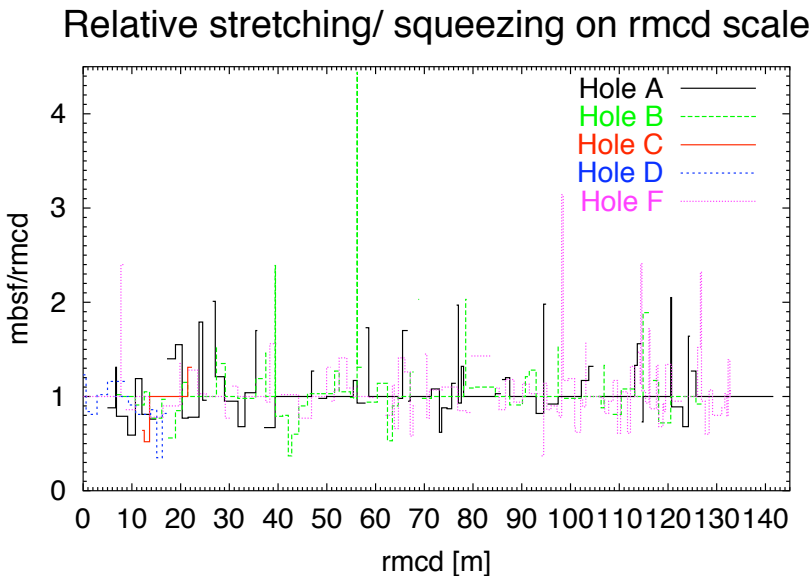

Figure 3.4: This shows the relative amount of stretching and squeezing that was performed within each core from a Hole in order to create the rmcd scale. Values greater than one indicate that a particular interval had to be squeezed to make it fit to the data from other holes and implies stretching in the recovered core. This follows the work of Hagelberg *et al.* (1995) [99]

[99]. This is expressed as the ratio Δmbsf/Δrmcd, where a value of one indicates that a particular part of a core lies exactly on the reference scale, and values greater than one indicate that the original mbsf depth had to be compressed to make it fit stratigraphically to the reference scale.

Figure 3.4 shows that over most intervals the stratigraphic thickness of individual holes varies by a factor of $0.5 - 2$ compared to the rmcd reference scale. This is of the same order as what was observed by Hagelberg *et al.* (1995) [99]. Greater squeezing was typically required near the top and bottom of individual cores, which is most likely caused by the coring process rather than reflecting local variations in accumulation rate.

Overall, the rmcd scale is approximately 5% longer than the mbsf scale. This compares with a value of 10% typically found in the creation of mcd scales [99]. The process of adjusting mbsf depths to construct a new rmcd scale revealed several intervals where the proxy data from a particular section did not correspond to the other available holes, and where it was impossible to put these data into the correct stratigraphic context with confidence. The data that were not used in the construction of the stacked rmcd scale for this reason, or where XRF data were not available, spanned the following

intervals: Hole A (20.05-29.95 rmcd), Hole D (0-17.16 rmcd), Hole F (62.05-69.85 rmcd, 85.05-90.70 rmcd, 116.15-132.75 rmcd).

If core extension was only due to the drilling process and the extraction of the core, one would expect the shortest section from a particular interval to represent the "true" stratigraphic thickness. This hypothesis was tested by constructing a different reference curve, or "splice", by following the shortest path downwards, where possible. This rmcd scale is approximately 3-4% shorter than the actual depth below sea floor (mbsf), as measured by the length of the drill string, or 8% shorter than the rmcd scale that is considered to show the most representative stratigraphic succession. This strongly indicates that there are other factors affecting sediment accumulation that account for differences between holes, or that the coring process can also lead to the loss of material.

3.4.2 XRF and proxy results for the rmcd composite

Using the new rmcd scale, a composite record was constructed for the elemental counts determined by XRF, and for colour reflectance and magnetic susceptibility data. It was found that this stacking process significantly enhances the signal-to-noise ratio. The stacking procedure involved averaging data across different holes after alignment to the rmcd scale, excluding those intervals that did not seem to correlate well with other holes. All data were interpolated at 5 cm intervals using a Gaussian smoothing function with a 14 cm long window. The process of stacking and averaging involves a trade-off between enhancing the signal value of the data on the one hand, and reducing the resolution of the stacked data set on the other hand, the latter of which is determined by the maximal resolution to which holes can be correlated with confidence. Considering the scale to which individual holes were aligned on the rmcd scale, it can be estimated that the effective resolution of the composite record is of the order of decimetres, with optimum values approaching $\sim$5 cm.

The composite data set, with the XRF Ca, Fe and K data, the colour reflectance data (L^*, a^*, b^*), and magnetic susceptibility, is shown in figure 3.5. This figure displays several features that are of interest. Generally, the lower half of the record ($\sim$60–140 rmcd) shows decimetre to metre scale variations more clearly for all parameters than the upper half. This is particularly clear for the Fe counts as well as for the colour reflectance parameters L^* (lightness) and a^* (variation from green to red). In the lower half of the

interval studied, there is an apparent regular change in amplitude of this metre scale variability. These maxima are apparent at around 122 rmcd, 105 rmcd, 93 rmcd and 80 rmcd. The upper half of the studied interval shows variation that is less clear, and reflects disturbances observed in the record, such as frequent layers of harder chalk nodules embedded in foraminiferal ooze.

Magnetic susceptibility measurements are sensitive to the oxidation state of minerals containing iron, as well as to the proportion of diamagnetic calcium carbonate minerals. This is the reason why the XRF measurements for Fe show a much clearer signal than the susceptibility values, although both curves show similar features and show the same polarity, i.e. high iron contents corresponds to high magnetic susceptibility values. The counts for calcium are anti-correlated with the counts for iron.

Below ∼60 rmcd the average iron counts decrease, while the same occurs for potassium below ∼70 rmcd. At ∼30.9 rmcd the shipboard scientific party observed a distinct change in colour in all holes that reached this depth. This feature is most likely of diagenetic origin and is reflected by lower values in the lightness parameter L^* as well as a shift from red towards green (more negative a^* values) and from yellow towards blue (b^*), moving towards the base of the core. This change in colour values is approximately aligned across all holes on the rmcd scale.

3.5 Volcanic Ash Layers

Several volcanic ash layers were discovered in the sedimentary sequence from Blake Nose. The original composite depth scale (mcd) [100] was constructed to obtain a spliced record. The initial shipboard splice is constructed by adding a constant offset to the depth of each core, which could not align these prominent ash features. The new rmcd scale allows the alignment of ash marker beds, which can be used as additional tie points between holes. Table 3.2 lists individual ash layers that were recognised from core photographs, and from extreme values in the XRF and proxy data. Ash layers are also marked on figure 3.5. Most ash layers are present in all cores that span a given interval. Two ash layers from Hole A could not be aligned properly. These are within the interval from Hole A that was excluded in constructing the composite depth scale. Apart from ash layer I, all ash layers were covered by XRF measurements from at least one hole.

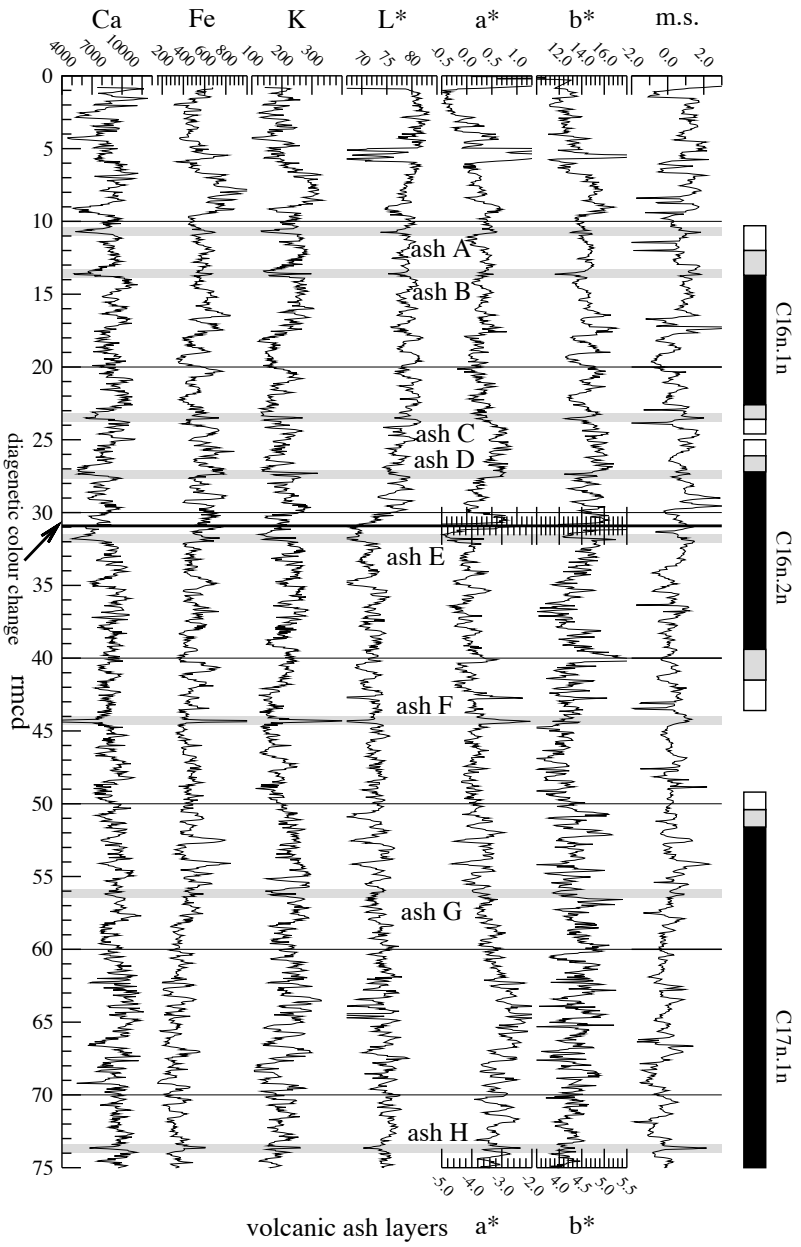

Figure 3.5: The stacked XRF data for calcium, iron and potassium obtained by XRF analysis, together with the colour reflectance parameters L*, a* and b* as well as magnetic susceptibility (ms). L* represents lightness, a* variations from red to green, and b* variations from yellow to blue. Also marked are the positions of identified volcanic ash layers. The right column in both panels shows the magnetic reversal sequence. Uncertainty intervals are marked by grey and white boxes. Ash layers were visually identified independently from the XRF data. At around ∼31 rmcd there is a distinct colour change, related to diagenetic processes. For this reason the scale of the parameters a* and b* was changed on this plot. (continued on following page)

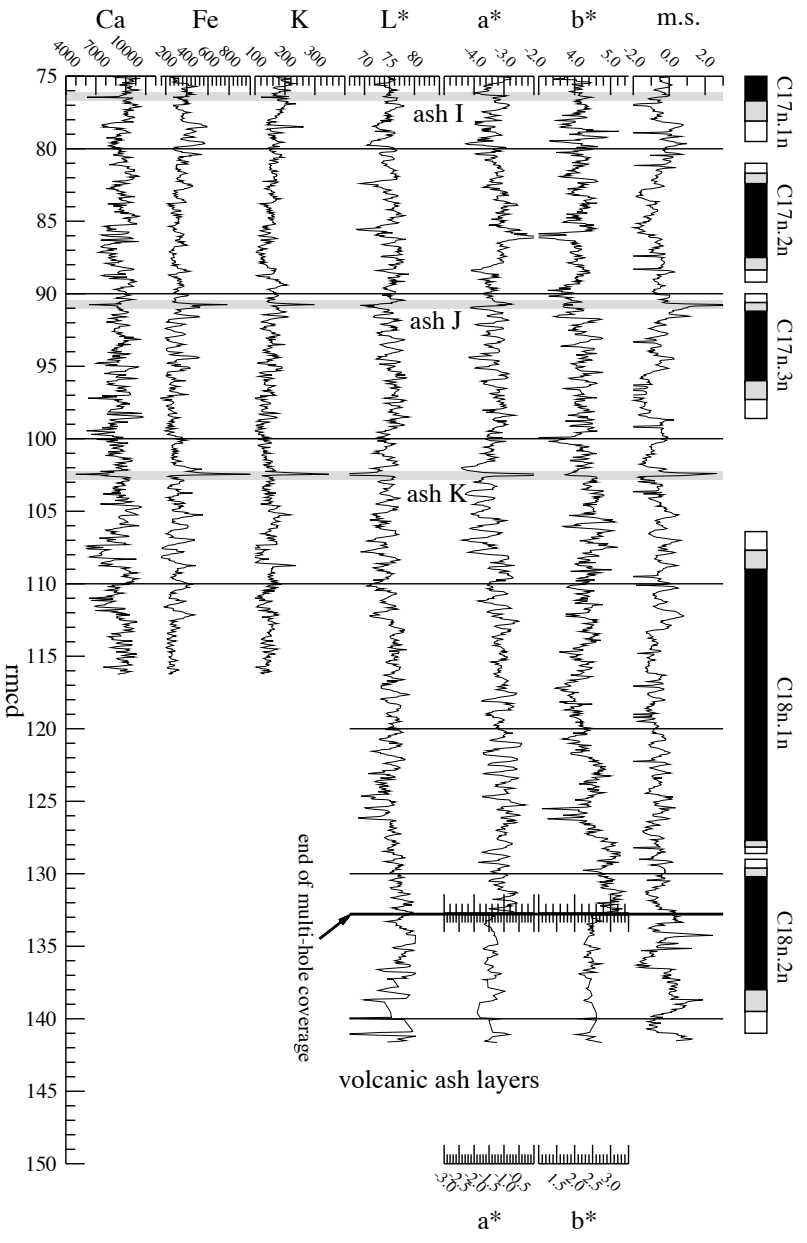

Figure 3.5 (continued)

Ash	**Hole A**			**Hole B**			**Hole F**		
	core	mbsf	rmcd	core	mbsf	rmcd	core	mbsf	rmcd
A	2X	8.07	10.78	2H	8.90	10.75	2H	11.20	10.68
B				2H	11.65	13.60	2H	14.13	13.61
C	3H	19.80	(22.91)	3H	19.90	23.49	3H	22.65	23.48
D	3H	22.63	(25.37)	3H	23.75	27.34	3H	26.59	27.35
E	4H	28.76	31.81	4H	27.87	31.77	4H	29.75	31.70
F	5H	38.79	44.41	5H	39.21	44.37	5H	41.63	44.11
G	6H	49.83	56.26				6H	53.61	56.20
H	8H	67.67	73.68	9H	66.60	73.62	8H	70.35	73.68
I				9H	69.38	76.40	8H	73.28	76.34
J	10H	84.91	90.81	11H	83.34	90.77	10H	87.20	90.78
K*	11H	96.28	102.48	12H	94.75	102.48	11H	99.01	102.53
Ash	**Hole C**			**Hole D**					
	core	mbsf	rmcd	core	mbsf	rmcd			
A				2H	13.68	10.75			
B	2H	10.40	13.65						

Table 3.2: Identified ash layers and their position in each hole, where present. Bracketed depths indicate a mismatch that arises from problems in the adjustment for upper parts of Hole A. This interval was not considered in the subsequent analysis. The asterisk $(^*)$ for ash-layer K indicates that glass-shards from this ash (Hole B) were radiometrically $^{39}Ar/^{40}Ar$ dated with a plateau age of 37.81 ± 0.91 Ma. The terminology for the ash layers was constructed in a similar way to that given by Reicherter and Pletsch (1998) [162] for the adjacent Site 1051.

Generally, ash layers are reflected in the data set by lower counts for calcium (Ca), and elevated counts for iron (F) and potassium (K). Although not shown here, these ash layers also show higher values in the counts for manganese (Mn) and titanium (Ti), and lower counts for copper (Cu) and strontium (Sr). It was not possible to calculate an end-member composition for the volcanically derived component. This would require a more detailed chemical analysis at higher resolution.

As expected, dark ash layers also coincide with low values in the colour reflectance lightness parameter L^*, and high values of the parameter a^* (a shift from green to red). Although not attempted here, it might be possible to correlate ash layers from Blake Nose with the thickest ones recovered by ODP Leg 165 in the Caribbean [163], which are thought to be derived from the same source [100].

Ash layer K contained glass shards that allowed reasonable $^{39}Ar/^{40}Ar$ dating (using sanidine), and revealed a plateau age of 37.81 Ma$\pm$0.91 Ma (Jan Wijbrans and Jan Smit, Free University Amsterdam, personal communication). In its magnetostratigraphic context, i.e. approximately half way within C17.3r, this corresponds to an age of $\sim$38.3 Ma on the Cande and Kent time scale [46]. In the context of the high-resolution time scale that is developed here, the uncertainty of the radiometric datum only allows the placement of geological data into the correct $\sim$2.4 My cycle. Ash layers disrupt the variability in the data set that might be due climatic forcing, and care has to be taken to identify the effects of excursions due to ash layers before further analysis. A decision was made to remove extreme data values that can be attributed to volcanic ash layers before further statistical analysis.

3.6 Cyclicity in the depth-domain

To evaluate whether cyclicity in the proxy measurements can be connected to Milankovitch style orbital forcing, this study followed Weedon (1993) [164] by performing a spectral analysis in the depth domain before any adjustment (tuning) to a time scale. Figure 3.6 shows the results obtained from an evolutive spectral analysis for the lightness parameter L^*, and the ratio of calcium to iron (Ca/Fe) from XRF measurements (figure 3.7). For the generation of these figures the multi-taper method [132] was used, with a window length of 22.5 m (451 values spaced at 0.05 m), and a step size of 2.5 m. Figures 3.6 and 3.7 demonstrate that spectral power is concentrated at distinct cycle length periods through the presence of horizontal bands. One distinct

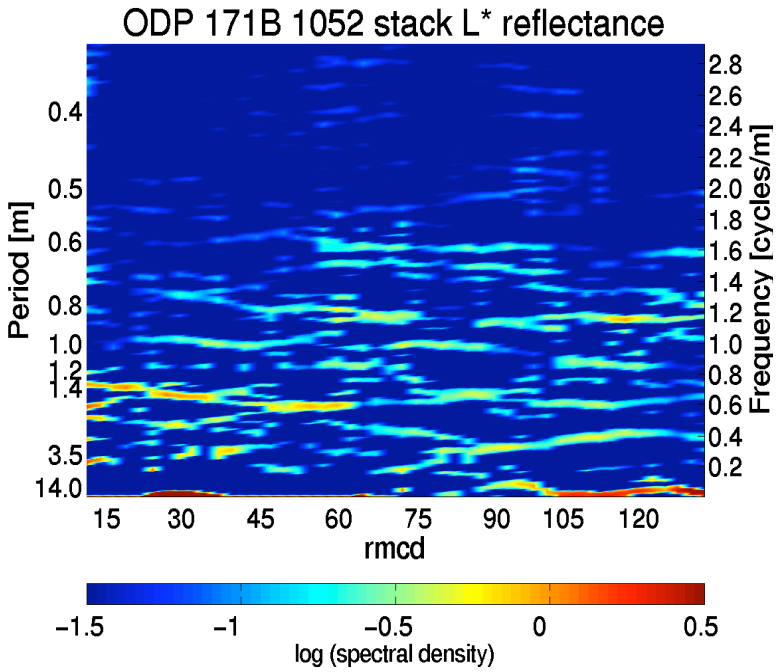

Figure 3.6: Evolutive spectral analysis in the depth domain for the colour lightness parameter L*. Note the distinct bands that run across the spectra at approximately 3.5, 1.4, 0.8 and 0.6 rmcd/ky. This figure does not extend to the end of the full data set because each window was plotted at its central position.

band varies around a 1.4 m period. Magnetostratigraphic data indicate that this could correspond to variations in the Earth's obliquity with a period of ~41 ky. This is supported by the presence of two distinct spectral bands that vary around 0.6 m and 0.8 m, which are interpreted as variations linked to the climatic precession. The amplitude of these cycles seems to increase below a depth of approximately 60 rmcd. The presence of weaker spectral peaks around ~1 m, ~2 m and ~3.5 m is consistent with the ~29 ky and ~54 ky components of obliquity and the short eccentricity cycle (~100 ky period). The window length is too short to reveal longer periods such as the long eccentricity cycle (~400 ky period).

3.7 Astronomical Tuning

3.7.1 Strategy

The amplitude modulation of climatic precession by the long eccentricity cycle (~400 ky period) is the most stable astronomical frequency over long time periods, and is independent of tidal dissipation and dynamical ellipticity which affect the frequency and

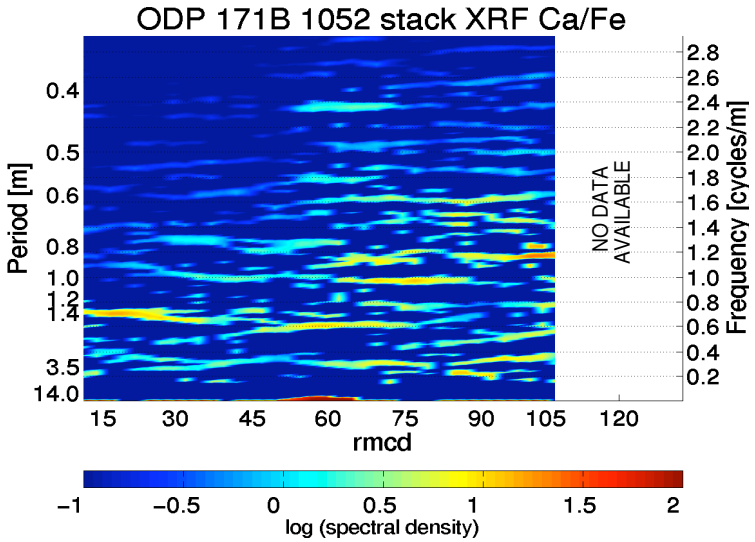

Figure 3.7: This figure is similar to figure 3.6, but shows an evolutive spectral analysis of the Ca/Fe ratio from the XRF data in the depth domain. Similar spectral lines as in figure 3.6 are visible. Note that the XRF record does not extend to the same depth as the lightness measurements.

phase relationship between climatic precession and obliquity [89]. This modulation is visible in the raw data, particularly in the lower half of the record, where amplitude maxima occur at around 122, 105, 93, 80, 68 and 55 rmcd. In this chapter the main aim is to create a relative (floating) time scale because at present this data set cannot be linked up with longer absolute time scales such as that given in [55], and because the astronomical calculations beyond ~25 Ma cannot be used as a tool to evaluate the exact position of longer term modulations in time [89].

Nevertheless, it is still useful to anchor the record at an absolute point in time. To accomplish this, the astronomical calibration in this study started with the magnetostratigraphic ages given by Cande and Kent (1995) [46]. It was found that amplitude maxima for precession cycles in the lower half of the record did not coincide with maxima of the orbital ~400 ky long eccentricity cycles in the Laskar [86] set of solutions on this time scale. It was decided to correlate climatic precession amplitude maxima in the data to 400 ky eccentricity maxima in the astronomical calculation of slightly younger (~200 ky) age. This is consistent with the radiometric $^{39}Ar/^{40}Ar$ age obtained from ash-layer K (see table 3.2), although it might be necessary to re-evaluate this decision in the light of additional data, or radiometric dates with smaller error estimates.

The exact phase relationship between obliquity and climatic precession is not

known for the Eocene. Pälike and Shackleton (2000) [155] evaluated the phase relationship, which is controlled by tidal dissipation effects, for the last 25 Ma, concluding that tidal dissipation effects probably have not changed much over this time.

It was shown by Herbert (1994) [108], that often the climatic precession cycles in geological data can only be demonstrated by fine-tuning the record. In the absence of detailed knowledge for the astronomical calculation, a decision was made to fine-tune the record to the Laskar *et al.* calculation (1993) [86], with current day values for tidal dissipation and dynamical ellipticity.

Following previous studies [55; 156], an artificial target curve was constructed by normalising eccentricity, obliquity and climatic precession values to zero mean and one standard deviation. These components were then added to create a mixed "ETP" curve. Northern hemisphere insolation contains the climatic precession signal with reversed polarity, and the polarity of climatic precession was reversed before adding to the other orbital components. As pointed out by Shackleton *et al.* (1999) [55], the uncertainties in the astronomical model are such that this cannot be tested at present, and the motivation was to stay consistent with previous studies.

The presence of amplitude modulation cycles in the data, as well as the close correspondence between periodicities of lithological cycles with those of orbital calculations, as demonstrated in the depth domain, strongly suggests that a significant part of the lithological variability is related to orbitally controlled climatic variations. One assumption made in this study is that maxima in calcium carbonate content (which correlate to high L^* and Ca/Fe values, and low values in magnetic susceptibility), are related to maxima in the target curve (i.e. high insolation values).

There are several possible scenarios of how the lithological signal is related to climatic variations. One feasible scenario is, for example, that increased mixing between shallow and deeper waters leads to an enhanced nutrient supply, thereby increasing biogenic carbonate productivity, or that a generally warmer atmosphere leads to enhanced continental precipitation, and thus increased run-off of terrestrial material across the ocean margin. Other possible scenarios include variations in the calcium carbonate compensation depth (CCD), controlling the dissolution of calcium carbonate, variations in ocean stratification and upwelling, and nutrient supply from external (e.g. aeolian or volcanic) sources. At present, the exact mechanism of how the orbital signal is transferred into the lithological record through the local and global climate

system is unresolved at Site 1052 during the Eocene. Regardless of which mechanism is invoked, the choice of one model over another only results in an uncertainty of half a precession cycle (∼10 ky) for age estimates, much less than the uncertainties in the stratigraphic position of magnetic reversals in this data set.

3.7.2 Time scale development

For the development of the time scale the AnalySeries package [106] was used. Figure 3.8 shows the results of astronomical tuning following the strategy described above.

The left column of figure 3.8 shows the sedimentation rate in cm/ky that results from tuning. The tie points that were used to generate ages from the rmcd scale are given in Appendix B. Also shown are bandpass filters for the XRF and reflectance data, computed at the main orbital frequencies. These generally show good agreement with the astronomical target curve (shown in the right-hand column). For the lower part of the record, only data and filters for the reflectance record are shown, as the XRF record does not extend this far. Also plotted are the magnetic reversal record for new ages, and the ages that arise from the time scale of Cande and Kent (1995)[46].

This time scale is based on "tuning" the XRF Ca/Fe ratio data, excluding identified volcanic ash layers, down to approximately the top of magnetochron C18n.1n, and on variations in L^* below that. Several key features are worth exploring in detail. The central four columns of the figure show filters that extract those variations in the data that fall within the astronomical frequency bands for climatic precession (∼22 ky), obliquity (∼41 ky), and the short and long eccentricity (∼100 ky, ∼400 ky). A change is visible at around 36.7 Ma, where the relative strength in the precession signal suddenly weakens towards the younger interval. This coincides with a strong increase in the average XRF counts for iron. It is unclear at present whether this can be attributed to a change in the climate system at large, or whether this change in response is due to local effects such as a change in terrestrial run-off, or tectonic processes that are less directly linked to climate.

The filter that extracts the climatic precession component shows a strong amplitude modulation with maxima that coincide with maxima in the orbital ∼400 ky eccentricity component. This demonstrates that the tuning strategy employed in this study was successful, at least for the lower part of the record where the response to precession is

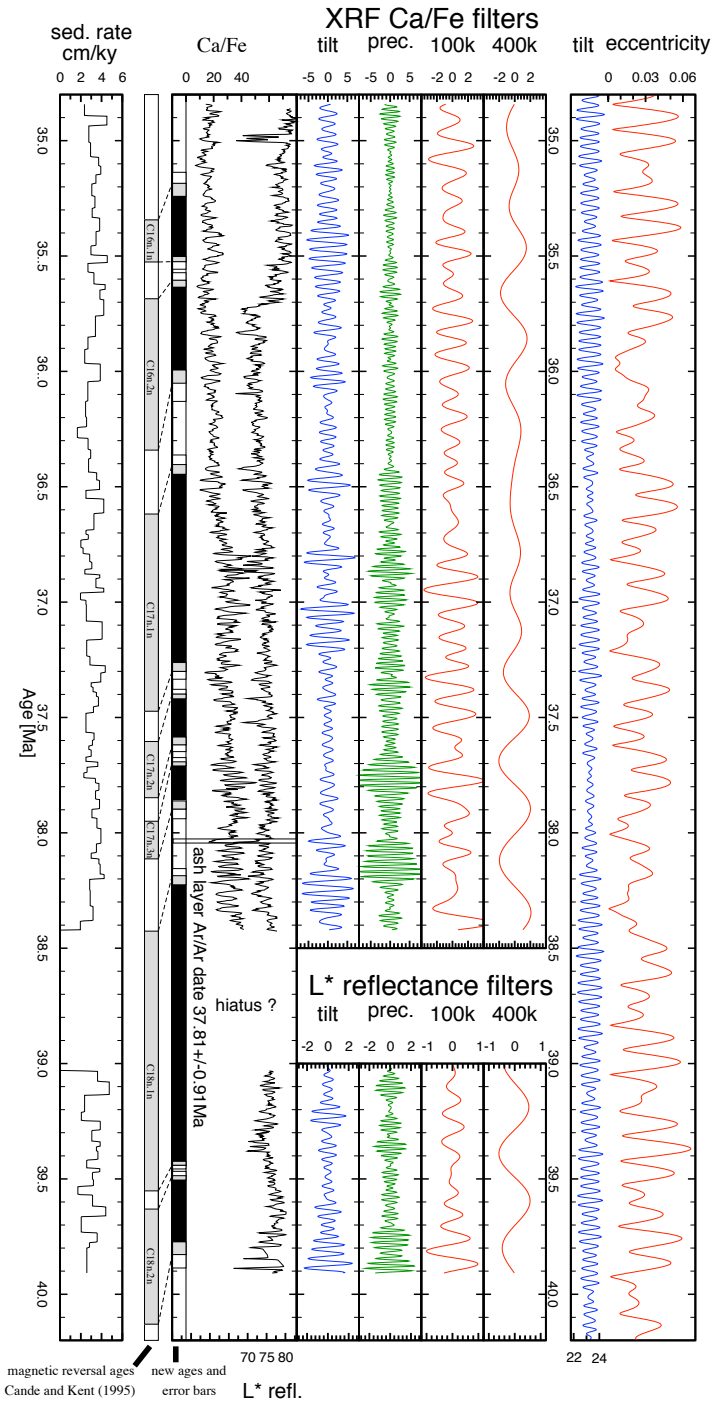

Figure 3.8: The stacked XRF Ca/Fe ratio and the lightness parameter L* on an age scale after astronomical tuning. Note the apparent change in the dominant orbital signal from a strong to a weaker climatic precession component at around 36.7 Ma.

strong. The tuning[3] relied mainly on obliquity cycles in the upper and younger part of the record, although a small contribution by climatic precession is still discernible. The data, filtered to extract the climatic precession frequency component, also display a modulation that co-varies with the short eccentricity orbital cycle (∼100 ky).

Interestingly, the data also show a relatively strong direct contribution of variability at eccentricity frequencies. The ∼100 ky cycle is clearly visible and again appears modulated in amplitude by the long eccentricity cycle, where maxima in the amplitude of the ∼100 ky filter of the data coincide with maxima in the ∼400 ky component of orbital eccentricity. The direct contribution of the long ∼400 ky cycle in the data is less clear, but appears to show a reverse polarity, where maxima in the data coincide with minima in the orbital curve for eccentricity at this frequency. The significance of this different response, if any, is unclear at the moment, but might be related to the climate system responding to the forcing with different time constants through the interaction with the carbon-cycle, or it might be linked in a non-linear fashion to the forcing by climatic precession.

3.8 Sedimentation rates and a possible hiatus

The process of tuning has not introduced geologically unreasonable large variations in sedimentation rates (shown in the left column of figure 3.8 in cm/ky). The average apparent sedimentation rate across all holes generally varies between 2 and 5 cm/ky. A few sudden jumps can be related to the construction of the rmcd scale as well as "tuning" to a target that probably does not reflect the real relationship between precession and obliquity correctly in detail. Using the ages from Cande and Kent (1995) [46] for magnetic reversals only would imply a sudden jump in sedimentation rate to only half the average value during chron C18n.1n. However, both variations, attributed to climatic precession as well as obliquity, do fit much better to a model that does not change sedimentation rate over this interval. Since no other chrons change significantly in terms of relative length, compared to the relative durations estimated by Cande and Kent [46] and Wei [153], and, more significantly, because a sudden loss in the amplitude of the orbital signal can be observed in the XRF, reflectance, and magnetic susceptibility data at around 114 rmcd, this implicates the presence of a hiatus at

[3]The mapping pairs from rmcd to time are listed in Appendix B, and are available in electronic form on the enclosed CD-ROM, as well as in downloadable form [123].

around this depth.

A detailed examination of the XRF data around this interval excludes the possibility that this could be due to an error in the construction of the rmcd scale. The length of this hiatus is estimated to be of the order of approximately 600 ky. This estimate is based on the amplitude modulation of climatic precession that can be seen in the L* record, which implies that the lower part of the record could only be shifted by multiples of approximately 400 ky. Making the implied hiatus shorter or longer by this amount of time would change the total duration of C18n.1n by more than 50%, which would imply geologically unreasonable changes in the sea-floor spreading rate. It must be pointed out, though, that the duration of this lower interval is much less well constrained than the upper interval, because it is not covered by data from more than one hole over some parts (see figure 3.5), and because the L* values seem to be partially corrupted in the lower-most part of the record due to a switch in the employed drilling method (core 1052A-16X). A confirmation of whether the interpretation of a hiatus is correct or not will have to await the availability of more data from different locations.

3.9 Spectral Analysis

In this section the spectral properties that arise from astronomically tuning the data set are examined. Figure 3.9 shows a Blackman-Tukey cross-spectral analysis between the ETP target curve and the XRF data above the inferred hiatus. Shackleton *et al.* (1995) [165] showed that there are pitfalls inherent in using spectral peaks and high coherency values to evaluate how "accurate" an astronomical tuning is. Here the only intention is to verify how well the time scale was adjusted to make the geological data fit to the target curve, while the plausibility of the age model is verified by amplitude modulation patterns, rather than by statistical measures such as coherency.

The upper panel shows that all major spectral peaks that are present in the astronomical calculation are also present in the "tuned" geological data. That this study has largely succeeded in creating a time scale that is consistent with orbital variations is shown by the very high coherency that is obtained for obliquity as well as the three separated peaks related to climatic precession. Coherency is above the 90% confidence level for the 54 ky and 29 ky frequencies that are associated with obliquity, high for the short eccentricity components, and weaker for the longer component. The phase plot re-iterates that the $\sim$100 ky component of the data is in phase with the target curve,

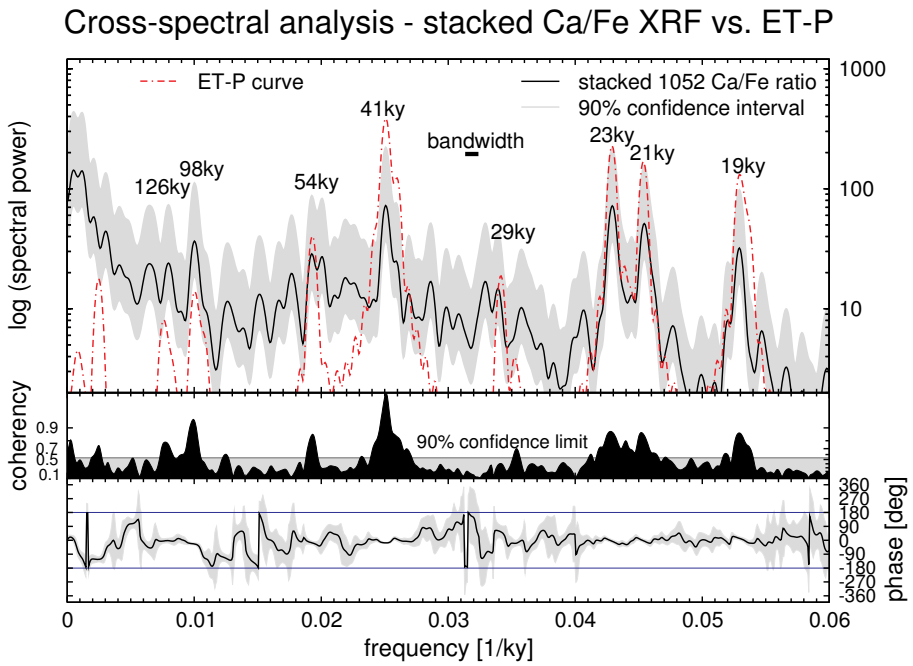

Figure 3.9: Cross-spectral analysis between the astronomically tuned XRF Cai /Fe data and the astronomical target curve. Note that all major astronomical spectral peaks are present in the data, including those at 54 ky and 29 ky. The middle panel shows coherency values which are particularly strong around the main obliquity frequency period (41 ky). The phase plot (bottom panel) shows that the tuning has put the short eccentricity component ($\sim$ 100 ky), obliquity and climatic precession into phase between the data and the target. The $\sim$ 400 ky component, however, seems to be out of phase by approximately 180 degrees (π radians).

while the $\sim$400 ky component shows a phase difference of 180 degrees.

Note that the relative amplitude of spectral peaks that arise in the orbital target curve is arbitrary in that the three components eccentricity, obliquity and climatic precession were added in arbitrary proportions, mainly to make the visual comparison of target and data easier. However, the relative amplitude of spectral peaks is fixed by the data, although they represent the average contribution over the entire interval studied. This does not take into account the distinct shift in power away from the climatic precession component towards the upper section of the record.

3.9.1 Amplitude modulation patterns obtained by complex demodulation

The amplitude modulation of the obliquity and climatic precession is a feature that cannot be easily introduced into a data set by the tuning process. Hence it is crucial to examine amplitude modulation patterns in the data set because it can give new in-

formation on both, how strongly an astronomical forcing is contained in the data, as well as allowing the extraction of information useful for improving astronomical calculations [89]. Amplitude modulations reflect a beat between fundamental astronomical frequencies as outlined in chapter one. The main patterns that are visible in astronomical calculations are the modulation of climatic precession by eccentricity (∼400 ky and ∼100 ky periods), as well as modulations with periods of the order of million years for the eccentricity, obliquity and climatic precession. These were described in more detail by Laskar (1999) [89], and were used to confirm the astronomical tuning for sediments of Oligocene to Miocene age (Shackleton *et al.* (1999) [55]; Hinnov (2000) [92]).

Here, three different types of modulation patterns are analysed. The initial basis for the tuning strategy was to use the ∼400 ky amplitude modulation of climatic precession. Figure 3.10 (a) shows the amplitude envelope of the climatic precession signal in the Ca/Fe data above the hiatus. This envelope was obtained by complex demodulation [166] at a central frequency of 0.04762 cycles/ky (∼21 ky period), using a 100 ky low-pass Parzen filter with 100 weights. This figure shows clearly how the amplitude of the climatic precession signal in the data is much stronger in the lower half of the record. This figure also suggests that this study has largely succeeded in making use of the ∼400 ky amplitude modulation cycle, as well as of the ∼100 ky amplitude modulation cycle. Figure 3.11 shows a Blackman-Tukey cross-spectral analysis between the amplitude envelope of the climatic precession signal and the ETP target curve, which was demodulated by using the same complex demodulation method in order to verify this processing step. Clear spectral peaks are visible, with a ∼400 ky period, as well as short eccentricity modulation terms with a period around ∼100 ky. Since the total amplitude of the climatic precession signal varies strongly across the record, i.e. the overall response is non-stationary, it is not possible to evaluate how closely the longer term (∼2 My) modulation pattern that is visible in the astronomical calculation is reflected by the data.

The amplitude envelope for the ∼100 ky component of the data (already described for the filtered time series in figure 3.8) was also computed. This complex demodulation was centred at a frequency of 0.009 cycles/ky (∼110 ky period) using 300 filter weights with a 200 ky Parzen low-pass filter. Figure 3.10 (b) shows that the ∼100 ky component is modulated by a ∼400 ky component in both, the astronomical calculation, as well as in the data. In addition, there is an approximately 2 My long modulation

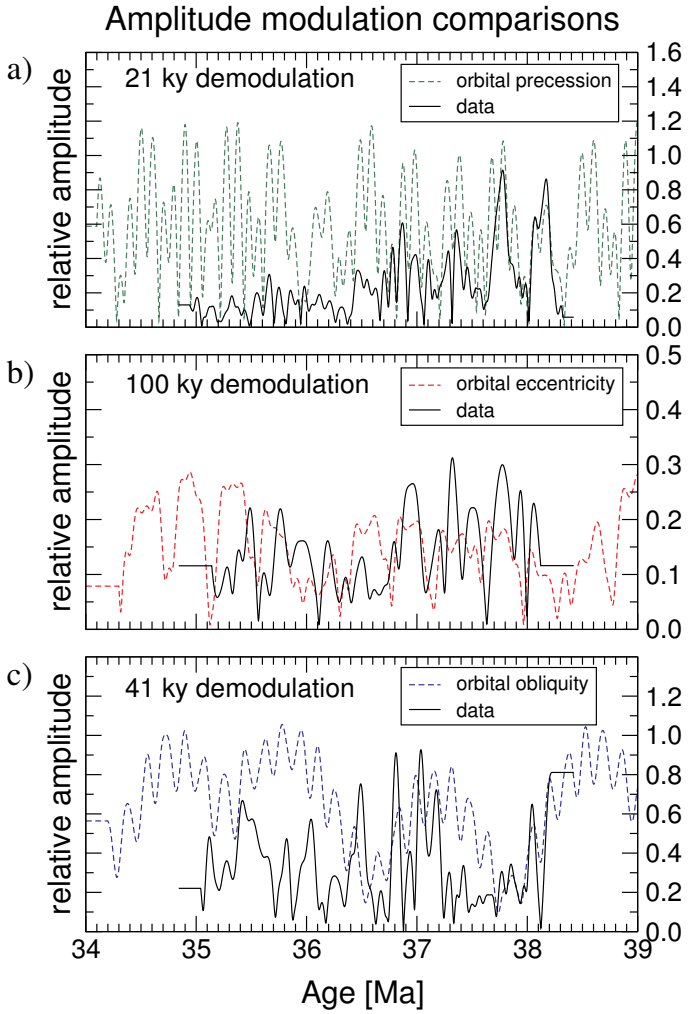

Figure 3.10: Panel a) shows the amplitude modulation of the climatic precession signal in the XRF Ca/Fe ratio and in the orbital calculation. Panel b) shows the amplitude modulation of the short eccentricity signal ($\sim$ 100 ky) in the data and in the orbital calculation. Note the surprisingly strong match between the data and the target curve. Also note the apparent long term modulation pattern. Panel c) shows the amplitude modulation of the obliquity signal ($\sim$ 41 ky) in the data and in the orbital calculation. All curves were obtained by complex demodulation [166].

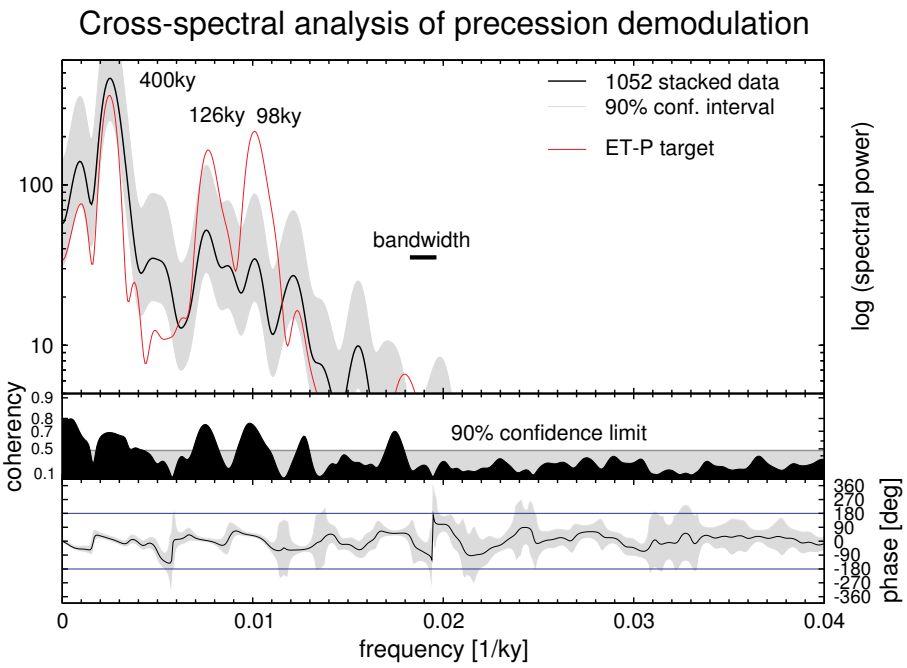

Figure 3.11: Cross-spectral analysis (Blackman-Tukey) obtained for the amplitude modulation at the climatic precession frequency (also see figure 3.10a) between the data and the astronomical target curve. Note that both long and short eccentricity modulate the amplitude of the precession signal in the data. In contrast to figure 3.9, the main eccentricity components around ∼100 ky and ∼400 ky are in phase.

present in the data. Compared to the astronomical calculation, this seems to be offset to slightly older ages by approximately 400 ky. If the astronomical calculation was correct, this would imply that all ages derived by astronomical tuning for this record are actually younger by this amount of time.

However, one can also compute the amplitude modulation for the obliquity cycle as shown in figure 3.10 (c). In this case the central demodulation frequency was 0.02439 cycles/ky ($\sim$41 ky period), employing a 133 ky low-pass filter with 200 weights. The modulation pattern obtained for the data is less clear than the previous modulation patterns but suggests, that the envelope for the obliquity amplitude in the data is shifted to younger ages, compared to the orbital calculation, by approximately 200 ky. Note that this apparent shift is in the opposite direction compared to that observed in the amplitude modulation of the $\sim$100 ky signal. In addition, one can see the presence of a $\sim$170 ky modulation in both, data and calculation.

Laskar [89] demonstrated that there can be a transition from a 2:1 ratio in the period of the long-term modulation of eccentricity and precession compared to that of obliquity (approximately 2.4 My : 1.2 My), to a 1:1 ratio, reverting back after a relatively short time. The data set does not span a long enough time to draw conclusions with confidence, but one might suggest that the long term pattern in the astronomical calculations is not consistent with the data over this time interval. As soon as other astronomically tuned geological records become available, this observation might be useful to improve astronomical calculations, and to put constraints on the timing of this transition. This will be investigated in more detail in chapter five.

Figure 3.12 shows an evolutive spectral analysis of the Ca/Fe XRF data after the tuning process in the time domain. Again a change in amplitude of the climatic precession signal is visible at around 36.7 Ma. Variation at the obliquity frequency is visible over most of the record. The short eccentricity cycle is also visible, and appears modulated. The frequency resolution in this figure could have been increased by choosing a longer spectral window but this would have decreased the resolution in time.

3.10 Implications for magnetostratigraphy

Table 3.1 lists the ages obtained from the astronomical age model for magnetostratigraphic datums. Figure 3.8 also shows a comparison of the Cande and Kent (1995) [46] and new ages. Within stratigraphic uncertainty bounds, indicated by grey and

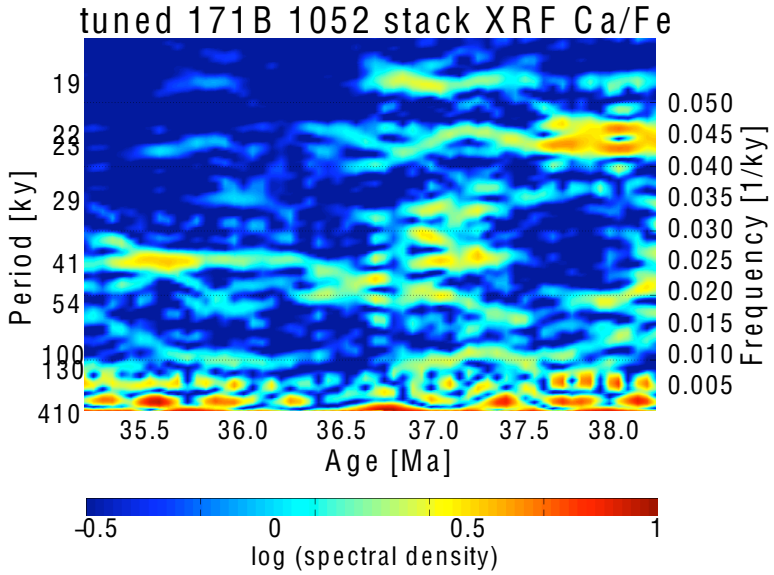

Figure 3.12: Evolutive spectral analysis in the time domain for the tuned XRF Ca/Fe data (compare with figure 3.7). Note the sudden change in amplitude at the main precession frequencies at around 36.7 Ma. The window length (500 ky) is too short to resolve the ∼400 ky eccentricity cycle but clearly shows the ∼100 ky cycle.

white boxes, the relative duration of all chrons that are present does not change significantly. An exception to this are the relative durations of sub-chrons within chron C16n, where C16n.1n is longer by ∼200 ky, and C16n.2n is shorter by ∼200 ky.

Based on the amplitude modulation of the climatic precession signal the absolute ages are younger by approximately 200 ky for all magnetic reversals. One can be quite confident for the new relative age estimates for chron C17, since the climatic precession signal is strong over this interval. Estimates for chron C16 are based largely on the variation in obliquity. Age estimates for chron C18 are less well constrained, due to the infered presence of a hiatus, and a tuning that was based on colour reflectance and magnetic susceptibility only. The lower-most interval is only covered by data from one hole. Hence estimates for C18n.2n should be interpreted as a minimum bound for its duration.

3.11 Results from XRF analysis of Site 1052: Summary

This study demonstrated that the collection of X-ray fluorescence elemental concentration data can greatly help the hole-to-hole integration of marine sediment cores.

This allowed the construction of a modified and revised composite depth scale (rmcd) which demonstrated that differential stretching and squeezing within each core is necessary to align stratigraphic markers on a decimetre scale. Employing the new rmcd scale, a stacked record was then created from multiple holes, thereby enhancing the signal-to-noise ratio in various proxy data records. This allowed the generation of a astronomically tuned relative time scale for the late Middle to Late Eocene.

Various techniques of time series analysis, particularly the study of amplitude modulation patterns that are present in the astronomical calculation as well as in the data, allow the verification of the age model. This leads to new estimates for the relative durations of magnetochrons C16 to C18 that, within error, agree well with the durations estimated previously by Cande and Kent [46] and Wei [153].

The amplitude modulation pattern that is visible in the climatic precession signal, and caused by a modulation through eccentricity, suggests that the absolute ages must be different by at least 200 ky. The data set is too short to allow a confident evaluation of the longer term amplitude modulation patterns, but it suggests that certain features in the astronomical calculations do not fit with the geological record during this time interval.

As soon as longer astronomically tuned records become available for the Paleogene, this hypothesis should be tested. The results from this study provide a further extension of the astronomically calibrated time scale into the Paleogene, verified by amplitude modulation patterns. For the first time, a distinct change in the relative strength of orbitally driven climatic obliquity and precession signals has been observed in the Eocene, which might be related to changes in the ocean circulation system and the dominant climatic regime. In addition, the data show an anticipated misfit with astronomical long term amplitude modulation patterns, which could be useful to further constrain astronomical models (see chapter five). The following sections document how additional geological data from ODP Leg 177, Hole 1090 B, can be used to verify and extend the new time scale.

3.12 Comparison with data from ODP Leg 177, Site 1090B

It is generally difficult to assess the accuracy of astronomically calibrated geological time scales. Although it is possible to compare spectral properties that are recorded in a geological data set with those expected from astronomical theory, the uncertainties

inherent in astronomical calculations increase back in time, as shown by Laskar (1999) [89]. Particularly for the Paleogene these uncertainties are considerable, and it would be useful to be able to compare geological data from different locations. For parts of the Neogene this was made possible through independent studies from deep-marine sediments and Mediterranean sections [47; 51; 52].

In order to test the consistency of ages derived for the magnetic reversal record from the Middle and Late Eocene presented in previous parts of this chapter, an attempt was made to find geological data from a different location. Unfortunately, previous attempts by the Deep Sea Drilling Project (DSDP) and Ocean Drilling Program (ODP) to recover deep-marine sediments from the Paleogene recovered sections that were shown to have very low sedimentation rates, or had incomplete recovery, thus preventing detailed studies of astronomically driven variations.

Fortuitously for the work presented here, ODP Leg 177 very recently recovered material from the Paleogene that appeared to be more promising [167]. The initial scientific objectives did not include recovery of Paleogene material, but an unexpected hiatus resulted in the recovery of an extended Paleogene record at one of the sites. Since the main objectives of Leg 177 did not focus on the Eocene, only Hole 1090 B penetrated a long Paleogene interval. Hence, the presence of core breaks means that it is not possible to use material from this hole on its own to create an astronomically calibrated time scale with confidence. However, since an initial astronomical tuning of data from Site 1052 is now available, an attempt was made to verify the consistency of this astronomical calibration with data from Hole 1090 B.

Sites from Leg 177 are located in the south-east Atlantic sector of the Southern Ocean. The location of Site 1090 is shown in figure 3.13. The present day water depth is $\sim$3700m, which is above the present day and last glacial maximum calcium carbonate compensation depth (CCD) [167].

Material recovered from Site 1090 B contains an excellent magnetic reversal record, with magnetic inclination values close to $\pm$70 degrees. The reversal record was not interpreted for the Paleogene part during the initial investigation [167]. However, using biostratigraphic datums reported in the ODP Initial Reports from this Site [167], it is indeed possible to propose a clear interpretation of magnetic reversals. As part of the study presented here, an initial bio- and magnetostratigraphic age model was developed, and is shown in figure 3.14.

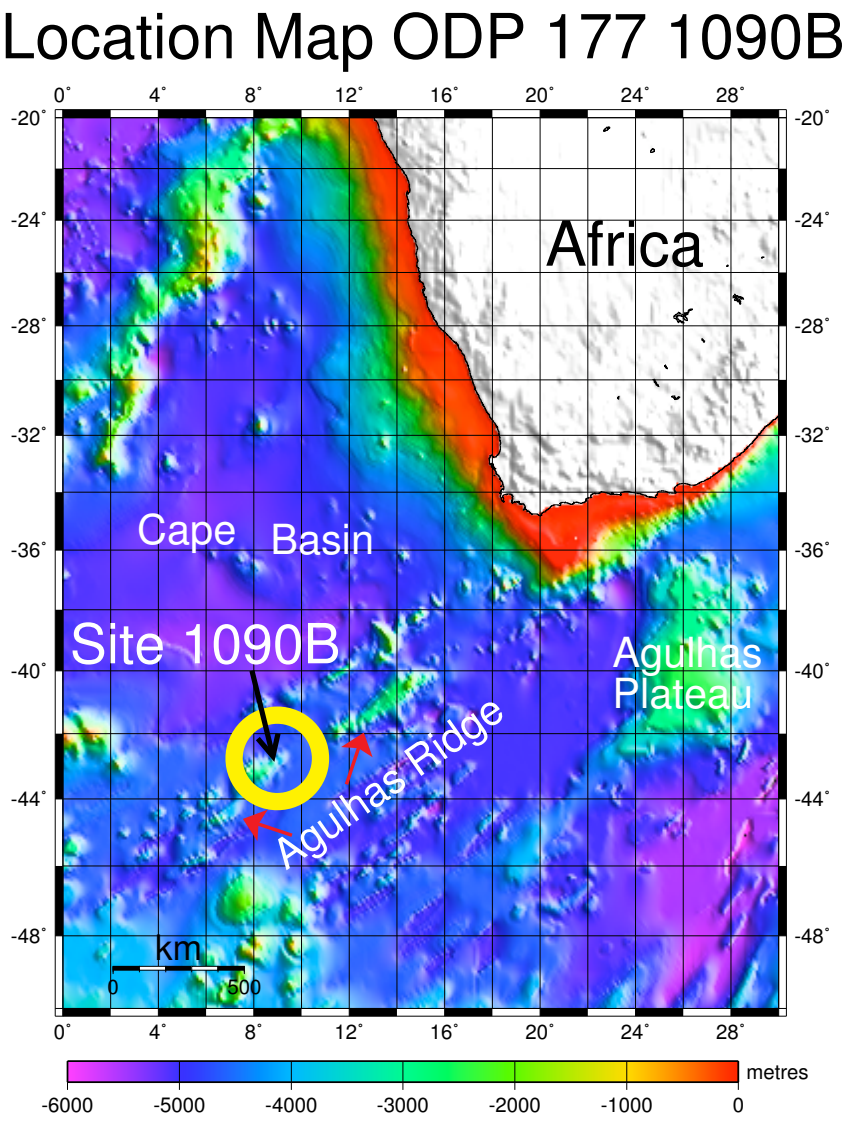

Figure 3.13: A bathymetric map showing the location of ODP 177 Site 1090. At this site the present day water depth is ~3700 m.

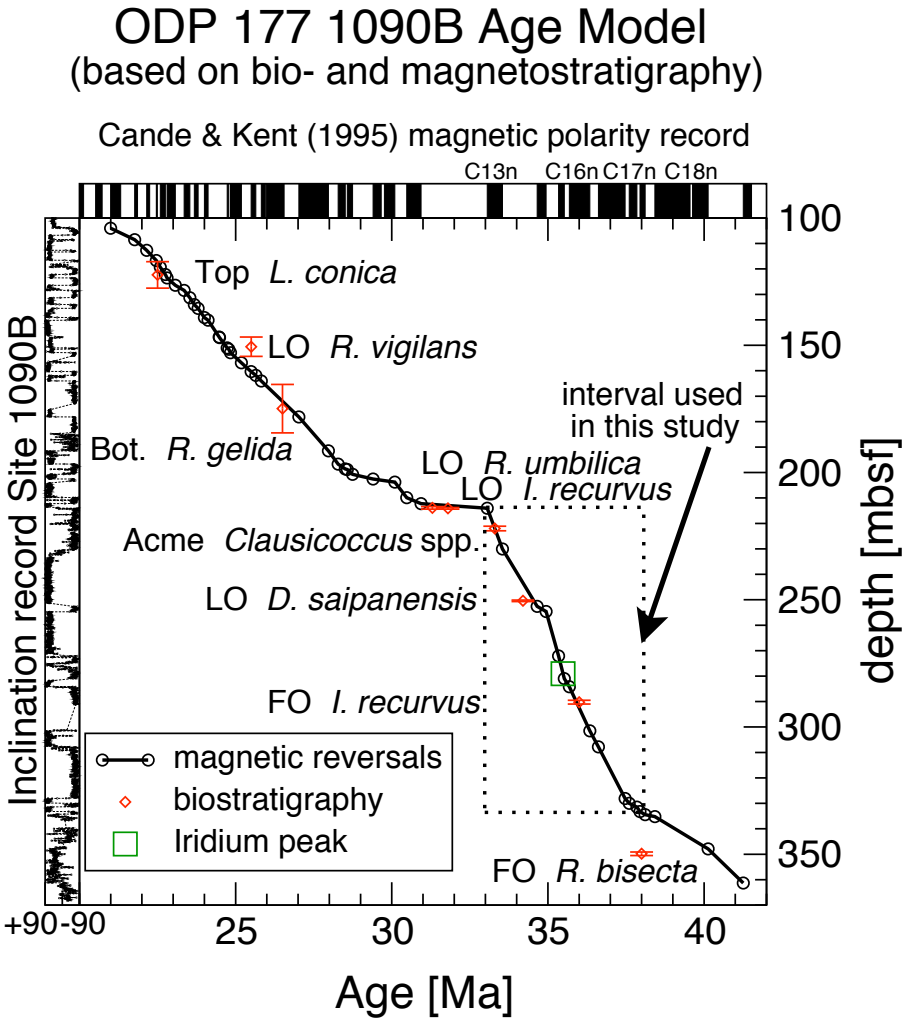

Figure 3.14: Bio- and magnetostratigraphic age model for Site 1090, Hole B. The magnetic polarity record from Hole 1090 B is of excellent quality, as shown in the left hand column of this figure. It is easily matched to the sea-floor composite record of Cande and Kent (1995) [46], and, together with the biostratigraphic data [168] indicated on the plot, allows the construction of an initial age model. Two sedimentary breaks are located just above magnetochron C13n, and possibly below C17n.3n. This study focused on the interval between these two breaks. The age model is confirmed by the presence of an iridium concentration peak, that was found within chron C16n at other sites world-wide (Kyte, 2001 [169]).

Ages for biostratigraphic events were taken from Berggren *et al.* (1995) [168], who also report the interpolated ages of magnetic reversals as defined by Cande and Kent (1995) [46]. The left panel of figure 3.14 shows the magnetic inclination record from Hole 1090 B, obtained by using the shipboard pass-through magnetometer after applying an alternating peak field de-magnetisation at 20 mT. On this figure, circles mark those reversals that were used to generate the initial age model, while diamonds show selected biostratigraphic events together with their uncertainty in depth. In Hole 1090 B, magnetic reversals can be identified in depth with an uncertainty of the order of decimetres, and it was not deemed necessary to mark uncertainty in depth for magnetic reversal events.

This initial age model is supported by the presence of a high concentration peak of iridium at $\sim$291.04 metres composite depth (279.05 metres below sea floor), as documented by Kyte (2001) [169]. This anomalous iridium concentration peak has been interpreted to be caused by a Late Eocene impact event, and was found previously in several other ODP sites, as well as in the Eocene type section near Massignano, Italy [139–142]. In all cases this event has been found near the top of magnetochron C16n. According to the age model proposed here, the iridium peak at Site 1090 occurs within chron C16n.1n, and is thus consistent with previous studies. This iridium anomaly is also marked on figure 3.14.

The bio- and magnetostratigraphic data from Site 1090 B suggest the presence of a several million year long hiatus just above magnetochron C13n, and possibly another break in continuous sedimentation near the base of C17n. Due to this finding, the work presented here focused on a selected interval only, as marked in figure 3.14. The average apparent sedimentation rate over this interval is approximately 2.5 cm/ky. Thus, the proposed age model suggests that material from Site 1090 Hole B could potentially be used for a comparison with data from Site 1052, but would only allow an extension of an astronomically calibrated geological time scale up to the top of magnetochron C13n, i.e. near the base of the Oligocene.

Core photographs from Hole 1090 B for this interval show prominent variations in sediment colour on a decimetre to metre scale, which are consistent with being driven by orbital variations (see figure 3.15 for a typical core photograph). Colour and lightness changes are due to variations in calcium carbonate content [167], which is generally only around 30% in the interval studied, although it suddenly increases to around

70% in the Early Oligocene. This increase is most likely related to profound changes in ocean chemistry and climate across the Eocene/Oligocene boundary, as reviewed and discussed by Zachos *et al.* (1996) [127], Lear *et al.* (2000) [170], and Zachos *et al.* (2001) [152] (and references therein).

Unfortunately it was not possible to sample sediments from Hole 1090 B using the XRF core scanner in Bremen due to machine unavailability. However, since the XRF Ca/Fe data generated for Site 1052 correlated well with colour and lightness changes, it was decided to compare the XRF data from Site 1052 with lightness variations in sediments from Site 1090. Unfortunately, spectrophotometer measurements above 262.50 mbsf are not available from Site 1090 B because the shipboard colour measurement system was faulty. However, it was possible to generate a high-resolution colour record from core photographs that are available in digital format [167]. This was a method also used by Cramer (2001) [171]. Cramer employed an algorithmic method to correct for lighting variations across scanned core photographs. Experiments conducted as part of this study show that these effects are important if a flat-bed scanner is used, as was done by Cramer. However, using the digital images that are available from ODP, these effects were not found to be strong, thus no attempt was made to adjust core photographs.

The digital images available from Site 1090 [167] have a resolution of approximately 1 pixel per 2 mm. Core photographs were cropped to separate individual core sections, avoiding obvious cracks in the core. From the digital data a lightness record was then computed, with a value of 255 being assigned to white, and a value of 0 to black. In order to keep the data set at a manageable size, and to provide a smoothing of data, pixel values were integrated, first across the core, and then along the core, to yield one data point every two centimetres[4].

Comparing with figure 3.15, this is a length scale of the same order as that at which bioturbation effects are visible. It would have been possible to employ a more sophisticated method to remove outliers in the data caused by core cracks and other disturbances. However, it was found to be more efficient to manually prune the data set by removing outliers in the data that are obviously related to core cracks and disturbances. Since the scale of lithological variations is of the order of decimetres, and outliers occur on a scale of centimetres, this treatment of the data has no effect on the subsequent interpretation and analysis.

[4]The complete data set is available in electronic form on the enclosed CD-ROM, as well as in downloadable form [123]. The nature of the data is illustrated in Appendix E.

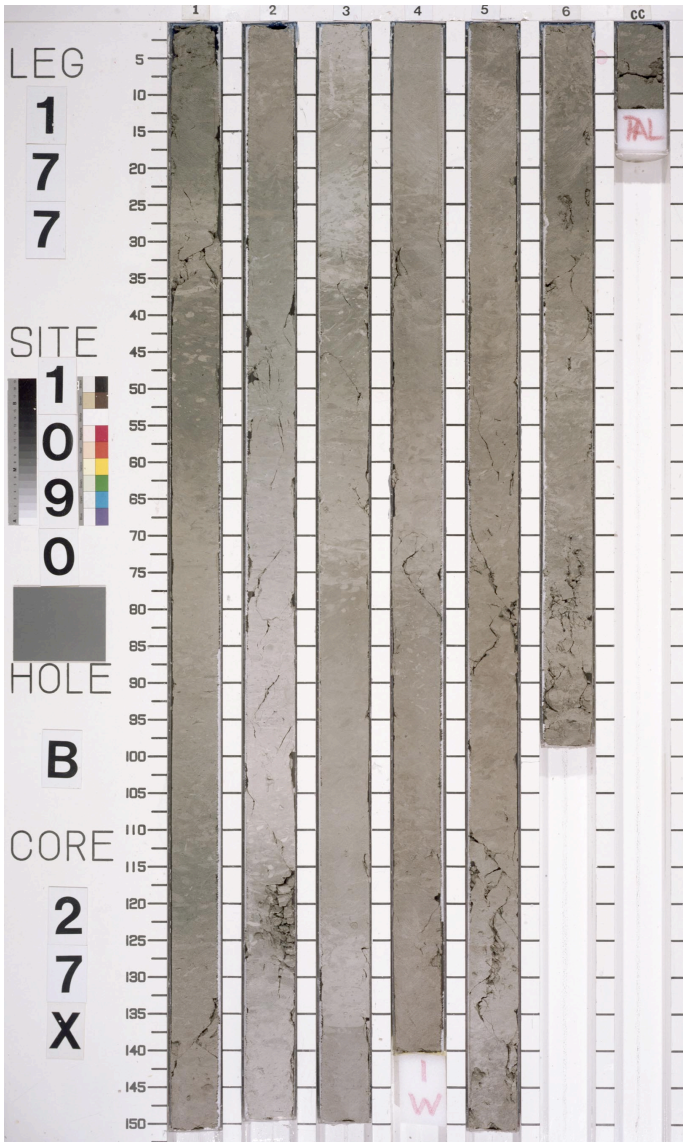

Figure 3.15: Core photograph from ODP 177, Site 1090, Hole B, Core 27X. This is a representative core photo that was used to create the lightness record from Hole 1090 B. Lightness variations reflect variations in % $CaCO_3$, and are clearly visible on this photograph. This core spans the depth interval 242.9–252.6 mbsf, which corresponds to an age interval from ~34.3 Ma to ~34.8 Ma on the time scale from ODP 171B, Site 1052.

The success of this methodology was confirmed by comparing the lightness values obtained here with spectrophotometer measurements in intervals where they are available. Both lightness records match very well. In fact, the method employed here seems to yield a data set that is more representative for lithological variations than those obtained by using the colour spectrophotometer. This can be explained by the integration of values across the entire core by using digitised images, while the spectrophotometer measurements are obtained from a footprint of approximately 5 mm^2 size.

The lightness record obtained from ODP Site 1090 was then compared to the XRF data available from Site 1052. This was accomplished by using the ages obtained for the magnetic reversal record from Site 1052 (table 3.1) as initial tie points for chrons C16 and C17. The Cande and Kent (1995) [46] ages for chron C13 were used as initial tie points. This was the best possible strategy, since the data from the single Hole 1090 B contain core gaps, thus preventing a strategy based on an astronomical calibration alone. The age of the Eocene/Oligocene boundary within chron C13r is supported by several good radiometric dates (Berggren *et al.* (1995) [168]). Based on an inter-calibration of magnetostratigraphic data with radiometric ages, the position of the Eocene/Oligocene boundary was placed in the younger part of chron C13r, such that 14% of the total length of C13r lies above this boundary (Berggren *et al.* (1992) [172]).

Based on these initial tie points, the data from Hole 1090 B appear very similar to those from Site 1052 when compared on a cycle by cycle basis. A direct match was then performed between the two records, resulting in a modification of the exact position of magnetic reversals from Hole 1090 B. Above the top of the record from Site 1052, data from Site 1090 were adjusted to astronomical calculations using a target curve based on the calculations of Laskar (1993) [86]. This astronomical calculation is identical to the one used for the calibration of data from Site 1052. The results of this work are illustrated in figure 3.16. The new age model for Site 1090 B is given in Appendix E[5].

In figure 3.16, the matched data are shown together with the output of two Gaussian bandpass filters that extract variation at the obliquity and climatic precession frequencies. The raw data show a very good match, with cycles of very similar character over most of the studied interval. The obliquity filter used was centred at a frequency of 0.025 cycles/ky, with a bandwidth of $\pm$0.06 cycles/ky. The central frequency and band-

[5]The complete data set is available in electronic form on the enclosed CD-ROM, as well as in downloadable form [123].

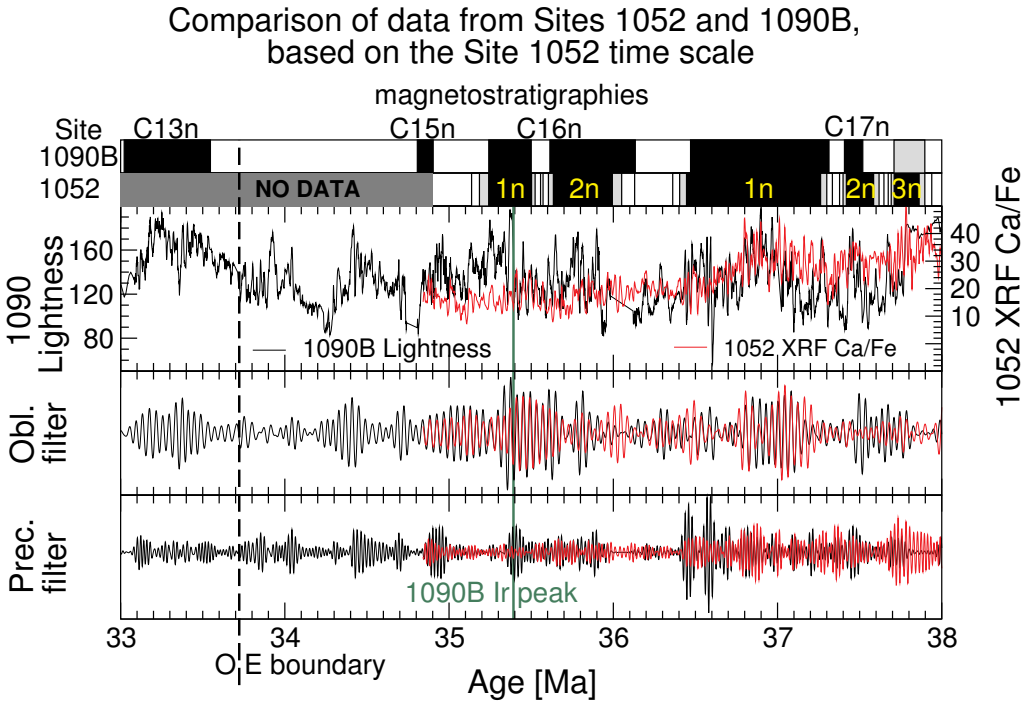

Figure 3.16: Comparison of the stacked XRF Ca/Fe ratio from ODP 171B, Site 1052, and the lightness record of sediments from ODP 177, Site 1090, Hole B. Data from Site 1090 were matched to those from Site 1052 based on magnetostratigraphic data. A close match is evident on the individual cycle scale. The upper part of the figure shows that the magnetostratigraphy from both sites is consistent. Ages for magnetochrons C13 and C15 are based on Cande and Kent (1995) [46]. The lower part of the figure shows a comparison of obliquity and climatic precession bandpass filters for data from both sites. A close match is observed for the amplitude modulation for both filters from both sites.

Chron (top)	CK1995 age [Ma]	Site 1052 age [Ma]	Site 1052 min. [Ma]	Site 1052 max. [Ma]	Site 1090 depth [mbsf]	Site 1090 age [Ma]
C13.n	33.058	N/A	N/A	N/A	213.80	33.021
C13.r	33.545	N/A	N/A	N/A	230.50	33.547
C15.n	34.655	N/A	N/A	N/A	? 252.60 ?	? 34.807 ?
C15.r	34.940	N/A	N/A	N/A	254.80	34903
C16.1n	35.343	35.185	35.137	35.241	272.80	35.242
C16.1r	35.526	35.524	35.502	35.557	281.40	35.500
C16.2n	35.685	35.605	35.572	35.635	284.20	35.615
C16.2r	36.341	36.051	35.994	36.130	301.50	36.134
C17.1n	36.618	36.404	36.362	36.446	307.80	36.470
C17.1r	37.473	37.300	37.262	37.334	328.10	37.314
C17.2n	37.604	37.399	37.378	37.419	330.06	37.407
C17.2r	37.848	37.618	37.585	37.648	331.50	37.519
C17.3n	37.950	37.941	37.674	37.710	? 333.25 ?	? 37.709 ?
C17.3r	38.113	37.897	37.862	37.939	? 334.45 ?	? 37.897 ?

Table 3.3: Comparison of relative age estimates for magnetic reversals from Sites 1090 (Hole B) and 1052. Columns one to five are taken from table 3.1. The depths and ages estimated for magnetic reversals from Site 1090, after matching the 1090 lightness data to the XRF data from Site 1052, are shown in columns six and seven. They generally agree well with those obtained from Site 1052. Question marks indicate uncertainties in the identification of magnetic reversals due to core gaps.

width for the climatic precession filter was 0.05 ± 0.012 cycles/ky. Individual obliquity cycles and their amplitude modulation from both sites match particularly well. The upper part of figure 3.16 shows the position of magnetic reversals that results from the matching of data as described above. The uncertainty in depth of magnetic reversals from Site 1052 is indicated by grey shaded boxes. It can be seen that both records match to within these uncertainty intervals, although this match is less certain below chron C17n.2n, where the magnetic record from Site 1090 is less clear. The position of the Eocene/Oligocene boundary, based on the magnetostratigraphy [172], is also indicated on this figure. The ages of magnetic reversals according to Cande and Kent (1995) [46], according to the age calibration of Site 1052, and according to the match of Site 1090 to 1052, are listed in table 3.3.

In order to evaluate the match between the two sites in a more numerical way, a cross-spectral analysis was performed between data from both sites where they overlap. This is shown in figure 3.17. Since the record from Site 1052 was stacked from several different holes, it is not surprising to find a stronger astronomical signal in the XRF

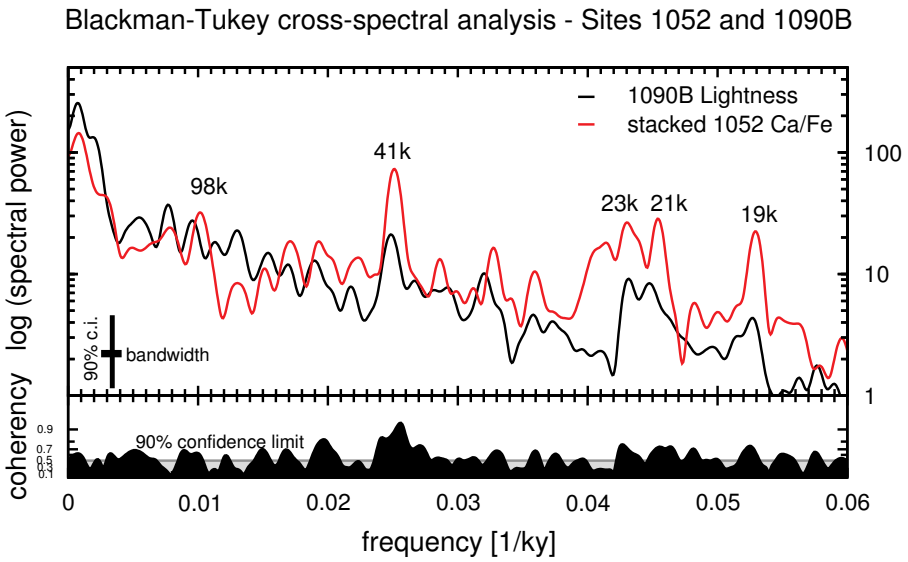

Figure 3.17: Blackman-Tukey cross-spectral analysis between the astronomically tuned XRF Ca/Fe data from Site 1052 and the matched light reflectance data from ODP 177 Site 1090B. The data from Site 1090B show a clear peak at the obliquity frequency, as well as less well resolved peaks at the three main climatic precession frequencies. The lower panel shows coherency values, which are particularly strong around the main obliquity period (~41 ky).

data from Site 1052. However, data from Site 1090, despite the presence of core breaks, and only a preliminary tuning, also clearly show the presence of spectral peaks at the obliquity and climatic precession frequencies, supported by high values of coherency when compared with data from Site 1052.

3.13 Summary of analysis of data from Site 1090

One can conclude from the comparison of lightness data from Site 1090 with the XRF Ca/Fe ratio from Site 1052 that new ages derived for magnetic reversals are consistent with the interpretation of lithological variations as an astronomically driven signal in both records. Given the spatial separation of both sites, the match between both records is surprisingly strong between individual obliquity cycles, as well as between their amplitude modulations. Relative age estimates for magnetochrons C13 and C15 are preliminary as of yet, and not fully astronomically calibrated. Nevertheless, the combination of data from ODP Sites 1090 and 1052 might facilitate a more detailed study of this time interval as soon as more geological data become available, as projected for the forthcoming ODP Legs 198 and 199.

3.14 Conclusions

This chapter discussed the findings from two different data sets that were obtained from the Late and Middle Eocene. The XRF data allowed the generation of an improved stratigraphic correlation of holes from Site 1052, facilitating an extension of the astronomically calibrated geological time scale into the Eocene for the first time. This results in new relative age estimates for magnetochrons C16, C17 and C18, which allow the stratigraphic correlation between data from different sites to a particular astronomical calculation. The amplitude modulation of astronomical cycles recorded by lithological variations in the sediment suggest that the astronomical calculation by Laskar *et al.* (1993) [86] might not be consistent with geological data in the Eocene any longer. This is investigated further in chapter five.

The newly developed age model was transfered from Site 1052 to Site 1090, allowing a verification of the consistency of generated ages, as well as tentatively extending the calibration up to the base of the Oligocene. These data will eventually allow a link to be made with existing astronomical calibrations that extend to the base of the Oligocene [53]. The data reported in this chapter will be used in chapter five. Employing the newly generated age model from Site 1052, the next chapter reports an investigation of high-resolution stable isotope records from Site 1052.

Chapter 4

Stable isotope data from ODP Leg 171B, Site 1052

4.1 Introduction

This chapter reports existing and newly generated stable oxygen and carbon isotope measurements that were obtained from Site 1052, making use of the new chronology obtained for Site 1052 and discussed in the previous chapter. So far, only relatively low resolution benthic stable isotope records exist for the Middle and Late Eocene (see [138; 147–149; 152] and references therein). The Late Eocene marks the transition from a minimally glaciated "doubt-house world" [137] to an "ice-house world" in the earliest Oligocene that is well documented by stable isotope measurements from different sites [127; 138]. The interest in this transition has recently increased because Mg/Ca ratios measured in foraminiferal calcite, which are thought to represent calcification temperature, seem to remain steady across the Eocene/Oligocene boundary, despite a large positive shift in oxygen isotope values (Lear *et al.*, 2000 [170]; Lear, 2001 [173]). The main impetus for work reported in this chapter is to evaluate whether changes in lithological parameters, that were used to create an astronomically calibrated time scale for Site 1052, are also reflected in the isotope record.

For Site 1052, intervals of long high-resolution benthic stable isotope data were generated separately by Shackleton (unpublished data), and by M. Katz, Rutgers University (unpublished data). In addition, following Wade *et al.* (2001) [151] who generated a high-resolution stable isotope record from planktonic foraminifera for ODP Site 1052, Wade also generated a high-resolution record of stable isotope measurements

from planktonic foraminifera using Middle Eocene material from Site 1052 (unpublished data). There is no overlap between the benthic records of Shackleton and Katz on the one hand, and the record of Wade on the other hand. For this reason, the benthic stable isotope records of Shackleton and Katz was extended as part of this study to make a comparison of benthic and planktonic data possible. The astronomical calibration described in the previous chapter now allows the investigation of changes in these records in the time domain for the first time. The palaeodepth estimate for Site 1052 in the Eocene is approximately 600 m, based on faunal studies [100]. The results reported here must be interpreted in the light of this when a comparison is made with other benthic records obtained from deeper sites.

4.2 Methods used for generation of stable isotope record

The stable isotope record generated in this study formed part of a collaboration with Bridget Wade in Edinburgh and Philip Sexton in Southampton. This collaboration was initiated to investigate whether large amplitude variations observed by Wade in the planktonic foraminifera stable isotope record are also reflected in the record from thermocline and benthic species, making use of the age model generated in this study. A short interval ($\sim$12 m long on the rmcd scale from Core 10 in Holes 1052B and F) was selected to be analysed for thermocline species in Southampton, and benthic species, as reported in this study.

As part of the collaborative effort, samples for isotopic analysis were first prepared in Edinburgh for a study of planktonic foraminiferal stable isotope ratios. This involved obtaining samples of 2.8 cm^3 volume at 10 cm intervals from Holes 1052 B and F (Core 10), following the original composite depth splice [100]. The samples were then dried, weighed, soaked in a Calgon/peroxide solution overnight, and wet sieved on a 63-μm mesh. The $>$63-μm size fraction was then oven dried at $<$50°C. Planktonic foraminifera were picked and analysed in Edinburgh. A similar study was performed by Wade *et al.* (2000) [174] with material from the adjacent Site 1051.

After the planktonic foraminifera work was completed in Edinburgh, the $>$63-μm size fraction of samples was sent to Cambridge and Southampton for analysis of benthic and thermocline species, respectively. For the analysis of benthic foraminifera of the species *Nuttalides truempyi*, the samples were sieved to obtain the $>$212μm size fraction. From this material, multiple specimens (typically 5-15) were picked under a

low-power ($\times$25) binocular microscope. All specimens were of similar size. The Paleogene sediments recovered at Blake Nose have not been deeply buried by overlying sediment and thus show little evidence of dissolution or diagenesis [151]. The picked foraminifera were then visually inspected to select a subset (typically 5-10) of high quality specimens to yield enough carbonate for the mass spectrometer analysis of carbon and oxygen stable isotopes.

The selected specimens were transferred to the laboratory, where laboratory staff performed the following work. Samples were lightly crushed, and soaked in hydrogen peroxide to remove possible organic contaminants that might adhere to the walls of foraminiferal tests. To this, analytical grade acetone was added, and the samples were cleaned ultrasonically. After the cleaning procedure, excess fluid was quickly siphoned off so as to remove fine-grained carbonate that had been loosened by the ultrasonic cleaning. Then the samples were dried in an oven at 60°C to be ready for analysis in the mass spectrometer.

Depending on machine availability and sample size, isotope analysis was performed in the Godwin Laboratory either on a VG PRISM mass spectrometer, or a VG SIRA mass spectrometer. The type of machine used is listed together with the individual measurements in Appendix D[1]. Results are reported with respect to the Vienna Peedee belemnite (VPDB) standard via the Godwin Laboratory Carrara marble standard, which was calibrated to VPDB through the NBS 19 standard [129]. Each run comprises five standard marble aliquots, an empty container as blank, twenty foraminiferal samples, and five additional aliquots of standard marble. Estimated by the marble samples, analytical reproducibility (precision) is typically $\pm$0.05% (1-σ) for standard sized samples ($\gtrsim$ 0.1 mg weight) [175], but less good for the smallest samples run on the VG SIRA machine.

The stable isotope data from this study were combined with existing records from Shackleton and from Katz, who generated a much longer series of benthic foraminifera and bulk fine fraction stable isotope measurements. In this study, measurements from various species of *Cibicidoides* were extracted from the complete and combined data sets of Shackleton and Katz. These data were prepared following the same procedures as described above and were all analysed on the VG PRISM mass spectrometer in the

[1]The complete data set is too extensive to be included as hard copy. It is available in electronic form on the enclosed CD-ROM, as well as in downloadable form [123]. Appendix D illustrates the nature of the data

Godwin laboratory. The bulk fine fraction data were obtained from the <63-μm size fraction and treated with hydrogen peroxide to remove surface organic contaminants.

4.3 Benthic stable isotopes from *Nuttalides truempyi*

The following section describes the data generated in this study, and compares the benthic stable isotope data with the planktonic data obtained by Wade, and the XRF data from previous parts of the previous chapter. Then, the combined record of all available stable isotope data is discussed.

Figure 4.1 illustrates the stable isotope composition of oxygen and carbon obtained from *Nuttalides truempyi*. All data are presented in the standard delta notation as per mil (‰) values [176] with respect to the standard VDPB. The age model used is that described in the previous chapter. Five data points are missing around 37.5 Ma because those samples were retained in Southampton. While the Ca/Fe ratio obtained by XRF measurements and the reflectance parameter L* show clear cyclicity, the benthic isotope record over this interval shows a very weak orbital signal. Oxygen and carbon isotope values match very well where the sample track changed from Hole 1052 F to 1052 B, independently indicating that the newly developed rmcd scale is plausible.

Towards the younger end of the interval studied ($\sim$37.4 Ma), there is a small general trend towards lower oxygen and carbon isotope delta values. Over some intervals there appears to be a very small amplitude signal in the oxygen isotope data that co-varies with the cycles seen in the XRF data and the reflectance data. For example, between $\sim$37.42 Ma and 37.6 Ma low oxygen isotope values seem to correspond to low values in the Ca/Fe ratio and coincide with low carbon isotope values. This will be investigated in more detail in following parts of this chapter. Overall, the evidence for cyclicity in the isotope data is not very convincing over this interval alone, and certainly variations are of very small amplitude, only reaching 0.2-0.3 ‰.

It was found in previous studies that stable isotope measurements from modern benthic foraminifera are not in equilibrium with the surrounding sea water (e.g. Duplessy *et al.*, 1970 [177]). Thus it is necessary to use adjustment factors in order to make data comparable between different benthic species. No adjustment seems to be necessary for planktonic foraminifera. Using a linear regression model, various studies have suggested that oxygen isotope values obtained from *Nuttalides truempyi* should be adjusted by adding 0.35‰ to 0.6‰ ([148; 178; 179] and references therein), with no correc-

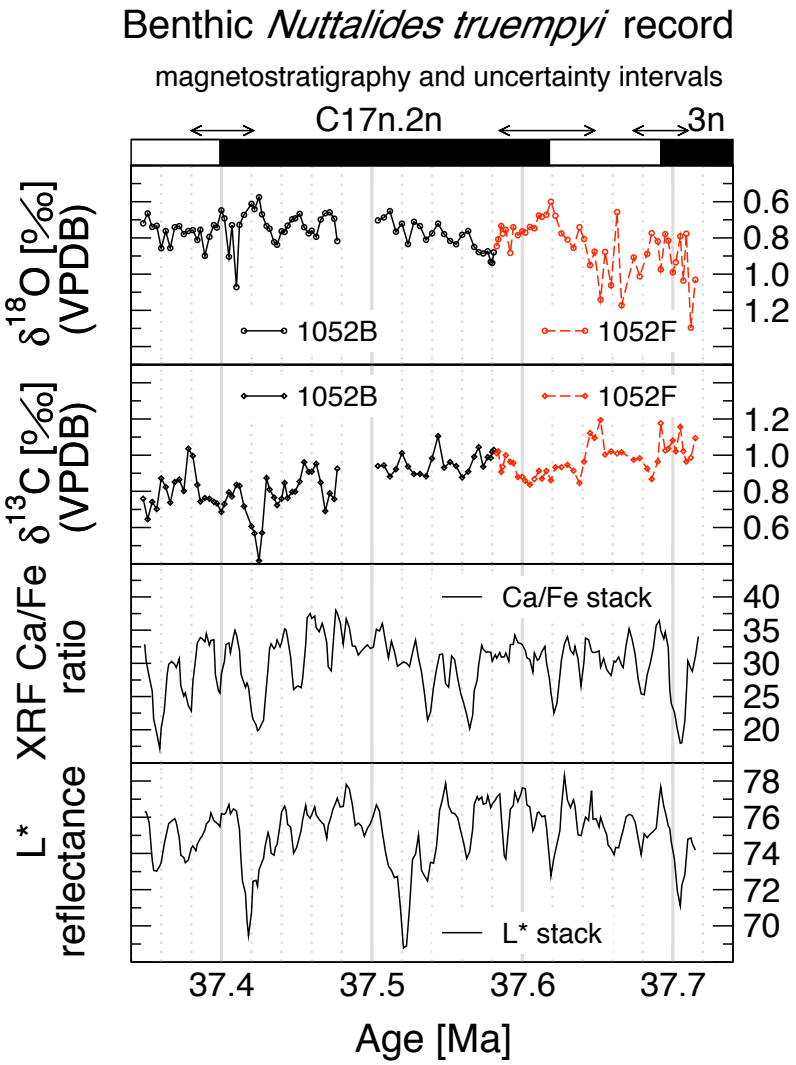

Figure 4.1: Stable isotope record from benthic species *Nuttalides truempyi*. This record is plotted on the time scale generated using the XRF Ca/Fe data. The magnetostratigraphic record and its uncertainty are shown for reference. For comparison, the two lower panels show the XRF Ca/Fe ratios and the reflectance parameter L*, which were introduced in chapter three.

tion necessary for carbon isotopic values. To stay consistent with previous studies, in this study a value of +0.4‰ is used to correct oxygen isotope values from *N. truempyi*. This value was also used in the study of Wade *et al.* (2001) [151].

Recently, Katz *et al.* (unpublished manuscript) conducted a study of species dependent offsets in isotopic values by statistically evaluating a large number of paired species measurements obtained from Paleogene material from ODP Site 1051, which is close to the site investigated here. It was found that 0.1‰ has to be subtracted from the oxygen isotope values obtained from *N. truempyi* to match those obtained from *Cibicidoides* spp., while a value of 0.34‰ has to be added to the carbon isotope values. Since previous studies [148; 178] established that *Cibicidoides* values should be corrected by adding 0.5‰ to the oxygen isotope values, and 0.0‰ to the carbon isotope values, this supports the adjustment of +0.4‰ for the oxygen isotope values. In light of the new results of Katz *et al.*, and in contrast to previous research, in this study carbon isotope values from *N. truempyi* are adjusted by adding 0.34‰. Throughout the remainder of this chapter the isotope values obtained from *N. truempyi* will be corrected by these adjustment factors. Later in this chapter a comparison will be made with data obtained from *Cibicidoides* spp., which will be adjusted by adding 0.5‰ to the oxygen isotope values, and leaving carbon isotope values unchanged with respect to the VPDB standard.

4.3.1 Comparison of *Nuttalides truempyi* and planktonic data

Wade *et al.* (2001) [151] studied planktonic and benthic foraminifera from ODP Site 1051 B, which is situated near the location from which material was recovered for this study (Site 1052). Wade *et al.* found very large, short term, amplitude variations in planktonic isotope values, reaching up to 1‰ in oxygen and 2.6‰ in carbon. Wade also generated stable isotope measurements for the samples discussed here, using the species *Globigerinatheka mexicana*. The planktonic record from Site 1051 was generated using the species *Morozovella spinulosa*. At Site 1052 this species becomes extinct in the core just below the interval studied here (Core 10).

Since *G. mexicana* is slightly deeper dwelling than *M. spinulosa*, isotope values given here were adjusted to represent sea surface conditions, and to allow comparison with the study of Wade *et al.* (2001) [151]. The adjustment values (from *G. mexicana* to *M. spinulosa*) are -0.28‰ for oxygen isotopes, and +0.77‰ for carbon isotope values

(Wade, personal communication). These data are shown in figure 4.2.

The complete record of Wade extends to ∼39.6 Ma, and shows the presence of variability at orbital frequencies (Wade, personal communication), using the age model developed in this study. As shown in figure 4.2, data from Site 1052 display very large and sharp transitions in the planktonic record, which are partly reflected in the benthic isotope record, but only with a very small amplitude. In particular, one can see two intervals in the record with a sudden shift in planktonic oxygen isotope values of ∼1‰ at around 37.6 Ma and 37.5 Ma. These are not reflected at all in either the carbon or the oxygen benthic record. Some possible implications of these findings will be discussed next.

4.3.2 Temperature estimates from benthic and planktonic oxygen isotopes and carbon isotope gradients

The stable isotope values obtained in this study allow the calculation of parameters that are relevant to interpretations of the late Middle Eocene climate system. The oxygen isotope values obtained from foraminifera depend on the isotopic value of the sea water from which isotope fractionation takes place, the local water temperature, species dependent biological fractionation effects, as well as subsequent diagenetic alteration. The isotopic composition of sea water depends on the global ice volume, and the local salinity of sea water.

In the absence of a detailed knowledge of all of these factors, several assumptions and estimates have to be made to attempt an interpretation for a given set of oxygen isotope values. First, diagenetic alteration of oxygen isotope values is assumed to be negligible. Even though the material recovered from Site 1052 seems to be well preserved, this assumption might seriously overestimate the true oxygen isotope values in the past (Pearson, 2001 [180]). Second, an assumption has to be made for the global ice volume, which preferentially locks up ^{16}O from the oceans. During the Eocene, assuming that there was no significant volume of continental ice, the global average oxygen isotope composition of the oceans has been estimated to be ∼-1‰ relative to the "Standard Mean Ocean Water" (SMOW) that is taken to represent today's average composition of the global oceans and is assigned a value of 0‰ (Shackleton and Kennett, 1975 [147]). The ∼-1‰ difference reflects the mixing into the ocean of the present-day ice sheets.

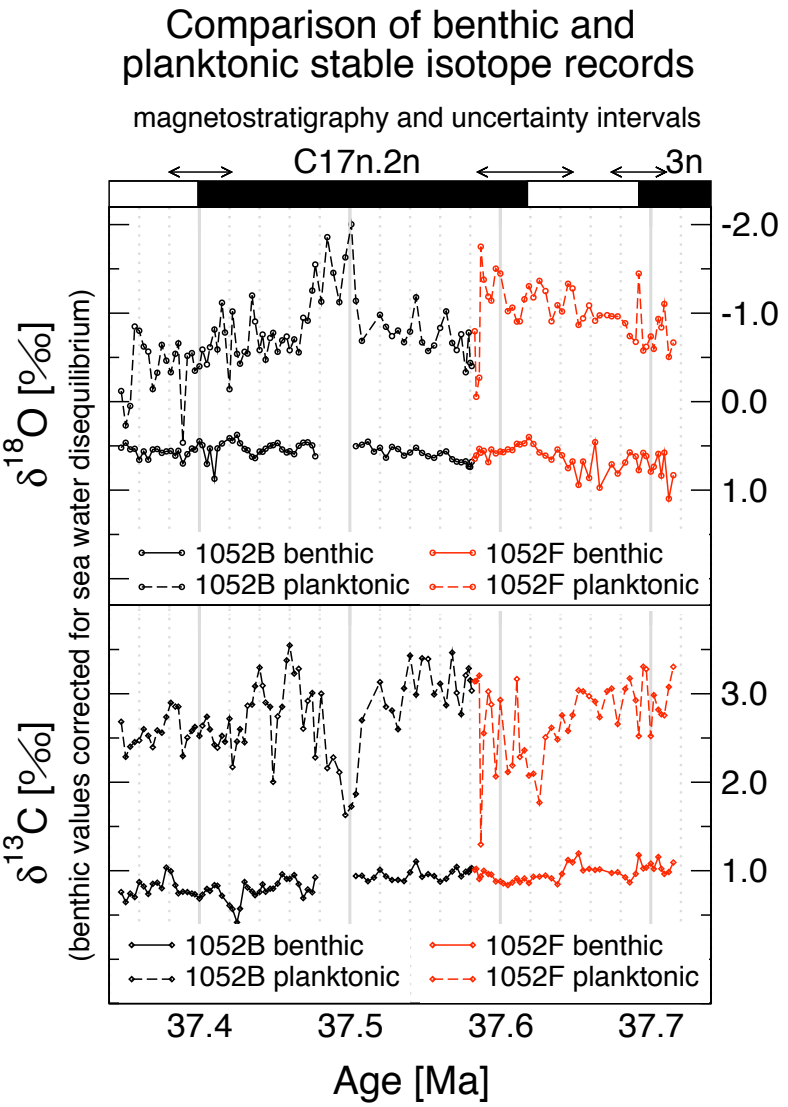

Figure 4.2: Comparison of benthic and planktonic stable isotope records from foraminifera. The benthic data are those shown in figure 4.1, but in this case corrected for sea water disequilibrium. The planktonic data were generated by Bridget Wade in Edinburgh (personal communication). The species used for the generation of the planktonic record was *Globigerinatheka mexicana*, with an adjustment of isotope values to *Morozovella spinulosa* as described in the text.

Third, an estimate is required for the effect of local salinity variations, which affect stable isotope ratios because of their association with evaporative surface effects and dilution with meteoric water, which has a different oxygen isotope composition. For benthic foraminifera, this effect is assumed to be negligible, although salinity variations can still occur as the result of changes in the source area for bottom waters. Generally, it is not known whether there were rapid and local variations in local salinity.

For planktonic foraminifera, which are expected to record surface water conditions, Zachos *et al.* (1994) [179] developed an empirical relationship to correct for effects of evaporation, precipitation, and atmospheric vapour transport in the open ocean on surface water oxygen isotope values as a function of latitude. Assuming that the zonally averaged meridional surface water gradient of oxygen isotope composition was similar to that of today, the application of the equation given by Zachos *et al.* leads to an estimate for the regional surface water $\delta^{18}O_{sw}$ of -0.36‰. This value takes into account the -1.0‰ difference due to negligible continental ice volume.

The values of -1.0‰ and -0.36‰ are both used to estimate sea surface temperatures from oxygen isotope values of planktonic foraminifera, while -1.0‰ is used for benthic foraminifera. Employing the value that results from the correction given by Zachos *et al.* results in an increase of temperature estimates by approximately 3 °C. Climate modelling studies of the Eocene suggest that the assumption of a similar latitudinal $\delta^{18}O$ sea water gradient in the oceans compared to today is feasible (Sloan and Rea, 1996 [181]).

To estimate water temperatures from oxygen isotope values, previous studies have developed empirical equations that calculate temperature as a function of carbonate and sea water oxygen isotope composition. One version of these that was used in the studies of Wade *et al.* (2001) [151] and Zachos *et al.* (1994) [179], and which is also employed in this study, is that of Erez and Luz (1983) [182]:

$$T°C = 16.998 - 4.52(\delta^{18}O_{cc} - \delta^{18}O_{sw}) + 0.028(\delta^{18}O_{cc} - \delta^{18}O_{sw})^2 \qquad (4.1)$$

where $\delta^{18}O_{cc}$ is the oxygen isotope measurement of foraminiferal carbonate, species corrected and adjusted to sea water equilibrium, and $\delta^{18}O_{sw}$ is the assumed value for sea water. Using this equation, and making the assumptions given before, palaeotemperatures were calculated from adjusted benthic and planktonic foraminiferal oxygen isotope measurements. These are shown in figure 4.3, together with the calculated surface to deep temperature difference.

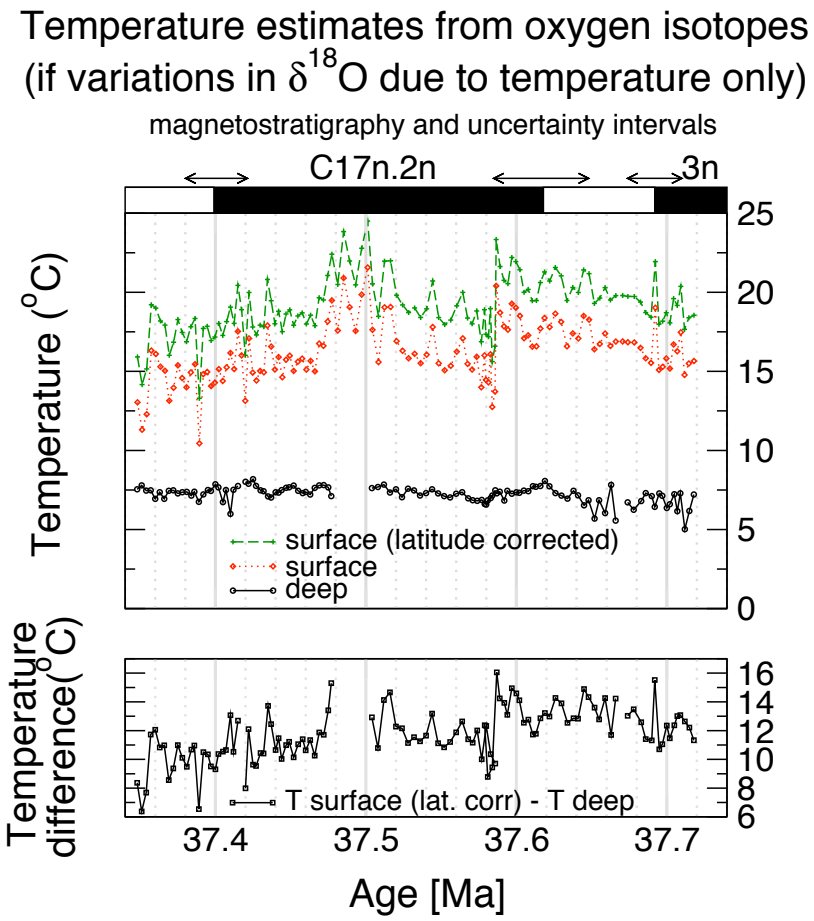

Figure 4.3: Temperature estimates from benthic and planktonic oxygen isotope data, using the assumption that variations in oxygen isotope values reflect changes in water temperature only (rather than salinity or ice volume). Benthic oxygen isotope values were species corrected for sea water disequilibrium effects (see text). Calculations were performed using the equation from Erez and Luz (1983) [182]. For the planktonic data, a second calculation was performed to correct for latitude dependent salinity variations in surface waters (Zachos *et al.*, 1994 [179]). The bottom panel shows the difference between latitude corrected surface water temperature and those estimated from the benthic record.

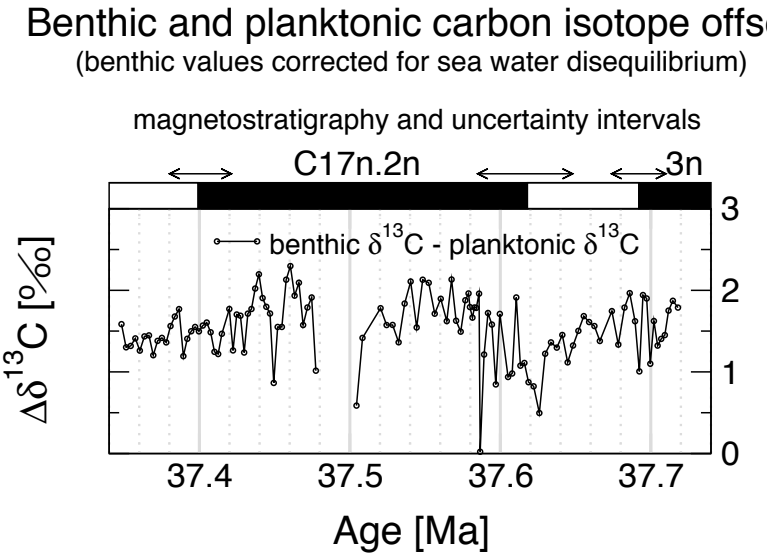

Figure 4.4: Difference between planktonic and benthic δ^{13}C from *Nuttalides truempyi* data. Benthic data were corrected for sea water disequilibrium.

The temperatures inferred from benthic oxygen isotope values generally lie between five and seven degrees centigrade (°C). This is comparable with other estimates [138; 179]. The temperatures obtained from planktonic foraminifera also agree well with previous studies, and lie between 17 and 22 °C, if the latitudinal correction of Zachos *et al.* is used. The data shown in figure 4.3 indicate a slight cooling trend of ∼2–3°C, starting in the middle of magnetochron C17n.2n. This is not the case for temperatures inferred from benthic foraminifera. This small difference in temperature evolution is evident in the lower panel of figure 4.3, which shows the temperature difference between surface and bottom water temperature estimates. However, these temperature estimates assume that the local salinity has not varied rapidly, and thus might not be correct.

More information about the oceanic system at this location might be gained by investigating the surface to deep carbon isotope gradient. Figure 4.4 shows the difference between the carbon isotope composition of surface and deep waters, as inferred from foraminifera. This shows that the surface to benthos carbon isotope gradient generally is between one and two per mil. After applying species dependent adjustments, this is similar to values obtained from the Pacific ODP Site 865B (Bralower *et al.* (1995) [138]). This is partly surprising, given that the estimated palaeodepth at Site 865B is 1300-1500m [183], but only 600 m for Site 1052 [100].

Climate modelling studies that were performed for the Eocene [184; 185] predict

Ekman driven upwelling, and large, highly seasonal, variations in continental run-off in the eastern North American margin in response to a precessional orbital forcing. Upwelling of deep water masses to the surface should result in planktonic isotope variations, where higher oxygen isotope ratios coincide with lower carbon isotope ratios. Figure 4.2 shows that the opposite is observed in the record from Site 1052. However, the high abundance of siliceous biogenic material in samples from Site 1052 would support this scenario.

Wade *et al.* (2001) [151] proposed various other explanations for the observed large scale fluctuations in planktonic isotope values, including a periodic large scale discharge of warm, low-salinity water from the Mississippi outflow entrained in the proto Gulf Stream that was transported from the Gulf of Mexico to Blake Nose (Pinet and Popenoe, 1985 [186]). If this is true, then the temperature estimates presented here will obviously be in error. On the other hand, Wade *et al.* argued that there must be at least some temperature contribution to explain the changes in isotopic composition, since a 2‰ shift in δ^{18}O would require a 4‰ change of salinity at constant temperature, which is probably not consistent with an open ocean setting as present at Blake Nose.

It is most likely that temperature changes, changes in salinity, as well as upwelling all played a role at Site 1052 in the Eocene, but further studies are needed to separate the individual contributions. One possibility would be the study of other proxies, such as Mg/Ca ratios in foraminiferal tests, which are assumed to reflect variations in calcification temperature, or Cd/Ca ratios, which can give palaeoproductivity estimates [173; 187].

4.4 Extending the benthic isotope record

The development of an astronomically calibrated relative time scale for the late Middle and Late Eocene based on XRF elemental data allows the combination of benthic stable isotope data presented in previous sections with benthic isotope data generated from Site 1052 by Shackleton and by Katz (unpublished data). Stable isotope measurements of various species of *Cibicidoides* were extracted from the data sets of Katz and Shackleton and combined with data from *Nuttalides truempyi* by applying a 0.5‰ offset to oxygen isotope values, and no offset to carbon isotopes from *Cibicidoides*. The resulting high-resolution data set is shown in figure 4.5. The shaded interval in the figure marks an unusual succession of events in both, stable isotope records, as well as in the

XRF data, and will be discussed in a separate section of this chapter. This interval will be marked on all subsequent figures for comparison.

Figure 4.5 also shows identified magnetochrons from Site 1052, and the XRF Ca/Fe data that were used to generate the age model. In addition, a compilation of benthic isotope values from various Pacific and high southern latitude sites is plotted, as given by Zachos *et al.* (2001) [152]. These data are mainly from the genus *Cibicidoides*, and were initially adjusted by adding 0.64‰ to the oxygen isotope values. The data shown on figure 4.5 were re-calculated with an adjustment of 0.5‰ to make data comparable. Carbon isotope values were not changed, neither in the study of Zachos *et al.*, nor in this study.

The ages used by Zachos *et al.* are based on the time scale of Cande and Kent (1995) [46], and are interpolated between magnetic reversals. The initial ages of Zachos *et al.* were recalculated to be consistent with those obtained by astronomical tuning in this study. However, it is not likely that the relative ages and stratigraphic relationships of data from the Zachos *et al.* compilation and those obtained from Site 1052 are identical. This is because the compilation of Zachos *et al.* contains data from many different locations, and the uncertainty of magnetic reversals from each site adds uncertainty to individual ages. Additional uncertainty is introduced by the linear interpolation between magnetic reversals. This has to be born in mind when comparing the data from the compilation and those from Site 1052. Small scale effects of this uncertainty were slightly suppressed by using the five point running mean as given by Zachos *et al.*

The data shown in figure 4.5 represent the longest high-resolution astronomically calibrated stable isotope time series from the Eocene yet, and several very interesting features are apparent. First, it is clear that the high-resolution record shows a much larger variability than what was observed in previous, lower resolution studies. This might result from different sampling resolutions, but shows the importance of working with high-resolution data. Apart from an unusual interval that is marked on figure 4.5, the trend in oxygen isotope values from Site 1052 remains relatively stable from 37.7 to 35.5 Ma, before oxygen isotope delta values gradually increase by almost 1‰ towards the latest Eocene. Carbon isotopes show a less steady trend, with values of between 1 to 1.5‰ in the late Middle Eocene generally increasing to values around 1.5‰ in the latest Eocene. Again, there is a strong excursion event visible in the younger part of chron C17n.1n, which will be discussed in more detail in section 4.7 of this chapter.

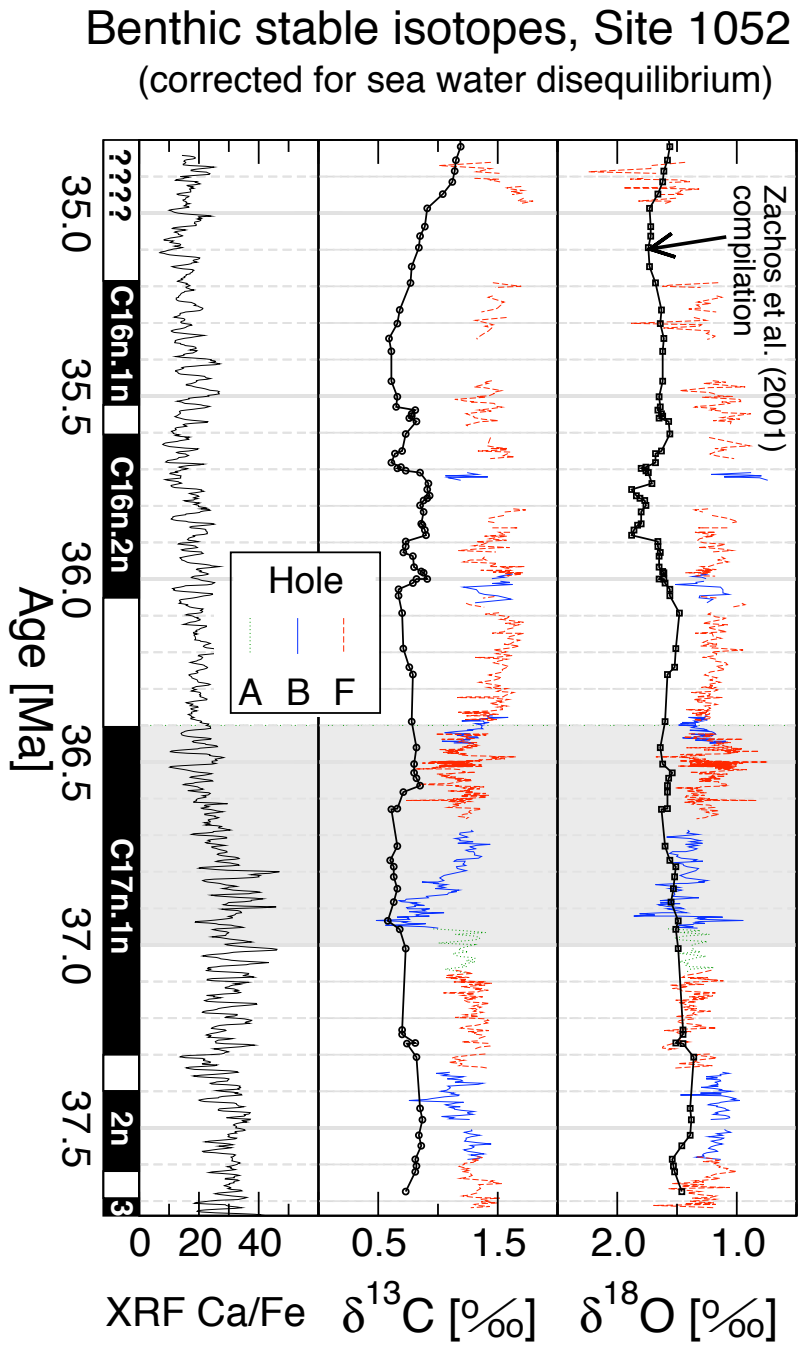

Figure 4.5: Extended stable isotope record from *Cibicidoides* spp. and *Nuttalides truempyi*, and XRF Ca/Fe ratios. All isotope data were corrected for sea water disequilibrium using species specific adjustment factors described in the text. Also shown is the age adjusted data compilation of stable isotope data from Zachos *et al.* (2001)[152]. The shaded interval marks a distinct stable isotope excursion event.

Throughout most of the record, positive excursions in the oxygen isotope data coincide with positive excursions in the carbon isotope data. The data from Site 1052 show a significant offset for both oxygen and carbon isotopes if compared with the compiled data of Zachos *et al.*, which are generally from locations with deeper palaeobathymetries. From ~37.7 Ma to ~36.0 Ma the oxygen isotope values from Site 1052 are lighter by less than 0.5‰, but begin to deviate more strongly at around the base of C16n.2n, before showing a more positive trend that is not evident from the lower resolution data compilation of Zachos *et al.* Carbon isotope data from Site 1052 show a much stronger and more variable offset, with a consistent positive offset of approximately 1‰ from the top of magnetochron C17n.1n to approximately 35 Ma on the newly developed time scale of this study. In the late Middle Eocene, this positive offset was less than ~0.5‰. The direction of this offset can be expected, as shallower and warmer water masses generally lead to a positive offset. The magnitude of this offset is in good agreement with inter-oceanic offsets observed across the present day oceans [188].

Although most of these differences can probably be explained in terms of different water depths at individual sites during deposition, a significant component, and particularly the higher frequency variations, might be related to changes in ocean circulation patterns around Blake Nose, which were implicated by the planktonic foraminifera stable isotope data. This is supported by the trend and transition discussed for the XRF data in the previous chapter, which also lie within the interval that is shaded in figure 4.5. This is clearly a time of critical transitions at Site 1052 and will be discussed separately in section 4.7.

4.5 Obliquity variations in the benthic oxygen isotope record

While astronomically driven variations have been clearly demonstrated in the XRF Ca/Fe record, a detailed analysis is more difficult for the combined stable isotope record. Spectral analysis methods were applied to oxygen and carbon data, but sharp transitions in the data prevent the determination of phase lags and coherencies when applying cross-spectral analysis. The oxygen isotope data show some spectral power at the obliquity frequency, but only a very weak to non-existent climatic precession component. The signal in the carbon isotope data is even more noisy, and thus excluded from further analysis. However, one can directly compare the oxygen isotope data with the XRF data, for which a more detailed analysis was possible, as shown in section 3.9 of the

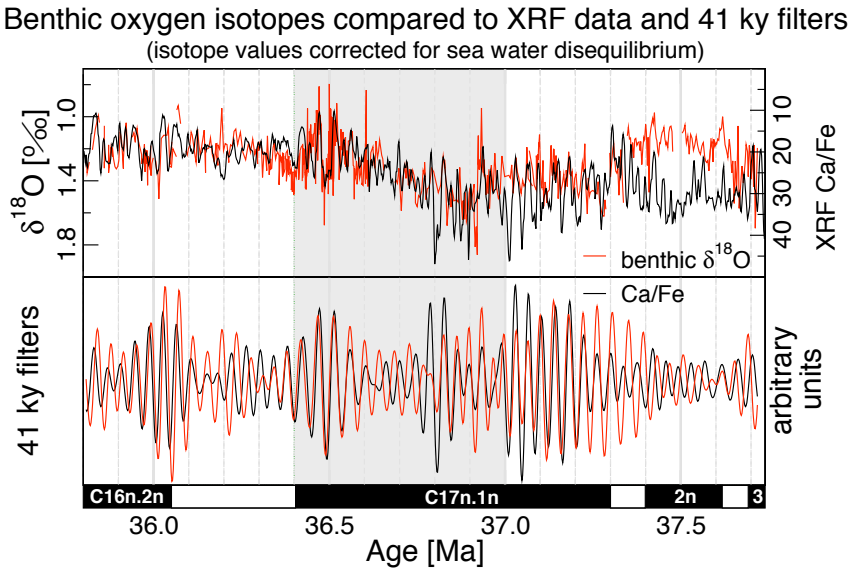

Figure 4.6: The evolution of benthic oxygen isotope values and the XRF Ca/Fe ratio, including the interval of the isotope excursion event (see section 4.7 and figure 4.8). Note that the XRF data are reversed on this plot.

previous chapter. This comparison is shown in figure 4.6 for the interval where isotope measurements were continuous enough to allow filtering in the time domain.

Figure 4.6 shows the oxygen isotope data over the interval where the sampling record is continuous, together with the XRF Ca/Fe data. For times younger than ~37.3 Ma on the astronomically calibrated time scale, the match between the two different curves is astonishing. Individual cycles that are present in the XRF data are clearly visible in the oxygen isotope record. This supports the age model as developed in this study, since it was generated completely independently from the isotope record. It also supports the underlying assumption that changes in the XRF data at Site 1052 are related to changes in the climate system. Even more astonishing, for times younger than ~37.3 Ma the XRF data also mirror to a high degree the more gradual background trend in the oxygen isotope data across the transition interval. This has significant implications for the interpretation of causal relationships, which will be discussed at a later stage. Why the match is not good for older times is not clear at present. It is possible that the XRF Ca/Fe record at ~37.5 Ma is not of high fidelity (see figure 3.5), given that the XRF iron counts are quite low and possibly distorted by noise at this time, while the Ca counts also seem less convincing than during other time intervals.

The lower part of figure 4.6 shows bandpass filters that were applied to the oxygen isotope as well as the XRF data in order to extract variations at the main obliquity

frequency. The filter used has a central frequency of 0.025 ± 0.006 cycles/ky. At this period, both records match very well, too, demonstrating the presence of a quite strong obliquity signal in the oxygen isotope values that can be identified in the unfiltered data above. There does not seem to be any significant lead or lag of one data set over the other, and low values in the Ca/Fe ratio correspond to low oxygen isotope ratios. It would be interesting to be able to separate the individual contributions and phase relationships between calcium and iron, and oxygen isotopes, to establish a causal relationship. Unfortunately, this is not possible at present, because calcium, iron, as well as oxygen isotope values co-vary with no discernible phase lag. However, one important observation is that the ramp shaped transition in the XRF data set is caused by an increase in the iron counts, while calcium counts retain their average background intensity (see figure 3.5 above $\sim$60 rmcd). This will be discussed further in section 4.7.

An important observation can be made with respect to the relationship between the oxygen isotope and XRF Ca/Fe ratio climate proxies. Figure 4.6 demonstrates that, at least at the obliquity frequency, low (light) oxygen isotope values are correlated with low Ca/Fe count ratios. This either suggests an increase in carbonate content with colder benthic temperatures, or an increase of iron counts with warmer benthic temperatures, if the ice volume is assumed to be negligible during late Middle Eocene times.

4.6 Isotope data from bulk fine fraction

The unpublished data set of Shackleton from Site 1052 also contains a series of bulk fine fraction stable isotope measurements that span approximately 800 ky from $\sim$36.6 Ma to $\sim$35.8 Ma. Although the use of bulk sediments for stable isotope analysis has the great advantage of being very fast, serious doubts remain as to their interpretation in terms of climatic variations and the implications of δ^{13}C bulk measurements on the global organic and inorganic carbon budget. Some of the problems that arise in the interpretation of stable isotope measurements from bulk sediments were discussed by Broecker and Woodruff (1992) [189], and a thorough review was given by Shackleton and Hall (1995) [190]. Unfortunately, no stable isotope measurements from planktonic foraminifera are available from Site 1052 over this interval, hence it is not possible at present to investigate whether the bulk fine fraction measurements reflect surface conditions, or are significantly different from the planktonic record. Regardless of the detailed interpretation of bulk fine fraction data, they could prove useful for correlation

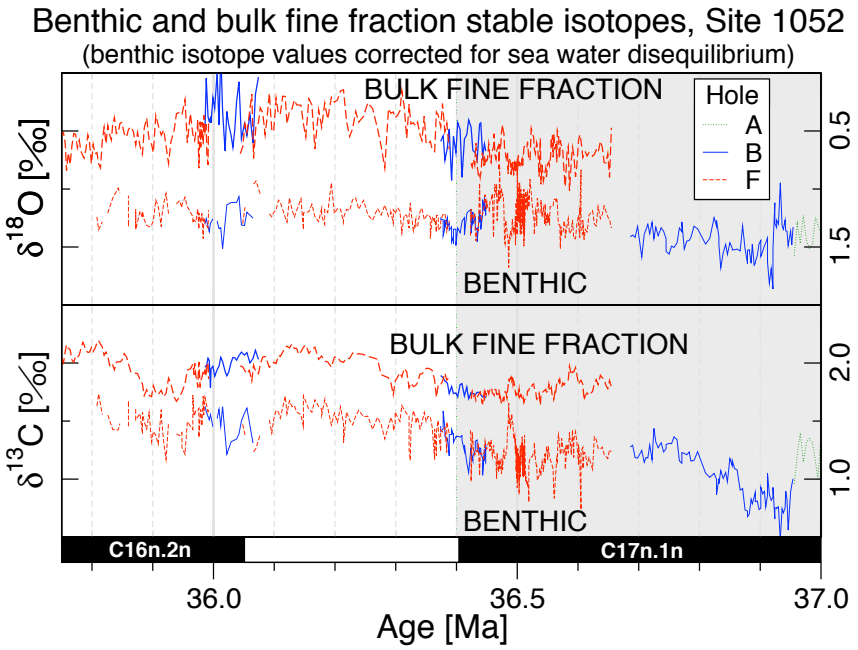

Figure 4.7: Benthic isotope values and bulk fine fraction measurements available. The average offset between benthic oxygen isotopes and the bulk record is approximately 0.7‰. The average offset of the carbon isotope values is ~0.5‰.

work, particularly since an astronomically calibrated time scale is now available from this study. The bulk fine fraction measurement data are shown in figure 4.7.

At Site 1052, stable isotope measurements obtained from the bulk fine fraction are on average ~0.8‰ lighter for oxygen, compared to the benthic data, and ~0.5‰ heavier for carbon isotopes. These offsets are significantly smaller than those seen in the planktonic record from an older interval, as shown in figure 4.2. The exact nature of the relationship between isotopic measurements from bulk sediment samples and those from picked planktonic foraminifera still needs to be established. The bulk fine fraction carbon isotope values are similar to those obtained by Shackleton and Hall (1984) [191]. Figure 4.7 shows that variations in the benthic isotope record, which were shown to contain at least some orbitally driven component in figure 4.6, are also reflected in the bulk measurements. This is particularly evident in the uppermost ~300 ky of magnetochron C17n.1n.

4.7 Unusual stable isotope and lithological events at Site 1052

In the previous discussion of stable isotope data the shaded interval shown in figure 4.5 has been excluded. It will be discussed in detail in this section, since it is possible to

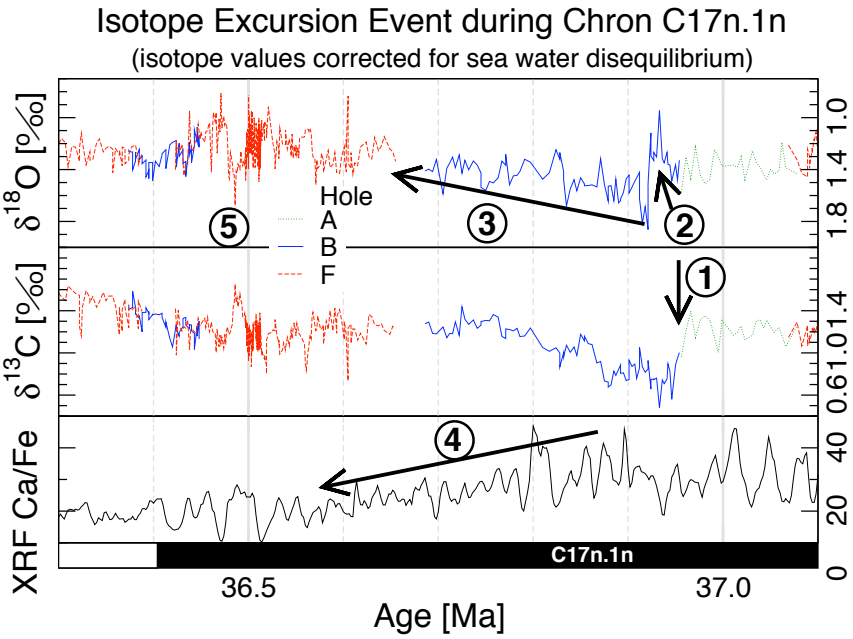

Figure 4.8: This figure shows an newly identified isotope excursion event during magnetochron C17n.1n. Circled numbers indicate the interpreted timing of events and are discussed in the text.

observe a very interesting succession of events in the upper two thirds of magnetochron C17n.1n, extending from approximately 37 Ma to 36.4 Ma on the time scale developed in this study. Figure 4.8 shows this time interval in detail, allowing an interpretation of the possible timing of events. Circled numbers on this figure correspond to individual features that are discussed here.

The benthic stable isotope data follow their longer term steady trend with only little variations up to an age of approximately 37 Ma. At around 36.95 Ma a strong excursion is visible in the carbon and oxygen isotope records. The carbon isotope values undergo a ~0.8‰ shift towards lighter values within only several thousand years. Unfortunately the sampling track was switched from Hole A to Hole B at the midpoint of this transition. However, a detailed examination of the XRF data used to construct the rmcd scale reveals that the splicing of data from the two holes is probably correct.

It appears that this sudden shift in carbon isotope values, marked as ①, precedes a small shift towards lighter values in the oxygen isotope data, which decrease by ~0.4‰ over approximately 20 ky, before values move towards more positive values, overshooting the initial baseline to create a sudden shift to a maximum value of 1.8‰. These two events are marked as ② on figure 4.8. Both events ① and ② seem to occur at the same time as a disturbance that is visible in the XRF Ca/Fe ratio. After these two initial

events both carbon and oxygen isotope values slowly move back to their initial baseline values over approximately 200 ky, marked on figure 4.8 as ③.

This recovery in the isotope baseline values seems to be followed approximately 50 ky later by a steady change in the XRF Ca/Fe ratios, marked as ④. Scrutinising the individual XRF counts for Ca and Fe in figure 3.5 of the previous chapter (between ∼65-55 rmcd) seem to suggest that this ramp shaped transition in the XRF Ca/Fe ratios is mostly caused by an increase in the Fe counts. After this transition, Fe counts remain higher on average than before this transition. Thus, although the carbon and oxygen isotope values show an initial sharp shift with a subsequent recovery, the XRF data only show a change across the transition interval but do not recover back to the initial baseline values. In addition, it is exactly this interval that marks a change in the orbital signature recorded in the XRF data (see section 3.7.2 in the previous chapter), with the climatic precession signal in the XRF data being significantly weaker above this transition.

After the recovery of the stable isotope values to the baseline level there is a ∼150 ky long period with increased large and high-frequency variations in the oxygen and carbon isotope data. It is not clear whether this period, marked as ⑤, is part of the chain of events that follow the initial isotope excursions, or whether it is independent.

The very close match of the XRF Ca/Fe data and the benthic oxygen isotope measurements visible in figure 4.6, in terms of their evolution over this transitional interval, as well as on the obliquity cycle level, strongly suggests a direct coupling between these two types of data. Indeed, if the hypothesis that the Fe concentration in the sediment reflects terrestrially derived material is correct, than the measurements obtained would imply that warmer temperatures, as indicated by lower benthic oxygen isotope ratios, might lead to an increased run-off carrying this material, which in turn increases the proportion of Fe in the sediment. However, it is not clear why the XRF Ca/Fe ratios do not recover after the transitional event, as could be expected. The very strong initial excursion in the carbon isotope values can be interpreted as either a sudden change in the strength of the biological pump, or as a change in the water masses bathing this part of Blake Nose. Alternatively, Sigurdsson *et al.* (2000) [143] report a strong activity of volcanism during the Middle to Late Eocene, based on frequent ash layers observed in Site 999 of ODP Leg 165. However, figure 3.5 shows that at Site 1052 there is no volcanic ash layer observed during this interval. Several studies report evidence for intense cos-

mic bombardment during the Middle and Late Eocene [139–142], however, the earliest proposed tektite horizon occurs within magnetochron C16 and the main event is found within chron C13, post-dating the transition event found here.

Previous interpretations for the oceanic circulation system around Blake Nose [151; 185; 186] certainly suggest that very fast changes in the surface water circulation patterns are possible as the result of a changing path of the proto Gulf Stream. Given that the palaeodepth estimate for Site 1052 during the Eocene was only ~600 m, one could invoke a local change in circulation conditions and principal water mass sources, combined with changes in terrestrial run-off that result from simultaneously occurring ocean temperatures, to explain some, but not all, of the features of this record. However, given that a continuous obliquity signal, as recorded by the XRF data, is more indicative of changes of the global ocean system, the initial trigger for the carbon isotope event might well have been related to changes in the ocean circulation system elsewhere.

To investigate this succession of events further it will be necessary to obtain high-resolution records over this interval from different ocean basins. This is scheduled to be investigated with material to be recovered on the forthcoming ODP Legs 198 and 199.

4.8 Conclusions based on stable isotope data

The stable isotope data reported in this study, in conjunction with a newly generated astronomical calibration, show that the variability of oxygen and carbon stable isotopes was larger than what previous studies suggested. Although this is mostly a function of sample resolution, an unusual isotope event was identified. This event might be related to a 1‰ oxygen shift described by Miller (1992) [149], but shows the detailed succession of events in stable isotope and lithological data at high-resolution for the first time, as well as providing the longest astronomically calibrated high-resolution stable isotope record for parts of the late Middle to Late Eocene time yet.

A correlation was found between low oxygen isotope delta values and low XRF Ca/Fe ratios. Comparing the planktonic and benthic records, very large variations in oxygen and carbon isotope values observed in the planktonic record by Wade are not reflected in the benthic isotope data. This suggests that the variations in data from the surface ocean at Site 1052 are related to more local changes in upwelling, surface currents, and/

or salinity. In contrast, the close match of lithological data and the evolution of benthic stable isotopes does suggest a close link between the two. These two contrasting observations will need to be resolved as soon as data from different Atlantic locations, and from other ocean basins, become available.

Chapter 5

Extracting astronomical parameters from geological data

5.1 Introduction

This chapter presents two studies of how it is possible to extract Earth and solar system parameters from the geological record to improve and constrain existing astronomical models. One of the assumptions that is made, when astronomically calibrating a geological time scale, is that one can match geological data to a known astronomical solution. Unfortunately, there are many problems that arise from this assumption. These problems can be classified into two categories: the determination of how an assumed forcing is transferred through Earth system processes into the geological record, and the need to determinate parameters that are required to generate astronomical calculations in the first instance.

The process by which the climatic forcing by incoming solar radiation at a particular location and time is transferred into the geological record is not very well known. This has lead to a vigorous scientific debate about the exact timing of changes in geological data with respect to a given forcing, particularly for the last few glacial cycles. It is now clear that the climate system can respond to an imposed orbital forcing on a very local scale. Contrasting views on the nature of timing and lags between forcing and the geological recording have been given, for example, by Henderson and Slowey (2000) [32] and Herbert *et al.* (2001) [33]. Since geological records at a given site can be influenced by a combination of forcings from many different locations, and with varying time lags, this is a very difficult problem, and requires a multi-proxy approach

using data from many different sites. An important contribution of how it is possible to separate the effects of multiple forcings in geological records was recently given by Shackleton (2000) [68].

However, apart from a lack of detailed knowledge about the climate and ocean system processes that define the transfer function from forcing to recording, there is an even more fundamental problem in that there are potentially time varying parameters that go into the calculation of astronomical solutions, and thus lead to uncertainties in the astronomical calculations that are used as an assumed known forcing. Parameters that need to be determined include tidal dissipation terms and changes of the dynamical ellipticity of the Earth that arise from a redistribution of mass, for example due to changes in the distribution and volume of ice and changes in the mantle convection pattern. Tidal dissipation and dynamical ellipticity directly control the evolution of astronomical frequencies over time.

In addition, Laskar (1990) [85] has shown that the evolution of the solar system is chaotic. This is related to the presence of resonances that arise from the interaction of the different planets. This feature, together with additional uncertainties in the knowledge of quantities that define the astronomical solutions, such as the masses, positions and momentum of different planets, means that detailed calculations of the Earth's eccentricity, obliquity and climatic precession become less reliable as one goes back in time. Laskar (1999) [89] attempted to show the limits and uncertainties that are inherent in astronomical calculations. The validity of current astronomical models is estimated to be of the order of $\sim$10-30 My [85], although average frequencies might be valid over a longer time span.

Thus, if astronomical calculations are to be used to generate astronomically calibrated geological time scales, an attempt has to be made to constrain parameters that are needed to define orbital solutions with data extracted from the geological record. This process leads to a potential circularity, since the extraction of astronomical parameters from geological data requires these data to be on a high-resolution time scale. If astronomical calculations are used to generate this time scale, features of this particular astronomical solution might be transferred into the geological data. Hence, extreme care has to be taken to make the parameters extracted from geological data independent of orbital solutions used to create a geological time scale in the first instance.

The first section of this chapter introduces a new method that has been employed

to extract from geological data the most likely average values for tidal dissipation and dynamical ellipticity over the last 25 My. In addition to giving constraints for astronomical calculations, this research also provides potentially valuable information for mantle convection models. Parts of this research have previously been published by Pälike and Shackleton, 2000 [155]. Data that were used in this study are archived in electronic form [155].

Very recently, a new astronomical calculation was performed by Laskar *et al.* (2001, unpublished). Section 5.3 of this chapter compares and evaluates this new calculation with the orbital solution of Laskar *et al.* (1993) [86] and with geological data to decide which solution is better supported by the data. The main difference between long term orbital calculations arises from the effects of the chaotic nature of the solar system. The fingerprint of this chaotic nature is particularly well reflected in long term amplitude modulation patterns for the orbital elements, and includes the effects of switching resonance terms, as discovered by Laskar *et al.* [85; 86; 89]. The findings from this research thus not only help to extend and constrain the validity of astronomical computations, but also have important repercussions for the evolution of the solar system as a whole.

5.2 Extracting tidal dissipation and dynamical ellipticity from geological data

Recent attempts to tune geological time scales to orbital cycles rely on matching features in proxy records to astronomically calculated eccentricity, obliquity, precession and insolation cycles (the "target" curve). The calculation of these target curves was first performed by quasi-periodic expansions of fundamental frequencies by Berger (1978) [38], and by direct numerical integration by Laskar (1988)[84], who recognised the chaotic nature of the planetary system (Laskar, 1990 [85]). Following Quinn *et al.* (1991) [97], Laskar *et al.* (1993) [86] refined their calculations by including a tidal dissipation term, and showed that the exact position of insolation peaks in time depends on the parameters chosen for the dynamical ellipticity and tidal dissipation (the "Earth model"). It is necessary to constrain this Earth model in order to develop more accurate time scales for the pre-Pliocene based on astronomical target curves (Lourens *et al.*, 1996; Laskar, 1999) [89; 154]. These parameters have implications for geophysical models of the Earth and the history of the Moon.

Work reported in this section makes use of exceptionally well preserved cyclical magnetic susceptibility data obtained from Ocean Drilling Program (ODP) Leg 154 [192; 193] that have been astronomically tuned [53; 55; 194] to extract and constrain the parameters of the Earth model over large parts of the last 25 My. A significant advantage of the material recovered during Leg 154 was the detailed high-resolution stratigraphic correlation of data not only from different holes at the same site, but also between sites. This allowed the identification of sedimentary breaks and the construction of a continuous geological record. The work of Shackleton *et al.* (1999) [55] presented a long astronomical calibration of geological material from Leg 154 that was evaluated statistically by a variety of methods, and exploits the high-resolution correlation of many data sets from different holes.

A new method is developed here, based on using the interference pattern between geological data and a given astronomical solution, to constrain the possible range of parameters for different time intervals. This method makes it possible to compensate for the effects of choosing a tuning target to generate the geological time scale in the first instance, thus avoiding a potential circularity. One aim is to find those parameters in the Laskar *et al.* (1993) [86] set of astronomical solutions that best fit the geological data, and to evaluate the range of uncertainty associated with this estimate. The effect of tidal dissipation on the obliquity and precession frequencies leads to longer average periods as one approaches the present [81; 95; 195]. The absolute change in period length for obliquity and precession does not change in the same proportion.

The following discussion is concerned with existing observational constraints and astronomical theory, while section 5.2.4 introduces the interference method used for analysis. Section 5.2.11 describes the results of analysis and modelling using the ODP Leg 154 data, and section 5.2.14 discusses the implications of the findings obtained.

5.2.1 What causes tidal dissipation?

The Sun and the Moon induce tidal stresses leading to deformations of the Earth and the Moon. The delay of the Earth's non-elastic response to tidal stresses leads to a displacement of the tidal bulge with respect to the Earth-Moon axis. The torque created by the gravitational attraction of the tidal bulge towards the Moon leads to an exchange of angular momentum between the Earth and the Moon, with time increasing forward resulting in a slowly decreasing spin velocity of the Earth, an increase in the lunar dis-

tance, and a change in the lunar rotational velocity (Lambeck, 1980 [88]). This tidal energy dissipation results in a change of the length of day and, due to the change in spin velocity, to a redistribution of mass on the Earth that results in a changing dynamical ellipticity.

Other factors that can alter the climate and angular momentum of the Earth, and hence its rotational characteristics, are changes in sea level, ice loading leading to a visco-elastic response of the crust and upper mantle, accretionary core-growth, and mantle convection [88; 95; 196–204]. The implications of geological data for the Earth's orbital evolution were discussed by Williams (1998) [205], and deSurgy and Laskar (1997) [87].

5.2.2 Current estimates for tidal dissipation

The current value of lunar recession is 3.82 ± 0.07 cm/year (Dickey *et al.*, 1994 [206]), and would imply that the Moon was near the Roche limit at around 1.5 Ga [207]. The Roche limit is the distance between a planet and a satellite where the gravitational pull of the planet is larger than the self-gravitation of the satellite, leading to the fragmentation of the satellite. This is not compatible with constraints for the age of the Moon, obtained, for example, by radiometric dating of the crystallisation age of lunar highland rocks [208] (4.5×10^9 years ago).

Currently there are several approaches of constraining the Earth model parameters [88] to address this paradox. While present day estimates for the lunar recession and rotational velocity can be directly obtained from lunar laser ranging methods [206; 209], other estimates are obtained from astronomical observations of the Moon, Sun and Mercury, and ancient solar eclipse observations [88]. Geological observations of laminated tidal sediments and coral growth patterns have been used to estimate tidal periods and the length of day from sediments ranging in age between 250 and 900 Ma [205; 207; 210–213].

The effects of chaotic behaviour of the solar system preclude the calculation of accurate orbital solutions further back in time than $\sim$30 Ma [86; 89]. From the point of view of astronomical tuning this suggests that it is only possible to constrain the Earth model parameters over roughly this time scale, since the target curve approach will become invalid beyond this interval with present models [89].

An evaluation of the orbital model was attempted by Lourens *et al.* (1996) [154], who

compared different astronomical solutions with sapropel thickness observations, and with a Mediterranean marine proxy record, over the Plio-Pleistocene interval. They concluded that the astronomical solution that best fitted their geological data is one that uses the Laskar 1993 algorithm [86] with present day values for tidal dissipation and dynamical ellipticity. However, they also conceded that a model with no tidal dissipation does also reflect all of their sedimentary cycle patterns, and shows obliquity lags close to those expected. They rejected solutions that were computed using different astronomical algorithms and solutions with values that would be expected during glaciations.

The study reported here tries to improve their findings by using data covering a longer time interval (25 My), and by employing a more quantitative approach that allows the estimation of associated uncertainties. In order to improve on the findings of Lourens *et al.* [154] this study will have to: a) achieve the same sensitivity in analysis as the cycle-by-cycle comparison approach of Lourens *et al.* [154], b) reproduce their results over the last $\sim$5 My, with associated error bars, and c) improve the precision by extending the time interval of observation.

5.2.3 Astronomical frequencies and parameters

The physical parameter of interest is the temporal evolution of the precession constant p, which allows the computation of other parameters, such as the length of day and the lunar recession rate [88; 95]. As outlined in chapter one, obliquity and precession frequency components can be approximated in the form $p + s_n$ and $p + g_n$ respectively, where s_n and g_n are fundamental frequencies arising from the planetary perturbations [85; 95]. In contrast, all eccentricity frequencies and amplitude modulation terms are of the form $g_n + g_m$, and are thus independent of p.

Although s_n and g_n undergo quasi-periodic changes over time, they can be assumed to be invariant for any two astronomical solutions that only differ in the Earth model parameters, as long as the dynamical ellipticity does not lead to a resonance between the precession frequency and a secular resonance term related to the perihelion of Saturn and Jupiter, as discovered by Laskar (1990,1993) [85; 86]. This result has been discussed previously [198–200; 202].

Any change in tidal dissipation or dynamical ellipticity will hence influence p but not s_n or g_n. The measured present day value for p is $50.290966\,''/a$ [214]. The value of p

Eccentricity		
term	frequency (″/a)	Period (ky)
$g_2 - g_5$	3.1996	406.182
$g_4 - g_5$	13.6665	94.830
$g_4 - g_2$	10.4615	123.882
$g_3 - g_5$	13.1430	98.607
$g_3 - g_2$	9.9677	130.019

Obliquity		
term	frequency (″/a)	Period (ky)
$p + s_3$	31.6132	40.996
$p + s_4$	32.6799	39.657
$p + s_3 + g_4 - g_3$	32.1827	40.270
$p + s_6$	24.1277	53.714
$p + s_3 - g_4 + g_3$	31.0981	41.674
$p + s_1$	44.8609	28.889

Climatic precession		
term	frequency (″/a)	Period (ky)
$p + g_5$	54.7064	23.690
$p + g_2$	57.8949	22.385
$p + g_4$	68.3691	18.956
$p + g_3$	67.8626	19.097
$p + g_1$	56.0707	23.114

Table 5.1: Principal frequencies in the astronomical solution La93$_{(1,0)}$ analysed over the last 4 My, reproduced from [89].

varies slowly around its average value of $\sim 50.4712\,''/a$, derived from a frequency analysis of orbital calculations over the last 18 My without tidal dissipation [86]. Table 5.1 shows the major eccentricity, obliquity and climatic precession components over the last 4 My, adopted from Laskar (1999) [89].

As a first order approximation, one will try to find one set of average Earth model parameters that best fits the geological data. In the Laskar [86] algorithm the tidal dissipation is parameterised with respect to the current day value of the rate of change in the mean motion of the Moon $\dot{n}_{M0}/n_{M0}$, such that Laskar's tidal dissipation parameter is the ratio between the assumed change in $\dot{n}_{M0}/n_{M0}$ and its present day value.

The dynamical ellipticity of the Earth can be defined as $E_D = \frac{(C-A)}{C}$, where C and A are the principal moments of inertia of the Earth. In order to keep the angular momentum νC conserved, where ν is the angular velocity of the Earth, Laskar [86] defined the parameter $\gamma = \frac{E_D}{\nu}$. Changes of this value are incorporated into the algorithm of Laskar [86] in the form of the normalised parameter $\frac{\gamma}{\gamma_0}$, where γ_0 is the present day nominal

value. From now on Laskar's solutions with different values for the parameterised dynamical ellipticity ell and tidal dissipation td will be denoted by La93$_{(ell,td)}$.

Critically, when $ell = 0.9977$, the precession is driven into resonance with a Jupiter-Saturn perturbation term, and the effects of dynamical ellipticity on the precession constant p will strongly deviate from a linear form when $ell \lesssim 0.9980$ [86]. The effect of ice sheets on the astronomical frequencies has been investigated first by Berger *et al.* (1990) [215]. They show a minor contribution because of the characteristic time scales of ice sheets and isostatic rebound. The possibility that ice-age cycles could place the Earth system into resonance with the Jupiter-Saturn forcing was first raised by Laskar *et al.* (1993) [86].

Subsequent work [196; 197; 200–202] showed that this conclusion was only valid for very high viscosity Earth models, and that published viscosity models yielded perturbations to the dynamical ellipticity that are an order of magnitude smaller than estimates of Laskar *et al.* [86], obtained by assuming a rigid Earth. This subsequent work yields values for the dynamical ellipticity that are lower than the threshold necessary for resonance to occur. Forte and Mitrovica (1997) [202] suggested that changes in mass distribution due to mantle advection would have led to an increase in ell over the last ~20 My. They were the first to point out that this effect works in the opposite direction to tidal dissipation. This was also discussed by Laskar (1999) [89].

In this study it will be assumed initially that a linear relationship can be used to describe the relationship between ell and the rate of change of p. It is difficult to assess how fast changes in the parameters ell and td can occur, and it is assumed that they are slow over geological time. It was shown [198; 200] that an assumption of average values is probably justified in the case of glacial cycles. This assumption is not necessarily true for convection related effects, and breaks down if the planetary system enters resonance.

A first order linear approximation for the rate of change in p, using present day values for tidal dissipation and dynamical ellipticity, leads to a value of $m \approx -2.365 \times 10^{-8}\,''/a^2$, where the evolution of p over time is of the form $p(t) \approx p_0 + mt$, with time t positive for the past (Laskar, personal communication). For example, 10 million years before present the strongest obliquity component, with a frequency of $\sim 31.6132''/a$ (40.996 ky period), would have been

$$31.6132''/a + 2.365 \times 10^{-8}\,''/a^2 \times 10^7 a \approx 31.8497''/a$$

(40.691ky period). This corresponds to a change of approximately 0.75%. Similarly, the strongest precession component with a frequency of $54.7064''/a$ (23.690ky period) would have been $54.9429''/a$ (23.588ky period), a change of ∼0.4%. This demonstrates how a change in p has a proportionally larger effect for lower frequencies. In both cases, the total number of cycles after 10 My, compared to a solution with invariant p, would have changed by only $\frac{\frac{1}{2}mt^2}{A} \cong 0.91$, with $A = 360 \times 60 \times 60$ to convert from arc-seconds to cycles.

5.2.4 Method to detect changes in p: interference patterns and beats

It was shown above that the change in frequency and in the number of cycles with a different value of p is very small after 10 million years. Most frequency analysis methods are designed for time-invariant signals, and do not have a high enough resolution to detect such a small change. It was found that one can extract changes in p by using a method based on interference patterns instead, as described next.

Small differences in frequency can be measured by superimposing two signals and observing their interference ("beat") pattern. This is used, for example, to evaluate small changes in elevation and shape during the evolution of a magma chamber underneath a volcano, which inspired the method used in this study. Consider two simple cosine functions, one with a constant frequency, the other with a frequency linearly changing over time:

$$y_1 = \cos\left(2\pi\frac{(p_0 + s_n)}{A}t\right) \tag{5.1}$$

$$y_2 = \cos\left(2\pi\frac{(p_0 + s_n + \frac{1}{2}mt)}{A}t\right) \tag{5.2}$$

where t is time in years, p_0 is the value of the precession constant p at time zero, averaged to exclude planetary perturbations, in $''/a$, s_n is the value of a particular astronomical fundamental frequency, m is the linear rate of change of p, and A is a constant with a value of $360 \times 60 \times 60$ to convert units from arc-seconds to cycles. Note that the expression $\frac{1}{2}m$ is introduced by the integration of $\frac{\mathrm{d}p_A}{\mathrm{d}t} = p_0 + mt$ leading to $\frac{1}{2}mt^2 + p_0t$.

Interfering equation 5.1 with equation 5.2 and using standard trigonometric identities leads to

$$y_1 + y_2 = 2\cos\left[\frac{2\pi(p_0 + s_n)t + \frac{1}{2}\pi mt^2}{A}\right]\cos\left[\frac{-\frac{1}{2}\pi mt^2}{A}\right] \tag{5.3}$$

This interference signal will have maximum amplitude where the last cosine term is ± 1. Squaring equation 5.3 (which makes subsequent analysis of geological data easier)

then gives

$$(y_1 + y_2)^2 = \frac{1}{2}\left[1 + \cos\left(\frac{4\pi(p_0 + s_n)t + \pi m t^2}{A}\right)\right] \times 2\left[1 + \cos\left(\frac{-\pi m t^2}{A}\right)\right] \quad (5.4)$$

The last term of equation 5.4 is the amplitude modulation of the squared interfering signal which is independent of the carrier frequency $\frac{p_0+s_n}{A}$. In general, the amplitude modulation can be obtained also by using a Hilbert transform [216]. Note that the same beat pattern is produced for negative and positive m since the last term is an even function. Destructive interference occurs when the last term is equal to zero. Figure 5.1 shows a plot over 25 My of the interference pattern generated when two La93 precession solutions are added and squared, one with tidal dissipation set to the present day value, and one with no tidal dissipation (La93$_{(1,1)}$ and La93$_{(1,0)}$). Superimposed is a function that consists of the last term of equation 5.4 with the best fitting slowdown rate m.

By taking the difference between two solutions one can eliminate the effects of planetary perturbations (which affect the s_n and g_n fundamental frequencies) that are the same for both solutions. The sensitivity of the interference method increases with larger time intervals, as illustrated in figure 5.1. Each peak corresponds to one more cycle present in La93$_{(1,1)}$ compared to La93$_{(1,0)}$ (solution without tidal dissipation).

5.2.5 Correcting for astronomical tuning to a target

So far, only the feasibility of using interference patterns between two special astronomical solutions has been shown. In the general case, one would want to interfere a set of geological data with an astronomical solution to extract the evolution of p over time. One very important problem to be solved first, independent of the method used, is the fact that all geological data are put on a time scale by tuning to a specific target curve, thus implicitly contaminating the geological time series with the dominant frequencies of the target solution, including the slowdown in p.

One way to check the accuracy of astronomically tuned geological data is to put them into the correct eccentricity amplitude "envelope", since this is independent of the parameter p. This was verified for the ODP 154 data set in [53]. In principle, this alone would allow the determination of p from the exact position of obliquity and precession peaks with respect to the eccentricity envelope. However, noise in the data, the

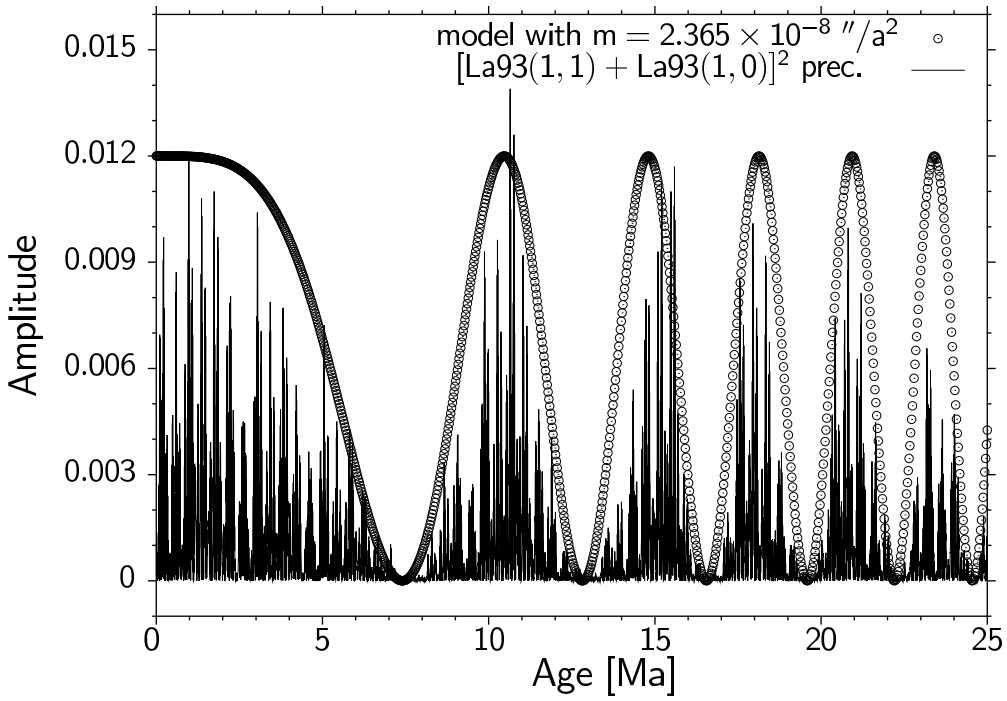

Figure 5.1: Interference pattern between two different astronomical precession solutions over the last 25 My ($La93_{(1,1)}$ and $La93_{(1,0)}$). The short term cyclicity at the precession frequency is modulated in amplitude by a long term interference pattern. High amplitude values correspond to times when both solutions are in phase (constructive interference). Zero amplitude corresponds to times when the two solution are out of phase by exactly 180° (destructive interference). Each successive peak corresponds to times when the $La93_{(1,1)}$ solution is exactly one more cycle ahead due to the effect of tidal dissipation. Superimposed (circles) is a model derived in section 5.2.7 that reproduces the effect of slowdown of the precession constant.

uncertainty in identifying the exact position of the eccentricity modulation to within a fraction of an obliquity or precession cycle, and the possibility of missing cycles in the data, make this method infeasible.

To make the analysis independent of the chosen tuning target it is now considered what happens to the relative position of obliquity and precession peaks when tuned to a specific target curve. Figure 5.2 shows what happens during an idealised tuning procedure where the tuning target does not correspond to the "real" evolution of p as simulated in an idealised data set. It is assumed that the data are tuned such that a particular astronomical frequency $f_{obl}(t)$ is brought exactly into phase between the data and the tuning target.

In this case, the geological depth series will be stretched or squeezed such that the underlying slowdown rate m_r, which is equal for the frequencies f_{obl} and frequency f_{prec}, matches that of the target (m_t). In the lower half of figure 5.2, the lines marked with the slopes m_r, m_t and m_{ref} correspond to the underlying "real" value for slowdown, that of the tuning target, and an arbitrary slope that is used as a reference for the interference method, respectively.

Crucially, if a tuning is performed for the geological data in the obliquity frequency band ("$p_{or}(t)$") to a target curve that has a higher slowdown rate in p ("$p_{ot}(t)$"), as shown at the bottom in figure 5.2, the interference pattern in the precession frequency band will show a greater offset in frequency, as shown in the top of figure 5.2. The offset between $p_{presult}(t)$ and $p_{pt}(t)$ allows the computation of by how much the slowdown rate in p of the target curve deviates from the "real" slowdown rate that is contained in the geological data, thus allowing a correction to be made for the initial choice of the target curve, and avoiding a potential circularity.

5.2.6 Semi-analytical approximation of Laskar's solution

In order to extract Laskar's parameters td and ell from a value that is obtained for m_{real}, one first needs to parameterise m in terms of the tidal dissipation and dynamical ellipticity parameters. The linear evolution of the precession constant p as a function of td and ell over time can be approximated by writing $p(t) = p_0 + mt$, where $p(t)$ and p_0 are in $''/a$ and t is in years (zero for the year 2000 AD). Note that by convention, astronomical equations use the time t such that positive values refer to the future, and negative ones to the past. The opposite convention is normally used in palaeoclimatic studies. Also

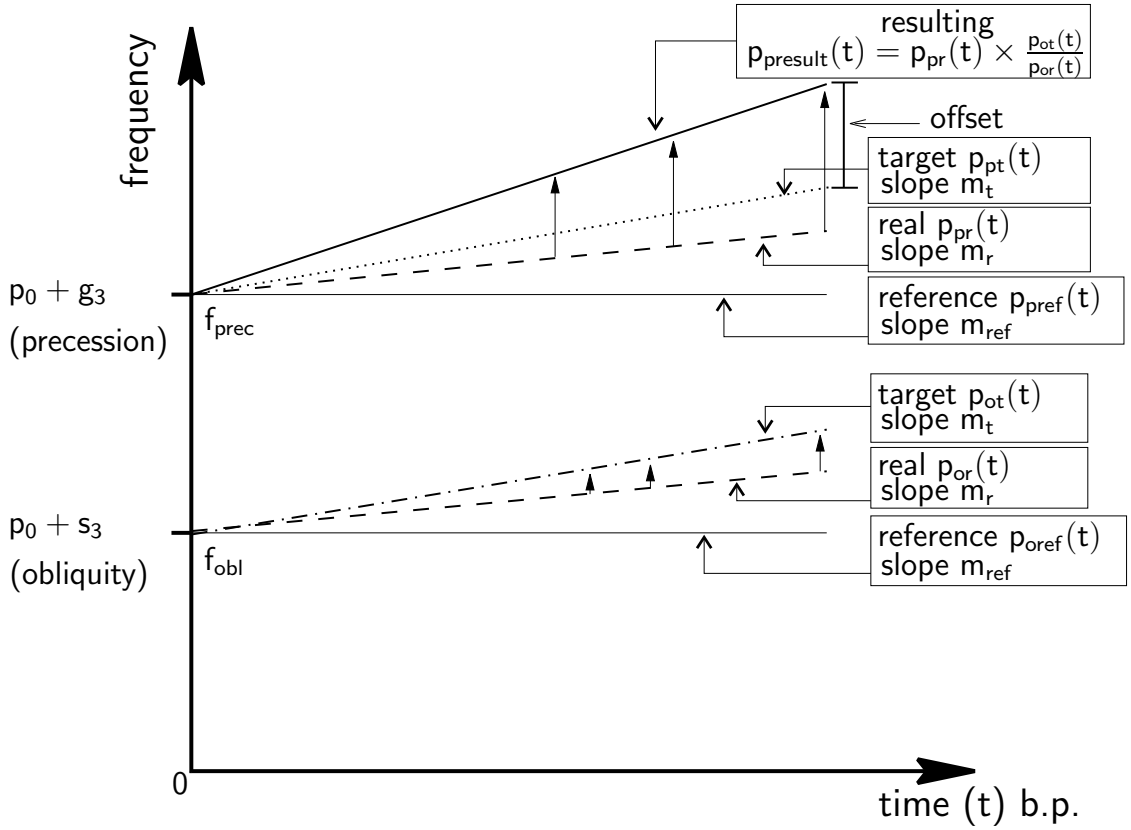

Figure 5.2: This schematic diagram illustrates the effect of tuning to the wrong target curve and how one can correct for this. The "real" slowdown rate of the geological data is indicated by m_r. In the obliquity frequency band (f_{obl}) this is forced to match the target curve with slope m_t, as indicated by the arrows. The effect in the precession band is shown by the curve $p_{presult}$ and is derived in section 5.2.7. Note that this does not correspond to the slope m_t in the climatic precession frequency band (f_{prec}) and the difference between the two are used to find the value of m_r. The curve with slope m_{ref} is arbitrary since it is only used to generate the interference pattern.

measured precession constant	$p_{t=0}$	=	$50.290966\,''/a$
present day obliquity:	ϵ_0	=	$23.43929111^\circ = 0.4090928042$ radians
present day spin rate of the Earth	ν_0	=	$474659981.59757\,''/a$
present day mean motion of the Moon	n_{M0}	=	$17325593.4318\,''/a$
semi-major axis Earth-Moon	a_M	=	384747980.645m
Gaussian gravitational constant	k	=	0.01720209895
numerical constant (see [86])	C_{10}	=	$37.526603\,''/a$
numerical constant (see [86])	C_{20}	=	$-0.001565\,''/a$
numerical constant (see [86])	C_{30}	=	$0.000083\,''/a$
numerical constant (see [86])	C_{40}	=	$34.818618\,''/a$
numerical constant (see [86])	M_0	=	496303.3×10^{-6}
numerical constant (see [86])	M_2	=	-0.1×10^{-6}
	$\frac{\dot{n}_{M0}}{n_{M0}}$	=	$-4.6 \times 10^{-18} s^{-1} = -1.45165 \times 10^{-10} a^{-1}$
geodesic precession due to gen. rel.	p_g	=	$0.019188\,''/a$

Table 5.2: Summary of astronomical constants used in derivations. Adopted from Laskar (1993) [86].

note that p_0 denotes the precession constant at time zero in the absence of planetary perturbations. It is thus different from the measured precession constant $p_{t=0}$.

A linear approximation is used instead of following Berger *et al.* (1989,1992) [81; 95] for reasons of computational speed. Elementary derivations, constants and symbols are adopted from Laskar [86], and a selection of constants used is given in table 5.2.6.

The equation for the general precession in longitude p_A can be written as [86]:

$$\frac{\mathrm{d}p_A}{\mathrm{d}t} = R(\epsilon) - \cot\epsilon[PP] - p_g \tag{5.5}$$

The term $\cot\epsilon[PP]$ is determined by planetary perturbations which are assumed not to be affected by a slowdown in precession. Hence this term will be ignored. $R(\epsilon)$ can then be approximated by

$$R(\epsilon) \cong C_1 \cos(\epsilon) + C_4 S_0 \cos(\epsilon)$$

where C_1 and C_4 are the expressions

$$\begin{aligned} C_1 &= C_{10}(1 + \frac{\dot{\nu_0}}{\nu_0}t)(1 + 2\frac{\dot{n}_{M0}}{n_{M0}}t) \\ C_4 &= C_{40}(1 + \frac{\dot{\nu_0}}{\nu_0}t) \end{aligned}$$

The full equation for $R(\epsilon)$ also contains terms for C_2 and C_3. These are very small (e.g. $C_2 \sim C_1/1000$), and are neglected here. Using constants from table 5.2.6 and the ex-

pression $\dot{\nu}_0 = 51\dot{n}_{M0}$ by Lambeck (1980) [88] this leads to[1]

$$\frac{\dot{n}_{M0}}{n_{M0}} = \frac{\dot{\nu}_0}{\nu_0} \times \frac{1}{51}\frac{\nu_0}{n_{M0}} = \frac{\dot{\nu}_0}{\nu_0} \times 0.5371855514$$

Hence, depending on the tidal dissipation relative to the present day value (td), one can write

$$\frac{\dot{\nu}_0}{\nu_0} = -2.70232435779 \times 10^{-10} a^{-1} \times td$$

In addition, the following equations are used:

$$\begin{aligned} S_0 &= \frac{1}{2}(1-e^2)^{-3/2} - 0.5222 \times 10^{-6} \\ C_{10} &= \frac{3k^2 m_M}{a_M^3 \nu}\frac{C-A}{C}(M_0 - M_2/2) \\ C_{40} &= \frac{3k^2 m_\odot}{a_\odot^3 \nu}\frac{C-A}{C}S_0 \end{aligned}$$

Both C_{10} and C_{40} are proportional to the dynamical ellipticity parameter ell [86]. This leads to

$$R(\epsilon) = [C_{10}(1 + 2\frac{\dot{n}_{M0}}{n_{M0}}t + \frac{\dot{\nu}_0}{\nu_0}t + 2\frac{\dot{n}_{M0}}{n_{M0}}\frac{\dot{\nu}_0}{\nu_0}t^2) + S_0 C_{40}(1 + \frac{\dot{\nu}_0}{\nu_0}t)]\cos(\epsilon)$$

The term $2\frac{\dot{n}_{M0}}{n_{M0}}\frac{\dot{\nu}_0}{\nu_0}t^2$ is very small indeed and can be neglected. Substituting for $\frac{\dot{n}_{M0}}{n_{M0}}$ and collecting terms then leads to

$$\begin{aligned} R(\epsilon) &\cong [C_{10}(1 + 1.074371103\frac{\dot{\nu}_0}{\nu_0}t + \frac{\dot{\nu}_0}{\nu_0}t) + S_0 C_{40}(1 + \frac{\dot{\nu}_0}{\nu_0}t)]\cos(\epsilon) \\ &\cong (C_{10} + S_0 C_{40})\cos(\epsilon) + [2.074371102 C_{10}\frac{\dot{\nu}_0}{\nu_0} + S_0 C_{40}\frac{\dot{\nu}_0}{\nu_0}]\cos(\epsilon)t \end{aligned}$$

This last expression can now be written in the form $p(t) = mt + p_0$, where p is the precession constant, m a slope, and p_0 a constant offset. A computation of average values for the eccentricity e and obliquity ϵ from 0-16 Ma gives

$$\begin{aligned} \overline{e} &= 0.0278062 \\ \overline{\epsilon} &= 0.4060947\text{rad} \end{aligned}$$

which in turn leads to

$$\begin{aligned} S_0 &= 0.5005752275 \\ \cos(\overline{\epsilon}) &= 0.9186705142 \end{aligned}$$

[1] Note that this corrects a mistake in the Laskar *et al.* (1993) [86] paper, where the expression $\frac{\dot{\nu}_0}{\nu_0} = -4.6 \times 10^{-18} s^{-1}$ is quoted.

Using these values finally yields expressions for p_0 and m:

$$p_0 \cong (C_{10} + S_0 C_{40}) \cos(\bar{\epsilon}) \times ell - p_g \tag{5.6}$$

or

$$\begin{aligned} p_0 &\cong (37.526603\,''/a + 0.500575 \times 34.818618\,''/a) \times 0.918671 \times ell - p_g \\ &\cong 50.47\,''/a \end{aligned} \tag{5.7}$$

This would be the present day value of the precession constant $p_{t=0}$ in the absence of planetary perturbations. Inverting the sign of t, the slope m can be identified as

$$\begin{aligned} m \cong & -\left[2.074371102 C_{10} \frac{\dot{\nu}_0}{\nu_0} + S_0 C_{40} \times \frac{\dot{\nu}_0}{\nu_0}\right] \\ & \times \cos(\bar{\epsilon}) \times ell \times td \end{aligned}$$

or

$$m \cong 2.365 \times 10^{-8}\,''/a^2 \times ell \times td \tag{5.8}$$

Note that p_0 does depend on ell and thus enables the independent determination of ell and td. This approximation ignores the effects of secular planetary perturbations and is thus only valid if one interferes two solutions of this kind so that the neglected constant terms cancel. This approximation makes use of the same assumptions as the underlying Laskar algorithm, where the effects of mantle viscosity and lithospheric loading are not considered.

5.2.7 Principles of tuning correction

This section describes in detail the mathematical principles used to develop expressions for the effect of correcting geological data that were tuned to a particular astronomical solution.

Referring to figure 5.2, one can write different linear functions for the evolution of a particular astronomical frequency $p(t)$ over time, where o and p denote frequencies in the obliquity and climatic precession band, and without the secular variation in the ecliptic:

	f_{obl} ($_o$)	f_{prec} ($_p$)
real ($_r$)	$p_{or}(t) = p_{0r} + s_r + m_r t$	$p_{pr}(t) = p_{0r} + g_r + m_r t$
target ($_t$)	$p_{ot}(t) = p_{0t} + s_t + m_t t$	$p_{pt}(t) = p_{0t} + g_t + m_t t$
reference ($_{ref}$)	$p_{oref}(t) = p_{0ref} + s_{ref} + m_{ref} t$	$p_{pref}(t) = p_{0ref} + g_{ref} + m_{ref} t$

Different p_0 values denote the value of the precession constant at time $t = 0$ as a function of ell as calculated using equation 5.8, and represent not the present day measured value but the value one would obtain without the secular variation in the ecliptic. The different s and g values are adjusted such that p_0+s and p_0+g yield values for a particular astronomical frequency of interest (see table 5.1 for a selection). In this study, all s and g values are equal. One can set $s = -18.851''/a$, corresponding to s_3 and taken from [85], and $g = 5.8525''/a$ to cover both g_2 and g_5 frequencies from table 5.1 since they are too close together to separate. In combination, the chosen values correspond to the strongest obliquity and two strongest climatic precession terms, with present day periods of ∼40.996ky and 23 ky. The tuning of geological data with the "real" slowdown m_r to a target curve with the slowdown m_t around the lower obliquity frequency f_{obl} will not result in a slowdown that matches the slowdown of the target curve $p_{pt}(t)$, however, but in

$$p_{presult}(t) \quad = \quad p_{pr}(t) \times \frac{p_{ot}(t)}{p_{or}(t)} \tag{5.9}$$

Interfering and squaring the resulting curve of equation 5.9 and the reference curve for f_{prec} will then result in the amplitude modulation term that describes an interference pattern in the precession frequency band as in equation 5.4:

$$\begin{aligned} 2 + 2\cos \quad & \left[\frac{\pi t}{A}(p_{presult} - p_{pref})\right] \\ = 2 + 2\cos \quad & \left[\frac{\pi t}{A}\{(m_r(m_t - m_{ref}))t^2\right. \\ & +(m_r(s_t - g_{ref} + p_{0t} - p_{0ref}) \\ & +m_t(g_r + p_{0r}) - m_{ref}(s_r + p_{0r}))t \\ & +p_{0r}(s_t - g_{ref} + p_{0t} - p_{0ref}) \\ & +g_r(s_t - p_{0t}) - s_r(g_{ref} + p_{0ref})\} \\ & \left.\times(m_r t + s_r + p_{0r})^{-1}\right] \end{aligned} \tag{5.10}$$

The numerical values for the target and reference curve parameters are known, and the tidal dissipation and dynamical ellipticity parameters can then be found by fitting function 5.10 to the resulting interference pattern in the precession frequency band. In this study, this was accomplished by using the numerical optimisation tool "Solver" available as part of the software package Microsoft Excel.

5.2.8 Analytical precision

The effect of the approximations used to parameterise the astronomical solutions on the precision of the method were tested by tuning the obliquity component of the La93$_{(1,1)}$ solution, which is used as hypothetical geological data with an unknown evolution of p, to the La93$_{(1,0)}$ solution over 25 My and using La93$_{(1,0)}$ as a reference curve. The interference pattern obtained was inversely modelled using equation 5.10. The values obtained for (ell,td) were $(0.9995, 1.001)$ instead of $(1, 1)$, indicating a precision of approximately ± 0.0005 for ell and ± 0.001 for td.

5.2.9 Processing of data

Using the mathematical framework of the previous sections, the various steps of data processing performed are now described in detail. This study makes use of magnetic susceptibility data from the ODP 154 data set [53], which was initially tuned to the La93$_{(1,1)}$ solution. The obliquity component of the geological data around 41 ky was then moved exactly into phase with the astronomical target curve. For this step the software package AnalySeries [106] was employed. This changes the initial time scale [53] but keeps each obliquity cycle within the same astronomical cycle. The complete data set, and example data illustrating the processing steps, are available as background set [155].

One objection to tuning to obliquity exactly in phase might be the consideration of time lags in response of the climate system to the forcing, for example related to ice sheet growth and decay. This was described by Hilgen *et al.* (1993) [49] and Lourens *et al.* (1996) [154], and recently evaluated more directly by Shackleton (2000) [68]. Any effective time lag will always be less than one forcing cycle, and it will not vary as a linear function of time so that it is possible to separate such effects when using the interference method approach. The influence of a change in time lags is apparent in the data used here for the last $\sim$2 My, and will be discussed in a later section.

Next, Gaussian bandpass filters are used to extract precession and obliquity components from the data and from the astronomical solution. The central frequency of the filter used for precession is $0.04347826 \frac{cycles}{ky}$, corresponding to a 23 ky period, half way between the two strongest precession frequencies of table 5.1. The bandwidth chosen was $\pm 0.003 \frac{cycles}{ky}$. The obliquity component is filtered at $0.0243926 \frac{cycles}{ky}$, with a bandwidth of $\pm 0.001 \frac{cycles}{ky}$. This corresponds to a period of 40.996 ky. These filters might

seem narrow, but improve the accuracy of the interference method. To test the validity of this approach, an experiment was conducted using a wider precession filter that is centred around a period of 21 ky, and encompasses the 19 ky and 23 ky components of climatic precession. Figure 5.4 compares both approaches and shows that using such a narrow filter does not degrade the quality of the interference pattern. To obtain a better accuracy in the mathematical analysis of the interference patterns obtained, this study proceeds by using the initial narrow precession band filter.

In order to directly compare the astronomical calculations with the geological data, the four filtered data sets are then normalised to zero mean and unit variance. Next, all four filter outputs are clipped such that positive values are set to 1 and negative values to -1. This increases the noise in the data but eliminates amplitude modulations that would otherwise obscure the results of the interference method. During this process, the phase of the astronomical obliquity filter is flipped by 180° because magnetic susceptibility minima correspond to Northern Hemisphere insolation maxima at this site [53] (Northern Hemisphere insolation consists of a flipped climatic precession signal).

The next step is the adding and squaring of the corresponding filtered and clipped precession and obliquity data from the geological and astronomical time series that were re-sampled at 1 ky intervals. Finally, a running mean over 300 ky is applied to reduce noise, and to integrate over the average amplitude. By fitting equation 5.10 to the interference pattern obtained for the precession component one can now extract the best fitting ell and td parameters.

5.2.10 Sensitivity of the interference method

To test the sensitivity of the interference method one can calculate the effect on the climatic precession frequency that results from tuning the solutions La93$_{(1,0)}$, La93$_{(1,0.5)}$, La93$_{(0.998,0.5)}$ and La93$_{(1.002,0.5)}$ to a "wrong" obliquity target curve La93$_{(1,1)}$, and interfering the climatic precession with a La93$_{(1,0)}$ reference solution. The results are shown in figure 5.3. In the case of obliquity, the resulting interference pattern in all four cases matches that of figure 5.1, because the obliquity cycles were forced to match those of the La93$_{(1,1)}$ target curve exactly.

The "wrong" choice of target curve, however, leads to interference peaks and troughs that are offset. This offset becomes greater as one goes back in time, while it is not very large over the last 5 My if tidal dissipation is the only parameter that is

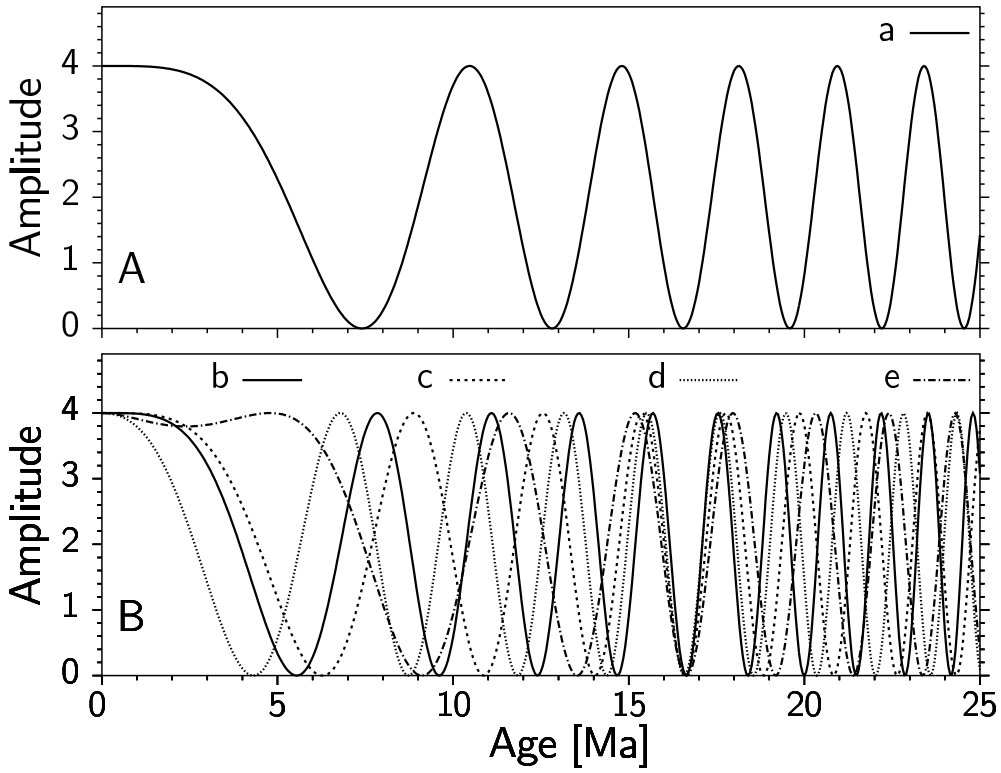

Figure 5.3: Sensitivity of the interference method. Curve a corresponds to the interference pattern in the obliquity band, obtained by tuning to La93$_{(1,1)}$ and using La93$_{(1,0)}$ as a reference curve, as shown in figure 5.2. The curves in panel B show the effect that tuning has in the precession frequency band, using hypothetical geological data that correspond to the solutions La93$_{(1,0)}$ (curve b), La93$_{(1,0.5)}$ (curve c), La93$_{(0.998,0.5)}$ (curve d) and La93$_{(1.002,0.5)}$ (curve e).

varied (curves b and c in figure 5.3). For the solution e, where the effect of dynamical ellipticity is increased, the effect of ell on the offset p_0 in the precession frequency is clearly visible (see equation 5.8, leading to a first destructive interference trough much later in time than for the other solutions. The sensitivity of the interference method increases as one goes back in time.

5.2.11 Modelling with geological data

The main step of the analysis can be performed by tuning the obliquity component of the ODP 154 magnetic susceptibility record to a target curve, and inverse model the parameters (ell,td) from the effect this has on the precession frequency band interference. Here the La93$_{(1,1)}$ solution was chosen as a target curve, and the La93$_{(1,0)}$ solution as a reference curve. Then the re-tuned time series is processed according to the procedure given in section 5.2.9. The upper part (A) of figure 5.4 shows that the obliquity component was successfully put into phase with the target curve, except for a short interval around 3 Ma, where it was difficult to reconcile obliquity and precession peaks.

Figure 5.4 also shows that the interference pattern obtained for the precession signal in the data does seem to deviate from the prediction of the model over the last $\sim$2 My. One interpretation of this finding could be that this is caused by a change of the phase relationship between obliquity and precession as recorded in the data, possibly related to an increase in Northern Hemisphere ice volume [204]. The effect of large ice sheets on the climatic response to orbital forcing was probably most pronounced during the last 1.5 My. In fact, if one incorporates previous estimates of time lags for the precession and obliquity signal into the model, one can obtain an interference pattern that more closely resembles the interference pattern obtained from geological data. Previous estimates for time lags were found to be $\sim$3 ky for climatic precession, based on radiometric dating of the youngest Mediterranean sapropels, and $\sim$6-8 ky for obliquity, based on cross-spectral analysis of oxygen isotope data. A detailed review of these phase lag estimates was given by Hilgen *et al.* (1993) [49], and independent estimates were obtained by Shackleton (2000) [68]. Unfortunately the interference method presented here, in conjunction with the available data, does not provide enough sensitivity to allow an improvement of previous findings. However, the improvement of the fit between model and data after introducing a 3 ky lag for precession and 7 ky lag for obliquity suggests that the growth of Northern Hemisphere ice volume can indeed be

implicated in the apparent mismatch between a non-lagged model and geological data for the time interval ∼0-2.5 Ma.

The data quality between ∼11.5 Ma and ∼17.5 Ma is poor, as shown in [55], and the interference pattern over this interval should not be considered. This is not obvious after processing and normalising the data but is evident when examining the original data. It can be seen that the chosen tuning target La93$_{(1,1)}$ was almost correct, since the offset between the obliquity (A) and precession (B) interference patterns is very small over the time interval 0–11.5 Ma and 17.5–25 Ma.

It was then decided to use a different reference curve to artificially move more interference peaks and troughs into those time intervals where the data quality is considered to be good. By choosing La93$_{(1,-2)}$ as an artificial reference curve one can cause the difference in $p(t)$ between the target curve and the reference curve to appear earlier in the sequence. This does not change the accuracy of the analysis but is a simple mathematical trick to investigate whether the interference that is seen between 11.5 Ma and 17.5 Ma is real or not. The result of this is shown in figure 5.5.

Now an attempt is made to find the best fitting parameter set (ell, td) by fitting equation 5.10 to the observed interference pattern in the precession band. Two measures are used to obtain error bars. Firstly, a computation is made of the sum of the differences squared between the data and different models, normalised by the number of points that were used for fitting a solution. This measure is also used during the fitting step. Secondly, one can independently vary ell and td such that the last trough or peak of the model in the time interval considered falls to within one third of the corresponding peak or trough in the geological data. These computations are performed for consecutively longer time intervals, starting at the present day.

5.2.12 Analysis from 0-5 Ma

Using the same precession interference pattern as shown in figure 5.5, the nominally best fitting solution over the last 5 My is La93$_{(1.0006,0)}$. This solution is superimposed on top of the interference pattern in figure 5.6(A). With the definition for error bars as given in the previous section one can now compute the minimum and maximum value for td, keeping the best fitting $ell = 1.0006$. These are $td_{min} = 0.000$ and $td_{max} = 1.255$.

Keeping the best fitting $td = 0.000$ results in $ell_{min} = 0.9990$ and $ell_{max} = 1.0018$. The expected interference patterns for these values are shown in (B) for td and (C) for

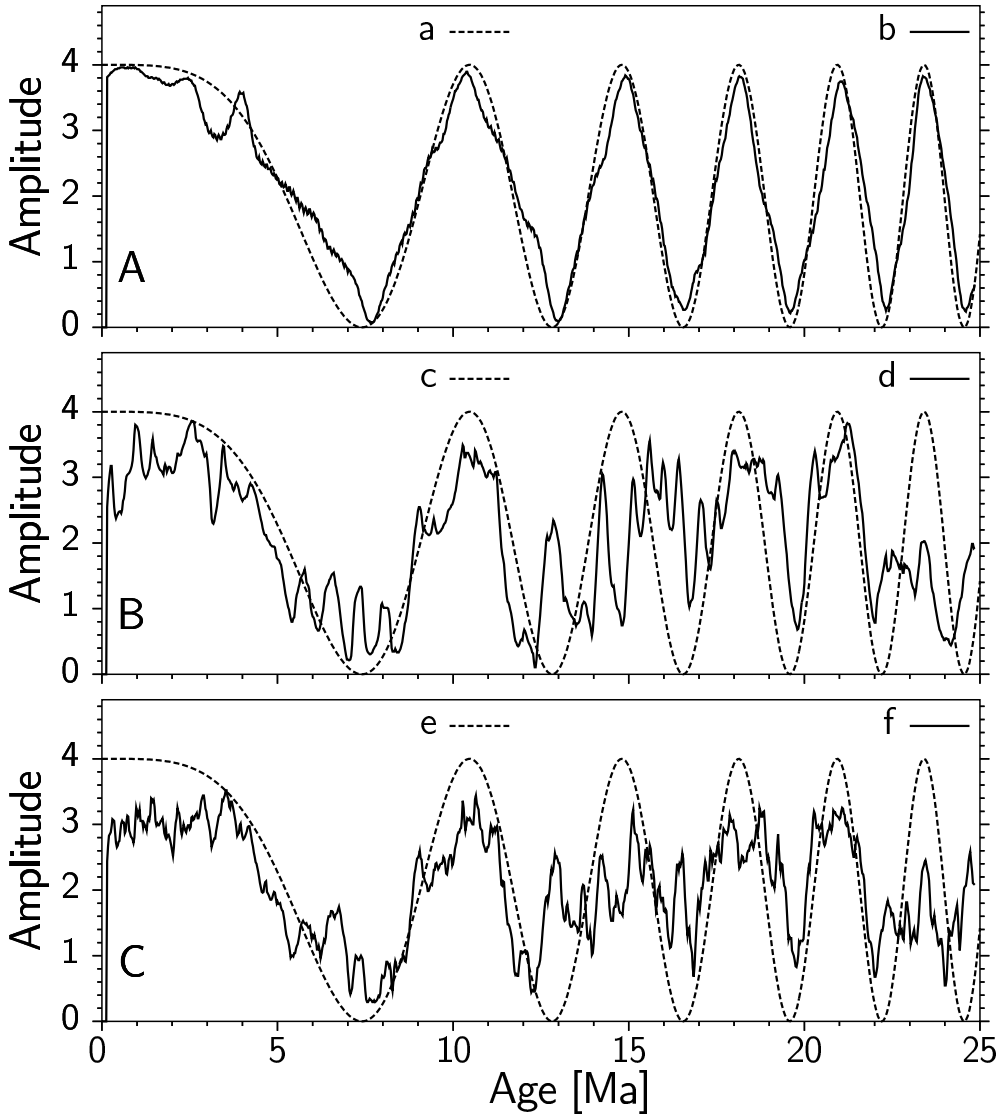

Figure 5.4: Tuning the ODP154 data to La93$_{(1,1)}$ and using a La93$_{(1,0)}$ reference curve results in interference patterns shown here. Panel A shows the results in the obliquity band, where the geological data (curve b) agree very well with the model it was forced to by tuning (curve a). Panel B shows the result in the climatic precession frequency band, where curve d is obtained from the geological data and curve c is the model, assuming that the La93$_{(1,1)}$ solution is correct. In this case the data were filtered with a narrow filter, only extracting the 23 ky period component. Panel C shows the same as Panel B with a wider filter that also passes the 19 ky period component. Note that the quality of the orbital signal in the geological data is not very good over the 11.5–17.5 Ma time interval and should be ignored.

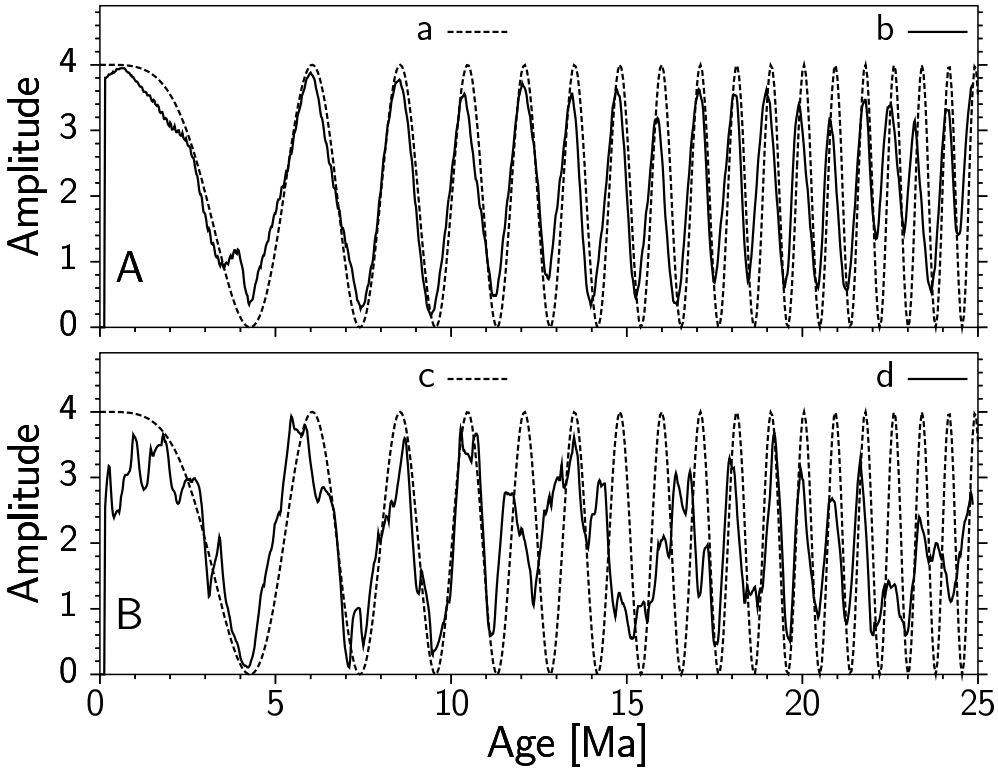

Figure 5.5: This plot is obtained by using the same procedure as for figure 5.4, but choosing $\mathrm{La93}_{(1,-2)}$ as reference curve. This artificially moves more interference cycles into the time intervals where the data quality is considered to be good (0–11.5 Ma and 17.5–24 Ma). The key is the same as in figure 5.4

Time interval 0–5.0 Ma, fitted to 100 points			
ell	td	misfit	type
1.0000	1.000	0.5508	standard
1.0006	0.000	0.4880	best fit
1.0006	0.000	0.4880	trough #1, td_{min}
1.0006	1.255	0.9323	trough #1, td_{max}
0.9990	0.000	1.8176	trough #1, ell_{min}
1.0018	0.000	1.0620	trough #1, ell_{max}

Table 5.3: Results of fitting to the geological interference pattern from 0–5 Ma. The model was fitted to points that are spaced at 50 ky intervals, resulting in 100 points over this interval. The third column shows a misfit measure between the model and the geological interference pattern, obtained by computing the sum of the differences between model and data squared over all points and normalised (divided) by the number of points. The fourth column indicates the type of solution obtained, "standard" denoting the La93$_{(1,1)}$ solution and "best" the solution with the lowest misfit. The rows denoted $td_{min,max}$ and $ell_{min,max}$ show the results used to define error bars and the corresponding interference peak or trough in figures 5.6 and 5.7.

ell. From these rather large error bars it is clear that the La93$_{(1,1)}$ solution could also easily be accommodated (see figure 5.5) and results in a misfit that is only marginally larger than that of the nominal best solution. Table 5.3 summarises the results obtained from the analysis over the 0–5 Ma time interval. For example, one can also exclude the solution La93$_{(0.9977,0)}$, as done by Lourens *et al.* [154], because this value of ell falls outside the interval given by ell_{min} and ell_{max} from table 5.3.

5.2.13 Increasing the time interval of analysis

Tables 5.4 to 5.8 list the values obtained for various time intervals for which the analysis was repeated. It can be seen that the error bars become smaller for longer time intervals. The values converge to a best solution close to La93$_{(1,1)}$ if one fits equation 5.10 to all data that are considered to be of high quality. The result can be seen in figure 5.7.

In figure 5.7 the error bars are quite small, and the best fitting solution is converging towards La93$_{(0.9999,1.004)}$. This indicates that a solution was found that is stable over the last $\sim$25 My, without the need to change the parameter set over this time interval. Of particular significance is the very good fit between the best fitting model parameter set and the short interference cycles from 17.5–23 Ma, since they indicate that one can probably interpolate across the time interval where the quality of the ODP154 data is not very good.

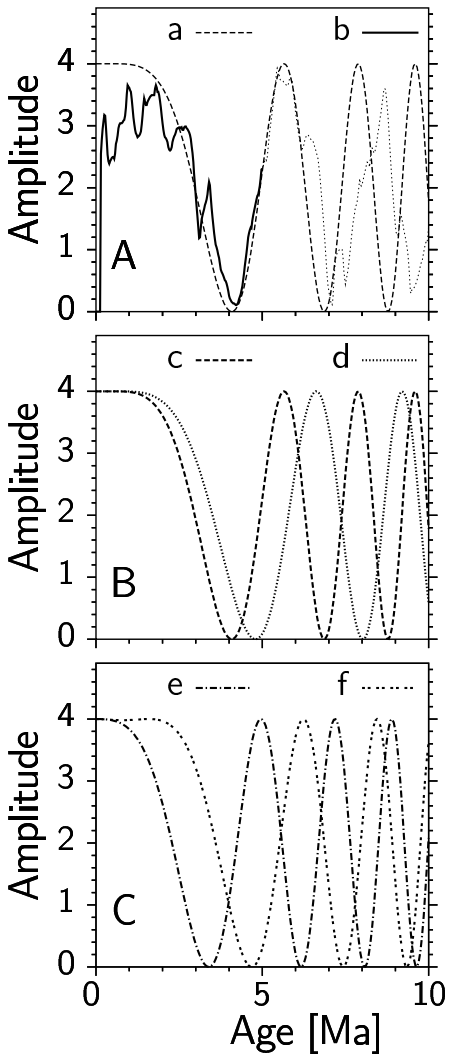

Figure 5.6: Panel A shows the best fitting solution obtained by fitting a model with $ell = 1.0006$ and $td = 0.000$ (curve a) to the interference pattern from geological data in the precession band over the time interval 0–5 Ma (solid part of curve b). Panel B shows the models that define error bars as given in section 5.2.11 for the tidal dissipation term td, corresponding to the solutions La93$_{(1.0006,0.000)}$ (curve c) and La93$_{(1.0006,1.255)}$ (curve d). Panel C shows the variation that is allowed for the parameter ell, corresponding to the solutions La93$_{(0.9990,0.000)}$ (curve e) and La93$_{(1.0018,0.000)}$ (curve f).

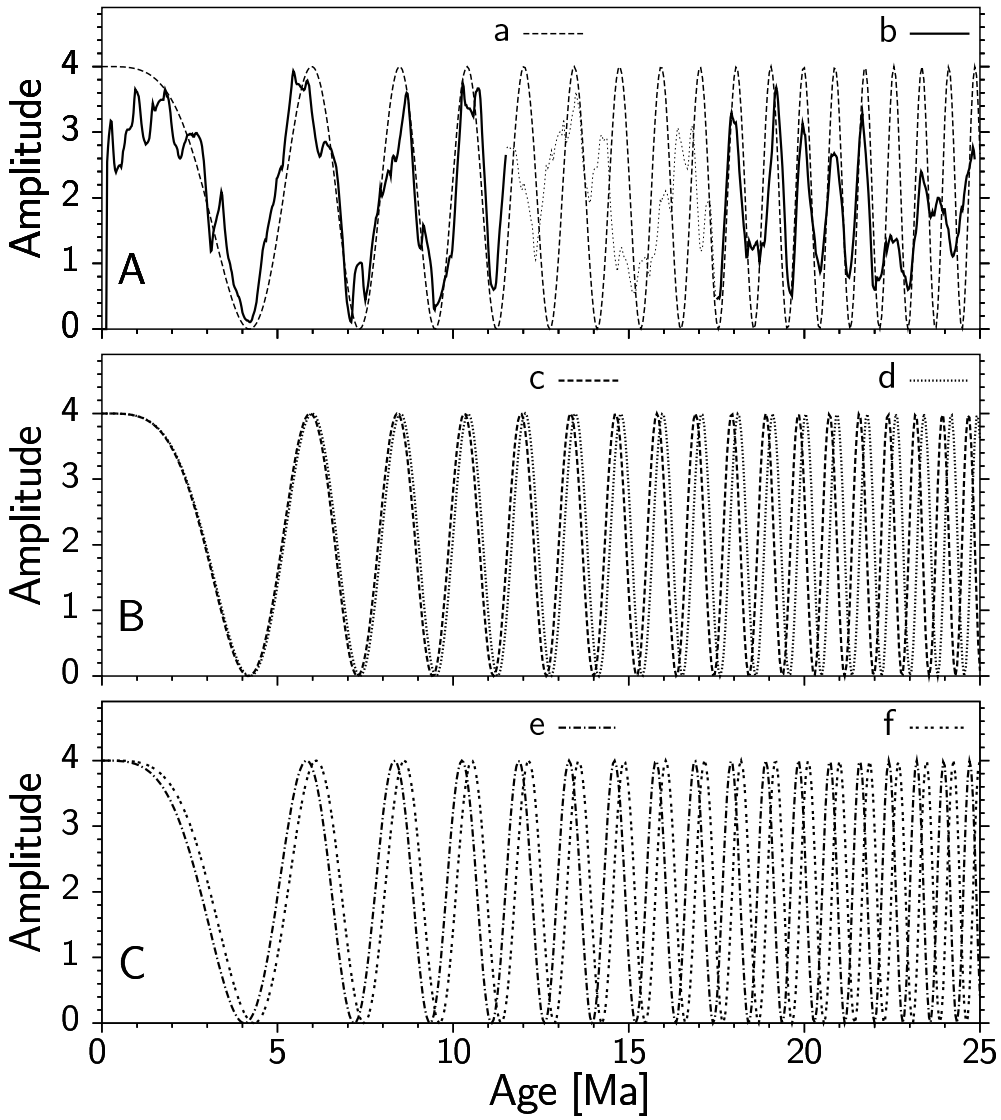

Figure 5.7: Best fitting solution over the time intervals 0–11.5 Ma and 17.5–25 Ma. The interval over which the geological data are considered to be good is indicated by the solid part of curve b. The best fitting model over this time interval corresponds to the solution La93$_{(0.9999,1.004)}$. The error bounds shown in panels B and C are smaller than in figure 5.6, and the values for td_{min} (curve c), td_{max} (curve d), ell_{min} (curve e) and ell_{max} are listed in table 5.8.

Time interval 0–6.5 Ma, fitted to 131 points			
ell	td	misfit	type
1.0000	1.000	0.5775	standard
1.0001	0.515	0.4184	best fit
1.0001	0.000	0.7811	peak #1, td_{min}
1.0001	1.250	0.9443	peak #1, td_{max}
0.9989	0.515	1.7214	peak #1, ell_{min}
1.0010	0.515	0.9867	peak #1, ell_{max}

Table 5.4: Results of fitting to the geological interference pattern from 0–6.5 Ma. See table 5.3 for a description of the columns.

Time interval 0–8 Ma, fitted to 161 points			
ell	td	misfit	type
1.0000	1.000	0.5235	standard
0.9996	1.092	0.4193	best fit
0.9996	0.480	1.2729	trough #2, td_{min}
0.9996	1.450	0.7311	trough #2, td_{max}
0.9987	1.092	1.3476	trough #2, ell_{min}
1.0002	1.092	0.8631	trough #2, ell_{max}

Table 5.5: Results of fitting to the geological interference pattern from 0–8 Ma. See table 5.3 for a description of columns.

Time interval 0–9 Ma, fitted to 181 points			
ell	td	misfit	type
1.0000	1.000	0.5327	standard
0.9995	1.157	0.4501	best fit
0.9995	0.850	0.7957	peak #2, td_{min}
0.9995	1.450	0.7061	peak #2, td_{max}
0.9988	1.157	1.1646	peak #2, ell_{min}
1.0001	1.157	0.8655	peak #2, ell_{max}

Table 5.6: Results of fitting to the geological interference pattern from 0–9 Ma. See table 5.3 for a description of columns.

Time interval 0–11.5 Ma, fitted to 231 points

ell	td	misfit	type
1.0000	1.000	0.5200	standard
0.9994	1.231	0.4638	best fit
0.9995	0.980	0.9548	peak #3, td_{min}
0.9995	1.458	.8679	peak #3, td_{max}
0.9989	1.231	1.0289	peak #3, ell_{min}
1.0001	1.231	1.3078	peak #3, ell_{max}

Table 5.7: Results of fitting to the geological interference pattern from 0–11.5 Ma. See table 5.3 for a description of columns.

Time interval 0–11.5 Ma and 17.5–24 Ma, fitted to 362 points

ell	td	misfit	type
1.0000	1.000	1.7489	standard
0.9999	1.004	1.5501	best fit
0.9999	0.945	2.4506	trough #13, td_{min}
0.9999	1.025	1.6845	trough #13, td_{max}
0.9996	1.004	2.4820	trough #13, ell_{min}
1.0001	1.004	2.2783	trough #13, ell_{max}

Table 5.8: Results of fitting to the geological interference pattern from 0–11.5 Ma and 17.5–24 Ma. See table 5.3 for a description of columns.

5.2.14 Discussion

It was shown that it is possible to extract very small changes in the precession constant p due to tidal dissipation from geological data with the same sensitivity as Lourens *et al.* [154] over the last 25 My, achieving the main objectives as set out in section 5.2.2. Results show that it is possible to put numerical constraints on the tidal dissipation parameter td and the dynamical ellipticity parameter ell, and that these values are very likely to have remained close to the present day values over the last ∼25 My. The best fitting solution obtained here is La93$_{(0.9999,1.004)}$, with a range of uncertainty of 0.9996–1.0001 for ell and 0.945–1.025 for td. Within error, the model does not require changes in these parameters over the last 25 My, and shows that using the La93$_{(1,1)}$ as a tuning target does not introduce large errors into the chronology: as ell and td both go into the calculation of the slowdown rate as factors, their combined effect of $0.9999 \times 1.004 \approx 1.0039$ implies that the number of obliquity and precession cycles at 25 Ma was different from the solution La93$_{(1,1)}$ by only a few cycles. These findings have several important implications.

As pointed out earlier, the present day values for tidal dissipation and dynamical ellipticity lead to an unacceptably young age for the Moon. Bills and Ray (1999) [207] pointed to a possible solution for this problem by arguing that the tidal dissipation is likely to have been lower in the past, due to different configurations of the ocean system leading to different resonance systems. Assuming that the tuning in references [53; 55] is roughly correct, the analysis presented here shows that this change has probably not occurred over the last 25 My.

Even more interestingly, Forte and Mitrovica (1997) [202] modelled the effect of mantle advection over the last 20 My, showing an important effect on the dynamical ellipticity that was not considered in the algorithm of Laskar [86]. As discussed in detail by Forte and Mitrovica (1997) [202], and Laskar (1999) [89], the effect of mantle advection on the precession constant p is such that it works in the opposite direction to that of tidal dissipation. Mantle advection models of Forte and Mitrovica (1997) [202] result in an increase of the precession frequency p over the last ∼20 My. Hence, the real value for tidal dissipation would have been even higher than what is seen in the geological record (Laskar, personal communication). This is because the analysis presented here indicates that the Earth's precession constant p has not crossed the resonance term of Jupiter and Saturn during the past 25 My, while Forte and Mitrovica (1997) [202] pre-

dicted that this should have occurred at around 8 Ma. It would thus be very interesting to see the interference method applied to geological data that cover older time intervals.

After this work was completed, a more recent study by Lourens *et al.* (2001) [156] also reported an attempt to find the best fitting astronomical solution for a short geological data set from the Mediterranean. Their work is based on a record interpreted to be approximately 500 ky long, and showing a very strong climatic signal, as recorded by the Ti/Al ratio in marine sediments. This ratio is thought to reflect variations in the relative proportion of aeolian and fluvial material at the study site. The conclusion reached by Lourens *et al.* from their record, which spans ∼2.4-2.9 Ma, was that during this time period the best fitting astronomical solution was La1993$_{(1,0.5)}$, which corresponds to a significantly smaller slowdown due to tidal dissipation than at present. Their methodology has the advantage that it does not rely on a parameterisation of astronomical solutions as such. However, they assume a constant lag between the obliquity and climatic precession cycles recorded in the geological record. This assumption is questionable, given the presence of ice sheets in the Pliocene.

Furthermore, their study was based on computing regression coefficients between their data and astronomical solutions, and their best fitting model shows a regression coefficient that is only marginally greater than those obtained for the astronomical solutions La1993$_{(1,1)}$ or La1993$_{(1,0)}$, and several other different solutions. Although it is likely that the effects of tidal dissipation and dynamical ellipticity underwent short term secular changes, their findings are not in direct conflict with values obtained in this study, nor with a previous study by Lourens *et al.* (1996) [154]. The work reported in this chapter is probably more robust, since it makes use of a much longer geological data set, thus eliminating variations that might occur on short time scales.

To resolve the difference between the study of Lourens *et al.* (2001) and work reported here, it would be necessary to extend the methodology of Lourens *et al.* to a longer time interval, as well as to repeat the investigation with data from different locations. The last point is of particular importance, since small variations in the relative amplitude of different peaks in the data might lead to drastically different conclusions. The interference method reported here was also applied to an oxygen stable isotope data set that was used by Lourens *et al.* (1996), supporting the findings reported here.

5.3 Evaluating different astronomical calculations using geological data

As was shown by Laskar (1999) [89], the chaotic nature of the solar system limits the time over which it is possible to calculate with confidence variations in the Earth's orbital parameters. Based on these findings, Laskar *et al.* very recently completed a new orbital calculation that tries to go to the limits of accuracy currently possible. The new calculation now also incorporates aspects into the model that were not considered before, e.g. the oblateness of the sun (J2), and by resolving the Earth-Moon system separately. The results of this new work have not been published yet, but the author was one of the first to be allowed access to this new solution, and to carry out a comparison of the new solution with geological data.

5.3.1 Why is there a need for an improved astronomical solution?

Due to the chaotic nature of the orbital system it is difficult to assess the accuracy of any new astronomical calculation without observational constraints. Here an attempt is made to evaluate the differences between the older solution of Laskar *et al.* from 1993 (La1993) [86], and the new solution (La2001) in order to see whether there are distinguishing features that could also be seen in the geological record. Results from this comparison, and an assessment of features from the geological record, are then used to evaluate which solution is more consistent with observation. For the remainder of this section, astronomical solutions from Laskar (1993 and 2001) with present day values for tidal dissipation and dynamical ellipticity will be denoted by "La1993" and "La2001", respectively.

The choice of which astronomical solution is used to calibrate the geological record has direct consequences for what ages are assigned to a given time interval. Moreover, recent studies have proposed hypotheses that directly link unusual orbital configurations to transient events in the global climate system (Zachos *et al.*, 2001 [126]). This makes an evaluation of the best fitting astronomical solution an important research topic, because it might allow to test such hypotheses, and to improve the basis for the astronomical calibration of the geological time scale.

5.3.2 Comparison of astronomical solutions: La2001 and La1993

An attempt is now made to evaluate the differences between the solutions from 1993 and the more recent one, and how they might be constrained by geological observation. It is important to realise that the limits of the astronomical solutions for geological time scale development discussed in Laskar (1999) [89] are still valid.

It is possible to compare different astronomical solutions and geological data on several levels. If the objective is to calibrate geological data of pre-Neogene times, one important aspect is that of average frequency for eccentricity, obliquity and climatic precession components (see, e.g. Berger, Loutre and Dehant (1989) [95; 195], and Berger, Loutre and Laskar (1992) [81]). The frequency components of obliquity and climatic precession are influenced by the effects of tidal dissipation, tidal friction and dynamical ellipticity.

In contrast, the frequencies of the long and short eccentricity cycles are independent of these additional parameters. Generally it will be very hard to differentiate between two different astronomical models on the basis of average frequencies alone because differences are generally very small over a Cenozoic time scale [55; 155]. Tables 5.9 to 5.11 show estimates for eccentricity, obliquity and climatic precession frequency components over 20 My intervals from 0 to 50 Ma for the leading terms of the solutions La1993 and La2001, using present day values for tidal dissipation and dynamical ellipticity. Terms are given in order of decreasing amplitude. These estimates were obtained using a very high resolution frequency analysis method developed by Laskar (1990) [85], and performed by Benjamin Levrard during a recent collaboration at the Bureau des Longitudes in Paris. The analysis was truncated at a specified relative amplitude, such that not all leading terms might have been computed for all solutions. Note that this method approximates chaotic astronomical calculations assuming the presence of quasi-periodic terms to obtain a Fourier expansion. Thus, the results should be treated with caution, and should not be used to reconstruct individual astronomical solutions (Laskar *et al.* (1993) [86]).

Table 5.9 shows that for both solutions La1993 and La2001, the strongest leading term is the long eccentricity cycle with a period of approximately 405 ky. All solutions also show two short eccentricity cycles with periods close to ∼96 ky, and two periods close to ∼127 ky. The interference within each frequency pair leads to a characteristic beat pattern with a period of ∼2.4 My, while the interference across both pairs again

Leading eccentricity terms 0-20 Ma

La1993$_{(1,1)}$			La2001$_{(1,1)}$		
Period $[ky]$	Amplitude	Phase $[deg]$	Period $[ky]$	Amplitude	Phase $[deg]$
∞	0.0276	0.00	∞	0.0276	0.00
404.328	0.0052	-164.23	405.649	0.0053	-161.71
94.853	0.0041	-117.10	94.886	0.0040	-124.25
123.923	0.0032	52.03	123.881	0.0032	48.09
98.822	0.0027	90.71	98.855	0.0027	85.34
130.799	0.0023	-101.66	130.712	0.0023	-111.27
2363.955	0.0018	168.43	2368.837	0.0016	166.38

Leading eccentricity terms 10-30 Ma

La1993$_{(1,1)}$			La2001$_{(1,1)}$		
Period $[ky]$	Amplitude	Phase $[deg]$	Period $[ky]$	Amplitude	Phase $[deg]$
∞	0.0275	0.00	∞	0.0274	0.00
403.870	0.0051	87.69	405.433	0.0052	65.25
94.925	0.0038	37.26	94.823	0.0040	-18.24
124.100	0.0032	-51.41	123.760	0.0032	-78.95
98.892	0.0025	145.00	98.810	0.0028	105.31
130.961	0.0022	56.95	130.663	0.0023	42.52
2388.052	0.0019	-100.28	2351.430	0.0019	-110.36

Leading eccentricity terms 20-40 Ma

La1993$_{(1,1)}$			La2001$_{(1,1)}$		
Period $[ky]$	Amplitude	Phase $[deg]$	Period $[ky]$	Amplitude	Phase $[deg]$
∞	0.0280	0.00	∞	0.0275	0.00
403.985	0.0050	-4.45	404.841	0.0050	-68.81
95.278	0.0035	169.53	94.978	0.0040	142.50
99.171	0.0027	-157.19	124.161	0.0032	-134.15
124.693	0.0027	177.62	99.005	0.0029	-175.86
100.443	0.0021	-62.76	131.054	0.0023	-107.54
131.441	0.0021	-154.49	2389.335	0.0020	-11.84

Leading eccentricity terms 30-50 Ma

La1993$_{(1,1)}$			La2001$_{(1,1)}$		
Period $[ky]$	Amplitude	Phase $[deg]$	Period $[ky]$	Amplitude	Phase $[deg]$
∞	0.0280	0.00	∞	0.0276	0.00
404.215	0.0050	-95.67	404.407	0.0049	171.14
95.359	0.0035	133.17	95.056	0.0041	-154.58
124.791	0.0031	-130.08	124.267	0.0033	39.21
99.192	0.0025	108.66	99.086	0.0030	161.07
100.547	0.0021	99.64	131.233	0.0024	-11.61
131.416	0.0019	-159.92	2320.938	0.0020	34.40

Table 5.9: Leading eccentricity terms for La1993$_{(1,1)}$ and La2001$_{(1,1)}$

Leading obliquity terms 0-20 Ma

	La1993$_{(1,1)}$			La2001$_{(1,1)}$	
Period	Amplitude	Phase	Period	Amplitude	Phase
$[ky]$	$[rad]$	$[deg]$	$[ky]$	$[rad]$	$[deg]$
∞	0.4061	0.00	∞	0.4057	0.00
40.690	0.0040	-1.66	40.655	0.0037	-29.57
40.816	0.0021	-145.18	40.777	0.0021	-178.26
40.556	0.0021	13.12	40.514	0.0022	-20.39
39.335	0.0015	-44.34	39.311	0.0014	-61.85
39.982	0.0011	-58.80	39.945	0.0010	-97.23
53.169	0.0010	109.38	N/A	N/A	N/A

Leading obliquity terms 10-30 Ma

	La1993$_{(1,1)}$			La2001$_{(1,1)}$	
Period	Amplitude	Phase	Period	Amplitude	Phase
$[ky]$	$[rad]$	$[deg]$	$[ky]$	$[rad]$	$[deg]$
∞	0.4061	0.00	∞	0.4054	0.00
40.369	0.0041	-175.55	40.311	0.0035	-121.52
40.508	0.0023	77.80	40.174	0.0029	-106.81
40.249	0.0027	-148.68	38.963	0.0016	-17.74
39.050	0.0018	0.40	40.429	0.0015	105.47
39.738	0.0012	-6.55	40.531	0.0014	-168.56
52.656	0.0010	101.16	39.617	0.0011	-86.79

Leading obliquity terms 20-40 Ma

	La1993$_{(1,1)}$			La2001$_{(1,1)}$	
Period	Amplitude	Phase	Period	Amplitude	Phase
$[ky]$	$[rad]$	$[deg]$	$[ky]$	$[rad]$	$[deg]$
∞	0.4061	0.00	∞	0.4051	0.00
40.094	0.0046	38.41	39.988	0.0035	-159.87
39.971	0.0021	67.52	39.852	0.0031	-144.54
40.303	0.0019	-34.90	40.101	0.0020	47.94
40.218	0.0017	-88.13	39.759	0.0018	-113.71
38.768	0.0016	-141.33	38.654	0.0015	104.57
52.150	0.0010	28.56	N/A	N/A	N/A

Leading obliquity terms 30-50 Ma

	La1993$_{(1,1)}$			La2001$_{(1,1)}$	
Period	Amplitude	Phase	Period	Amplitude	Phase
$[ky]$	$[rad]$	$[deg]$	$[ky]$	$[rad]$	$[deg]$
∞	0.4062	0.00	∞	0.4046	0
39.877	0.0033	-99.64	39.637	0.0041	130.94
38.564	0.0019	174.48	39.760	0.0023	0.43
39.742	0.0021	-56.70	39.511	0.0021	146.45
39.630	0.0018	-64.06	38.320	0.0014	-176.03
51.657	0.0010	-97.23	38.976	0.0011	-0.26
40.115	0.0009	155.28	N/A	N/A	N/A

Table 5.10: Leading obliquity terms for La1993$_{(1,1)}$ and La2001$_{(1,1)}$

Leading climatic precession terms 0-20 Ma

	La1993$_{(1,1)}$			La2001$_{(1,1)}$	
Period $[ky]$	Amplitude	Phase $[deg]$	Period $[ky]$	Amplitude	Phase $[deg]$
23.583	0.0073	108.50	23.567	0.0068	74.89
22.287	0.0061	-25.30	22.278	0.0059	-49.46
18.890	0.0048	17.65	18.886	0.0045	26.98
23.539	0.0046	130.21	22.236	0.0043	-45.16
23.626	0.0038	-30.33	23.521	0.0039	83.37
19.040	0.0034	-151.80	23.611	0.0036	-45.61

Leading climatic precession terms 10-30 Ma

	La1993$_{(1,1)}$			La2001$_{(1,1)}$	
Period $[ky]$	Amplitude	Phase $[deg]$	Period $[ky]$	Amplitude	Phase $[deg]$
23.482	0.0073	-3.64	23.452	0.0070	28.77
22.193	0.0063	96.20	22.175	0.0058	123.63
18.823	0.0058	26.50	18.803	0.0051	16.49
23.438	0.0046	19.32	23.408	0.0048	40.76
18.983	0.0040	-148.23	23.496	0.0039	-101.94
23.525	0.0038	-139.90	18.954	0.0036	144.01

Leading climatic precession terms 20-40 Ma

	La1993$_{(1,1)}$			La2001$_{(1,1)}$	
Period $[ky]$	Amplitude	Phase $[deg]$	Period $[ky]$	Amplitude	Phase $[deg]$
23.381	0.0073	-172.32	23.337	0.0068	-3.91
22.103	0.0062	-166.21	18.733	0.0057	131.40
18.774	0.0043	9.44	22.066	0.0057	-58.31
18.944	0.0038	-117.80	23.293	0.0049	11.61
23.337	0.0036	-158.67	18.885	0.0037	-177.46
23.423	0.0036	61.77	23.381	0.0036	-112.13

Leading climatic precession terms 30-50 Ma

	La1993$_{(1,1)}$			La2001$_{(1,1)}$	
Period $[ky]$	Amplitude	Phase $[deg]$	Period $[ky]$	Amplitude	Phase $[deg]$
23.281	0.0074	-46.78	23.220	0.0066	-14.59
22.014	0.0066	-131.44	21.960	0.0055	162.30
18.724	0.0046	-156.07	23.176	0.0049	-1.05
23.323	0.0038	176.74	18.655	0.0045	122.33
23.239	0.0036	-26.67	18.811	0.0037	141.93
18.899	0.0035	8.76	23.264	0.0036	-116.50

Table 5.11: Leading climatic precession terms for La1993$_{(1,1)}$ and La2001$_{(1,1)}$

results in the ∼405 ky cycle. The ∼405 ky eccentricity cycle is also modulated in amplitude by the ∼2.4 My cycle (Laskar, personal communication). This is an important feature that will be discussed in more detail in a later part of this section. The frequency analysis for the solution La2001 shows the direct presence of the ∼2.4 My long term for all time intervals considered, while it disappears from the six leading terms in the solution La1993 for analyses covering the time interval from 20–50 Ma. This table also shows that the exact periods of individual eccentricity cycles not only vary slightly for different time intervals over which the analysis was performed, but also between the two solutions La1993 and La2001.

Table 5.10 shows the first few leading frequency terms obtained for obliquity for the two solutions over different time intervals. The effects of tidal dissipation and dynamical ellipticity were incorporated into both astronomical models, and an increase in the periods of the main obliquity is clearly visible as one approaches the present. However, the difference in the average period between the strongest obliquity periodic component (∼41 ky at present) for the time intervals between 30–50 Ma and 0–20 Ma is only of the order of 1 ky, thus demonstrating that it would be very hard to extract this change from geological data. The interference between the leading terms in the periodic expansion of obliquity again results in several longer term beat patterns. For example, considering the values obtained from the solution La1993 from 0–20 Ma, the interference between cycles with a 40.690 ky period with those of a 39.335 ky period results in a $(1/40.69\mathrm{ky} - 1/39.335\mathrm{ky})^{-1} \simeq$1.2 My amplitude modulation cycle, the interference between cycles with periods of 39.335 ky and 39.982 ky results in a ∼2.4 My cycle, while the interference between the 40.690 ky period and 53.169 ky period results in an amplitude modulation cycle with a period of ∼170 ky. Later analysis will show how the relationship between these "beat" terms has changed over time, more so for the solution La1993 than for La2001.

Table 5.11 lists the leading terms obtained for the calculations of climatic precession values over different time intervals. Again the effects of tidal dissipation and dynamic ellipticity are clearly visible, in this case resulting in an increase in the average period of the strongest term by ∼0.3 ky when considering the average over the intervals 30–50 Ma and 0–20 Ma. The interference between different terms reflects the amplitude modulation of climatic precession by eccentricity, and also contains the longer term ∼2.4 My long amplitude modulation cycles for some of the intervals, as discussed for

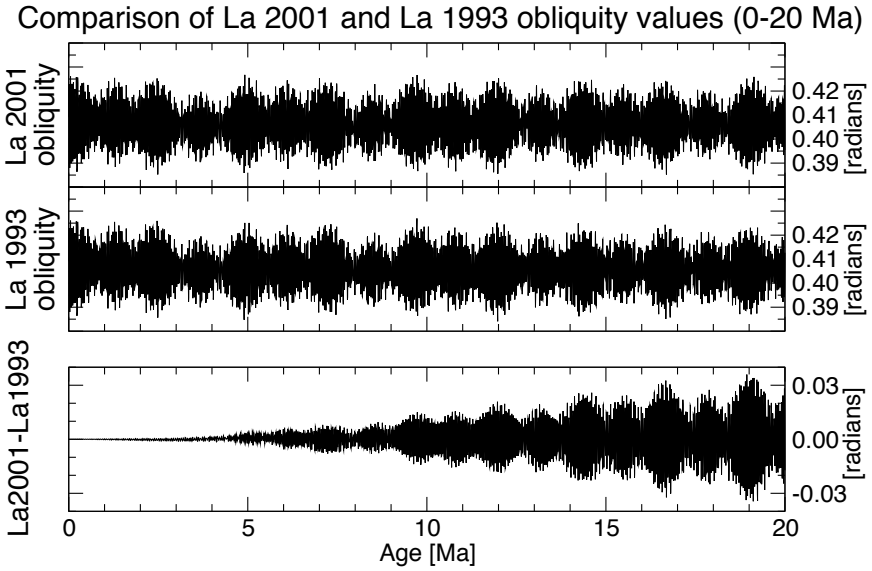

Figure 5.8: Comparison of obliquity calculations La1993 and La2001 from 0-20 Ma. Over this time interval the ∼1.2 My long amplitude modulation pattern seems to agree well between the two solutions. The bottom panel shows the difference between the two solutions and illustrates that the detailed phase relationship between the two solutions changes at around 10 Ma.

eccentricity. The exact behaviour of long term amplitude modulation patterns will be discussed for all three orbital components at a later stage in this section.

Figures 5.8 and 5.9 show the differences between the calculated obliquity and eccentricity solutions over the last 20 My. It is visible that the solutions are very similar over approximately 10 My, before which individual phases begin to diverge. Note that for the obliquity the long term (∼1.2 My) modulation pattern is very similar for both solutions over the last 20 My. Also note that there are some quite recent intervals where the relative amplitude of individual cycles is significantly different. This is, for example, the case for the two eccentricity maxima at around 13.5 Ma and 17.5 Ma, which are marked on the plot.

In addition to the average frequency components, the close proximity of some of the terms in tables 5.9 to 5.11 is related to amplitude modulations, or "beats", that are characteristic for a given astronomical solution. Laskar *et al.* (1993,1999) [86; 89] showed how these terms are related to the interaction between the fundamental astronomical frequencies of the eccentricity and the orbital inclination of different planets. Herbert (1992, 1994, 1999) [58; 61; 108], Rial (1999) [217], and Hinnov (2000) [92] also dis-

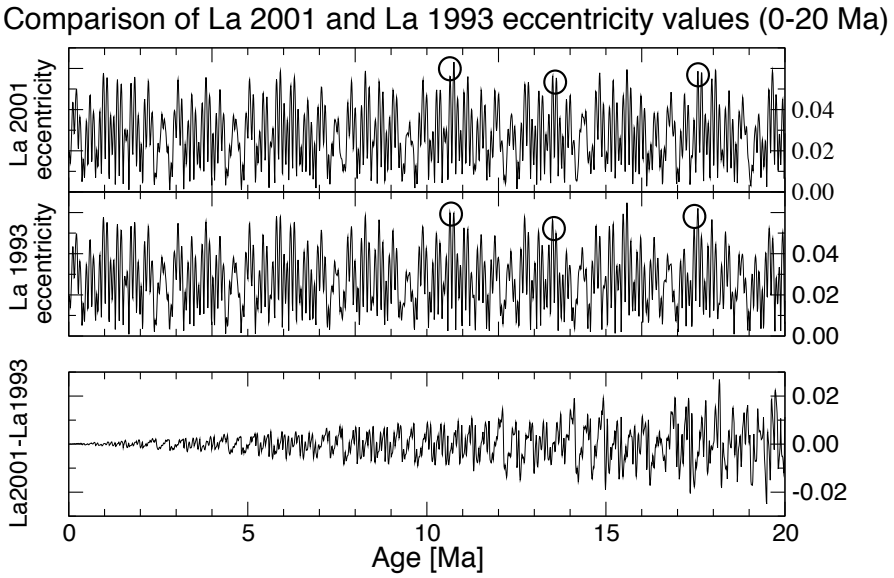

Figure 5.9: Comparison of eccentricity calculations La1993 and La2001 from 0-20 Ma. Over this time interval the ∼2.4 My long amplitude modulation pattern seems to agree well between the two solutions. A cycle-by-cycle comparison shows small differences in the relative amplitude of individual cycles, though, as indicated by circles. The bottom panel shows the difference between the two solutions and illustrates that the detailed phase relationship between the two solutions does change such that the two solutions are out of phase for ages older than ∼15 Ma. Note that the difference plot in the bottom panel of the figure is very sensitive to very small changes in the phase relationship between the two solutions. Back to ∼15 Ma the main contribution to the difference seems to arise from the ∼ 400 ky cycle, and thus corresponds to a change of only $\frac{0.5}{15000/400} \approx 1.3\%$ in the average frequency of the ∼400 ky cycle between the two solutions.

cussed additional frequency modulation terms that can be considered. The variation in these modulation patterns can be demonstrated very clearly by computing evolutionary spectral estimates, or through wavelet analysis. Figures 5.10 and 5.11 show wavelet plots for an arbitrary mixture of normalised eccentricity, tilt, and climatic precession ("ETP") for the two solutions, and figure 5.12 shows a difference plot for the two. These plots represent the true "fingerprint" of the astronomical solutions and contain many important features that will be discussed next. The wavelet analysis was performed using software developed by Prokoph *et al.* (1990,1996) [93; 94].

The wavelet plots very clearly show the dominant astronomical frequencies near 19, 22 and 23 ky for climatic precession; 29, 41 and 54 ky for obliquity; and 96, 126 and 400 ky for eccentricity, as well a multitude of amplitude modulation patterns. The colour range from blue (dark) to red (light) corresponds to the amplitude at a given time, and is displayed on a logarithmic scale. Several amplitude modulation patterns are visible, most notably an approximately ∼1.2 My long amplitude modulation pattern at around 41 ky, and a ∼2.4 My modulation pattern in the short ∼100 ky eccentricity, as well as in the ∼19 ky climatic precession frequency band. This same pattern is also present in the ∼400 ky long eccentricity band, but exactly out of phase compared to the short eccentricity band. These amplitude modulation patterns are independent of the tidal dissipation and dynamical eccentricity terms, and result from the amplitude modulation by the $(g_3 - g_4)$ term for the eccentricity and climatic precession, and by the $(s_3 - s_4)$ term for obliquity (Laskar 1990,1993,1999 [85; 86; 89]). The difference plot between La2001 and La1993 demonstrates that the amplitude modulation patterns begin to differ significantly before ca. 15 Ma for eccentricity and climatic precession, and before ca. 20 Ma for obliquity. This is mainly the result of a change in the relationship between the two modulation terms, and will be investigated next. These amplitude modulation terms were also discussed by Laskar (1993,1999) [86; 89].

5.3.3 Resonance and phase lock between eccentricity and obliquity

Laskar (1990) [85] noted that there is a secular resonance between the $(g_4 - g_3)$ and $(s_4 - s_3)$ terms in that these two terms are presently in a phase-locked "libration" such that $2(g_4 - g_3) - (s_4 - s_3) = 0$. This means that the amplitude modulation frequency of both eccentricity and precession, and obliquity, are in a $1 : 2$ ratio (∼2.4 My : ∼1.2 My periods), and phase locked. However, Laskar also showed that this system can change

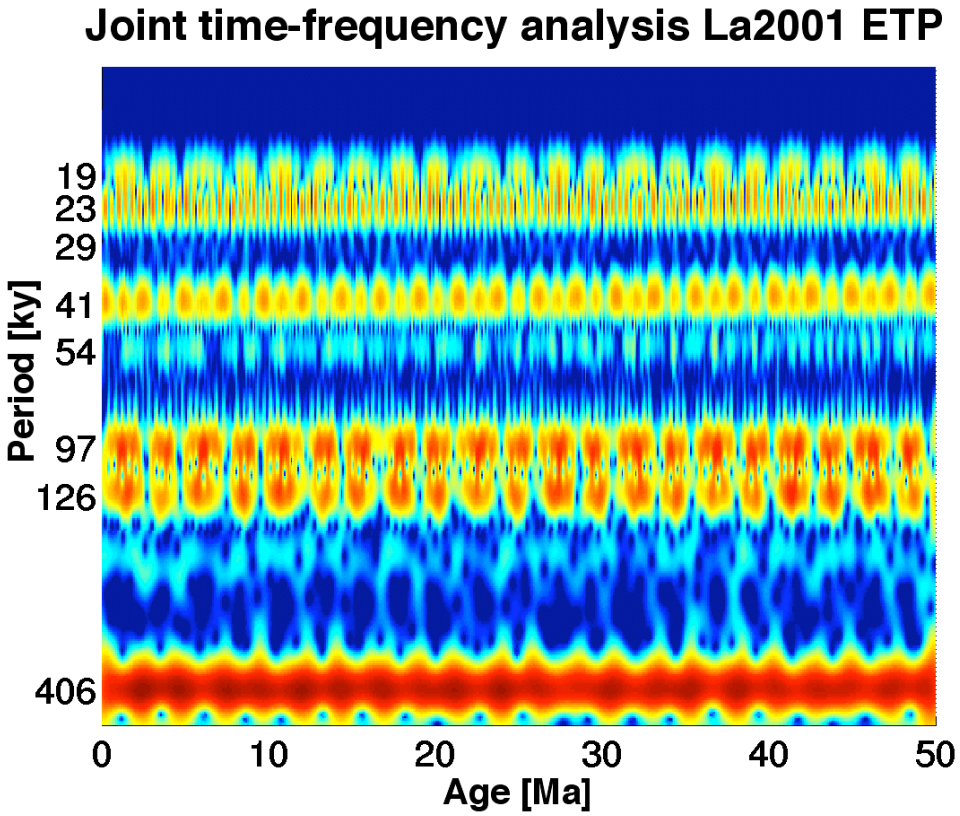

Figure 5.10: Joint time-frequency wavelet analysis for La2001 from 0-50 Ma. The orbital components from the astronomical calculation La 2001 were combined to generate an "ETP" curve. Orbital components were weighted to facilitate a visual comparison of the climatic precession, obliquity and eccentricity components, the periods of which are marked along the frequency axis. Note the apparent amplitude modulation patterns visible. The climatic precession is modulated by eccentricity with ∼100 ky and ∼400 ky periods. Both eccentricity and precession also show a longer term amplitude modulation with an average period of ∼2.4 My over the entire time interval. The ∼41 ky obliquity component is modulated with a period of ∼1.2 My, which in turn shows a distinct bundling that has the same origin as the ∼2.4 My pattern visible in the eccentricity and precession components. Also clearly visible on this plot is the effect of tidal dissipation, as the frequency of the climatic precession and obliquity components decreases from 50 Ma to the present. Tidal dissipation does not affect the frequencies of eccentricity, and thus there is an apparent slope between the frequency lines of obliquity and eccentricity.

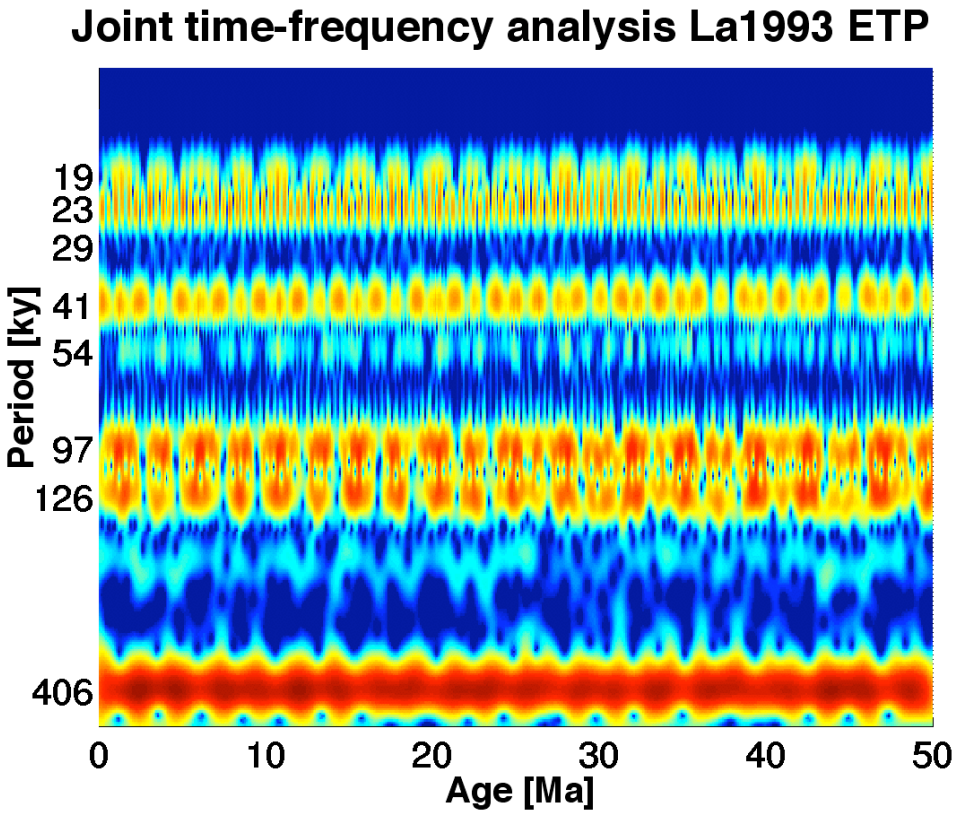

Figure 5.11: Joint time-frequency wavelet analysis for La1993 from 0-50 Ma. This figure was generated in the same way as figure 5.10. Comparing with figure 5.10, note that the long term modulation pattern ($\sim$2.4 My for eccentricity and precession, and $\sim$1.2 My for obliquity) undergoes a distinctive disturbance and re-organisation between $\sim$24-30 Ma. This is due to a resonance switch from 2:1 to 1:1 in the $\sim$2.4 My and $\sim$1.2 My modulation terms, which is not visible in the solution La2001.

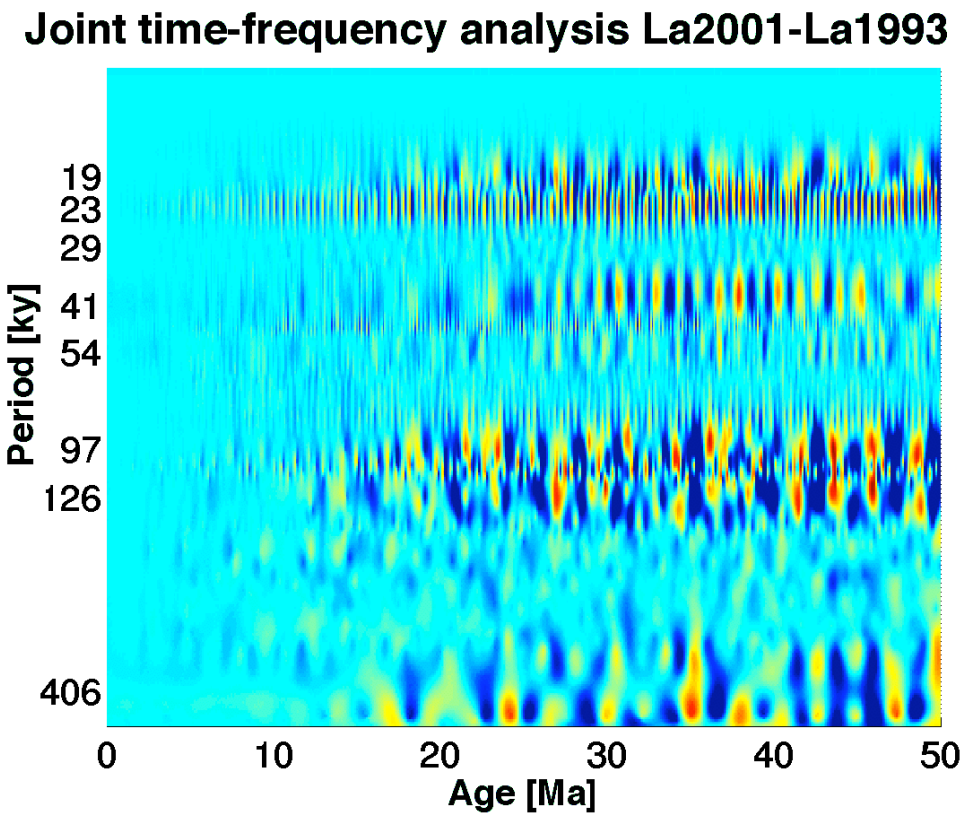

Figure 5.12: Difference plot of joint time-frequency wavelet analyses for La2001 and La1993 from 0-50 Ma. This figure was generated by subtracting the amplitude values of solution La1993 from those of La2001 (figures 5.11 and 5.10). The difference plot shows that between the two solutions the amplitude modulation pattern for both eccentricity and climatic precession diverges at around ∼19 Ma, while that of obliquity diverges slightly longer back into the past. At around ∼25 Ma all components are significantly out of phase. The reason has been identified to be the absence of a switch from a 2:1 to a 1:1 resonance between the ∼2.4 and 1.2 My long amplitude modulation patterns of eccentricity and obliquity in the solution La2001.

to a new resonance, where libration occurs with a $1:1$ frequency ratio through a change in the difference of the term $(g_4 - g_3)$. The term $(g_4 - g_3)$ also appears as an amplitude modulation term in the obliquity and is visible as a bundling of one high amplitude with one lower amplitude $\sim$1.2 My cycle during a resonance with at a $1:2$ ratio, and as $\sim$1.2 My cycles of similar amplitude when the resonance occurs at a $1:1$ ratio. In order to investigate the behaviour of both astronomical solutions, the amplitude modulation patterns of eccentricity and obliquity were computed by complex demodulation (see Bloomfield, 1976 [166]). This method extracts the amplitude variation in a signal at a specified frequency, and can be thought of as the "envelope" of a bandpass filter. It corresponds to a cross-section through the wavelet plots introduced earlier along the time axis. Figure 5.13 shows the complex demodulation method applied to both astronomical solutions, with the additional computation of the difference in amplitude modulation between the two solutions. Figure 5.14 shows the same procedure applied to the short ($\sim$100 ky period) eccentricity cycle.

In figure 5.13, the switch to a $1:1$ ratio is visible between $\sim$25 and $\sim$29.5 Ma in the solution La1993, and appears as a change in the "bundling" of the obliquity amplitude modulation. This is also apparent in the comparison of the wavelet plots for the two solutions (figures 5.10 and 5.11). The solution La1993 also shows a more irregular appearance in the eccentricity amplitude modulation (figure 5.14). In contrast, this switch in resonance from a $2:1$ to $1:1$ ratio does not seem to occur in the more recent solution La2001 over the last 50 My, where the modulation pattern for eccentricity as well as for obliquity is generally much more regular. This is an important observation since one of the reasons for the limitation in the calculation of the astronomical solution into the past is the occurrence of this switch in the resonance behaviour.

This qualitative difference between the two solutions will provide a means to use geological data to verify the calculations. On both complex demodulation plots times where this distinct switch is observed for the La1993 solution are marked by a box. Evaluating figures 5.13 and 5.14, it is now possible to select time intervals where the difference between the astronomical models La1993 and La2001 is greatest for the long term amplitude modulations. This should provide those crucial time intervals when geological data might be able to test which model is more consistent with geological data.

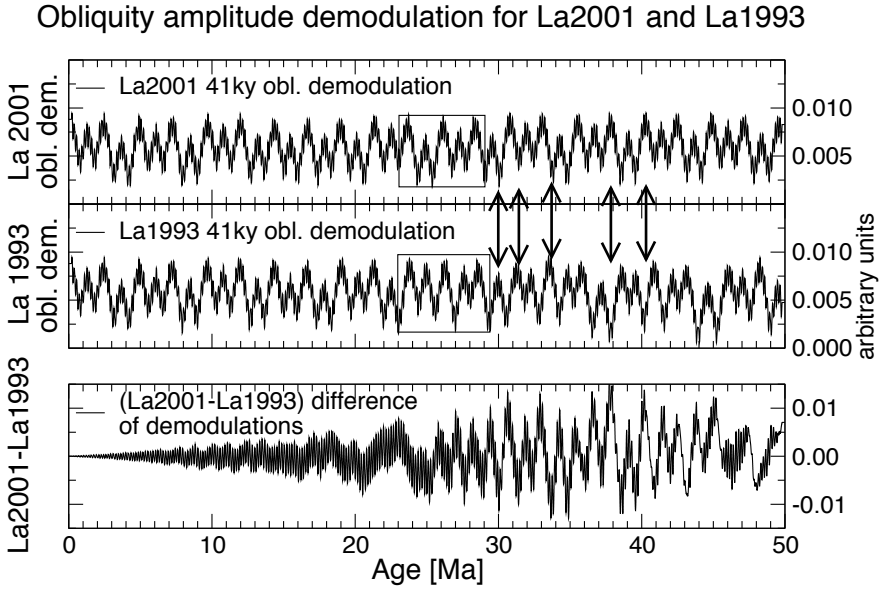

Figure 5.13: Comparison of obliquity amplitude complex demodulation for La1993 and La2001 from 0–50 Ma. These curves reflect the amplitude of the obliquity cycle that results from the interference of different frequency components, producing distinctive "beat" patterns. Three main components are visible: very small scale cycles with a period of ∼170 ky, larger scale cycles with a ∼1.2 My period, as well as a succession of large and small ∼1.2 My cycles, corresponding to a ∼2.4 My amplitude modulation cycle. A critical transition is visible in the resonance behaviour between the ∼1.2 My and ∼2.4 My amplitude modulation cycle for the La1993 solution, but not for the La2001 solution (as indicated by boxes from ∼23-29 Ma). This has been identified as the main reason for the longer term difference between the two solutions, as shown in the difference plot at the bottom of the figure. Arrows mark those times particularly suitable for a test with geological data, since both solutions are out of phase during these times.

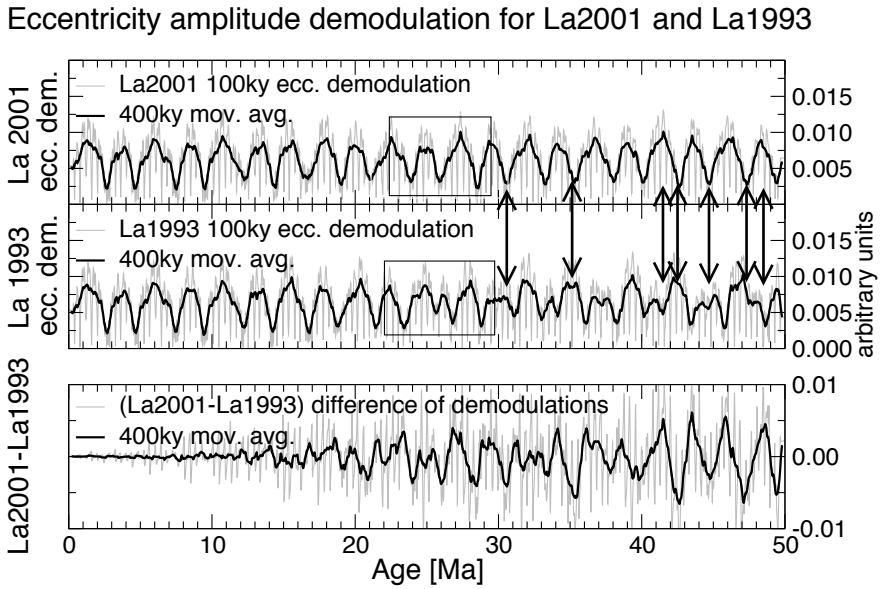

Figure 5.14: Comparison of ∼100ky eccentricity amplitude complex demodulation from La1993 and La2001 for 0-50 Ma. These curves reflect the amplitude of the eccentricity cycle that results from the interference of different frequency components, producing distinctive "beat" patterns. Similar to figure 5.14, three main components are visible. Sharp small scale cycles with a period of ∼400 ky reflect the modulation of the ∼100 ky eccentricity cycle by the ∼400 ky eccentricity component. Longer term cycles are accentuated in this figure by applying a 400 ky long running mean to the demodulation, and illustrate a ∼2.4 My long cycle. This is in resonance with the ∼1.2 My long cycle visible in the obliquity record (see figure 5.13). Again, a change in this resonance occurs in the La1993 solution, but not in the La2001 solution, as indicated by boxes. During this interval the La1993 solution shows a short switch from a ∼2.4 My long cycle to a ∼1.2 My long cycle. This has been identified as the main reason for the longer term difference between the two solutions, as shown in the difference plot at the bottom of the figure. Arrows mark those times particularly suitable for a test with geological data, since both solutions are out of phase.

5.3.4 Differences in obliquity amplitude modulation

Figure 5.13 demonstrates that both solutions are very similar with respect to the position of the ∼1.2 My amplitude modulation terms, back to an age of approximately 20 Ma. Beyond this interval, one can see that the ∼1.2 My amplitude modulation in the solution La1993 is of very similar amplitude between ∼24 and ∼29 Ma, whereas the solution La2001 shows a continuation of a regular pattern over this time interval. This is the first effect of the change in the resonance behaviour mentioned before. Before 29 Ma, the amplitude modulation cycles are consistently out of phase. At certain times, there is a very strong difference between the two, e.g. where the old solution showed a 0.6 My half-cycle of strong obliquity amplitude, this is now weak in the new solution and vice versa. The time intervals that would be interesting to test with geological data for this reason are at ∼30, 31, 35, 38 and 40 Ma, as marked on figure 5.13.

5.3.5 Differences in the eccentricity modulation

Figure 5.9 shows that on short time scales, the old and new solutions show differences already for ages younger than ∼8 Ma. This is the result of a new average frequency, particularly in the 400 ky cycle, which is still the most stable cycle as discussed in Laskar (1999) [89]. For ages older than 10 Ma, the two solutions are also significantly different in their longer term (∼2.4 and ∼1.2 My) modulation patterns. Intervals that are suitable for a geological "test" (because troughs are close to peaks) are marked on figure 5.14, and include the times of ∼35, 41.5, 42.5, 45, 47, and 48.5 Ma.

By combining evidence from eccentricity and obliquity modulation patterns, geological data should be able to discern between the two astronomical models if one considers times older than 30 Ma. Evaluating these amplitude modulation terms is generally preferable to comparing individual cycles. This is because it should be easier to remove the effects of "noise" and other geological processes, and exact timing is not crucial to the same level as if one was to compare individual precession cycles. Thus, amplitude modulation patterns allow a greater amount of uncertainty in time. Drawbacks of considering long term amplitude modulation cycles are that a long record of geological data is required, and that during that time interval the main transfer function from the forcing to deposition must not change significantly.

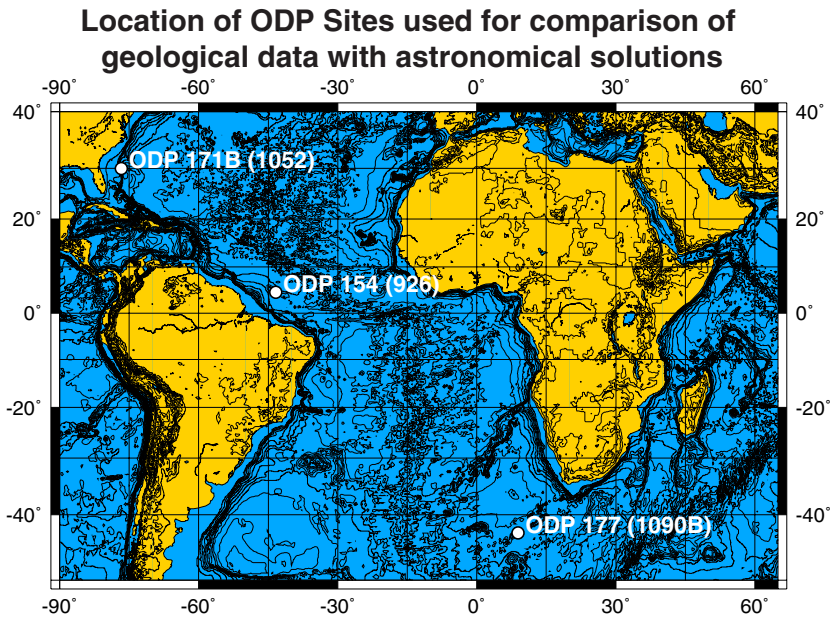

Figure 5.15: Location map of ODP sites that were used to compare predictions from different astronomical solutions with geological data.

5.3.6 Analysis of geological data and their limitations

An investigation is now made whether geological data are able to differentiate between the two astronomical models, evaluating various time intervals. In this study data from three different sites will be considered. Data are required that have been astronomically tuned, and span at least several million years such that it is possible to discern variations in the amplitude modulation. Figure 5.15 shows ODP Sites that are considered for this comparison. Data from ODP Leg 154 were already discussed in this chapter, while data from ODP Legs 171B and 177 were presented in chapter three. These sites are located in the equatorial Atlantic (ODP Leg 154), the western North Atlantic (ODP Leg 171B), and the Southern Ocean (ODP Leg 177). Here, model and data will be compared over the time intervals 18-30 Ma, and 33.5-39.5 Ma. Between the present and 18 Ma there is no significant difference in the amplitude modulation terms of the two astronomical solutions, so no attempt is made to investigate the time interval younger than 18 Ma, even though individual phase relationships between the two solutions are different then.

At this stage it is appropriate to point out some of the problems that are inherent in working with geological data to extract information about the forcing. First, there is always a considerable amount of variation that does not arise from a response to orbital

forcing of the climate system. In this context, this can be called "noise". However, part of this "noise" is also a corruption of the sediment record that arises through changes in the climate and ocean circulation system, e.g. via changes in dissolution cycles via variations in the carbonate compensation depth (CCD), changes in productivity according to up-welling and down-welling regimes, changes in terrestrial sediment supply etc. These factors have to be carefully considered before taking geological data at face value with respect to orbital variations.

Second, there is invariably a considerable amount of uncertainty in the absolute dating, even of astronomically calibrated sections, and this uncertainty generally increases as one goes back in time. The uncertainty arises through many different factors, and partly involves the fact that astronomically tuned data will be calibrated to a certain astronomical model, making several assumptions of the Earth system as a whole. For this reason it is best to evaluate long term amplitude modulation patterns, because they occur on a time scale that is comparable to realistic uncertainties in the absolute ages of geological material, even if "tuned" to a different astronomical model. This requires very long data series that are rare, and very time consuming to generate and calibrate.

Moreover, it might be necessary to compare data from several different sites for a given time interval, because otherwise it will be difficult to assess whether changes in the amplitude response to a forcing at a certain frequency are local or global in origin. This problem can be partly addressed by analysing different proxy records, such as stable isotopes in conjunction with lithological parameters like magnetic susceptibility. This is restricted, though, by the fact that there is only a limited amount of data available.

5.3.7 Feature comparison of data and models from 18 to 28 Ma

The astronomical tuning that was carried out by Shackleton *et al.* (1999) [55] with data from ODP Leg 154 (Ceara Rise) provides the longest, astronomically tuned record that can be used to evaluate astronomical models so far. Good quality data are available from this location, covering the time interval from 18-28 Ma, with further data, that are less well constrained, back to 30 Ma. This record was astronomically calibrated to the $La1993_{(1,1)}$ time scale by considering the variation inherent in the magnetic susceptibility and colour reflectance data. The strongest variation was found to occur in the

obliquity (∼41 ky) frequency band, with additional power in the precession frequency band, and a smaller amplitude variation in the eccentricity frequency band. Recently, material from this record was used to generate stable isotope records over the time interval from ∼20 to 25 Ma (Paul *et al.*, 2000 [218]; Zachos *et al.*, 2001 [126]). These individual proxy records can now be analysed to evaluate which astronomical solution is more consistent with the data over this time interval. A deliberate decision was made to use the data tuned to the solution La1993, since it will provide additional independence for the evaluation of the new solution. Furthermore, it is necessary to establish which solution is the better one before embarking on further analysis.

5.3.8 Obliquity amplitude modulation

It is the obliquity signal that is strongest in the lithological data from ODP Leg 154, and therefore it is likely that this is the best "carrier" signal to record amplitude modulations with fidelity. Complex demodulation (Bloomfield, 1976 [166], Shackleton *et al.*, 1999 [55]) was used to compute the amplitude envelope for the obliquity in the two astronomical models and the geological data. Then, singular spectrum analysis (SSA) (Yiou *et al.*, 1996 [219]) was used in conjunction with lowpass filters to extract the ∼1.2 My cycle. This last step is not strictly necessary but allows an easier visual comparison of the long term amplitude modulation. The SSA method can be thought of as a data-adaptive filter, and is used to suppress the ∼170 ky modulation that arises from the interference of the 54 ky and 41 ky components of obliquity (Hinnov, 2000 [92]).

Figure 5.16 shows how the signal that is contained in the ODP 154 geological data (magnetic susceptibility and colour reflectance) compares with the two astronomical models. Generally, the new solution La2001 fits much better to the data than the solution La1993. Vertical grey bars are used in the figure to demonstrate those intervals in time where the geological data seem to support the solution La2001 over La1993. This is evident through a difference in phase, i.e. the position of peaks and troughs, as well as a persistent variation in amplitude. As outlined before, the ∼2.4 My long cycle is also present in the obliquity amplitude modulation for the solution La2001, but briefly absent in the solution La1993 over the time interval ∼23.6-28.4 My. This succession of larger and smaller ∼1.2 My amplitude modulation cycles, that is characteristic for the absence of a switch in the resonance behaviour, can be seen in the data, and thus also supports the solutions La2001. At around 29.5 Ma the geological data show a

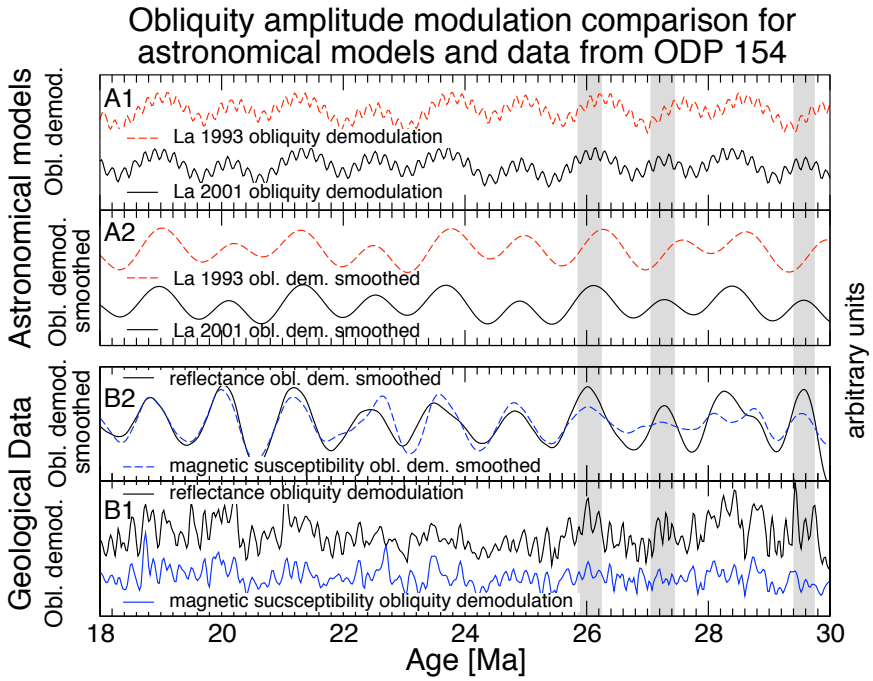

Figure 5.16: Obliquity amplitude modulation comparison for astronomical models La 2001 and La1933, and data from ODP 154 (18-30 Ma). Panel A1 shows the amplitude modulation of the 41 ky obliquity component. This has been smoothed to extract the ~1.2 My long modulation component (panel A2). Panel B1 shows the amplitude modulation of the 41 ky obliquity cycle in the colour reflectance and magnetic susceptibility data, and also smoothed in panel B2. The grey shaded areas show time intervals where the geological data strongly support the solution La 2001. These are times when the ~1.2 My amplitude cycles of La 1993 and La2001 are considerably out of phase. The geological data were tuned to the La1993 solution, thus being completely independent from the new solution La2001.

peak in amplitude, which agrees well with the solution La2001, but not with the solution La1993. The amplitude variation is much weaker in the solution La1993 due to the onset of a $1:1$ resonance regime (the disappearance of the ∼2.4 My cycle).

5.3.9 Eccentricity and climatic precession amplitude modulation

The variability associated with climatic precession and eccentricity in the sediments from ODP Leg 154 is weaker than that associated with variations in obliquity. This means that it is more difficult to extract a modulation signal that is as clear as that obtained from obliquity variations. Indeed, Shackleton *et al.* (1999) [55] demonstrated that the amplitude modulation of the precession is present in the magnetic susceptibility data, but they failed to extract a clear signal that is associated with the ∼2.4 My amplitude modulation related to the $(g_4 - g_3)$ term. In order to improve on these findings, one can make use of the theoretical presence of this modulation term in the climatic precession signal as well as in the eccentricity (Laskar, 1999), and gain more information by combining the information encoded in both signals simultaneously. Indeed, the term $(g_4 - g_3)$ is present in the modulation of the short eccentricity cycle (∼96 and 126 ky periods), as well as in the ∼400 ky cycle, which in turn are both modulating the climatic precession signal. The presence of the ∼2.4 My amplitude modulation cycle is a new finding, and is visible in figures 5.10 and 5.11. The presence of the terms $(g_4 - g_3)$ and $(s_4 - s_3)$ in the amplitude modulation of the ∼400 ky cycle does not arise from the linear parts of the astronomical solution but are in fact some of the first nonlinear terms (Laskar, personal communication), which is qualitatively different to the presence of these terms in the obliquity and short eccentricity amplitude modulation. An attempt was made to enhance the signal-to-noise ratio of this signal in the data by 1. combining the eccentricity and precession component, and 2. combining the signal inherent in the magnetic susceptibility as well as colour reflectance.

Figure 5.17 shows the results of this procedure. The first processing step computed, by complex demodulation, the amplitude modulation of the climatic precession signal in the two magnetic susceptibility and colour reflectance data sets. This reflects the amplitude modulation of precession by eccentricity and thus extracts both the long and short eccentricity variability. The output was then demodulated again to extract the amplitude modulation of the ∼100 ky component (which should be the ∼400 ky cycle). The eccentricity amplitude modulation of the ∼100 ky cycle was then also de-

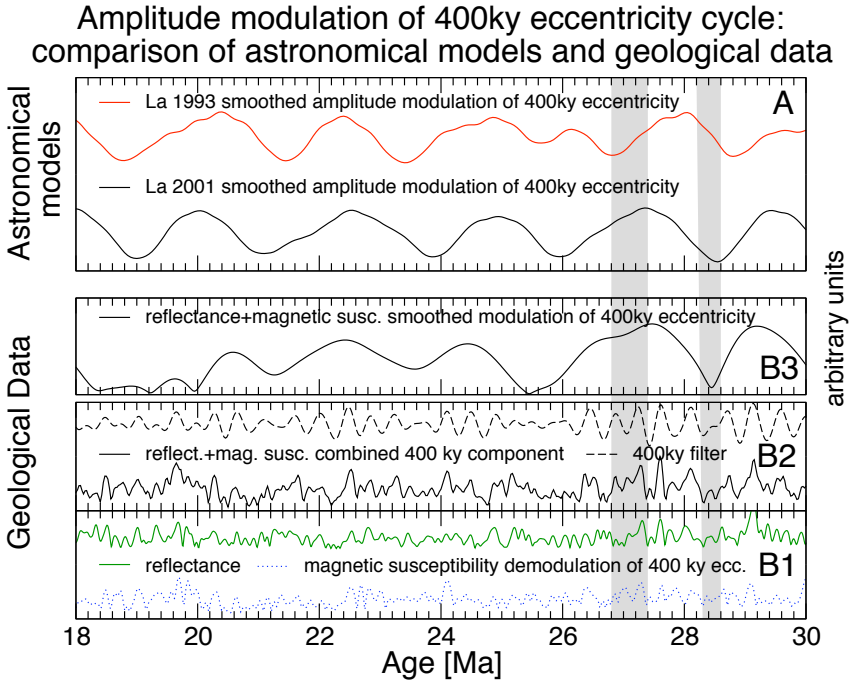

Figure 5.17: Comparison of the amplitude modulation of the 400 ky eccentricity cycle in the astronomical models La2001 and La1993, and data from ODP 154 (18–30 Ma). It was not possible to extract directly the ∼2.4 My amplitude modulation cycle from the data. Thus, it was extracted from several sources and combined. Panel B1 shows the amplitude demodulation of the 400 ky eccentricity cycle for magnetic susceptibility and colour reflectance. These two contributions were added and filtered, as shown in panel B2. Finally, the amplitude modulation was computed from this filter, and is shown in panel B3. This can be compared with the same type of signal, as extracted from the astronomical solutions La1993 and La2001. Due to the additional processing steps, the data cannot be interpreted with the same confidence as the obliquity demodulation shown in figure 5.16. However, the grey-shaded areas indicate that it is again the La2001 solution that is more consistent with the data over this interval.

modulated directly in the two data sets. For each data set there are now two time series that should reflect the ∼400 ky cycle and its amplitude variation. To enhance the signal one can now add the normalised contributions from eccentricity and climatic precession for each data set (shown in panel B1 of figure 5.17), and add these two curves to further enhance the signal (panel B2). This process gave an enhanced signal compared to amplitude modulation of eccentricity and climatic precession considered on their own for each data set. One can then extract the ∼400 ky cycle by bandpass filtering (panel B2, top) and finally extract the long-term amplitude variation (panel B3).

This can now be compared to the long term variation due to the term $(g_4 - g_3)$ that can be found in the astronomical models (figure 5.17, panel A). Grey shaded areas on the plot mark those times where geological data seem to be able to differentiate between the two astronomical models. It is clear that the signal of the term $(g_4 - g_3)$ extracted from geological data is not as evident and stable as that extracted from variations in obliquity. However, it is possible to see that this comparison again favours the astronomical solution La2001. At around 26 Ma a switch in resonance leads to a short peak in amplitude in the solution La1993, which is not visible in the data. At around ∼27 Ma and ∼28.5 Ma the data also support the new solution. Note that the data were "tuned" to the solution La1993. In the solution La2001 the 400 ky eccentricity cycles are offset towards older ages by approximately 100 ky compared to the solution La1993 over this time interval, leading to an even better fit between geological data and the solution La2001.

5.3.10 Comparison of data and models from 33 to 38 Ma

In this section a comparison is made between the predictions of astronomical models and geological data that were presented in chapter three. During the late Eocene, the computations for obliquity and eccentricity between the solutions La1993 and La2001 are very different in terms of their position of amplitude modulation minima and maxima. This is due to the absence of a resonance switch in the new solution La2001. Figure 5.18 shows a comparison of the obliquity amplitude modulation present in the two solutions La1993 and La2001, compared with data from ODP Sites 1052 and 1090.

Figure 5.18 is analogous to figure 5.16, although here no smoothing was performed to suppress the ∼170 ky component of amplitude modulation because the available data span a shorter time span. Considering data from Sites 1052 and 1090 together

again suggests that the new solution La2001 is more consistent with the data. This record should be interpreted more cautiously than that obtained from Ceara Rise (Leg 154) for younger time intervals, due to the switch in the recording of orbital forcing discovered in chapter three for data from Leg 171B, and because the data from ODP Leg 177 are only from one hole, not allowing the complete elimination of core breaks.

An attempt was also made to extract the amplitude modulation patterns from both sites for the eccentricity and climatic precession components. These signals are much weaker in both records. Due to this, and due to the disruption of the precession signal in data from Site 1052, the amplitude modulation patterns from both sites for eccentricity and climatic precession do not agree very well with each other, nor do they agree very well with either of the two astronomical solutions. Therefore, amplitude modulation patterns for eccentricity and climatic precession from ODP Sites 1052 and 1090 are not suitable for a comparison with astronomical calculations, and are excluded from further analysis.

5.3.11 Comparison of solution La2001 with an independent calculation

In addition to the new astronomical calculation La2001 by Laskar, very recently a completely independent calculation was performed by Varadi *et al.* [220]. As of yet, data are not published but available upon request from the author. Varadi *et al.* did not attempt to calculate solutions for the obliquity or climatic precession component, but included similar additional terms as in the 2001 solution of Laskar, such as a separate treatment of the Earth-Moon system. Because this calculation was obtained completely independently from that of Laskar, it can serve to give an indication of the robustness of these astronomical calculations.

Figure 5.19 shows the eccentricity calculation of the new solution La2001, as well as the difference between the eccentricity from La2001, and that obtained by Varadi *et al.* in their most recent model run "R10". Both calculations agree remarkably well over the last 40 My, beyond which they diverge significantly. The close resemblance of the two calculations over the last 40 My implies that the solution of Varadi *et al.* does not contain a switch in the $(g_4 - g_3)$ term over this time interval, which would be responsible for a change from the $\sim$2.4 My amplitude modulation cycle to one with a period of $\sim$1.2 My. This finding is encouraging and also implies that geological data will fit well with the solution of Varadi *et al.* No comparison can be made for the obliquity or climatic

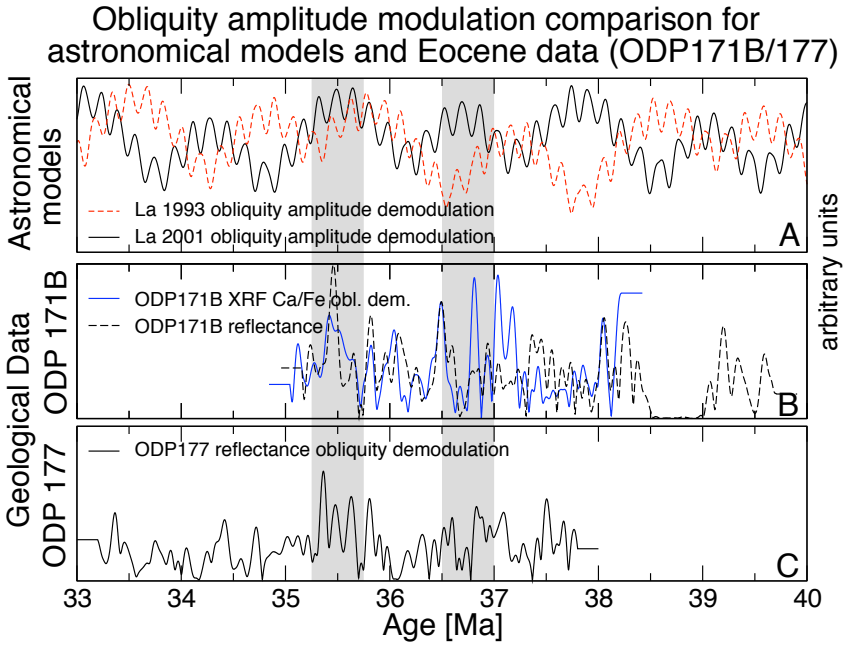

Figure 5.18: Obliquity amplitude modulation comparison for astronomical models La2001 and La1993, and data from ODP 171 and 177 (33-40 Ma). Similar to figure 5.13, panel A shows the amplitude modulation of the 41 ky obliquity component for the astronomical solutions La1993 and La2001. It is clear that in the Eocene these two solutions are almost exactly out of phase with respect to their modulation pattern. Panel B shows the same analysis performed for colour reflectance and XRF elemental data from ODP 171B, as discussed in chapter three. Panel C shows the amplitude demodulation for obliquity from reflectance data of ODP 177, also discussed in chapter 3. Comparing B and C with A, astronomical model La2001 is more consistent with the data, particularly where indicated by grey shaded areas. Data from both sites are subject to more noise and some core breaks, and thus should be interpreted with more caution than data from ODP 154.

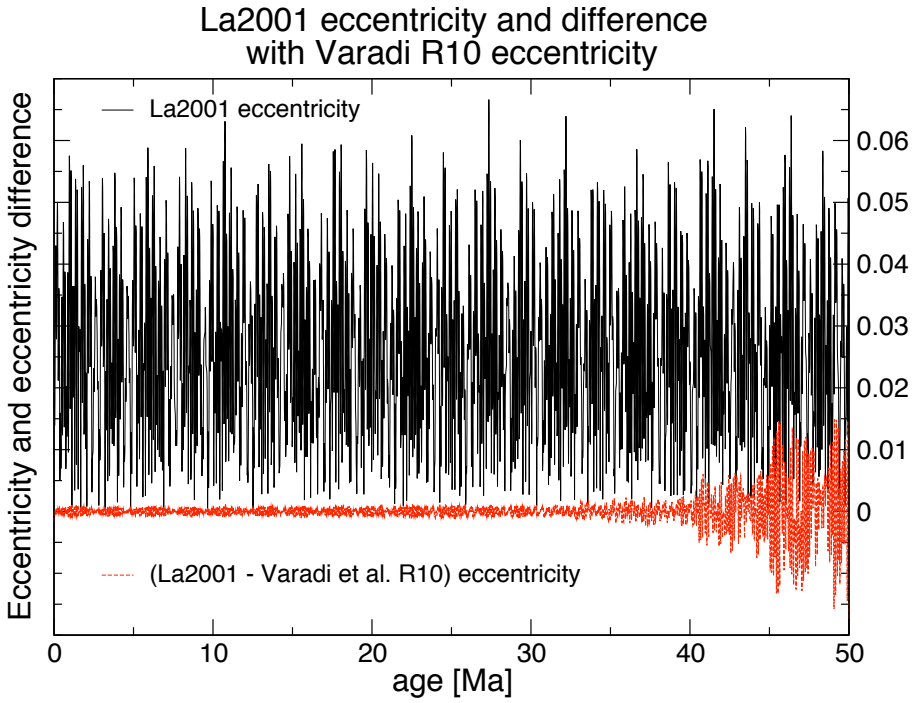

Figure 5.19: Comparison of eccentricity calculations La2001 and Varadi *et al.* (calculation R10) [220] from 0-50 Ma. Back to approximately 40 Ma the two solutions are almost identical, but diverge before this time. The calculation by Varadi *et al.* was obtained completely independently from that of Laskar, and also does not show a switch in the ∼2.4 My amplitude modulation term. Varadi *et al.* did not compute variations of obliquity or climatic precession, hence no further analysis was possible as to why the solutions diverge before 40 Ma.

precession components.

5.3.12 Is a rare orbital anomaly the trigger for the unusual oxygen and carbon isotope ("Mi-1") event?

An additional implication of the findings presented here is that one of the hypotheses proposed by Zachos *et al.* (2001) [126] is not compatible with the new astronomical solution La2001, which is the solution supported by geological data. Zachos *et al.* suggested that a major transient oxygen and carbon isotope event (the "Mi-1 event") at the Oligocene/Miocene epoch boundary (∼23 Ma) might be related to a response of the climate system to an unusual alignment of a weak obliquity amplitude and low eccentricity values. This speculation was prompted by the coincidence of the Mi-1 event with the orbital elements, according to the astronomical calibration of Shackleton *et al.*

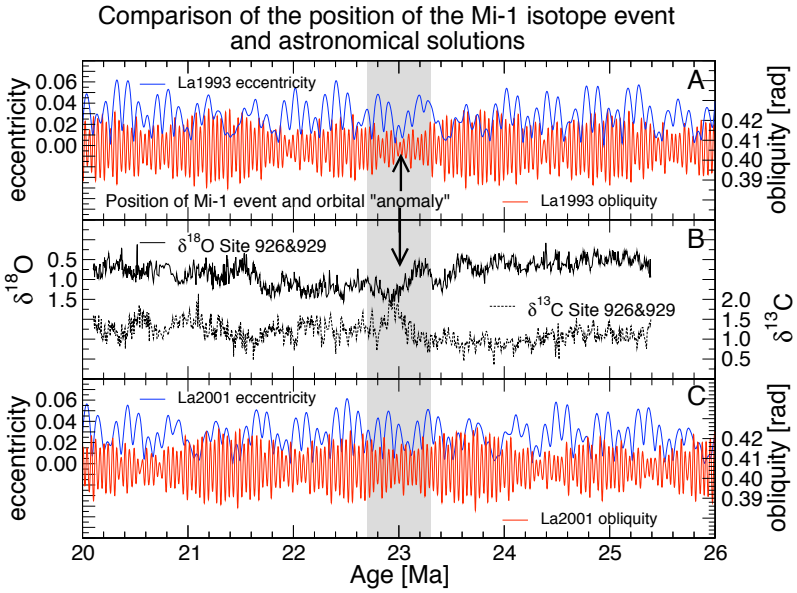

Figure 5.20: Comparison of orbital calculations (panel A: Laskar 1993, panel C: Laskar 2001) and the Mi-1 stable isotope event (panel B: stable isotope data from ODP 154, Zachos *et al.* (2001) [126]). The new astronomical solution La2001 does not show the rare congruence of a very low obliquity amplitude and low eccentricity values at the Oligocene/Miocene boundary at ∼23 Ma. It is thus incompatible with one of the hypotheses put forward by Zachos *et al.* (2001) [126] to explain the origin of the Mi-1 event.

(1999) [55].

However, this rare orbital congruence does not exist in the new orbital solution at exactly this time, as shown in figure 5.20. A similar, but less extreme, orbital alignment of low obliquity amplitude and low eccentricity occurs in the solution La2001 at ∼24.3 Ma.

The results presented in this chapter, illustrated by figures 5.16 and 5.17, broadly strengthen the age calibration of Shackleton *et al.* and make it very unlikely that any modification would move the Mi-1 event to ∼24.3 Ma. On the contrary, the astronomically calibrated age of the Oligocene/Miocene boundary [221] is supported by long term amplitude modulation patterns, and does fit equally well with both astronomical solutions. This implies that the hypothesis put forward by Zachos *et al.* is not likely to be correct.

5.3.13 Findings from evaluation of astronomical solutions

It has been demonstrated that the established astronomical calculation of Laskar *et al.* (1993) [86] is quite different to a more recent calculation that was completed by Laskar in 2001. The main difference between the two astronomical models was found to be the absence of a switch in the resonance behaviour between obliquity and eccentricity amplitude modulation terms in the more recent calculation. This leads to significant differences between the two solutions before ~20 Ma, which would result in different ages for studies that make use of long term amplitude modulation terms.

This study showed that it is possible to extract the amplitude modulation terms that are indicative for a switch in resonance from long, high-resolution geological time series. A comparison between geological data from different locations and astronomical models demonstrates convincingly that the more recent astronomical calculations show a significantly better fit with the signal extracted from different geological data, at least as far back as ~37 Ma. This important finding will significantly aid in the further extension of an astronomically calibrated time scale, and also demonstrates for the first time that geological data can be used to validate the predictions of astronomical models with respect to the presence of resonance features in the solar system. These findings also imply that small changes (of the order of possibly 100-300 ky) will result from the re-adjustment of established astronomically calibrated time scales to the more recent astronomical calculations. The arguments in favour for the astronomical solution La2001 now warrant its adoption, and re-tuning of data from Leg 154 to the new solution.

5.4 Conclusions

In this chapter it was shown how it is possible to extract various parameters that are necessary to define astronomical calculations from geological data. The first section demonstrated that the tidal dissipation and dynamical ellipticity of the Earth are likely to have been very similar to present day values over the last ~25 My. This puts important constraints on astronomical and mantle convection models. A new interference method was developed, which allows the detection of very small changes in the precession constant p, while at the same time allowing the elimination of effects that due to using a particular astronomical solution to generate a geological age model.

The second part of this chapter evaluated a new improved astronomical calculation by extracting long term amplitude modulation patterns from astronomical solutions and geological data. Results indicate that this new computation does fit geological data significantly better over the last ∼35 My. This implies that over this time interval there has not been a switch in the resonance system of the solar system, thus providing additional constraints for astronomical calculations. The new solution should now be used for further astronomical calibrations. Moreover, the new solution provides additional support for the Oligocene/Miocene time scale constrained by Shackleton *et al.* (1999) [55], implying that a re-tuning of geological data to the new astronomical solution La2001 should be relatively straightforward.

Chapter 6

Conclusions and future work

6.1 Introductory remarks

The astronomical theory set out in chapter one demonstrated the rich set of features that are inherent in astronomical calculations of the behaviour of the solar system. These features form the basis for the identification of orbital signals in the geological record. It was demonstrated that of particular significance are long term modulations in the amplitude (and frequency) of specific orbital elements, which potentially allow geological data to be placed in the correct position with respect to orbital calculations. This, in turn, then allows the extraction of astronomical signals from the geological record to improve orbital calculations. Constraints on orbital parameters obtained this way should eventually facilitate detailed modelling studies that relate the modifications the orbital signal undergoes before it is encoded in the geological record, to specific features of climatic, ocean and atmospheric circulation processes.

6.2 Conclusions: An automated astronomical tuning method

In chapter two the need for an objective numerical method of stratigraphic correlation and astronomical calibration was established. It was shown that a speech recognition algorithm can be usefully adapted to provide an objective method for adjusting multiple geological data to a "target curve", which could be either an astronomical model, or a different set of geological data, subject to a set of constraints for parameters such as sedimentation rate, or specific calibration datums. It was possible to demonstrate, using synthetic data sets, that superior correlation results can be obtained by incorporat-

ing dynamic bandpass filtering into the automated correlation algorithm. By applying this modified algorithm to real geological data, and specifying a set of different boundary conditions, it was shown that it is possible to obtain an objective measure for the sensitivity of the calibration process to non-orbital signals in the geological record, as well as a measure of uncertainty arising from the unknown exact position of tie points.

6.3 Conclusions: A new age calibration of the late Eocene

Chapter three documents how a high-resolution late Middle to Late Eocene record of elemental concentration data was generated by using an X-ray fluorescence (XRF) core scanner to perform measurements on marine sediments recovered during ODP Leg 171B from Site 1052. The XRF data allowed the establishment of a detailed stratigraphic correlation across cores from different holes. This work showed that it is necessary to compensate for intra-core stretching and squeezing by matching common features of proxy records on a decimetre scale. This compensation resulted in the generation of a new "rmcd" depth scale, which in turn facilitated the stacking of data from different holes. The stacking process resulted in an improved signal-to-noise ratio.

The XRF data were then used to generate an astronomically calibrated age model, making use of amplitude modulation variations in the data that reflect the most stable [89] ~400 ky orbital eccentricity. New estimates were obtained for the relative duration of magnetochrons C16 through C18, which are similar to previous estimates based on an interpolation between radiometrically dated control points (Cande and Kent, 1995 [46]).

An additional significant finding was that certain long term amplitude modulation patterns imply that the most recently published astronomical calculation of Laskar *et al.* (1993) [86] is not compatible with the geological record during the late Eocene. For the first time, a distinct change in the relative strength of orbitally driven obliquity and climatic precession signals has been observed during the late Eocene. This event awaits confirmation from studies from other locations, but might represent a sudden change in the climatic and ocean circulation system at this time, and will be potentially useful as a stratigraphic marker.

The new age model from Site 1052 was successfully transferred to ODP Site 1090 (Leg 177) by correlation of the XRF record from Site 1052 with the colour reflectance record from Site 1090. The presence of orbitally driven variability of data from Site

1090 allowed a verification of the consistency of magnetic reversal ages estimated from Site 1052, as well as extending the astronomical calibration upwards to the base of the Oligocene.

6.4 Conclusions: A detailed stable isotope record from the Eocene

Chapter four reported results from an investigation of high-resolution stable isotope records from Site 1052. The newly established astronomically calibrated time scale from Site 1052 facilitated a detailed evaluation of orbitally driven variations in the climate system, as represented by oxygen and carbon stable isotope proxies. The stable isotope data exhibit a weak orbital signal that is consistent with the time scale generated from the XRF record. Unexpectedly, the stable isotope data recorded an unusual succession of events that coincide with the depth at which the XRF and colour records show a switch in the dominant orbital signal. The causes for this unusual event are unidentified as of yet, and require a comparison with data from additional locations when they become available.

In conjunction with the detailed chronology developed, the combined record of climate system proxies should provide constraints on climate modelling studies that might improve the understanding of the interaction of processes that control the climate system. The availability of planktonic as well as benthic stable isotope data will facilitate this process.

6.5 Conclusions: Extraction of orbital parameters encoded in geological data

Chapter five presented two studies that, together with a new late Eocene time scale, provide some of the most significant results reported in this dissertation. A new method, based on interference patterns between orbital signals, was developed, which allowed the estimation of the average values of the Earth's precession constant p over the last 25 million years. This result provides constraints for which astronomical models are most consistent with geological data, and has significant implications for the study of mantle convection and the viscosity structure of the Earth's mantle. It was

found that the values of the Earth's tidal dissipation and its dynamical ellipticity are likely to have remained similar to present day values over the last 25 million years.

In addition, chapter five shows how geological data spanning the last ~37 million years were used to extract long term amplitude modulation patterns of the climatic signal encoded in the geological record. A comparison of the long term amplitude modulation derived from astronomical calculations on the one hand, and those derived from a new calculation on the other hand (Jacques Laskar, 2001, unpublished), shows that the geological record supports the validity of the newer solution. This implies that the solar system has not experienced a switch in its resonance behaviour, thus providing for the first time constraints on its chaotic nature. In addition, this work supports a previous astronomical time scale calibration near the Oligocene/Miocene boundary [55; 221]. These results are, however, not compatible with the orbital anomaly hypothesis of Zachos *et al.* (2001) [126].

6.6 Future work

- Work presented here provides the first astronomical calibration of the geological time scale for the late Middle to Late Eocene. However, it is crucial to generate suitable data from additional locations to verify and refine the results obtained here.

- At present, the late Eocene chronology is still floating in time. Additional data are also needed to connect the record presented here with the study of Shackleton *et al.* (1999) [55], which provides a (tentative) calibration to the base of the Oligocene.

- The extension and verification of the new late Eocene chronology will be facilitated by employing the newly developed automated tuning algorithm. This algorithm can be improved further by including additional filtering constraints. Work is in progress to dynamically match amplitude modulation patterns between data and the target curve. This involves the application of complex demodulation methods, and has still to be tested thoroughly.

- Although XRF data display a stronger orbital signal than previously used lithological proxies such as magnetic susceptibility, the exact origin of this signal has

yet to be established. The calcium and iron concentration data obtained by XRF measurements correlate well with chemical measurements of calcium carbonate content. Detailed petrographic and mineralogical studies are needed to establish which mineral phases contain what proportions of different elements.

- Additional stable isotope measurements from planktonic, thermocline, and benthic foraminifera are required from different locations and palaeodepths to establish the exact nature of the ocean circulation system during late Eocene time.

- Additional high-resolution stable isotope records should also be generated across the unusual stable isotope excursion event reported in chapter four. This would help to establish whether the record is local or global in origin.

- The determination of the evolution of tidal dissipation and dynamical ellipticity of the Earth might be possible without the intermediate step of parameterisation of the astronomical model, as was done in this study. This will require considerable computational facilities, which should be available in the soon future. Together with additional high quality data, this would also allow to resolve the apparent conflict between results reported in this study, and those reported by Lourens *et al.* (2001) [156].

- Astronomically calibrated ages should be used to re-estimate spreading rates of individual plate segments. Work is in progress to provide an updated compilation of spreading profiles.

This study provides the necessary framework for a further extension and consolidation of the astronomically calibrated geological time scale. It is now time for a coordinated strategy between different research groups to make progress towards a continuous astronomical calibration for the entire Cenozoic, and beyond. A first step towards this goal might be provided by the two forthcoming ODP Legs 198 and 199, which are scheduled to recover deep-marine sediments from the Paleogene. An overview of attempts to astronomically calibrate sections of the Cenozoic is given in figure 6.1, and demonstrates that work in the field of astronomical time scale calibration will provide work for many researchers for years to come, with the promise of exciting and important results that will have an impact on the entire field of Earth sciences.

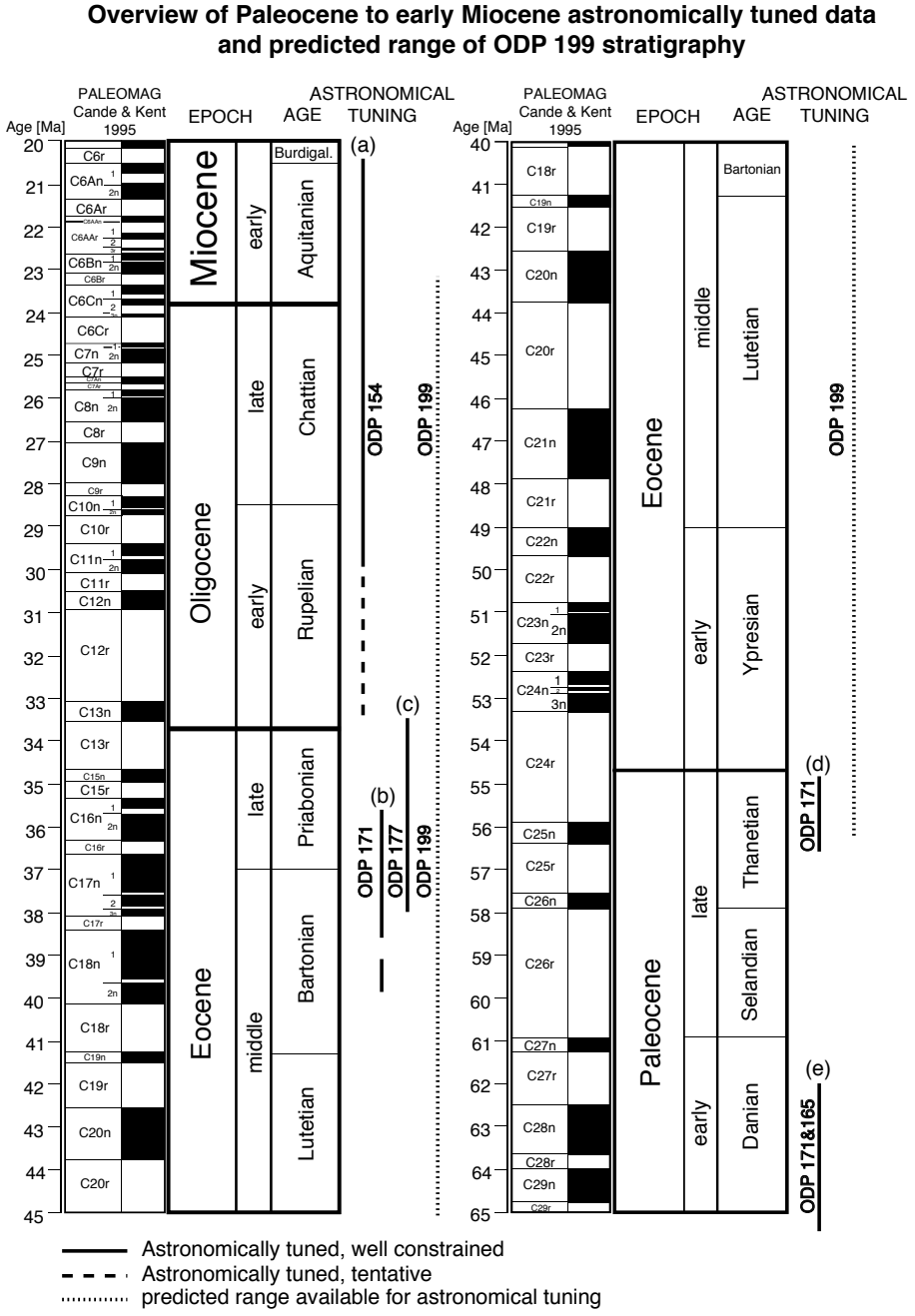

Figure 6.1: An overview of geological data that have been astronomically calibrated for parts of the Cenozoic. The dotted line shows the stratigraphic range predicted for the recovery of material during ODP Leg 199. The oldest age of sediment from Leg 199 is constrained by the estimated age of basement (∼56-57 Ma). References to the calibrated sections are (a) [55; 155] (b) this study, and [135], (c) this study, (d) [161; 222], and (e) [103]. The time scale is that of Cande and Kent (1995) [46].

References

[1] J. H. Lesher, Xenophanes of Colophon-Fragments: Text and Translation with Notes and Commentary, Presocratics Volume IV of Phoenix Supplementary Volume XXX, University of Toronto Press, Toronto, 1992.

[2] Herodotus, The History of Herodotus/ translated by George Rawlinson, The library of living classics volume IX, Tudor, New York, 1934.

[3] F. Raab, Leonardo da Vinci als Naturforscher: Ein Beitrag zur Geschichte der Naturwissenschaft im Zeitalter der Renaissance, Sammlung gemeinverständlicher wissenschaftlicher Vorträge, 15. Ser; 350, Habel, Berlin, 1880.

[4] J. Ussher, The annals of the world: deduced from the origin of time, and continued to the beginning of the Emperour Vespasians reign, and the total destruction and abolition of the temple and common-wealth of the Jews: containing the historie of the Old and New Testament, with that of the Macchabees, also the most memorable affairs of Asia and Egypt, and the rise of the empire of the Roman Caesars under C. Julius, and Octavianus: collected from all history, as well sacred, as prophane, and methodically digested/ by ... James Ussher (1581-1656), volume [10], 907, 54 p., Printed by E. Tyler, for J. Crook and for G. Bedell, London, 1658, this was a posthumous edition of the 1650 original entitled Annales veteris testamenti a prima mundi origine deducti (The Annals of the Old Testament, Deduced from the First Origin of the World).

[5] J. Hutton, Theory of the Earth: with proofs and illustrations. In four parts. By James Hutton, Printed for Messrs Cadell, Junior, and Davies, London; and William Creech, Edinburgh, 1795, two volumes only.

[6] J. Hutton, Theory of the Earth: with proofs and illustrations/ by James Hutton; edited by Sir Archibald Geikie, volume 3, Geological Society, London, 1899.

[7] C. Lyell, Principles of Geology volumes I-III, John Murray, London, 1830-1833.

[8] W. Smith, Memoir to the map and delineation of the strata of England and Wales, with part of Scotland, John Cary, London, 1815.

[9] W. Thomson, On the rigidity of the Earth, Proceedings of the Royal Philosophical Society of Glasgow V, 16, 1862.

[10] A. H. Becquerel, Sur les radiations invisibles émises par les sels d'uranium, Comptes Rendus de l'Académie des Sciences 122, 689–694, 1896.

[11] B. B. Boltwood, On the ultimate disintegration products of the radio-active elements. Part II. The disintegration products of uranium., American Journal of Science 23, 77–88, 1907.

[12] S. A. Bowring and I. S. Williams, Priscoan (4.00-4.03 Ga) orthogneisses from northwestern Canada, Contributions to Mineralogy and Petrology 134, 1, 3–16, 1999.

[13] H. H. Hess, The history of ocean basins, in: Petrologic studies: a volume to honor A.F. Buddington, A. E. J. Engel et al., eds., 599–620, Geological Society of America, Boulder, CO, U.S.A., 1962.

[14] F. J. Vine and D. H. Matthews, Magnetic anomalies over oceanic ridges, Nature 199, 947–949, 1963.

[15] A. Cox, R. R. Doell and G. B. Dalrymple, Geomagnetic polarity epochs and Pleistocene geochronometry, Nature 198, 1049–1051, 1963.

[16] J. Imbrie and K. Palmer-Imbrie, Ice ages; Solving the mistery, Enslow Publishers, Short Hills, NJ, U.S.A., 1979.

[17] J. L. R. Agassiz, Upon glaciers, moraines, and erratic blocks; address delivered at the opening of the Helvetic History Society at Neuchâtel, 24 Luly 1837 by its president, New Philosophy Journal Edinburgh 24, 864–883, 1838.

[18] J. L. R. Agassiz, Etudes sur les glaciers, privately published, Neuchâtel, Switzerland, 1840.

[19] J. Adhémar, Révolution des Mers, Déluges Périodiques, privately published, Paris, 1842.

[20] U. J. J. Le Verrier, On the long term evolution of the spin of the Earth, Annales de l'Observatoire de Paris vol. II, 1856, Paris: Mallet-Bachelet.

[21] J. Croll, Climate and time in their geological relations: a theory of secular changes of the Earth's climate, Daldy, Tsbister and Co., London, 1875.

[22] G. K. Gilbert, Sedimentary measurement of Cretaceous time, Journal of Geology III, 121–127, 1895.

[23] J. J. Murphy, The glacial climate and the polar ice-cap, Quarterly Journal of the Geological Society of London 43, 400–406, 1875.

[24] R. Spitaler, Das Klima des Eiszeitalters, Prague, 1921.

[25] M. Milankovitch, Théorie mathématique des phénomènes thermiques produits par la radiation solaire, Académie Yougoslave des Sciences et des Arts de Zagreb, Gauthier-Villars, Paris, 1920.

[26] M. Milankovitch, Kanon der Erdbestrahlung und seine Anwendung auf das Eiszeitenproblem, volume 33, Royal Serbian Sciences, special publication 132, section of Mathematical and Natural Sciences, Belgrad, 1941, ("Canon of Insolation and Ice Age Problem", English translation by Israël Program for Scientific Translation and published for the U.S. Department of Commerce and the National Science Foundation, Washington DC, 1969).

[27] W. Schwarzacher, Die Großrhythmik des Dachsteinkalkes von Lofer, Tschermak's Mineralogisch Petrographische Mitteilungen 4, 44–54, 1954.

[28] W. Schwarzacher, An application of statistical time-series analysis of a limestone-shale sequence, Journal of Geology 72, 195–213, 1964.

[29] J. D. Hays, J. Imbrie and N. J. Shackleton, Variations in the Earth's orbit: Pacemaker of the Ice Ages, Science 194, 4270, 1121–1131, 1976.

[30] C. Emiliani, Pleistocene temperatures, Journal of Geology 63, 6, 538–578, 1955.

[31] C. Emiliani, Isotopic paleotemperatures, Science 154, 851–857, 1966.

[32] G. M. Henderson and N. C. Slowey, Evidence from U-Th dating against Northern Hemisphere forcing of the penultimate deglaciation, Nature 404, 6773, 61–66, 2000.

[33] T. D. Herbert, J. D. Schuffert, D. Andreasen, L. Heusser, M. Lyle, A. Mix, A. C. Ravelo, L. D. Stott and J. C. Herguera, Collapse of the California Current during glacial maxima linked to climate change on land, Science 293, 5527, 71–76, 2001.

[34] CLIMAP Project Members, The surface of the ice-age Earth, Science 191, 1131–1137, 1976.

[35] J. Imbrie and J. Z. Imbrie, Modelling the climatic response to orbital variations, Science 207, 4434, 942–953, 1980.

[36] J. Imbrie, J. D. Hays, D. G. Martinson, A. McIntyre, A. C. Mix, J. J. Morley, N. G. Pisias, W. L. Prell and N. J. Shackleton, The orbital theory of Pleistocene climate: Support from a revised chronology of the marine δ^{18}O record, in: Milankovitch and Climate, Part 1, A. L. Berger et al., eds., 269–305, Reidel Publishing Company, 1984.

[37] D. G. Martinson, N. G. Pisias, J. D. Hays, J. Imbrie, T. C. Moore and N. J. Shackleton, Age dating and the orbital theory of the Ice Ages: Development of a high-resolution 0 to 300,000 year chronostratigraphy, Quaternary Research 94, 27, 1–29, 1987.

[38] A. Berger, Long term variations of daily insolations and Quaternary climatic changes, Journal of the Atmospheric Sciences 35, 12, 2362–2367, 1978.

[39] N. G. Pisias and T. C. Moore Jnr., The evolution of Pleistocene climate: a time series approach, Earth and Planetary Science Letters 52, 2, 450–458, 1981.

[40] W. F. Ruddiman, A. McIntyre and M. E. Raymo, Matuyama 41,000-year cycles: North-Atlantic Ocean and northern-hemisphere ice sheets, Earth and Planetary Science Letters 80, 1-2, 117–129, 1986.

[41] N. J. Shackleton, A. Berger and W. R. Peltier, An alternative astronomical calibration of the lower Pleistocene timescale based on ODP Site 677, Transactions of the Royal Society of Edinburgh: Earth Sciences 81, 251–261, 1990.

[42] A. K. Baksi, V. Hsu, M. O. McWilliams and E. Farrar, ^{40}Ar/^{39}Ar dating of the Brunhes-Matuyama geomagnetic field reversal, Science 256, 5055, 356–357, 1992.

[43] F. J. Hilgen, Astronomical calibration of Gauss to Matuyama sapropels in the Mediterranean and implication for the geomagnetic polarity time scale, Earth and Planetary Science Letters 104, 2-4, 226–244, 1991.

[44] F. J. Hilgen, Extension of the astronomically calibrated (polarity) time scale to the Miocene/Pliocene boundary, Earth and Planetary Science Letters 107, 2, 349–368, 1991.

[45] S. C. Cande and D. V. Kent, Ultrahigh resolution marine magnetic anomaly profiles: a record of continuous paleointensity variations?, Journal of Geophysical Research - Solid Earth 97, B11, 15,075–15,083, 1992.

[46] S. C. Cande and D. V. Kent, Revised calibration of the geomagnetic polarity timescale for the Late Cretaceous and Cenozoic, Journal of Geophysical Research - Solid Earth 100, B4, 6093–6095, 1995.

[47] D. V. Kent, Orbital tuning of geomagnetic polarity time-scales, Philosophical Transactions of the Royal Society of London Series A - Mathematical Physical and Engineering Sciences 357, 1757, 1995–2007, 1999.

[48] W. G. H. Z. ten Kate and A. Sprenger, Rhythmicity in deep-water sediments, documentation and interpretation by pattern and spectral analysis, Ph.D. thesis, Institute of Earth Sciences, Free University, Amsterdam, The Netherlands, 1992.

[49] F. J. Hilgen, L. J. Lourens, A. Berger and M. F. Loutre, Evaluation of the astronomically calibrated time scale for the late Pliocene and earliest Pleistocene, Paleoceanography 8, 5, 549–565, 1993.

[50] R. Tiedemann, M. Sarnthein and N. J. Shackleton, Astronomic timescale for the Pliocene Atlantic δ^{18}O and dust flux records of Ocean Drilling Program Site-659, Paleoceanography 9, 4, 619–638, 1994.

[51] N. J. Shackleton, S. J. Crowhurst, T. Hagelberg, N. G. Pisias and D. A. Schneider, A new late Neogene timescale: Application to Leg 138 sites, in: Proc. ODP, Sci. Res., N. G. Pisias, L. A. Mayer, T. R. Janecek, A. Palmer-Julson and T. H. van Andel, eds., volume 138, 73–101, Ocean Drilling Program, College Station, TX, 1995.

[52] F. J. Hilgen, W. Krijgsman, C. G. Langereis, L. J. Lourens, A. Santarelli and W. J. Zachariasse, Extending the astronomical (polarity) time scale into the Miocene, Earth and Planetary Science Letters 136, 3-4, 495–510, 1995.

[53] N. J. Shackleton and S. J. Crowhurst, Sediment fluxes based on an orbitally tuned time scale 5 Ma to 14 Ma, Site 926, in: Proc. ODP, Sci. Res., N. J. Shackleton, W. B. Curry, C. Richter and T. J. Bralower, eds., volume 154, 69–82, Ocean Drilling Program, College Station, TX, 1997.

[54] F. Hilgen, H. Aziz, W. Krijgsman, C. Langereis, L. Lourens, J. Meulenkamp, I. Raffi, J. Steenbrink, E. Turco, N. van Vugt, J. Wijbrans and W. Zachariasse, Present status of the astronomical (polarity) time-scale for the Mediterranean Late Neogene, Philosophical Transactions of the Royal Society of London Series A - Mathematical Physical and Engineering Sciences 357, 1757, 1931–1947, 1999.

[55] N. J. Shackleton, S. J. Crowhurst, G. P. Weedon and J. Laskar, Astronomical calibration of Oligocene-Miocene time, Philosophical Transactions of the Royal Society of London Series A - Mathematical Physical and Engineering Sciences 357, 1757, 1907–1929, 1999.

[56] P. Olsen, Periodicity of lake-level cycles in the Late Triassic Lockatong Formation of the Newark Basin (Newark Supergroup, New Jersey and Pennsylvania), in: Milankovitch and Climate, Part 1, A. L. Berger et al., eds., 129–146, Reidel Publishing Company, 1984.

[57] L. A. Hinnov and R. K. Goldhammer, Spectral-analysis of the middle Triassic Latemar limestone, Journal of Sedimentary Petrology 61, 7, 1173–1193, 1991.

[58] T. D. Herbert, Paleomagnetic calibration of Milankovitch cyclicity in Lower Cretaceous sediments, Earth and Planetary Science Letters 112, 15–28, 1992.

[59] A. S. Gale, J. R. Young, N. J. Shackleton, S. J. Crowhurst and D. S. Wray, Orbital tuning of Cenomanian marly chalk successions: towards a Milankovitch time-scale for the Late Cretaceous, Philosophical Transactions of the Royal Society of London Series A - Mathematical Physical and Engineering Sciences 357, 1757, 1815–1829, 1999.

[60] T. D. Herbert, A long marine history of carbon cycle modulation by orbital-climatic changes, Proceedings of the National Academy of Sciences of the United States of America 94, 16, 8362–8369, 1997.

[61] T. D. Herbert, Toward a composite orbital chronology for the Late Cretaceous and Early Palaeocene GPTS, Philosophical Transactions of the Royal Society of London Series A - Mathematical Physical and Engineering Sciences 357, 1757, 1891–1905, 1999.

[62] L. A. Hinnov and J. J. Park, Strategies for assessing early Middle (Pliensbachian - Aalenian) Jurassic cyclochronologies, Philosophical Transactions of the Royal Society of London Series A - Mathematical Physical and Engineering Sciences 357, 1757, 1831–1859, 1999.

[63] P. E. Olsen and D. V. Kent, Long-period Milankovitch cycles from the Late Triassic and Early Jurassic of eastern North America and their implications for the calibration of the Early Mesozoic time-scale and the long-term behaviour of the planets, Philosophical Transactions of the Royal Society of London Series A - Mathematical Physical and Engineering Sciences 357, 1757, 1761–1786, 1999.

[64] W. Yang and M. A. Kominz, Testing periodicity of depositional cyclicity, Cisco Group (Virgillian and Wolfcampian), Texas, Journal of Sedimentary Research 69, 6, 1209–1231, 1999.

[65] D. A. Short, J. G. Mengel, T. J. Crowley, W. T. Hyde and G. R. North, Filtering of Milankovitch cycles by Earth's geography, Quaternary Research 35, 2, 157–173, 1991.

[66] J. M. Barnola, D. Raynaud, Y. S. Kovotkevich and C. Lorius, Vostok ice core provides 160,000 year record of atmospheric CO_2, Nature 329, 6138, 408–414, 1987.

[67] J. R. Petit, D. Raynaud, N. I. Barkov et al., Climate and atmospheric history of the past 420,000 years from the Vostok ice core, Antarctica, Nature 399, 6735, 429–436, 1999.

[68] N. J. Shackleton, The 100,000-year ice-age cycle identified and found to lag temperature, carbon dioxide, and orbital eccentricity, Science 289, 5486, 1897–1902, 2000.

[69] A. Berger, J. Imbrie, J. Hays, G. Kukla and B. Saltzman, eds., Milankovitch and Climate: understanding the response to astronomical forcing, Proceedings of the NATO Advanced Research Workshop on Milankovitch and Climate (1982, Palisades, N.Y), volume 126 of Series C, Mathematical and physical sciences, NATO ASI series, D. Reidel Publishing Company, Dordrecht; Boston, 1984, two volumes.

[70] G. Einsele, W. Ricken and A. Seilacher, eds., Cycles and Events in Stratigraphy, Springer Verlag, Berlin, 1991.

[71] W. Schwarzacher, Cyclostratigraphy and the Milankovitch theory, volume 52 of Developments in Sedimentology, Elsevier, Amsterdam, 1993.

[72] P. L. de Boer and D. G. Smith, eds., Orbital forcing and cyclic sequences (IAS Special Publication), volume 19, Blackwell Scientific Publications, Oxford, 1994.

[73] M. R. House and A. S. Gale, eds., Orbital forcing timescales and cyclostratigraphy, volume 85 of Geological Society Special publication, The Geological Society, London, 1995.

[74] N. J. Shackleton, I. N. McCave and G. P. Weedon, eds., Astronomical (Milankovitch) calibration of the geological time-scale (9-10 December 1998, London), volume 357, number 1757 of Philosophical Transactions of the Royal Society of London Series A - Mathematical Physical and Engineering Sciences, The Royal Society, London, 1999.

[75] J. Laskar, La stabilité du Système Solaire, in: Chaos et Déterminisme, A. Dahan-Dalmédico, J. L. Chabert and K. Chemla, eds., Seuil, Points, 1992, ISBN : 2-02015-182-0.

[76] J. Laskar, Large scale chaos and marginal stability in the solar system, in: Proceedings of the XIth International Congress of Mathematical Physics, D. Iagolnitzer, ed., International Press, Somerville, MA, U.S.A., 1994, ISBN: 1-57146-030-6.

[77] J. Laskar, Chaos à grande échelle dans le Système Solaire et implications planétologiques, Comptes Rendus de l'Académie des Sciences 322, série II a, 163–180, 1996.

[78] M. F. Loutre, Paramètres orbitaux et cycles diurne et saisonnier des insolations, Ph.D. thesis, Faculté des Sciences, Université Catholique de Louvain, Louvain-La-Neuve, Belgium, 1993.

[79] A. Berger, Preface, in: Milutin Milanković 1879-1958: From his autobiography with comments by his son, Vasko and a preface by André Berger, v–xiii, European Geophysical Society, Katlenburg-Lindau, Germany, 1995.

[80] A. Berger and M. F. Loutre, Insolation values for the climate of the last 10000000 years, Quaternary Science Reviews 10, 4, 297–317, 1991.

[81] A. Berger, M. F. Loutre and J. Laskar, Stability of the astronomical frequencies over the Earth's history for paleoclimate studies, Science 255, 5044, 560–566, 1992.

[82] A. Berger, M. F. Loutre and C. Tricot, Insolation and Earth's orbital periods, Journal of Geophysical Research 98, D6, 10341–10362, 1993.

[83] J. Laskar, Secular terms of classical planetary theories using the results of general-theory, Astronomy and Astrophysics 157, 1, 59–70, 1986.

[84] J. Laskar, Secular evolution of the solar system over 10 million years, Astronomy and Astrophysics 198, 341–362, 1988.

[85] J. Laskar, The chaotic motion of the solar-system - A numerical estimate of the size of the chaotic zones, Icarus 88, 2, 266–291, 1990.

[86] J. Laskar, F. Joutel and F. Boudin, Orbital, Precessional, and Insolation Quantities for the Earth from -20 Myr to +10 Myr, Astronomy and Astrophysics 270, 1-2, 522–533, 1993.

[87] O. N. deSurgy and J. Laskar, On the long term evolution of the spin of the Earth, Astronomy and Astrophysics 318, 3, 975–989, 1997.

[88] K. Lambeck, The Earth's variable rotation: Geophysical causes and consequences, Cambridge University Press, Cambridge, 1980.

[89] J. Laskar, The limits of Earth orbital calculations for geological time-scale use, Philosophical Transactions of the Royal Society of London Series A - Mathematical Physical and Engineering Sciences 357, 1757, 1735–1759, 1999.

[90] D. J. Thomson, Quadratic inverse spectrum estimates; applications to palaeoclimatology, Philosophical Transactions of the Royal Society of London Series A - Mathematical Physical and Engineering Sciences 332, 1627, 539–597, 1990.

[91] D. P. Rubincam, Insolation in terms of Earth's orbital parameters, Theoretical and Applied Climatology 48, 4, 195–202, 1994.

[92] L. A. Hinnov, New perspectives on orbitally forced stratigraphy, Annual Review of Earth and Planetary Science 28, 419–475, 2000.

[93] A. Prokoph and F. P. Agterberg, Detection of sedimentary and stratigraphic completeness by wavelet analysis: An application to late Albian cyclostratigraphy of the Western Canada sedimentary basin, Journal of Sedimentary Research 69, 4, 862–875, 1990.

[94] A. Prokoph and F. Barthelmes, Detection of nonstationarities in geological time series: Wavelet transform of chaotic and cyclic sequences, Computers and Geosciences 22, 10, 1097–1108, 1996.

[95] A. Berger, M. Loutre and V. Dehant, Influence of the changing lunar orbit on the astronomical frequencies of pre-Quaternary insolation patterns, Paleoceanography 4, 5, 555–564, 1989.

[96] A. Berger and M. F. Loutre, Astronomical forcing through geological time, in: Orbital forcing and cyclic sequences (IAS Special Publication), P. L. de Boer and D. G. Smith, eds., volume 19, 15–24, Blackwell Scientific, 1994.

[97] T. Quinn, S. Tremaine and M. Duncan, A 3 million year integration of the Earths orbit, Astronomical Journal 101, 6, 2287–2305, 1991.

[98] M. I. Kuz'min, E. B. Karabanov, T. Kawai et al., Deep drilling on Lake Baikal: main results, Geologiya I GeoFizika 42, 1-2, 8–34, 2001.

[99] T. K. Hagelberg, N. G. Pisias, N. J. Shackleton, A. C. Mix and S. Harris, Refinement of a high-resolution, continuous sedimentary section for studying Equatorial Pacific Ocean paleoceanography, Leg 138, in: Proc. ODP, Sci. Results, N. G. Pisias, L. A. Mayer, T. R. Janecek, A. Palmer-Julson and T. H. van Andel, eds., volume 138, 31–46, Ocean Drilling Program, College Station, TX, 1995.

[100] Shipboard Scientific Party, Site 1052, in: Proc. ODP, Init. Repts., R. D. Norris, D. Kroon, A. Klaus et al., eds., volume 171B, 241–319, Ocean Drilling Program, College Station, TX, 1998.

[101] N. J. Shackleton, H. Pälike and M. F. . Loutre, Improved astronomically tuned timescales for the late Neogene, Journal of Conference Abstracts 4, 1, 235, 1999.

[102] F. J. Sierro, F. J. Hilgen, W. Krijgsman and J. A. Flores, The Abad composite (SE Spain): a Messinian reference section for the Mediterranean and the APTS, Palaeogeography, Palaeoclimatology, Palaeoecology 168, 1-2, 141–169, 2001.

[103] U. Röhl, J. G. Ogg, T. L. Geib and G. Wefer, Astronomical calibration of the Danian time scale, in: Western North Atlantic Palaeogene and Cretaceous Palaeoceanography, D. Kroon, R. D. Norris and A. Klaus, eds., volume 183, 163–183, Geol. Soc. Spec. Publ., London, 2001.

[104] P. Bretagnon, Termes à longue périodes dans le système solaire, Astronomy and Astrophysics 30, 141–154, 1974.

[105] W. H. Press, S. A. Teukolsky, W. T. Vetterling and B. P. Flannery, Chapter 15 - Modeling of Data, in: Numerical Recipes in C - the art of scientific computing, 656–706, Cambridge University Press, Cambridge, 1992, 2nd edition.

[106] D. Paillard, L. Labeyrie and P. Yiou, Macintosh program performs time-series analysis, EOS Transactions AGU 77, 379, 1996, electronic supplement available at `http://www.agu.org/eos_elec/96097e.html`.

[107] ODP Logging Manual, Technical Report version 2.0, Borehole Research Group, Lamont-Doherty Earth Observatory, Palisades, NY, 2000, available in electronic form from `http://www.ldeo.columbia.edu/BRG/ODP/LOGGING/MANUAL/index.html`.

[108] T. D. Herbert, Reading orbital signals distorted by sedimentation: models and examples, in: Orbital forcing and cyclic sequences (IAS Special Publication), P. L. de Boer and D. G. Smith, eds., volume 19, 483–507, Blackwell Scientific, 1994.

[109] P. Schiffelbein and L. Dorman, Spectral effects of time-depth nonlinearities in deep sea sediment records: a demodulation technique for realigning time and depth scales, Journal of Geophysical Research 91, B3, 3821–3835, 1986.

[110] Brüggemann, W., A minimal cost function method for optimizing the age-depth relation of deep-sea sediment cores, Paleoceanography 7, 4, 467–487, 1992.

[111] M. A. Kominz and G. C. Bond, A new method of testing periodicity in cyclic sediments: application to the Newark supergroup, Earth and Planetary Science Letters 98, 233–244, 1990.

[112] M. A. Kominz and G. C. Bond, Documenting the reliability and utility of the γ method as applied to cyclic sections using forward modelling, Earth and Planetary Science Letters 113, 449–457, 1992.

[113] M. A. Kominz, Whither cyclostratigraphy? Testing the gamma method on upper Pleistocene deep-sea sediments, North Atlantic Deep Sea Drilling Project Site 609, Paleoceanography 11, 4, 481–504, 1996.

[114] L. A. Hinnov and J. Park, Detection of astronomical cycles in the stratigraphic record by frequency modulation (FM) analysis, Journal of Sedimentary Research 68, 4 Pt. B, 524–539, 1998.

[115] M. Nadler and E. P. Smith, Pattern recognition engineering, John Wiley and Sons, New York; Chichester, 1993.

[116] H. Sakoe and S. Chiba, Dynamic programming algorithm optimization for spoken word recognition, IEEE Transactions on Acoustics, Speech, and Signal Processing ASSP-26, 1, 43–49, 1978.

[117] A. Kassidas, Fault Diagnosis using speech recognition methods, Ph.D. thesis, Dept. of Chem. Eng., McMaster University, Ontario, Canada, 1997.

[118] A. Kassidas, J. F. MacGregor and P. A. Taylor, Synchronization of Batch Trajectories using Dynamic Time Warping, A.I.Ch.E (American Institute of Chemical Engineering) Journal 44, 4, 864–875, 1998.

[119] F. Itakura, Minimum prediction residual principle applied to speech recognition, IEEE Transactions on Acoustics, Speech, and Signal Processing ASSP-23, 1, 67–72, 1975.

[120] R. E. Bellman, Dynamic programming, Princeton University Press, Princeton, NJ, USA, 1957.

[121] R. E. Bellman and S. E. Dreyfus, Applied dynamic programming, Princeton University Press, Princeton, NJ, USA, 1962.

[122] D. K. Smith, Dynamic Programming: a practical introduction, Ellis Horwood series in mathematics and its applications, Ellis Horwood, New York, London, 1961.

[123] Pälike, H., Thesis Data collection, Technical report, Godwin Institute Library, Department of Earth Sciences, University of Cambridge, Cambridge, United Kingdom, 2001, available in electronic form from
`http://delphi.esc.cam.ac.uk/HPThesisData.html`.

[124] Signal Processing Software Library (libtsp), Technical report, Electrical & Computer Engineering, McGill University, Canada, available in electronic form from
`http://WWW.TSP.ECE.McGill.CA/reports/Software/index.html`.

[125] L. R. Rabiner, A. E. Rosenberg and S. E. Levinson, Consideration in Dynamic Time Warping Algorithms for discrete word recognition, IEEE Transactions on Acoustics, Speech, and Signal Processing ASSP-26, 6, 575, 1978.

[126] J. C. Zachos, N. J. Shackleton, J. S. Revenaugh, H. Pälike and B. P. Flower, Climate response to orbital forcing across the Oligocene-Miocene Boundary, Science 292, 5515, 274–278, 2001.

[127] J. C. Zachos, T. M. Quinn and K. A. Salamy, High-resolution (10^4 years) deep-sea foraminiferal stable isotope records of the Eocene-Oligocene climate transition, Paleoceanography 11, 3, 251–266, 1996.

[128] K. Steiglitz, T. W. Parks and J. F. Kaiser, METEOR: A Constraint-Based FIR Filter Design Program, IEEE Transactions on Signal Processing 40, 8, 1901–1909, 1992.

[129] N. J. Shackleton, M. A. Hall and D. Pate, Pliocene stable isotope stratigraphy of Site 846, in: Proc. ODP, Sci. Res., N. G. Pisias, L. A. Mayer, T. R. Janecek, A. Palmer-Julson and T. H. vanAndel, eds., volume 138, 337–353, Ocean Drilling Program, College Station, TX, 1995.

[130] H. A. Pfuhl, Palaeoceanography of the latest Miocene in the western tropical Atlantic, Ph.D. thesis, Department of Earth Sciences, University of Cambridge, Cambridge, United Kingdom, 2000.

[131] A. E. S. Kemp and J. G. Baldauf, Vast Neogene laminated diatom mat deposits from the eastern equatorial Pacific Ocean, Nature 362, 141–144, 1993.

[132] D. J. Thomson, Spectrum estimation and harmonic analysis, Proceedings of the IEEE 70, 9, 1055–1096, 1982.

[133] G. Plaut and R. Vautard, Spells of low-frequency oscillations and weather regimes in the Northern Hemisphere, Journal of the Atmospheric Sciences 51, 2, 210–236, 1994.

[134] N. Jiang, J. D. Neelin and M. Ghil, Quasi-quadrennial and quasi-biennial variability in the equatiorial Pacific, Climate Dynamics 12, 101–112, 1995.

[135] H. Pälike, N. J. Shackleton and U. Röhl, Astronomical forcing in late Eocene marine sediments, Earth and Planetary Science Letters (accepted for publication).

[136] D. R. Prothero and W. A. Berggren, eds., Eocene-Oligocene Climatic and Biotic Evolution, Princeton University Press, Princeton, NJ, USA, 1992.

[137] K. G. Miller, J. D. Wright and R. G. Fairbanks, Unlocking the Ice House - Oligocene-Miocene oxygen isotopes, eustasy, and margin erosion, Journal of Geophysical Research - Solid Earth and Planets 96, B4, 6829–6848, 1991.

[138] T. J. Bralower, J. C. Zachos, E. Thomas, M. Parrow, C. K. Paul, D. C. Kelly, I. P. Silva, W. V. Sliter and K. C. Lohmann, Late Paleocene to Eocene Paleoceanography of the Equatorial Pacific-Ocean - Stable Isotopes Recorded at Ocean Drilling Program Site-865, Allison-Guyot, Paleoceanography 10, 4, 841–865, 1995.

[139] A. Montanari, F. Asaro, H. V. Michel and J. P. Kennett, Iridium anomalies of Late Eocene age at Massignano (Italy), and ODP Site-689B (Maud-Rise, Antarctic), Palaios 8, 5, 420–437, 1993.

[140] K. A. Farley, A. Montanari, E. M. Shoemaker and C. S. Shoemaker, Geochemical evidence for a comet shower in the Late Eocene, Science 280, 5367, 1250–1253, 1998.

[141] H. B. Vonhof, J. Smit, H. Brinkhuis, A. Montanari and A. J. Nederbragt, Global cooling accelerated by early late Eocene impacts?, Geology 28, 8, 687–690, 2000.

[142] J. Whitehead, D. A. Papanastassiou, J. G. Spray, R. A. F. Grieve and G. J. Wasserburg, Late Eocene impact ejecta: geochemical and isotopic connections with the Popigai impact structure, Earth and Planetary Science Letters 181, 4, 473–487, 2000.

[143] H. Sigurdsson, S. Kelley, R. M. Leckie, S. Carey, T. Bralower and J. King, History of circum-Caribbean explosive volcanism: $^{40}Ar/^{39}Ar$ dating of tephra layers, in: Proc. ODP, Sci. Res., R. M. Leckie, H. Sigurdsson, G. D. Acton and G. Draper, eds., volume 165, 299–314, Ocean Drilling Program, College Station, TX, 2000.

[144] R. D. Norris, D. Kroon, A. Klaus et al., Proc. ODP, Init. Repts., volume 171B, Ocean Drilling Program, College Station, TX, 1998.

[145] L. C. Sloan and E. J. Barron, A comparison of Eocene climate model results to quantified paleoclimatic interpretations, Palaeogeography, Palaeoclimatology, Palaeoecology 93, 3-4, 183–202, 1992.

[146] L. C. Sloan and C. Morrill, Orbital forcing and Eocene continental temperatures, Palaeogeography Palaeoclimatology Palaeoecology 144, 1-2, 21–35, 1998.

[147] N. J. Shackleton and J. P. Kennett, Palaeotemperature history of Antarctic glaciation: oxygen and carbon isotope analyses in DSDP Sites 277, 279, and 281, in: Initial Reports of the Deep Sea Drilling Project, J. P. Kennett, R. E. Houltz et al., eds., volume 29, 743–755, US Government Printing Office, Washington, DC, 1975.

[148] J. C. Zachos, D. K. Rea, K. Seto, R. Nomura and N. Nitsuma, Palaeogene and Early Neogene deep water palaeoceanography of the Indian Ocean as determined from benthic foraminifer stable carbon and oxygen isotope records, in: Geophysical Monograph: Synthesis of Results of Scientific Drilling in the Indian Ocean, R. A. Duncan, D. K. Rea et al., eds., volume 70, 351–385, American Geophysical Union, 1992.

[149] K. G. Miller, Middle Eocene to Oligocene stabe isotopes, climate and deep-water history: The terminal Eocene event?, in: Eocene-Oligocene Climatic and Biotic Evolution, D. R. Prothero and W. A. Berggren, eds., Princeton University Press, Princeton, NJ, USA, 1992.

[150] B. S. Wade, D. Kroon and R. D. Norris, Upwelling in the late middle Eocene at Blake Nose?, GFF 122, 174–175, 2000.

[151] B. S. Wade, D. Kroon and R. D. Norris, Orbitally forced climate change in late mid-Eocene time at Blake Nose (Leg 171B): evidence from stable isotopes in foraminifera, in: Western North Atlantic Palaeogene and Cretaceous Palaeoceanography, D. Kroon, R. D. Norris and A. Klaus, eds., volume 183, 273–292, Geol. Soc. Spec. Publ., London, 2001.

[152] J. C. Zachos, M. Pagani, L. Sloan, E. Thomas and K. Billups, Trends, rhythms, and aberrations in global climate 65 Ma to present, Science 292, 5517, 686–693, 2001, online data are available from
`http://www.es.ucsc.edu/~silab/ZACPUBDATA/2001CompilationData.txt`.

[153] W. C. Wei, Revised age calibration points for the geomagnetic polarity time-Scale, Geophysical Research Letters 22, 8, 957–960, 1995.

[154] L. J. Lourens, A. Antonarakou, F. J. Hilgen, A. A. M. Van Hoof, C. Vergnaud-Grazzini and W. J. Zachariasse, Evaluation of the Plio-Pleistocene astronomical timescale, Paleoceanography 11, 4, 391–413, 1996.

[155] H. Pälike and N. J. Shackleton, Constraints on astronomical parameters from the geological record for the last 25 Myr, Earth and Planetary Science Letters 182, 1, 1–14, 2000, data are available in electronic form from the Elsevier web server at
`http://www.elsevier.nl/gej-ng/10/18/23/88/24/24/79/show/index.htt`.

[156] L. J. Lourens, R. Wehausen and H. J. Brumsack, Geological constraints on tidal dissipation and dynamical ellipticity of the Earth over the past three million years, Nature 409, 6823, 1029–1033, 2001.

[157] J. G. Ogg and L. Bardot, Aptian through Eocene magnetostratigraphic correlation of the Blake Nose Transect (Leg 171B), Florida continental margin, in: Proc. ODP, Sci. Res. [Online], D. Kroon, R. D. Norris and A. Klaus, eds., volume 171B [Online], Ocean Drilling Program, College Station, TX, 2000, available from World Wide Web:
`http://www-odp.tamu.edu/publications/171B_SR/chap_05/chap_05.htm`.

[158] L. Lanci, W. Lowrie and A. Montanari, Magnetostratigraphy of the Eocene/Oligocene boundary in a short drill-core, Earth and Planetary Science Letters 143, 37–48, 1996.

[159] U. Röhl and L. J. Abrams, High-resolution, downhole, and nondestructive core measurements from Sites 999 and 1001 in the Caribbean Sea: application to the Late Paleocene Thermal Maximum, in: Proc. ODP, Sci. Res., R. M. Leckie, H. Sigurdsson, G. D. Acton and G. Draper, eds., volume 165, 191–203, Ocean Drilling Program, College Station, TX, 2000.

[160] J. H. F. Jansen, S. J. Van der Gaast, B. Koster and A. J. Vaars, CORTEX, a shipboard XRF-scanner for element analyses in split sediment cores, Marine Geology 151, 1-4, 143–153, 1998.

[161] U. Röhl, T. J. Bralower, R. D. Norris and G. Wefer, New chronology for the late Paleocene thermal maximum and its environmental implications, Geology 28, 10, 927–930, 2000.

[162] K. Reicherter and T. Pletsch, Eocene ash layers from ODP Leg 171B, Site 1051 (Blake Nose, offshore Florida): petrography, geochemistry and stratigraphic correlation, Mitteilungen des Geologisch-Paläontologischen Instituts der Universität Hamburg 81, 185–202, 1998.

[163] H. Sigurdsson, R. M. Leckie, G. D. Acton et al., Caribbean volcanism, Cretaceous/ Tertiary impact, and ocean-climate history; synthesis of Leg 165, in: Proc. ODP, Init. Repts., H. Sigurdsson, R. M. Leckie, G. D. Acton, L. J. Abrams, T. J. Bralower et al., eds., volume 165, 377–400, Ocean Drilling Program, College Station, TX, 1997.

[164] G. P. Weedon, The recognition and stratigraphic implications of orbital-forcing of climate and sedimentary cycles, Sedimentology Review 1, 31–50, 1993.

[165] N. J. Shackleton, T. K. Hagelberg and S. J. Crowhurst, Evaluating the success of astronomical tuning; pitfalls of using coherence as a criterion for assessing pre-Pleistocene timescales, Paleoceanography 10, 4, 693–697, 1995.

[166] P. Bloomfield, Fourier analysis of time series: an introduction, Wiley Series in Probability and Mathematical Statistics, John Wiley and Sons, New York-London-Sydney, 1976.

[167] Shipboard Scientific Party, Site 1090, in: Proc. ODP, Init. Repts. [Online], R. Gersonde, D. A. Hodell, P. Blum et al., eds., volume 177, Ocean Drilling Program, College Station, TX, 1999, available from World Wide Web:
`http://www-odp.tamu.edu/publications/177_IR/177toc.htm`.

[168] W. A. Berggren, D. V. Kent, C. C. Swisher and M. P. Aubry, A revised Cenozoic geochronology and chronostratigraphy, in: Geochronology, time scales and global stratigraphic correlation (SEPM Special Publication), W. A. Berggren, D. V. Kent, M. P. Aubry and J. Hardenbol, eds., volume 54, 129–212, Society for Sedimentary Geology (SEPM), Tulsa, OK, 1995.

[169] Kyte, F. T., Identification of Late Eocene impact deposits at ODP Site 1090, in: Proc. ODP, Sci. Res. [Online], R. Gersonde, D. A. Hodell and P. Blum, eds., volume 177, Ocean Drilling Program, College Station, TX, 2001, available from World Wide Web:
`http://www-odp.tamu.edu/publications/177_SR/chap_04/chap_04.htm`.

[170] C. H. Lear, H. Elderfield and P. A. Wilson, Cenozoic deep-sea temperatures and global ice volumes from Mg/ Ca in benthic foraminiferal calcite, Science 287, 2451, 269–272, 2000.

[171] B. S. Cramer, Latest Paleocene-earliest Eocene cyclostratigraphy: using core photographs for reconnaissance geophysical logging, Earth and Planetary Science Letters 186, 2, 231–244, 2001.

[172] W. A. Berggren, D. V. Kent, J. D. Obradovich and C. C. Swisher III, Towards a revised Paleogene geochronology, in: Eocene-Oligocene Climatic and Biotic Evolution, D. R. Prothero and W. A. Berggren, eds., Princeton University Press, Princeton, NJ, USA, 1992.

[173] C. H. Lear, Evolution of Cenozoic ocean composition and temperature from foraminiferal trace element proxies, Ph.D. thesis, Department of Earth Sciences, University of Cambridge, Cambridge, United Kingdom, 2001.

[174] B. Wade, R. D. Norris and D. Kroon, 5. Data Report: High-resolution stable isotope stratigraphy of the late Middle Eocene at Site 1051, Blake Nose, in: Proc. ODP, Sci. Res. [Online], D. Kroon, R. D. Norris and A. Klaus, eds., volume 171B [Online], Ocean Drilling Program, College Station, TX, 2000, available from World Wide Web:
`http://www-odp.tamu.edu/publications/171B_SR/chap_05/chap_05.htm`.

[175] N. J. Shackleton and M. A. Hall, The Late Miocene stable isotope record, Site 926, in: Proc. ODP, Sci. Res., N. J. Shackleton, W. B. Curry, C. Richter and T. J. Bralower, eds., volume 154, 367–373, Ocean Drilling Program, College Station, TX, 1997.

[176] H. C. Urey, H. A. Lowenstam, S. Epstein and C. R. McKinney, Measurement of paleotemperatures and temperatures of the Upper Cretaceous of England, Denmark, and the southeastern United States, Bulletin of the Geological Society of America 62, 399–416, 1951.

[177] J. C. Duplessy, C. Lalou and A. C. Vinot, Differential isotopic fractionation in benthic foraminifera and palaeotemperatures reassessed, Science 168, 3928, 250–251, 1970.

[178] N. J. Shackleton, M. A. Hall and A. Boersma, Oxygen and carbon isotope data from Leg 74 foraminifers, in: Initial Reports of the Deep Sea Drilling Project, T. C. Moore Jnr., P. D. Rabinowitz et al., eds., volume 74, 599–612, US Government Printing Office, Washington, DC, 1984.

[179] J. C. Zachos, L. D. Stott and K. C. Lohmann, Evolution of early Cenozoic marine temperatures, Paleoceanography 9, 2, 353–387, 1994.

[180] P. Pearson, Pristine planktonic foraminifera from the hot tropics? New evidence from Tanzania, in: Book of abstracts - Palaeoceanography and climate change. The William Smith meeting of the Geological Society, London, 25-26 April 2001, 2, The Geological Society, London, 2001.

[181] L. C. Sloan and D. K. Rea, Atmospheric carbon dioxide and early Eocene climate: a general circulation modeling sensitivity study, Palaeogeography, Palaeoclimatology, Palaeoecology 119, 3-4, 275–292, 1995.

[182] J. Erez and B. Luz, Experimental palaeo-temperature equation for planktonic foraminifera, Geochimica and Cosmochimica Acta 47, 6, 535–538, 1983.

[183] E. Thomas and N. J. Shackleton, The Paleocene-Eocene benthic foraminiferal extinction and stable isotope anomalies, in: Geological Society Special Publications: Correlation of the early Paleogene in Northwest Europe, R. W. O. B. Knox, R. M. Corfield and R. E. Dunay, eds., volume 101, 401–441, Geological Society of London, London, 1996.

[184] K. L. Bice, L. C. Sloan and E. J. Barron, Comparison of early Eocene isotopic paleotemperatures and the three-dimensional OGCM temperature field; the potential for use of model-derived surface water delta ^{18}O, in: Warm climates in Earth history, B. T. Huber, K. G. MacLeod and S. L. Wing, eds., University of Cambridge. Cambridge, United Kingdom. 2000., 2000.

[185] L. C. Sloan and M. Huber, North Atlantic climate variability in early Palaeogene time: a climate modelling sensitivity study, in: Western North Atlantic Palaeogene and Cretaceous Palaeoceanography, D. Kroon, R. D. Norris and A. Klaus, eds., volume 183, 253–272, Geol. Soc. Spec. Publ., London, 2001.

[186] P. R. Pinet and P. Popenoe, A scenario of Mesozoic-Cenozoic ocean circulation over the Blake Plateau and its environs, Geological Society of America Bulletin 96, 5, 618–626, 1985.

[187] R. E. M. Rickaby, Planktonic foraminiferal Cd/Ca: A new perspective on Southern Ocean palaeoproductivity, Ph.D. thesis, Department of Earth Sciences, University of Cambridge, Cambridge, United Kingdom, 1999.

[188] W. S. Broecker and T.-H. Peng, Tracers in the sea, LDGO Press, Palisades, NY, U.S.A., 1982.

[189] W. S. Broecker and F. Woodruff, Discrepancies in the oceanic carbon isotope record for the last fifteen million years?, Geochimica and Cosmochimica Acta 56, 8, 3259–3264, 1992.

[190] N. J. Shackleton and M. A. Hall, Stable isotope records in bulk sediments (Leg 138), in: Proc. ODP, Sci. Res., N. G. Pisias, L. A. Mayer, T. R. Janecek, A. Palmer-Julson and T. H. vanAndel, eds., volume 138, 797–805, Ocean Drilling Program, College Station, TX, 1995.

[191] N. J. Shackleton and M. A. Hall, Carbon isotope data from Leg 74 sediments, in: Initial Reports of the Deep Sea Drilling Project, T. C. Moore Jnr., P. D. Rabinowitz et al., eds., volume 74, 613–619, US Government Printing Office, Washington, DC, 1984.

[192] W. B. Curry et al., Proceedings of the Ocean Drilling Program, Initial Reports, volume 154, Ocean Drilling Program, College Station, TX, 1995.

[193] G. P. Weedon, Data report: measurements of magnetic susceptibility for the Oligocene and Lower Miocene of Site 925, in: Proceedings of the Ocean Drilling Program, Scientific Results, N. Shackleton, W. Curry, C. Richter and T. Bralower, eds., volume 154, 529–532, Ocean Drilling Program, College Station, TX, 1997.

[194] R. Tiedemann and S. O. Franz, Deep-water circulation, chemistry, and terrigenous sediment supply in the equatorial Atlantic during the Pliocene, 3.3–2.6 Ma and 5–4.5 Ma, in: Proceedings of the Ocean Drilling Program, Scientific Results, N. Shackleton, W. Curry, C. Richter and T. Bralower, eds., volume 154, 299–318, Ocean Drilling Program, College Station, TX, 1997.

[195] A. Berger, M. F. Loutre and V. Dehant, Pre-Quaternary Milankovitch frequencies, Nature 342, 6246, 133, 1989.

[196] J. X. Mitrovica, R. Pan and A. M. Forte, Late Pleistocene and Holocene ice mass fluctuations and the Earth's precession constant, Earth and Planetary Science Letters 128, 3-4, 489–500, 1994.

[197] J. X. Mitrovica and A. M. Forte, Pleistocene glaciation and the Earth's precession constant, Geophysical Journal International 121, 1, 21–32, 1995.

[198] X. H. Jiang and W. R. Peltier, Ten million year histories of obliquity and precession: The influence of the ice-age, Earth and Planetary Science Letters 139, 1-2, 17–32, 1996.

[199] W. R. Peltier and X. H. Jiang, Glacial isostatic adjustment and Earth rotation: Refined constraints on the viscosity of the deepest mantle, Journal of Geophysical Research-Solid Earth 101, B2, 3269–3290, 1996.

[200] J. X. Mitrovica, A. M. Forte and R. Pan, Glaciation-induced variations in the Earth's precession frequency, obliquity and insolation over the last 2.6 Ma, Geophysical Journal International 128, 2, 270–284, 1997.

[201] J. Mitrovica and A. Forte, Radial profile of mantle viscosity: results from the joint inversion of convection and postglacial rebound observables, Journal of Geophysical Research 102, B2, 2751–2769, 1997.

[202] A. M. Forte and J. X. Mitrovica, A resonance in the Earth's obliquity and precession over the past 20 Myr driven by mantle convection, Nature 390, 6661, 676–680, 1997.

[203] S. L. Marcus, Y. Chao, J. O. Dickey and P. Gegout, Detection and modeling of nontidal oceanic effects on Earth's rotation rate, Science 281, 5383, 1656–1659, 1998.

[204] M. A. Maslin, X. S. Li, M. F. Loutre and A. Berger, The contribution of orbital forcing to the progressive intensification of Northern Hemisphere glaciation, Quaternary Science Reviews 17, 4-5, 411–426, 1998.

[205] G. E. Williams, Precambrian tidal and glacial elastic deposits: implications for Precambrian Earth-Moon dynamics and palaeoclimate, Sedimentary Geology 120, 1-4, 55–74, 1998.

[206] J. O. Dickey, P. L. Bender, J. E. Faller, X. X. Newhall, R. L. Ricklefs, J. G. Ries, P. J. Shelus, C. Veillet, A. L. Whipple, J. R. Wiant, J. G. Williams and C. F. Yoder, Lunar laser ranging - a continuing legacy of the Apollo program, Science 265, 5171, 482–490, 1994.

[207] B. G. Bills and R. D. Ray, Lunar orbital evolution: A synthesis of recent results, Geophysical Research Letters 26, 19, 3045–3048, 1999.

[208] W. K. Hartmann, R. J. Phillips and T. G. J., Origin of the Moon, Lunar and Planetary Institute, Houston, 1986.

[209] J. O. Dickey and J. G. Williams, Geophysical applications of Lunar laser ranging, EOS Transactions AGU 82, 63, 301, 1982.

[210] J. P. Vanyo and S. M. Awramik, Length of day and obliquity of the ecliptic 850 Ma ago - preliminary results of a stromatolite growth model, Geophysical Research Letters 9, 10, 1125–1128, 1982.

[211] C. P. Sonett, E. P. Kvale, A. Zakharian, M. A. Chan and T. M. Demko, Late Proterozoic and Paleozoic tides, retreat of the moon, and rotation of the Earth, Science 273, 5271, 100–104, 1996.

[212] C. P. Sonett and M. A. Chan, Neoproterozoic Earth-Moon dynamics: Rework of the 900 Ma Big Cottonwood Canyon tidal laminae, Geophysical Research Letters 25, 4, 539–542, 1998.

[213] E. P. Kvale, H. W. Johnson, C. P. Sonett, A. W. Archer and A. Zawistoski, Calculating lunar retreat rates using tidal rhythmites, Journal of Sedimentary Research 69, 6B, 1154–1168, 1999.

[214] E. Müller and A. Jappel, eds., Transactions of the IAU: Proceedings of the Sixteenth General Assembly Grenoble, France, August 24 - September 21, 1976, volume XVIB, D. Reidel, Dordrecht, The Netherlands, 1976.

[215] V. Dehant, M. Loutre and A. Berger, Potential impact of the Northern Hemisphere Quaternary ice sheets on the frequencies of the astro-climatic orbital parameters, Journal of Geophysical Research 95, D6, 7573–7578, 1990.

[216] D. Vakman, On the analytical signal, the Teager-Kaiser energy algorithm, and other methods for defining amplitude and frequency, IEEE Transactions Signal Processing 44, 4, 791–797, 1996.

[217] J. A. Rial, Pacemaking the ice ages by frequency modulation of the Earth's orbital eccentricity, Science 285, 564–568, 1999.

[218] H. A. Paul, J. C. Zachos, B. P. Flower and A. Tripati, Orbitally induced climate and geochemical variability across the Oligocene/Miocene boundary, Paleoceanography 15, 5, 471–485, 2000.

[219] P. Yiou, E. Baert and M. F. Loutre, Spectral analysis of climate data, Surveys in Geophysics 17, 6, 619–663, 1996.

[220] F. Varadi, M. Ghil and B. Runnegar, Possible ultimate cause of the K-T impact, in: Programme and Abstract volume of the Earth System Processes conference, 24-28 June 2001, Edinburgh, 92, The Geological Society of America and the The Geological Society of London, London, 2001, additional information in electronic form from `http://pentalith.astrobiology.ucla.edu/~varadi/`.

[221] N. J. Shackleton, M. A. Hall, I. Raffi, L. Tauxe and J. Zachos, Astronomical calibration age for the Oligocene/Miocene boundary, Geology 28, 5, 447–450, 2000.

[222] R. D. Norris and U. Röhl, Carbon cycling and chronology of climate warming during the Paleocene/Eocene transition, Nature 401, 775–778, 1999.

Appendix A

Raw XRF data from ODP 171B-1052

XRF measurements from ODP 171B, Site 1052, Hole A													
Leg	**Site**	**Hole**	**Core**	**Sec**	**cm**	**mbsf**	**K**	**Ca**	**Ti**	**Mn**	**Fe**	**Cu**	**Sr**
								[counts per second]					
171B	1052	A	2X	1	4	3.54	164	10206	3	33	440	37	303
171B	1052	A	2X	1	8	3.58	204	11026	13	39	783	28	334
171B	1052	A	2X	1	17	3.67	132	7523	6	45	638	46	75
171B	1052	A	2X	1	24	3.74	129	7782	4	30	465	57	56
171B	1052	A	2X	1	25	3.75	153	9057	3	31	490	78	57
171B	1052	A	2X	1	32	3.82	156	8961	0	36	564	56	62
171B	1052	A	2X	1	38	3.88	125	8692	2	30	631	39	55
171B	1052	A	2X	1	47	3.97	142	7579	6	46	992	64	58
171B	1052	A	2X	1	56	4.06	142	8300	0	58	857	60	87
171B	1052	A	2X	1	61	4.11	106	8611	7	35	764	11	81
171B	1052	A	2X	1	73	4.23	210	8778	3	61	354	86	50
171B	1052	A	2X	1	83	4.33	161	10951	0	11	227	42	45
171B	1052	A	2X	1	88	4.38	181	9472	2	7	210	75	58
171B	1052	A	2X	1	99	4.49	250	12557	9	39	424	42	57
171B	1052	A	2X	1	104	4.54	203	11049	7	35	591	21	79
171B	1052	A	2X	1	112	4.62	223	11189	2	55	475	46	59
171B	1052	A	2X	1	120	4.70	201	10624	0	64	406	72	61
171B	1052	A	2X	1	128	4.78	220	9856	5	38	564	66	49
171B	1052	A	2X	1	136	4.86	233	9113	0	24	521	56	61
171B	1052	A	2X	1	144	4.94	226	10024	0	31	496	85	63
						...							
						...							
						...							
						remaining data of this table can be found on the enclosed CD-ROM							
						...							
						...							
						...							
171B	1052	A	12H	6	88	107.08	117	8609	0	22	201	62	51
171B	1052	A	12H	6	96	107.16	108	8274	2	20	197	55	61
171B	1052	A	12H	6	104	107.24	142	9606	3	28	294	63	55
171B	1052	A	12H	6	112	107.32	177	11665	3	27	320	30	61
171B	1052	A	12H	6	120	107.40	138	10388	0	31	268	43	62
171B	1052	A	12H	6	128	107.48	131	9305	0	23	213	59	57
171B	1052	A	12H	6	136	107.56	122	9453	3	20	203	44	49
171B	1052	A	12H	6	144	107.64	130	9078	2	8	205	44	64
171B	1052	A	12H	6	148	107.68	139	11264	0	18	270	40	73
171B	1052	A	12H	7	4	107.74	193	12543	3	19	297	59	68
171B	1052	A	12H	7	8	107.78	153	9877	3	29	272	64	55
171B	1052	A	12H	7	16	107.86	118	8642	0	18	220	64	62
171B	1052	A	12H	7	24	107.94	139	9046	2	19	224	54	73
171B	1052	A	12H	7	32	108.02	115	8095	3	26	185	52	57
171B	1052	A	12H	7	40	108.10	138	8631	3	14	195	44	59
171B	1052	A	12H	7	48	108.18	196	10988	4	24	279	54	58

Table A.1: XRF measurements from Leg 171B, Site 1052, Hole A. The data set is too large to be included as hard copy. The remainder of the data can be found on the enclosed CD-ROM, and a hard copy is available from the Godwin Laboratory [123].

XRF measurements from ODP 171B, Site 1052, Hole B													
Leg	**Site**	**Hole**	**Core**	**Sec**	**cm**	**mbsf**	**K**	**Ca**	**Ti**	**Mn**	**Fe**	**Cu**	**Sr**
								[counts per second]					
171B	1052	B	2H	1	4	5.04	212	6130	21	29	785	10	61
171B	1052	B	2H	1	8	5.08	256	7310	30	31	761	9	57
171B	1052	B	2H	1	11	5.11	166	5339	13	27	603	5	47
171B	1052	B	2H	1	19	5.19	216	12818	0	78	605	67	48
171B	1052	B	2H	1	25	5.25	358	11754	14	54	874	63	77
171B	1052	B	2H	1	33	5.33	285	7904	13	37	865	58	66
171B	1052	B	2H	1	40	5.40	280	8837	8	39	698	67	58
171B	1052	B	2H	1	50	5.50	265	7884	10	35	773	60	69
171B	1052	B	2H	1	56	5.56	272	8867	10	40	668	65	65
171B	1052	B	2H	1	64	5.64	282	10300	11	44	618	60	60
171B	1052	B	2H	1	72	5.72	264	9721	0	49	592	53	62
171B	1052	B	2H	1	80	5.80	277	9238	7	45	686	62	57
171B	1052	B	2H	1	88	5.88	278	8202	8	35	836	52	55
171B	1052	B	2H	1	96	5.96	279	8259	6	34	940	50	65
171B	1052	B	2H	1	104	6.04	314	8210	11	37	964	63	66
171B	1052	B	2H	1	112	6.12	322	9115	15	45	777	65	66
171B	1052	B	2H	1	120	6.20	289	8142	15	34	863	60	54
171B	1052	B	2H	1	128	6.28	282	8819	9	45	727	69	56
171B	1052	B	2H	1	136	6.36	292	9179	10	45	686	44	76
171B	1052	B	2H	1	144	6.44	278	9272	13	32	628	26	61
						...							
						...							
						...							
						remaining data of this table can be found on the enclosed CD-ROM							
						...							
						...							
						...							
171B	1052	B	13H	6	4	108.06	137	9615	4	37	290	78	53
171B	1052	B	13H	6	8	108.10	133	9016	5	38	261	98	60
171B	1052	B	13H	6	16	108.18	118	7405	3	21	216	49	58
171B	1052	B	13H	6	24	108.26	79	6241	2	22	194	63	64
171B	1052	B	13H	6	32	108.34	110	8304	5	17	203	66	51
171B	1052	B	13H	6	40	108.42	117	8015	0	19	207	63	65
171B	1052	B	13H	6	48	108.50	128	9339	4	7	233	74	66
171B	1052	B	13H	6	56	108.58	177	10533	3	63	405	69	68
171B	1052	B	13H	6	64	108.66	129	8915	4	35	302	65	74
171B	1052	B	13H	6	72	108.74	131	8931	0	24	299	58	65
171B	1052	B	13H	6	80	108.82	164	11337	3	44	330	89	67
171B	1052	B	13H	6	88	108.90	162	10917	2	21	258	56	69
171B	1052	B	13H	6	96	108.98	101	9563	4	26	249	54	65
171B	1052	B	13H	6	104	109.06	127	9706	0	26	228	48	55
171B	1052	B	13H	6	108	109.10	131	9217	4	40	231	85	57
171B	1052	B	13H	6	120	109.22	131	9190	4	25	259	72	58

Table A.2: XRF measurements from Leg 171B, Site 1052, Hole B. The data set is too large to be included as hard copy. The remainder of the data can be found on the enclosed CD-ROM, and a hard copy is available from the Godwin Laboratory [123].

XRF measurements from ODP 171B, Site 1052, Hole C													
Leg	**Site**	**Hole**	**Core**	**Sec**	**cm**	**mbsf**	**K**	**Ca**	**Ti**	**Mn**	**Fe**	**Cu**	**Sr**
								[counts per second]					
171B	1052	C	2H	1	9	9.59	244	8707	6	42	594	61	52
171B	1052	C	2H	1	16	9.66	230	7286	9	28	578	58	57
171B	1052	C	2H	1	24	9.74	250	9418	14	43	639	79	59
171B	1052	C	2H	1	32	9.82	191	8739	7	41	680	62	56
171B	1052	C	2H	1	40	9.90	192	9519	8	45	647	55	61
171B	1052	C	2H	1	48	9.98	170	8090	4	35	669	52	61
171B	1052	C	2H	1	56	10.06	166	8418	5	36	600	62	62
171B	1052	C	2H	1	64	10.14	137	7774	9	38	656	48	69
171B	1052	C	2H	1	72	10.22	141	6680	8	35	545	58	49
171B	1052	C	2H	1	80	10.30	170	6567	8	30	533	53	51
171B	1052	C	2H	1	88	10.38	270	5969	12	37	646	61	51
171B	1052	C	2H	1	96	10.46	163	9227	5	38	588	73	49
171B	1052	C	2H	1	104	10.54	209	9914	2	38	546	66	49
171B	1052	C	2H	1	112	10.62	282	10624	9	60	578	63	64
171B	1052	C	2H	1	120	10.70	257	9976	4	43	512	77	55
171B	1052	C	2H	1	128	10.78	250	10218	11	55	489	50	57
171B	1052	C	2H	1	136	10.86	277	10857	9	86	619	58	55
171B	1052	C	2H	1	144	10.94	243	10996	6	52	508	39	62
171B	1052	C	2H	2	4	11.03	269	11207	7	53	544	54	72
171B	1052	C	2H	2	8	11.07	269	10863	6	42	475	64	50
						...							
						...							
						...							
						remaining data of this table can be found on the enclosed CD-ROM							
						...							
						...							
						...							
171B	1052	C	2H	6	136	18.35	139	7924	4	28	509	33	62
171B	1052	C	2H	6	144	18.43	212	10304	7	48	580	55	76
171B	1052	C	2H	6	146	18.45	223	10696	5	41	571	51	66
171B	1052	C	2H	7	4	18.52	271	11410	15	43	656	17	85
171B	1052	C	2H	7	8	18.56	227	10602	7	34	582	68	75
171B	1052	C	2H	7	16	18.64	205	10610	4	41	518	68	70
171B	1052	C	2H	7	24	18.72	193	10628	3	43	492	75	70
171B	1052	C	2H	7	32	18.80	150	9856	7	25	449	53	65
171B	1052	C	2H	7	40	18.88	161	11005	4	44	424	69	73
171B	1052	C	2H	7	48	18.96	171	11192	2	64	436	61	61
171B	1052	C	2H	7	54	19.02	176	10911	2	63	404	40	68
171B	1052	C	2H	7	64	19.12	173	11077	3	47	397	35	66
171B	1052	C	2H	CC	3	19.17	172	12323	9	42	419	16	90
171B	1052	C	2H	CC	8	19.22	136	8737	2	37	303	47	66
171B	1052	C	2H	CC	16	19.30	150	10385	4	33	367	4	76
171B	1052	C	2H	CC	22	19.36	149	10495	2	42	431	35	76

Table A.3: XRF measurements from Leg 171B, Site 1052, Hole C. The data set is too large to be included as hard copy. The remainder of the data can be found on the enclosed CD-ROM, and a hard copy is available from the Godwin Laboratory [123].

XRF measurements from ODP 171B, Site 1052, Hole F													
Leg	**Site**	**Hole**	**Core**	**Sec**	**cm**	**mbsf**	**K**	**Ca**	**Ti**	**Mn**	**Fe**	**Cu**	**Sr**
								[counts per second]					
171B	1052	F	1H	1	24	0.24	132	4715	23	14	541	16	96
171B	1052	F	1H	1	80	0.80	143	7515	14	28	671	20	59
171B	1052	F	1H	1	88	0.88	229	12241	3	63	678	75	72
171B	1052	F	1H	1	96	0.96	217	10900	7	45	578	74	64
171B	1052	F	1H	1	104	1.04	215	9970	6	57	528	64	46
171B	1052	F	1H	1	112	1.12	192	9381	7	26	613	67	67
171B	1052	F	1H	1	120	1.20	166	7633	6	24	520	57	58
171B	1052	F	1H	1	128	1.28	201	8560	6	46	541	76	53
171B	1052	F	1H	1	136	1.36	187	9000	6	45	595	55	63
171B	1052	F	1H	1	144	1.44	190	8940	12	72	644	48	67
171B	1052	F	1H	1	148	1.48	233	10463	3	47	678	45	66
171B	1052	F	1H	2	4	1.54	243	13020	9	54	490	44	70
171B	1052	F	1H	2	8	1.58	219	11655	2	68	453	79	48
171B	1052	F	1H	2	16	1.66	262	11115	4	65	511	73	46
171B	1052	F	1H	2	24	1.74	165	8449	6	52	486	72	60
171B	1052	F	1H	2	32	1.82	180	8804	6	54	526	63	54
171B	1052	F	1H	2	40	1.90	178	8938	0	35	380	42	47
171B	1052	F	1H	2	48	1.98	132	6964	3	26	305	67	43
171B	1052	F	1H	2	56	2.06	226	11576	0	76	450	84	57
171B	1052	F	1H	2	64	2.14	192	8690	0	84	424	61	55
						...							
						...							
						...							
						remaining data of this table can be found on the enclosed CD-ROM							
						...							
						...							
						...							
171B	1052	F	13H	2	16	111.16	125	8890	3	9	219	14	66
171B	1052	F	13H	2	24	111.24	147	9646	6	19	233	0	77
171B	1052	F	13H	2	32	111.32	137	9724	3	15	223	18	70
171B	1052	F	13H	2	40	111.40	130	10037	0	29	2.10	21	71
171B	1052	F	13H	2	48	111.48	126	9792	0	16	215	20	63
171B	1052	F	13H	2	56	111.56	131	9790	4	16	227	15	60
171B	1052	F	13H	2	64	111.64	165	10386	4	20	230	14	69
171B	1052	F	13H	2	72	111.72	159	10268	0	34	280	14	65
171B	1052	F	13H	2	80	111.80	153	10987	0	29	318	10	69
171B	1052	F	13H	2	88	111.88	116	8737	4	10	235	8	70
171B	1052	F	13H	2	96	111.96	132	9904	2	37	239	11	74
171B	1052	F	13H	2	104	112.04	115	10458	3	25	274	19	57
171B	1052	F	13H	2	112	112.12	151	10888	3	28	286	17	80
171B	1052	F	13H	2	120	112.20	120	10119	5	31	273	11	79
171B	1052	F	13H	2	128	112.28	149	10217	3	30	263	10	78
171B	1052	F	13H	2	136	112.36	144	9229	4	16	211	6	80
171B	1052	F	13H	2	144	112.44	128	10837	9	36	316	10	60

Table A.4: XRF measurements from Leg 171B, Site 1052, Hole F. The data set is too large to be included as hard copy. The remainder of the data can be found on the enclosed CD-ROM, and a hard copy is available from the Godwin Laboratory [123].

Appendix B

Mapping tables for ODP 171B-1052 (mbsf to rmcd; rmcd to age)

Mapping pairs from mbsf to rmcd, Leg 171B, Site 1052, Hole A								
core	mbsf	rmcd	core	mbsf	rmcd	core	mbsf	rmcd
2	3.53	4.98	7	51.23	57.96	12	98.73	105.71
2	5.03	6.69	7	**52.37**	**58.61**	12	**99.32**	**106.29**
2	5.24	6.85	7	**58.43**	**64.67**	12	**106.17**	**113.14**
2	7.06	9.14	7	59.29	65.55	12	106.91	113.70
2	8.00	10.72	7	61.07	66.60	12	108.20	114.52
2	9.60	12.06						
2	10.88	13.63	8	60.73	66.66	13	108.23	114.60
2	11.92	15.00	8	**61.17**	**67.12**	13	**108.45**	**114.90**
			8	**65.52**	**71.47**	13	**114.11**	**120.56**
3	13.23	17.21	8	67.28	73.11	13	114.47	120.74
3	15.65	18.94	8	67.56	73.56	13	116.52	123.04
3	17.79	20.32	8	68.54	74.67	13	117.31	124.20
3	18.74	21.56	8	69.36	75.61	13	117.84	124.52
3	20.48	23.78	8	70.33	76.46			
3	21.82	24.53				14	117.73	124.70
3	22.60	25.34	9	70.23	76.63	14	**119.07**	**125.75**
			9	70.95	77.00	14	**127.57**	**134.25**
4	22.74	26.58	9	71.51	77.60			
4	23.82	27.12	9	**72.11**	**78.05**	15	**127.23**	**134.25**
4	26.10	29.00	9	**78.65**	**84.59**	15	**129.50**	**136.52**
4	28.73	31.77	9	79.80	85.71			
4	29.70	33.20				16	**129.73**	**136.52**
4	32.00	35.42	10	79.73	85.94	16	**134.83**	**141.62**
4	32.55	35.74	10	80.58	86.66			
			10	**81.63**	**87.53**			
5	32.23	37.11	10	**87.05**	**92.95**			
5	**33.77**	**39.39**	10	88.31	94.50			
5	**41.25**	**46.87**	10	89.31	95.00			
5	41.93	47.41						
6	41.74	48.26	11	89.23	95.29			
6	**43.40**	**49.95**	11	**91.22**	**97.46**			
6	**48.89**	**55.44**	11	**95.99**	**102.23**			
6	49.77	56.20	11	97.75	103.74			
6	51.38	57.94	11	99.04	104.72			

Table B.1: Mapping pairs from mbsf to rmcd for Site 1052, Hole A. Consecutive bold figures indicate that these points define the splice path, i.e. the depth of data between these points are not compressed or expanded. These data are also available in electronic form from the enclosed CD-ROM, and a hard copy is available from the Godwin Laboratory [123].

Mapping pairs from mbsf to rmcd, Leg 171B, Site 1052, Hole B								
core	mbsf	rmcd	core	mbsf	rmcd	core	mbsf	rmcd
2	5.03	6.89	6	43.03	48.85	11	81.53	88.85
2	**5.92**	**7.76**	6	45.14	50.90	11	82.69	90.13
2	**8.88**	**10.72**	6	45.86	51.60	11	83.32	90.75
2	10.54	12.54	6	47.04	52.53	11	84.28	91.55
2	11.67	13.62	6	48.69	54.10	11	**86.08**	**92.95**
2	13.62	16.15	6	49.47	54.85	11	**90.59**	**97.46**
2	14.82	17.39	6	50.11	55.50	11	91.22	97.88
			6	50.80	56.20			
3	14.53	17.43	6	51.02	56.25	12	91.03	98.68
3	15.38	18.94	6	52.31	57.24	12	**94.50**	**102.23**
3	16.55	20.32				12	**98.56**	**106.29**
3	**17.86**	**21.45**	7	52.53	58.18	12	99.09	106.90
3	**21.63**	**25.22**	7	54.59	60.37	12	99.60	107.28
3	23.76	27.35	7	56.97	62.45			
3	24.34	27.73	7	57.51	63.47	13	100.53	108.66
			7	**58.59**	**64.67**	13	101.94	110.41
4	24.03	28.25	7	**61.04**	**67.12**	13	**104.89**	**113.14**
4	**25.27**	**29.16**	7	61.91	67.82	13	**106.65**	**114.90**
4	**27.83**	**31.72**				13	109.26	116.28
4	31.46	35.42	8	62.04	68.77			
4	33.70	37.30	8	62.38	68.94	14	110.03	116.92
						14	111.39	118.09
5	33.53	37.35	9	62.53	69.51	14	**113.17**	**120.56**
5	**33.80**	**37.49**	9	**64.45**	**71.47**	14	**118.36**	**125.75**
5	**35.70**	**39.39**	9	**71.03**	**78.05**	14	119.66	127.17
5	35.88	39.47	9	71.53	78.50			
5	37.06	40.97	9	71.92	78.69			
5	37.96	42.09						
5	38.23	42.81	10	72.03	79.17			
5	39.09	44.24	10	73.35	80.38			
5	40.71	46.04	10	**77.99**	**84.59**			
5	43.30	48.55	10	**80.93**	**87.53**			
			10	81.70	88.38			

Table B.2: Mapping pairs from mbsf to rmcd for Site 1052, Hole B. Consecutive bold figures indicate that these points define the splice path, i.e. the depth of data between these points are not compressed or expanded. These data are also available in electronic form from the enclosed CD-ROM, and a hard copy is available from the Godwin Laboratory [123].

Mapping pairs from mbsf to rmcd Leg 171B, Site 1052, Holes C (left) and D (right)					
core	mbsf	rmcd	core	mbsf	rmcd
2	9.53	12.10	1	0.02	0.00
2	9.81	12.54	1	0.76	0.60
2	**10.38**	**13.63**	1	1.47	1.45
2	**18.20**	**21.45**	1	2.61	2.85
2	19.36	22.34	1	4.80	5.00
			1	9.47	9.04
			2	9.53	6.47
			2	12.36	9.30
			2	13.70	10.77
			2	16.19	13.85
			2	17.27	15.10
			2	17.67	16.23
			2	18.43	17.16

Table B.3: Mapping pairs from mbsf to rmcd for Site 1052, Holes C and D. Consecutive bold figures indicate that these points define the splice path, i.e. the depth of data between these points are not compressed or expanded. These data are also available in electronic form from the enclosed CD-ROM, and a hard copy is available from the Godwin Laboratory [123].

Mapping pairs from mbsf to rmcd, Leg 171B, Site 1052, Hole F								
core	mbsf	rmcd	core	mbsf	rmcd	core	mbsf	rmcd
1	**0.04**	**0.04**	7	57.04	62.05	12	100.04	103.99
1	**7.76**	**7.76**	7	58.15	63.45	12	102.35	106.30
1	9.33	8.42	7	58.60	63.85	12	103.05	107.01
			7	59.15	64.69	12	103.73	107.84
2	9.54	8.74	7	61.05	66.03	12	104.59	108.74
2	**11.24**	**10.72**	7	62.40	67.10	12	105.65	109.65
2	**14.15**	**13.63**	7	62.75	67.70	12	106.04	110.28
2	16.30	16.38	7	63.27	68.28	12	107.54	111.71
2	19.42	19.87				12	107.90	112.30
			8	66.54	70.12	12	109.05	113.17
3	19.04	20.32	8	67.14	70.53	12	109.74	113.86
3	20.20	21.57	8	67.54	71.05			
3	22.70	23.52	8	70.32	73.65	13	109.54	113.86
3	**24.46**	**25.22**	8	73.84	76.85	13	110.22	114.65
3	**28.40**	**29.16**	8	75.26	78.52	13	110.50	114.75
3	29.10	30.07	8	76.19	79.64	13	110.95	115.30
						13	111.63	115.60
4	28.54	30.61	9	76.04	79.66	13	112.35	116.10
4	**29.78**	**31.72**	9	81.69	83.62	13	112.70	116.30
4	**35.55**	**37.49**				13	113.85	117.63
4	36.32	38.31	10	81.04	84.76	13	114.25	117.93
4	38.40	39.64	10	81.68	85.35	13	114.40	118.10
			10	82.80	86.65	13	114.99	118.98
5	38.04	40.60	10	84.85	88.40	13	115.15	119.15
5	41.72	44.20	10	86.51	90.17	13	115.45	119.50
5	**43.79**	**46.87**	10	87.17	90.75	13	117.10	120.73
5	**46.87**	**49.95**	10	88.10	91.57	13	118.69	122.41
5	47.96	50.79	10	90.36	93.77	13	119.24	122.79
						13	119.29	123.04
6	47.54	50.94	11	90.54	94.05			
6	48.06	51.49	11	90.70	94.48	14	119.04	123.37
6	49.17	52.53	11	91.47	95.15	14	121.74	126.07
6	51.38	54.10	11	92.20	96.00	14	122.62	126.65
6	**52.85**	**55.44**	11	93.31	97.22	14	123.13	126.87
6	**56.02**	**58.61**	11	93.70	97.69	14	123.87	127.65
6	57.26	59.87	11	94.10	98.20	14	124.35	128.45
			11	95.04	98.50	14	125.10	129.15
			11	96.29	99.57	14	126.60	131.03
			11	97.80	100.84	14	127.15	131.65
			11	97.90	100.99	14	127.60	132.08
			11	98.57	102.07	14	127.79	132.33
			11	98.97	102.49	14	128.30	132.70
			11	99.55	103.14	14	128.35	132.75
			11	99.75	103.26			

Table B.4: Mapping pairs from mbsf to rmcd for Site 1052, Hole F. Consecutive bold figures indicate that these points define the splice path, i.e. the depth of data between these points are not compressed or expanded. These data are also available in electronic form from the enclosed CD-ROM, and a hard copy is available from the Godwin Laboratory [123].

Mapping pairs from rmcd to age, Leg 171B, Site 1052							
rmcd	age [Ma]	rmcd	age [Ma]	rmcd	age [Ma]	rmcd	age [Ma]
1.60	34.875	47.15	36.288	80.65	37.367	109.65	38.248
2.00	34.892	48.50	36.338	81.35	37.389	111.65	38.317
3.85	34.933	49.65	36.377	82.05	37.409	113.65	38.380
5.90	35.007	51.30	36.437	83.60	37.451	114.55	38.426
7.75	35.070	52.50	36.471	84.50	37.479	114.60	39.031
9.20	35.109	54.10	36.513	86.65	37.565	116.30	39.078
10.65	35.146	55.05	36.551	87.70	37.597	117.20	39.097
12.00	35.185	57.70	36.614	88.45	37.621	119.00	39.135
13.65	35.239	60.05	36.686	88.95	37.639	120.75	39.209
15.40	35.291	60.55	36.706	89.85	37.669	121.55	39.248
16.70	35.333	61.15	36.728	90.40	37.691	123.10	39.288
18.95	35.392	61.85	36.763	91.20	37.713	124.60	39.337
21.10	35.454	62.45	36.790	91.85	37.738	125.45	39.359
22.35	35.496	63.45	36.825	92.40	37.762	126.15	39.379
23.85	35.529	64.40	36.856	93.15	37.784	127.50	39.416
24.95	35.570	64.95	36.879	94.35	37.816	128.45	39.453
26.65	35.622	65.60	36.896	95.65	37.854	129.10	39.470
27.65	35.645	67.05	36.938	97.25	37.896	130.10	39.502
29.30	35.688	67.85	36.957	98.45	37.935	131.00	39.530
32.25	35.758	68.50	36.990	100.05	37.980	131.65	39.568
35.35	35.849	69.00	37.010	102.65	38.046	133.25	39.619
36.80	35.903	70.85	37.083	103.35	38.066	135.10	39.661
38.30	35.966	74.05	37.162	104.05	38.086	136.55	39.732
41.25	36.042	75.90	37.234	104.80	38.111	138.05	39.774
43.55	36.128	77.05	37.274	105.70	38.135	138.70	39.797
45.25	36.197	78.40	37.305	107.40	38.179	141.05	39.888
46.35	36.240	80.05	37.347	108.25	38.199		

Table B.5: Mapping pairs from rmcd to astronomically calibrated age for Site 1052. Ages were linearly interpolated between these tie points. These data are also available in electronic form from the enclosed CD-ROM, and a hard copy is available from the Godwin Laboratory [123].

Appendix C

Stacked colour reflectance and XRF data from ODP 171B-1052

Colour reflectance and XRF data (stacked and interpolated)				
depth [rmcd]	L*	a*	b*	XRF Ca/Fe
0.05	53.32	0.73	6.80	-
0.10	50.58	2.40	9.49	-
0.15	51.78	2.61	10.18	-
0.20	47.05	1.25	8.01	-
0.25	51.95	3.14	11.33	-
0.30	54.48	3.94	12.88	-
0.35	55.48	3.72	12.92	-
0.40	56.35	3.38	12.79	-
0.45	57.22	3.04	12.66	-
0.50	58.08	2.70	12.53	-
0.55	58.95	2.36	12.40	-
0.60	59.82	2.02	12.27	-
0.65	60.69	1.68	12.14	-
0.70	61.55	1.34	12.01	-
0.75	62.42	1.00	11.88	-
0.80	63.29	0.66	11.75	12.59
0.85	65.87	0.30	11.75	16.23
0.90	76.96	-0.12	12.43	18.01
0.95	79.28	-0.24	12.72	18.76
1.00	79.57	-0.44	12.75	18.86
1.05	80.10	-0.44	12.81	18.42
1.10	80.39	-0.35	13.06	15.87
1.15	81.10	-0.43	13.36	15.18
			...	
			...	
			...	
116.05	76.04	-3.15	4.25	36.30
116.10	75.64	-3.21	4.23	40.02
116.15	75.89	-3.32	4.19	38.57
116.20	75.66	-3.30	4.11	39.29
116.25	74.95	-3.23	3.95	36.86
116.30	74.13	-3.20	4.10	-
116.35	74.52	-3.24	4.41	-
116.40	75.15	-3.15	4.39	-
116.45	75.48	-3.05	4.36	-
			...	
			...	
remaining data of this table can be found on the enclosed CD-ROM				
			...	
			...	
141.50	78.03	-1.61	2.53	-
141.55	77.12	-1.51	2.61	-
141.60	75.28	-1.31	2.72	-

Table C.1: Interpolated and stacked XRF and colour measurements from Leg 171B, Site 1052. The data set is too large to be included as hard copy. The remainder of the data can be found on the enclosed CD-ROM, and a hard copy is available from the Godwin Laboratory [123].

Appendix D

Stable isotope measurements from ODP 171B-1052

Benthic stable isotope measurements Site 1052, Hole A											
Sample	Hole	Core	Sec	top cm	bot. cm	mbsf	rmcd	age [Ma]	Species	δ^{18}O (VPDB)	δ^{13}C (VPDB)
M98/2841	ODP1052A	8H	1	113	116	61.87	67.82	36.956	CIBEO	1.075	0.961
M98/2842	ODP1052A	8H	1	123	126	61.97	67.92	36.961	CIBEO	0.803	1.210
M98/2843	ODP1052A	8H	1	133	136	62.07	68.02	36.966	CIBEO	0.969	1.397
M98/2844	ODP1052A	8H	1	143	146	62.17	68.12	36.971	CIBEO	0.728	1.146
M98/2845	ODP1052A	8H	2	3	6	62.27	68.22	36.976	CIBEO	0.945	1.314
M98/2847	ODP1052A	8H	2	13	16	62.37	68.32	36.981	CIBEO	1.009	1.352
M98/2848	ODP1052A	8H	2	23	26	62.47	68.42	36.986	CIBEO	0.977	1.314
M98/2849	ODP1052A	8H	2	33	36	62.57	68.52	36.991	CIBEO	0.745	1.144
M98/2850	ODP1052A	8H	2	43	46	62.67	68.62	36.995	CIBEO	0.284	1.003
M98/2851	ODP1052A	8H	2	53	56	62.77	68.72	36.999	CIBEO	0.874	1.306
M98/2854	ODP1052A	8H	2	83	86	63.07	69.02	37.011	CIBEO	0.866	1.169
M98/2855	ODP1052A	8H	2	93	96	63.17	69.12	37.015	CIBEO	0.883	1.194
M98/2856	ODP1052A	8H	2	103	106	63.27	69.22	37.019	CIBEO	0.801	1.254
M98/2857	ODP1052A	8H	2	113	116	63.37	69.32	37.023	CIBEO	0.978	1.124
M98/2858	ODP1052A	8H	2	133	136	63.57	69.52	37.031	CIBEO	0.756	1.168
M98/2859	ODP1052A	8H	2	143	146	63.67	69.62	37.035	CIBEO	0.843	1.308
M98/2860	ODP1052A	8H	3	3	6	63.77	69.72	37.039	CIBEO	0.880	1.311
M98/2861	ODP1052A	8H	3	13	16	63.87	69.82	37.043	CIBEO	0.942	1.235
M98/2862	ODP1052A	8H	3	23	26	63.97	69.92	37.046	CIBEO	0.979	1.313
M98/2863	ODP1052A	8H	3	33	36	64.07	70.02	37.050	CIBEO	0.897	1.245
M98/2864	ODP1052A	8H	3	43	46	64.17	70.12	37.054	CIBEO	0.934	1.194
M98/2865	ODP1052A	8H	3	54	57	64.28	70.23	37.059	CIBEO	0.911	1.242
M98/2866	ODP1052A	8H	3	63	66	64.37	70.32	37.062	CIBEO	0.690	1.168
M98/2867	ODP1052A	8H	3	73	76	64.47	70.42	37.066	CIBEO	0.886	1.059
M98/2868	ODP1052A	8H	3	103	106	64.77	70.72	37.078	CIBEO	0.933	1.254

Table D.1: Benthic foraminiferal stable isotope measurements, Site 1052, Hole A. Isotope values are given as permil values relative to the VPDB standard. The first column gives the Godwin laboratory sample code: Codes beginning with "S" were measured using a VG Prism machine, "M" represents a VG Sira machine. The species code represents the genus and species, e.g. CIBEO represents *Cibicidoides eoceanus*, and NUTT stands for *Nuttalides truempyi*. These data are also available in electronic form from the enclosed CD-ROM, and a hard copy is available from the Godwin Laboratory [123].

Benthic stable isotope measurements Site 1052, Hole B											
Sample	Hole	Core	Sec	top cm	bot. cm	mbsf	rmcd	age [Ma]	Species	δ^{18}O (VPDB)	δ^{13}C (VPDB)
M98/3231	ODP1052B	4H	2	33	36	25.98	29.87	35.702	CIBPM	0.532	1.376
M98/3237	ODP1052B	4H	2	63	66	26.28	30.17	35.709	CIBMIC	0.380	1.244
M98/3238	ODP1052B	4H	2	73	76	26.38	30.27	35.711	CIBEO	0.513	1.274
M98/3239	ODP1052B	4H	2	83	86	26.48	30.37	35.714	CIBEO	0.715	1.334
M98/3241	ODP1052B	4H	2	93	96	26.58	30.47	35.716	CIBEO	0.398	1.257
M98/3243	ODP1052B	4H	2	103	106	26.68	30.57	35.718	CIBEO	0.294	1.062
M98/3244	ODP1052B	4H	2	113	116	26.78	30.67	35.721	CIBEO	0.606	1.417
M98/3245	ODP1052B	4H	2	123	126	26.88	30.77	35.723	CIBEO	0.310	1.087
M98/3242	ODP1052B	4H	3	3	6	27.18	31.07	35.730	CIBEO	0.241	1.190
M98/0918	ODP1052B	5H	2	33	35	35.37	39.06	35.986	CIBMEX	0.804	1.628
M98/0922	ODP1052B	5H	2	43	46	35.47	39.16	35.988	CIBEO	0.756	1.582
M98/0925	ODP1052B	5H	2	63	66	35.67	39.36	35.993	CIBEO	0.868	1.510
M98/0927	ODP1052B	5H	2	73	76	35.77	39.42	35.995	CIBEO	0.793	1.555
M98/0931	ODP1052B	5H	2	93	96	35.97	39.58	35.999	CIBEO	0.757	1.451
M98/0936	ODP1052B	5H	2	113	116	36.17	39.84	36.006	CIBEO	0.774	1.522
M98/0937	ODP1052B	5H	2	123	126	36.27	39.97	36.009	CIBEO	0.841	1.600
M98/0940	ODP1052B	5H	2	133	136	36.37	40.09	36.012	CIBPM	0.834	1.456
M98/0942	ODP1052B	5H	2	143	146	36.47	40.22	36.015	CIBPM	1.013	1.623
M98/0945	ODP1052B	5H	3	13	16	36.67	40.47	36.022	CIBEO	0.636	1.214
M98/0949	ODP1052B	5H	3	33	36	36.87	40.73	36.029	CIBEO	0.616	1.322
						...					
						...					
						...					
						remaining data of this table can be found on the enclosed CD-ROM					
						...					
						...					
						...					
M01/2280	ODP1052B	10H	5	53	56	78.53	85.13	37.504	NUTT	0.703	0.940
M01/2281	ODP1052B	10H	5	63	66	78.63	85.23	37.508	NUTT	0.687	0.944
M01/2282	ODP1052B	10H	5	73	76	78.73	85.33	37.512	NUTT	0.652	0.882
M01/2283	ODP1052B	10H	5	83	86	78.83	85.43	37.516	NUTT	0.766	0.922
M01/2284	ODP1052B	10H	5	93	96	78.93	85.53	37.520	NUTT	0.721	1.011
M01/2286	ODP1052B	10H	5	113	116	79.13	85.73	37.528	NUTT	0.711	0.895
M01/2287	ODP1052B	10H	5	123	126	79.23	85.83	37.532	NUTT	0.735	0.896
M01/2288	ODP1052B	10H	5	133	136	79.33	85.93	37.536	NUTT	0.810	0.883
M01/2289	ODP1052B	10H	5	143	146	79.43	86.03	37.540	NUTT	0.775	0.982
S01/0641	ODP1052B	10H	6	3	6	79.53	86.13	37.544	NUTT	0.721	1.105
S01/0642	ODP1052B	10H	6	13	16	79.63	86.23	37.548	NUTT	0.779	0.931
S01/0643	ODP1052B	10H	6	23	26	79.73	86.33	37.552	NUTT	0.817	0.962
S01/0644	ODP1052B	10H	6	33	36	79.83	86.43	37.556	NUTT	0.835	0.940
S01/0645	ODP1052B	10H	6	43	46	79.93	86.53	37.560	NUTT	0.783	0.877
S01/0646	ODP1052B	10H	6	53	56	80.03	86.63	37.564	NUTT	0.762	0.909
S01/0647	ODP1052B	10H	6	63	66	80.13	86.73	37.568	NUTT	0.850	0.991
S01/0648	ODP1052B	10H	6	73	76	80.23	86.83	37.571	NUTT	0.878	1.044
S01/0649	ODP1052B	10H	6	83	86	80.33	86.93	37.574	NUTT	0.886	0.936
S01/0650	ODP1052B	10H	6	93	96	80.43	87.03	37.577	NUTT	0.874	0.989
S01/0651	ODP1052B	10H	6	103	106	80.53	87.13	37.580	NUTT	0.938	1.018
S01/0652	ODP1052B	10H	6	113	116	80.63	87.23	37.583	NUTT	0.846	1.010
S01/0653	ODP1052B	10H	6	123	126	80.73	87.33	37.586	NUTT	0.734	0.907

Table D.2: Benthic foraminiferal stable isotope measurements, Site 1052, Hole B. The data set is too large to be included as hard copy. The remainder of the data can be found on the enclosed CD-ROM, and a hard copy is available from the Godwin Laboratory [123].

Benthic stable isotope measurements Site 1052, Hole F											
Sample	Hole	Core	Sec	top cm	bot. cm	mbsf	rmcd	age [Ma]	Species	δ^{18}O (VPDB)	δ^{13}C (VPDB)
M98/3457	ODP1052F	1H	1	84	86	1.08	1.08	34.853	CIBEO	1.062	1.222
M98/3460	ODP1052F	1H	1	104	106	1.28	1.28	34.861	CIBEO	0.932	1.443
M98/3462	ODP1052F	1H	1	124	126	1.48	1.48	34.870	CIBEO	1.217	1.009
M98/4041	ODP1052F	1H	1	144	146	1.68	1.68	34.878	CIBEO	1.219	1.443
M98/4043	ODP1052F	1H	2	14	16	1.88	1.88	34.887	CIBEO	1.741	1.323
M98/4044	ODP1052F	1H	2	24	26	1.98	1.98	34.891	CIBEO	1.175	1.515
M98/4047	ODP1052F	1H	2	54	56	2.28	2.28	34.898	CIBEO	1.101	1.353
M98/4051	ODP1052F	1H	2	84	86	2.58	2.58	34.905	CIBEO	1.282	1.305
M98/4052	ODP1052F	1H	2	94	96	2.68	2.68	34.907	CIBEO	1.393	1.507
M98/4053	ODP1052F	1H	2	104	106	2.78	2.78	34.909	CIBEO	0.987	1.437
M98/4056	ODP1052F	1H	2	124	126	2.98	2.98	34.914	CIBEO	0.893	1.511
M98/4057	ODP1052F	1H	2	134	136	3.08	3.08	34.916	CIBEO	1.064	1.539
M98/4063	ODP1052F	1H	3	34	36	3.58	3.58	34.927	CIBEO	1.010	1.697
M98/4066	ODP1052F	1H	3	44	46	3.68	3.68	34.929	CIBEO	1.036	1.617
M98/4069	ODP1052F	1H	3	54	56	3.78	3.78	34.931	CIBEO	1.451	1.577
M98/4070	ODP1052F	1H	3	64	66	3.88	3.88	34.934	CIBEO	0.815	1.611
M98/4111	ODP1052F	1H	3	74	76	3.98	3.98	34.938	CIBEO	0.969	1.711
M98/4113	ODP1052F	1H	3	84	86	4.08	4.08	34.941	CIBEO	0.970	1.610
M98/4114	ODP1052F	1H	3	94	96	4.18	4.18	34.945	CIBEO	1.016	1.707
...											
...											
...											
remaining data of this table can be found on the enclosed CD-ROM											
...											
...											
...											
S01/0677	ODP1052F	10H	4	13	16	85.63	89.23	37.648	NUTT	0.876	1.095
S01/0678	ODP1052F	10H	4	23	26	85.73	89.34	37.652	NUTT	1.141	1.195
S01/0679	ODP1052F	10H	4	33	36	85.83	89.44	37.655	NUTT	0.877	1.003
S01/0680	ODP1052F	10H	4	43	46	85.93	89.55	37.659	NUTT	1.062	1.021
S01/0681	ODP1052F	10H	4	53	56	86.03	89.66	37.663	NUTT	0.658	1.009
S01/0682	ODP1052F	10H	4	63	66	86.13	89.76	37.666	NUTT	1.172	1.016
S01/0683	ODP1052F	10H	4	83	86	86.33	89.98	37.674	NUTT	0.908	0.974
S01/0684	ODP1052F	10H	4	93	96	86.43	90.08	37.678	NUTT	1.013	0.983
S01/0685	ODP1052F	10H	4	103	106	86.53	90.19	37.683	NUTT	0.888	0.926
S01/0686	ODP1052F	10H	4	113	116	86.63	90.28	37.686	NUTT	0.774	0.868
S01/0687	ODP1052F	10H	4	123	126	86.73	90.36	37.690	NUTT	0.819	0.965
S01/0688	ODP1052F	10H	4	133	136	86.83	90.45	37.692	NUTT	0.974	1.176
S01/0689	ODP1052F	10H	4	143	146	86.93	90.54	37.695	NUTT	0.779	1.025
S01/0690	ODP1052F	10H	5	3	6	87.03	90.63	37.697	NUTT	0.815	1.036
S01/0691	ODP1052F	10H	5	13	16	87.13	90.71	37.700	NUTT	0.990	1.081
S01/0692	ODP1052F	10H	5	23	26	87.23	90.80	37.702	NUTT	0.935	1.021
S01/0693	ODP1052F	10H	5	33	36	87.33	90.89	37.705	NUTT	0.791	1.156
S01/0694	ODP1052F	10H	5	43	46	87.43	90.98	37.707	NUTT	1.036	1.022
S01/0791	ODP1052F	10H	5	53	56	87.53	91.07	37.709	NUTT	0.777	0.964
S01/0696	ODP1052F	10H	5	63	66	87.63	91.16	37.712	NUTT	1.296	0.986
S01/0697	ODP1052F	10H	5	73	76	87.73	91.24	37.715	NUTT	1.031	1.094
S01/0698	ODP1052F	10H	5	83	86	87.83	91.33	37.718	NUTT	0.795	0.934

Table D.3: Benthic foraminiferal stable isotope measurements, Site 1052, Hole F. The data set is too large to be included as hard copy. The remainder of the data can be found on the enclosed CD-ROM, and a hard copy is available from the Godwin Laboratory [123].

Stable isotope bulk sediment measurements Site 1052, Hole B									
Sample	Hole	Core	Sec	cm	mbsf	rmcd	age [Ma]	δ^{18}O (VPDB)	δ^{13}C (VPDB)
S98/0071	ODP1052F	4H	1	63	24.78	28.80	35.675	0.371	1.997
S98/0281	ODP1052B	5H	2	33	35.37	39.06	35.986	0.493	1.978
S98/0282	ODP1052B	5H	2	43	35.47	39.16	35.988	0.045	1.964
S98/0283	ODP1052B	5H	2	53	35.57	39.26	35.991	0.376	2.041
S98/0284	ODP1052B	5H	2	63	35.67	39.36	35.993	0.418	2.021
S98/0285	ODP1052B	5H	2	73	35.77	39.42	35.995	0.389	1.789
S98/0286	ODP1052B	5H	2	83	35.87	39.47	35.996	0.430	1.951
S98/0287	ODP1052B	5H	2	93	35.97	39.58	35.999	0.212	1.972
S98/0288	ODP1052B	5H	2	103	36.07	39.71	36.002	0.303	1.886
S98/0289	ODP1052B	5H	2	113	36.17	39.84	36.006	-0.005	1.942
S98/0290	ODP1052B	5H	2	123	36.27	39.97	36.009	0.446	1.972
S98/0291	ODP1052B	5H	2	133	36.37	40.09	36.012	-0.163	2.049
S98/0292	ODP1052B	5H	2	143	36.47	40.22	36.015	0.329	2.013
S98/0293	ODP1052B	5H	3	3	36.57	40.35	36.019	0.670	1.930
S98/0294	ODP1052B	5H	3	13	36.67	40.47	36.022	0.332	1.890
S98/0295	ODP1052B	5H	3	23	36.77	40.60	36.025	0.443	1.921
S98/0296	ODP1052B	5H	3	33	36.87	40.73	36.029	0.540	2.006
S98/0297	ODP1052B	5H	3	43	36.97	40.86	36.032	0.641	2.048
S98/0298	ODP1052B	5H	3	53	37.07	40.98	36.035	0.493	2.046
S98/0299	ODP1052B	5H	3	63	37.17	41.11	36.038	0.244	2.025
S98/0300	ODP1052B	5H	3	73	37.27	41.23	36.042	0.076	2.065
S98/0301	ODP1052B	5H	3	83	37.37	41.36	36.046	0.567	2.094
S98/0302	ODP1052B	5H	3	93	37.47	41.48	36.051	0.438	2.069
S98/0303	ODP1052B	5H	3	103	37.57	41.60	36.055	0.540	2.090
S98/0304	ODP1052B	5H	3	113	37.67	41.73	36.060	0.361	2.002
S98/0305	ODP1052B	5H	3	123	37.77	41.85	36.065	0.603	2.039
S98/0306	ODP1052B	5H	3	133	37.87	41.98	36.069	0.184	2.110
S98/0307	ODP1052B	5H	3	143	37.97	42.12	36.074	0.035	2.032
S98/0311	ODP1052B	6H	1	73	43.77	49.57	36.374	0.590	1.893
S98/0312	ODP1052B	6H	1	83	43.87	49.66	36.378	0.541	1.873
S98/0313	ODP1052B	6H	1	93	43.97	49.76	36.381	0.752	1.845
S98/0314	ODP1052B	6H	1	103	44.07	49.86	36.385	0.643	1.828
S98/0315	ODP1052B	6H	1	113	44.17	49.96	36.388	0.484	1.738
S98/0316	ODP1052B	6H	1	123	44.27	50.05	36.392	0.925	1.798
S98/0317	ODP1052B	6H	1	133	44.37	50.15	36.395	0.545	1.736
S98/0318	ODP1052B	6H	1	143	44.47	50.25	36.399	0.686	1.743
S98/0319	ODP1052B	6H	2	3	44.57	50.35	36.402	0.427	1.709
S98/0320	ODP1052B	6H	2	13	44.67	50.45	36.406	0.488	1.815
S98/0321	ODP1052B	6H	2	23	44.77	50.54	36.409	0.899	1.823
S98/0322	ODP1052B	6H	2	33	44.87	50.64	36.413	0.570	1.717
S98/0323	ODP1052B	6H	2	43	44.97	50.74	36.417	0.531	1.793
S98/0324	ODP1052B	6H	2	53	45.07	50.84	36.420	0.405	1.693
S98/0325	ODP1052B	6H	2	63	45.17	50.93	36.424	0.466	1.745
S98/0326	ODP1052B	6H	2	73	45.27	51.03	36.427	0.667	1.738
S98/0327	ODP1052B	6H	2	83	45.37	51.13	36.431	0.688	1.727
S98/0328	ODP1052B	6H	2	93	45.47	51.22	36.434	0.749	1.747
S98/0329	ODP1052B	6H	2	103	45.57	51.32	36.438	0.439	1.747
S98/0330	ODP1052B	6H	2	113	45.67	51.42	36.440	0.430	1.727
S98/0331	ODP1052B	6H	2	123	45.77	51.52	36.443	0.711	1.707
S98/0332	ODP1052B	6H	2	133	45.87	51.61	36.446	0.612	1.722
S98/0333	ODP1052B	6H	2	143	45.97	51.69	36.448	0.673	1.699

Table D.4: Stable isotope bulk sediment measurements, Site 1052, Hole B. The data are also available in electronic form from the enclosed CD-ROM, and a hard copy is available from the Godwin Laboratory [123].

Stable isotope bulk sediment measurements Site 1052, Hole F									
Sample	Hole	Core	Sec	cm	mbsf	rmcd	age [Ma]	δ^{18}O (VPDB)	δ^{13}C (VPDB)
C99/0001	ODP1052F	4H	1	63	29.21	31.21	35.733	0.530	1.930
C99/0041	ODP1052F	4H	1	63	29.21	31.21	35.733	0.480	1.890
C99/0081	ODP1052F	4H	1	63	29.21	31.21	35.733	0.350	1.950
S98/0071	ODP1052F	4H	1	63	29.21	31.21	35.733	0.371	1.997
S98/0101	ODP1052F	4H	1	63	29.21	31.21	35.733	0.647	2.001
C99/0002	ODP1052F	4H	1	73	29.31	31.30	35.735	0.940	2.030
C99/0042	ODP1052F	4H	1	73	29.31	31.30	35.735	0.790	1.980
C99/0082	ODP1052F	4H	1	73	29.31	31.30	35.735	0.660	1.980
S98/0072	ODP1052F	4H	1	73	29.31	31.30	35.735	0.384	2.018
S98/0102	ODP1052F	4H	1	73	29.31	31.30	35.735	0.350	2.022
C99/0003	ODP1052F	4H	1	83	29.41	31.39	35.738	0.940	2.070
C99/0043	ODP1052F	4H	1	83	29.41	31.39	35.738	0.740	1.990
C99/0083	ODP1052F	4H	1	83	29.41	31.39	35.738	0.610	2.010
S98/0073	ODP1052F	4H	1	83	29.41	31.39	35.738	0.437	2.071
S98/0103	ODP1052F	4H	1	83	29.41	31.39	35.738	0.403	2.011
C99/0004	ODP1052F	4H	1	93	29.51	31.48	35.740	0.870	2.120
C99/0044	ODP1052F	4H	1	93	29.51	31.48	35.740	0.940	2.040
C99/0084	ODP1052F	4H	1	93	29.51	31.48	35.740	0.690	2.040
S98/0074	ODP1052F	4H	1	93	29.51	31.48	35.740	0.440	2.071
S98/0104	ODP1052F	4H	1	93	29.51	31.48	35.740	0.386	2.065
C99/0005	ODP1052F	4H	1	103	29.61	31.57	35.742	0.700	2.010
C99/0045	ODP1052F	4H	1	103	29.61	31.57	35.742	0.690	2.010
C99/0085	ODP1052F	4H	1	103	29.61	31.57	35.742	0.720	2.000
				...					
				...					
				...					
				remaining data of this table can be found on the enclosed CD-ROM					
				...					
				...					
				...					
S98/0258	ODP1052F	6H	5	70	54.24	56.83	36.593	0.703	1.924
S98/0259	ODP1052F	6H	5	80	54.34	56.93	36.596	0.895	1.962
S98/0260	ODP1052F	6H	5	90	54.44	57.03	36.598	0.798	1.903
S98/0261	ODP1052F	6H	5	100	54.54	57.13	36.601	0.580	1.816
S98/0262	ODP1052F	6H	5	110	54.64	57.23	36.603	0.532	1.840
S98/0263	ODP1052F	6H	5	120	54.74	57.33	36.605	0.585	1.851
S98/0264	ODP1052F	6H	5	130	54.84	57.43	36.608	0.727	1.816
S98/0265	ODP1052F	6H	5	140	54.94	57.53	36.610	0.699	1.679
S98/0266	ODP1052F	6H	6	0	55.04	57.63	36.612	0.681	1.720
S98/0267	ODP1052F	6H	6	10	55.14	57.73	36.615	0.714	1.742
S98/0268	ODP1052F	6H	6	20	55.24	57.83	36.618	0.686	1.723
S98/0269	ODP1052F	6H	6	40	55.44	58.03	36.624	0.718	1.756
S98/0270	ODP1052F	6H	6	50	55.54	58.13	36.627	0.701	1.822
S98/0271	ODP1052F	6H	6	60	55.64	58.23	36.630	0.663	1.857
S98/0272	ODP1052F	6H	6	70	55.74	58.33	36.633	0.685	1.815
S98/0273	ODP1052F	6H	6	80	55.84	58.43	36.637	0.588	1.895
S98/0274	ODP1052F	6H	6	90	55.94	58.53	36.640	0.640	1.873
S98/0275	ODP1052F	6H	6	100	56.04	58.63	36.643	0.772	1.860
S98/0276	ODP1052F	6H	6	110	56.14	58.74	36.646	0.775	1.808
S98/0277	ODP1052F	6H	6	120	56.24	58.84	36.649	0.697	1.780
S98/0278	ODP1052F	6H	6	130	56.34	58.94	36.652	0.899	1.850
S98/0279	ODP1052F	6H	6	140	56.44	59.04	36.655	0.472	1.791

Table D.5: Stable isotope bulk sediment measurements, Site 1052, Hole F. The data set is too large to be included as hard copy. The remainder of the data can be found on the enclosed CD-ROM, and a hard copy is available from the Godwin Laboratory [123].

Appendix E

Reflectance data and age model from ODP 177-1090, Hole B

Lightness values from ODP Leg 177, Site 1090, Hole B interpolated at 2 cm intervals							
depth [mbsf]	light.	depth [mbsf]	light.	depth [mbsf]	light.	depth [mbsf]	light.
212.00	102.4	246.52	148.3	281.04	103.5	315.56	136.3
212.02	109.6	246.54	147.3	281.06	110.2	315.58	145.8
212.04	105.2	246.56	151.1	281.08	115.3	315.60	150.7
212.06	99.6	246.58	155.1	281.10	122.9	315.62	154.5
212.08	97.1	246.60	153.4	281.12	133.2	315.64	158.6
212.10	96.8	246.62	149.0	281.14	137.0	315.66	164.6
212.12	100.6	246.64	143.0	281.16	137.0	315.68	161.0
212.14	102.8	246.66	143.0	281.18	138.3	315.70	166.8
212.16	104.8	246.68	136.1	281.20	139.4	315.72	175.2
212.18	105.8	246.70	136.0	281.22	137.8	315.74	172.2
212.20	110.8	246.72	136.7	281.24	135.4	315.76	173.3
212.22	115.2	246.74	139.0	281.26	135.2	315.78	178.8
212.24	122.8	246.76	141.1	281.28	136.6	315.80	182.4
212.26	127.8	246.78	144.0	281.30	136.3	315.82	180.5
212.28	136.8	246.80	145.0	281.32	136.7	315.84	166.0
212.30	139.0	246.82	147.1	281.34	135.6	315.86	165.1
212.32	138.0	246.84	146.1	281.36	139.9	315.88	172.6
212.34	139.6	246.86	148.6	281.38	145.6	315.90	170.5
...							
...							
remaining data of this table can be found on the enclosed CD-ROM							
...							
...							
246.18	154.6	280.70	138.2	315.22	154.8	349.74	124.6
246.20	145.1	280.72	138.8	315.24	150.5	349.76	125.2
246.22	136.1	280.74	137.3	315.26	141.3	349.78	127.0
246.24	145.6	280.76	123.0	315.28	129.9	349.80	128.3
246.26	126.8	280.78	116.6	315.30	128.1	349.82	136.3
246.28	121.5	280.80	112.6	315.32	129.1	349.84	135.0
246.30	120.5	280.82	109.3	315.34	129.3	349.86	133.6
246.32	126.0	280.84	106.6	315.36	126.9	349.88	133.2
246.34	125.1	280.86	105.8	315.38	127.0	349.90	132.1
246.36	126.3	280.88	105.5	315.40	127.2	349.92	132.6
246.38	128.2	280.90	104.7	315.42	125.9	349.94	139.0
246.40	131.6	280.92	102.8	315.44	127.7	349.96	141.6
246.42	136.8	280.94	100.9	315.46	134.7	349.98	144.6
246.44	138.5	280.96	102.5	315.48	131.8	350.00	146.7
246.46	138.5	280.98	108.4	315.50	136.1		
246.48	143.2	281.00	102.6	315.52	131.8		
246.50	146.1	281.02	103.3	315.54	131.9		

Table E.1: Interpolated colour reflectance data from Leg 177, Site 1090, Hole B. Values can range from 0 (black) to 255 (white). The data set is too large to be included as hard copy. The remainder of the data can be found on the enclosed CD-ROM, and a hard copy is available from the Godwin Laboratory [123].

Mapping pairs from mbsf to age, Leg 177, Site 1090, Hole B					
mbsf	age [Ma]	mbsf	age [Ma]	mbsf	age [Ma]
212.02	32.126	246.54	34.487	303.40	36.199
213.92	33.082	246.90	34.509	304.86	36.287
215.04	33.101	247.18	34.529	305.40	36.328
215.82	33.123	248.08	34.578	306.94	36.439
216.42	33.137	248.70	34.621	307.54	36.457
216.98	33.160	249.60	34.658	308.62	36.512
217.68	33.180	249.94	34.676	310.14	36.578
220.58	33.251	250.22	34.693	311.08	36.615
221.20	33.281	251.34	34.733	312.04	36.685
222.48	33.321	253.00	34.830	312.52	36.706
223.44	33.364	254.24	34.883	313.54	36.779
225.74	33.407	254.78	34.903	315.34	36.824
228.06	33.467	256.70	34.925	317.46	36.898
229.20	33.495	258.66	34.949	318.94	36.967
230.28	33.533	263.00	35.007	320.44	37.024
233.98	33.760	266.64	35.106	321.90	37.062
234.76	33.804	269.76	35.185	322.82	37.087
235.60	33.852	274.86	35.280	324.26	37.117
236.10	33.875	278.66	35.373	325.74	37.191
237.52	33.948	279.36	35.407	326.18	37.214
238.42	34.002	280.48	35.451	327.92	37.305
238.86	34.021	281.94	35.529	330.68	37.437
239.52	34.042	282.64	35.570	331.36	37.498
240.26	34.090	285.30	35.646	331.72	37.552
242.56	34.265	286.38	35.685	332.80	37.670
243.20	34.298	288.22	35.756	334.22	37.781
244.06	34.347	289.68	35.811	335.50	38.186
244.64	34.385	291.16	35.849	348.00	39.828
245.62	34.428	293.90	35.911		
246.18	34.466	296.56	35.964		

Table E.2: Mapping pairs from mbsf to age for Site 1090, Hole B. These data are also available in electronic form from the enclosed CD-ROM, and a hard copy is available from the Godwin Laboratory [123].